in situ TEM Characterization and Modulation for Phase Engineering of Nanomaterials

Ying Han,[1] Liqiang Wang,[1] Ke Cao,[3] Jingzhuo Zhou,[1] Yingxin Zhu,[1] Yuan Hou[1], Yang Lu[2*]

[1]Department of Mechanical Engineering, City University of Hong Kong, Kowloon 999077, Hong Kong SAR, China
[2]Department of Mechanical Engineering, The University of Hong Kong, Pokfulam 999077, Hong Kong SAR, China
[3]School of Advanced Materials and Nanotechnology, Xidian University, Xi'an 710026, China

[*]Corresponding author: Y. Lu (ylu1@hku.hk)

Abstract

Solid state phase transformation is an intriguing phenomenon in crystalline or non-crystalline solids due to the distinct physical and chemical properties that can be obtained and modified by the phase engineering approach. Compared to bulk solids, nanomaterials exhibit enhanced ability for phase engineering due to their small sizes and high surface-to-volume ratios, to facilitate various emerging applications. To establish a comprehensive atomistic scale understanding of phase engineering, *in situ* electron microscopy techniques have emerged as a powerful tool, providing unprecedented atomic-resolution imaging, multiple characterization and stimulation mechanisms, and real-time integrations with various external physical fields. In this Review, we present a comprehensive overview of recent advances in *in situ* transmission electron microscopy (TEM) studies to characterize and modulate crystalline nanomaterials for their phase transformation under different stimuli, including mechanical, thermal, electrical, environmental, optical, and magnetic factors. We briefly introduce crystalline structures and polymorphism, and summarize phase stability and different phase transformation models for quantitative understanding. The advanced experimental setups of those *in situ* techniques are well outlined and the advantages of *in situ* TEM phase engineering are highlighted, as demonstrated via some representative low-dimensional material examples. In addition, we present the distinctive properties that can be obtained from such *in situ* phase engineering. Finally, some current challenges and future research opportunities in this emerging research field as well as their potential applications are suggested.

Contents

1. Introduction

The field of nanoscience and nanotechnology has emerged as a fascinating and rapidly growing area of research.[1-4] Nanomaterials, i.e., materials with dimensions at the nanoscale (typically ranging from 1 to 100 nm), have attracted significant attention due to their unique properties and potential applications in various fields, including catalysis, energy storage, solar cells, electronic devices, and biomedical applications. The increasing demand for nanomaterials with specific physicochemical properties has highlighted the need for both a comprehensive understanding and the ability to tune these properties. Achieving precise control over the properties of nanomaterials is crucial for tailoring their behaviours and optimizing their performance in various applications. Generally, several strategies have been adopted to tune the properties of materials, including alloying, doping, defect engineering, elastic strain engineering, and also phase engineering.[5, 6] Among these strategies, phase engineering modulates the crystalline structure, which changes the atom packing mode and leads to the significantly different properties of crystal materials.[7-9]

The root of the phase engineering is polymorphism, which is “the occurrence of different crystal structures for the same chemical entity” and leads to different properties, including stability,[10, 11] electrical,[12] optical,[13-16] electronic,[17] catalytic,[18] and magnetic[19] properties. For example, a comparison of the optical properties of 4H-Au and face-centered cubic (*fcc*)-Au has been reported,[10] showing the change of the absorption range in UV-vis spectrum, the vibration modes in Raman spectra, and the shift of the surface plasmon resonance (SPR) peaks in electron energy loss spectroscopy (EELS) spectra. A more explicit impact of the phase change is on the catalytic properties, which is associated with the surface geometry as well as the electronic structure, as demonstrated by the higher oxygen reduction reaction activity in face-centered tetragonal (*fct*) FePt@Pt core-shell nanoparticles compared to the *fcc* counterparts.[20, 21] Thus, the phase is of great importance for the physicochemical properties of crystal materials. In bulk materials, numerous phase transformations have been achieved and applied in realistic applications, such as the shape memory alloy used for the actuation tasks in the fields of aerospace, automotive, and biomedical[22], as well as the GeSbTe phase transformation materials used in rewritable optical discs and memories. When it comes to nanomaterials, the formation of metastable phases and phase transformations become easier due to the surface energy effect. This is because the competition between internal packing and minimum surface energy in nanomaterials becomes significant. The surface energy plays a dominant role in the total system energy, which makes the unconventional phase (including the amorphous structure) in nanoscale materials possible by modulating their surface energy.

It has been verified that the size can be a promising approach to expand the polymorphism of noble metals.[23]

By direct synthesis approaches, including various wet chemical methods such as seeded growth, surfactant mediated synthesis, and template growth, the nanomaterials with different sizes, morphologies, facets, dimensions, and phases, as well as even some unconventional phases have been successfully demonstrated,[24-29] such as *fcc*, 2H,[11] 4H,[10] body-centered cubic (*bcc*),[30] body-centered tetragonal (*bct*),[31] body-centered orthorhombic (*bco*),[31] 4H/*fcc* heterophase,[18] *fcc*-2H-*fcc* heterophase Au nanomaterials,[13] and unconventional hexagonal Pd.[32] These unconventional phases also exhibit different properties due to the changes in stacking order.[26] Not only the single element nanomaterials, the binary alloy,[33, 34] medium/high entropy alloy also have different phase.[35-38] Besides the metallic materials, the new family of materials, two-dimensional (2D) materials, also possess polymorphism, e.g., MoS_2 with 2H, 1T, and 1T' phases.[39, 40] Both theoretical research[41] and experimental research[42-44] have already verified that these polymorphisms can be modulated by external stimuli, such as mechanical,[45, 46] thermal,[47] electrical,[48] optical,[43] and environmental field,[49] which is called phase engineering of nanomaterials (PEN).[45, 50, 51]

However, the size of nanomaterials also poses challenges for their characterization and manipulation. The characterization of nanomaterials at the nanoscale requires the use of advanced analytical tools and techniques that can probe their structural, chemical, optical, and electronic properties. Transmission electron microscopy (TEM) is one of the most widely used techniques for the characterization of nanomaterials, allowing high-resolution imaging, structural analysis, microchemical analysis by X-ray energy dispersive spectroscopy (EDS), and the band structure characterization by EELS. It provides valuable information about the microstructure, chemical composition, defect, bonding, and oxidation state of nanomaterials. Besides, TEM can also be equipped with various *in situ* holders (such as thermal, electrical, mechanical, liquid, gas, optical, magnetic, and their combinations) that enable the characterization of nanomaterials under different environmental conditions or during specific processes.[52] These *in situ* holders expand the capabilities of TEM, the so-called TEM Nanolab,[53] allowing researchers to observe and analyse nanomaterials in real time while subjecting them to controlled external stimuli or environmental factors. These techniques provide the exceptional platforms to study the phase transformation mechanism and to modulate the phases of nanomaterials by different external stimuli with not only real time but also high resolution of the entire process. Even the chemical reaction can be observed *in situ* in the TEM Nanolab to demonstrate the atomic level dynamics and the divergent reaction pathways (displacement versus conversion reactions).[54] The valuable information obtained from the *in* *situ* modulation of nanomaterial phases will unveil the atomic mechanisms underlying phase transformations, thereby paving the way for phase engineering of nanomaterials.

There are several landmark review articles that provide comprehensive summaries of the recent advances in *in situ* TEM techniques. These articles cover a wide range of topics, including *in situ* heating, nanomechanical, electrical, optical, environmental, and magnetic studies.[52, 55-61] Here, we mainly focus on the use of *in situ* TEM in PEN. First, we introduce the typical crystal structures of nanomaterials with their characteristics. Second, we discuss the driving force and models of phase transformation. Third, we summarize the recently developed techniques in TEM used to characterize and modulate the phase transformation of nanomaterials, followed by demonstrating the strengths of *in situ* TEM in studying phase transformation for nanomaterials by selected examples. Fourth, the properties modulated by phase engineering are listed, showing the great potential of PEN. Finally, we conclude by offering remarks and delving into the challenges and opportunities within the field.

2. Crystal structures and polymorphics

Polymorphic refers to a crystal material that has different lattice structures within the same chemical composition. For example, the Fe_2O_3 metal oxides are α phase with a corundum-type rhombohedral structure under ambient conditions. However, as the temperature gradually increases, they change to β phase with *bcc* structure up to 773 K, γ phase with cubic spinel structure up to 933 K, and then ε phase with rhombic structure. When the polymorphic structures of a crystal material differ only in their stacking sequence, it is termed polytypism.[62] For example, silicon carbide (SiC) exhibits different repeating sequences for different phases, AB for 2H α-SiC, ABCB for 4H α-SiC, ABCACB for 6H α-SiC, ABCACBCABACABCB for 15R α-SiC, and ABC for 3C β-SiC.[63] And also, most of the polymorphic structures for two-dimensional (2D) materials are polytypisms due to different stacking sequences.[40] Another special polymorphism is called allotropy, which refers to the polymorphism for chemical elements. Take carbon for example, it possesses diamond, graphene, carbon nanotube (CNT), C_{60}, carbyne, graphite, and so on.[64] Also for metal, Fe possesses α-Fe with *bcc* structure under ambient conditions. However, it changes to γ-Fe with *fcc* structure under 912−1394 °C, δ-Fe with *bcc* structure under 1394−1528 °C and ε-Fe with hexagonal-close packed (*hcp*) structure under high pressure. In this section, we introduce the general and metastable crystal structures for low dimensional materials that we focus on for PEN.

The packing of crystals can be classified into two types, Barlow packing and non-Barlow packing. The key difference between them lies in their structural arrangement. Barlow packing refers to the close-packed structures where atoms are densely packed together. On the other hand, non-Barlow packing includes various types of structures beyond the realm of close-packed arrangements. These include *bcc* and simple cubic packing, among others. **Figure 1** shows *bcc* and simple cubic packing with coordination numbers of 8 and 6, respectively. In contrast, Barlow packings are configurations of atoms that are most efficiently arranged in a regular pattern so that each circle is tangent to other atoms with dense layers, always with a coordination number of 12 for each atom.

Well-known examples of Barlow packings are *hcp* and *fcc* packings, where the atoms are arranged in ABABAB… and ABCABC…, respectively (**Figure 1**). As ordered Barlow packings, the *fcc* stacking is also denoted as 3C. And the *hcp* structure is also abbreviated as 2H due to the laminar structure, where 2 represents the minimized periodic number of layers and H refers to the hexagonal Bravais lattice. The hexagonal cell undergoes a phase transition and changes from a 2H structure to different interlayer stacking orders along the <100> direction, i.e., 4H (ABCB), 6H (ABCACB), and 8H (ABCBCBAB), and the 4H phase tends to exhibit higher stability than the 2H phase.[11] The energy differences between 3C, 2H, 4H, and 8H are small enough to be susceptible to phase change.[65]

In addition, the recent emergence of atomically thin 2D materials attracts the attention of researchers due to their unique properties, especially the metal−insulator transition of MX_2, where M is a transition metal (e.g., W and Mo) and X is a chalcogen atom (e.g., S, Se, and Te). Most of the polymorphic structures for 2D materials are polytypism due to different stacking sequences (**Figure 2**).[40] The transition between polytypism of 2D materials can be triggered by different stimuli, such as mechanical strain, thermal treatment, and laser excitation, which is detailed in the following sections.

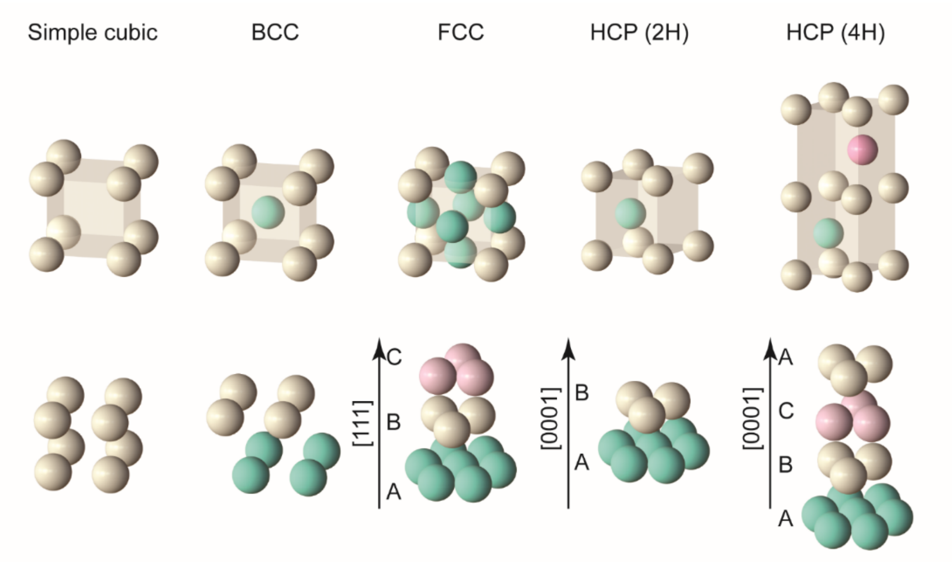

Figure 1. Schematic of the distinct layers in different crystal structures. The crystal structures depicted from left to right are simple cubic, *bcc*, *fcc*, hexagonal close-packed with 2H stacking (*hcp* 2H), and hexagonal close-packed with 4H stacking (*hcp* 4H).

2.1 Face-centered cubic (*fcc*) phase

The *fcc* stacking is a common packing pattern with an ABC stacking sequence (**Figure 1**) in metals with high stability. It belongs to the cubic crystal system and is characterized by the presence of an atom tangent to the atoms in the corners at the center of each face of the unit cell. It can be considered as a different type of interlayer stacking in hexagonal close stacking, so the transformation or mutual inclusion of *hcp* and *fcc* in phase transitions is possible due to their similar laminar and close stacking structures. One distinction is that *fcc* has a higher thermodynamic stability. It will be more ductile than *hcp* stacking due to more slip systems. It has been claimed that some *fcc* noble metal nanocrystals may have small regions containing *hcp* or other metastable phases due to stacking faults.[66] In addition, *fcc* materials usually have better electrical and thermal conductivity than *hcp* materials. However, *fcc* materials may be slightly less corrosion resistant than serval *hcp* materials. For example, titanium (Ti) with *hcp* structure possesses strong corrosion resistance.

The fct structure is similar to *fcc*, but one side of the cell structure is longer than the other. The *fct* structure only exists under certain conditions (e.g., high temperature and pressure) and can be found in certain materials, such as iron (Fe), Ti, and tungsten (W). However, at room temperature and pressure, these metals do not exhibit the *fct* structure. In addition, some intermetallic compounds, such as NiAl, can be observed as *fct* structure at high temperatures but usually exhibit a *bcc* structure at room temperature. Due to the lower packing efficiency, the *fct* structure is less stable than the *bcc* and *fcc* structures. At high pressures and temperatures, the structure is more likely to be destroyed compared to the *fcc* and *bcc* structures. A distortion from *fcc* to *fct* has been observed in Pd nanocubes with an average edge length of about 10 nm under 24.8 GPa pressure induction.[67] Similarly, *bct* and *fct* phases are also found in Ag nanostructures under high pressure, stemming from internal strain-induced deformation of the cubic silver lattice. Each silver nanowire is a core/shell structure with a strained core responsible for the *fct* phase being encased in a thin shell that protects the core with less strain. The core/shell structure, in turn, is capable of storing the high strains associated with tetragonal deformation in a solid core.[68]

2.2 Hexagonal-close packed (*hcp*) phase

The *hcp* stacking is one of the Barlow packings. Its bulk also tends to exhibit a hexagonal form. The unit cells are one third of their stacking type and three cells are present as one to demonstrate their symmetry and interlayer structure. The *hcp* phase can be categorized into 2H, 4H, and even 8H structures based on the periodicity of the interlayer stacking. The numerical value represents the number of layers forming one stacking period, while "H" is the abbreviation for *hcp*. The focus of this discussion is primarily on the more common 2H and 4H structures.

In the 2H structure, each particle is enclosed by six other hexagonal patterns in a dense layered pattern (ABABAB), and the particles in each layer are offset from the particles in the upper and lower layers, referred to as A/B layers, respectively. Materials with a 2H structure have many intriguing properties. Ti and its alloys possess high strength and stiffness as supporting compounds due to the high density of arrangement.[69] Several 2H metals, such as Ti and zirconium (Zr), offer excellent corrosion resistance. And most 2H metals feature high melting points, such as rhenium (Re), which has a melting point of 3174 °C. 2H materials perform special functions in specific applications. Beryllium (Be) and boron (B) have low thermal conductivity and are therefore used as thermal barrier coatings,[70] while GaN with the wurtzite structure is adopted for blue and UV light-emitting diodes (LEDs). This structure is also represented as 2H, which can be viewed as two interpenetrating *hcp* structures.[71]

The 4H structure is also found in some ceramic materials, noble metal alloy nanocrystals and epitaxially grown transition metals (mainly noble metals).[72] Its characteristics are preserved in hexagonal lattices, such as SiC,[73] Ag,[10] Pd, and PdAg.[74] The hexagonal cell undergoes a phase transition and changes from a 2H structure to different interlayer stacking orders along the <100> direction, i.e., 4H (ABCB), 6H (ABCACB), and 8H (ABCBCBAB). The 4H phase tends to exhibit higher stability than the 2H phase.[10] For instance, compared to 2H Au square sheets, 4H Au nanoribbons with a thickness of 2.0 to 6.0 nm exhibit enhanced stability.[75] It is worth noting that the first and last layers are still A/B, with different layers filling in. The crystal structure obtained as a 4H structure preserves a high degree of symmetry and with good structural stability.[65] The interlayer stacking order affects the properties and defects of the structure and is expected to lead to new possibilities for catalytic, plasma, optical, and electrical applications.[76]

It has been reported that aluminium (Al),[77] Ti,[78] Zr,[79] cobalt (Co),[80] copper (Cu), and Au,[81] all undergo a reversible phase transition from *hcp* to *fcc* phase. At certain high temperatures, some metals such as Co,[80] and Ti,[82] undergo a phase change from *hcp* to *bcc*. At the microscopic scale, the mechanism of the phase transition between *hcp* and *fcc* has been a question worthy of exploring. Generally, the phase transition from *hcp* tends to be towards a more stable *fcc* structure (e.g., Ag and Au) when the thickness is increased to bulk size (from ~2.4 to 6 nm). But at the nanoscale, the particle and phase stability are significantly affected by the surface effects. In ultrathin Au square sheets and Au nanowires, *hcp* favored *fcc* phase.[11] The detailed discussion will be included in the following part. Apart from the phase transition to a more stable *fcc*, *hcp* can also be modulated to allow different interlayer stacking structures. As is commonly observed for the 4H phase, its scientific research is considered to be a combination of 3C or 2H stacking modes by producing repetitive misstacked atomic sheets.[83] It is therefore limited to monometallic metals with relatively low layer dislocation energies, such as Au and Ag, which have been observed to crystallize in the 4H phase.

2.3 Body-centered cubic (*bcc*) phase

The *bcc* materials typically have a higher melting point than *fcc* and *hcp* materials, for example, W with a *bcc* structure has a very high melting point of 3410 °C. *Bcc* materials are often less ductile than *fcc* and *hcp* materials, but generally have higher strength.[84, 85] *Bcc* materials are also slightly inferior in terms of thermal and electrical conductivity and corrosion resistance.[86] In fact, in terms of electrical conductivity and thermal conductivity, *fcc* is generally superior to *hcp*, with *bcc* being the lowest among the three.[87] The difference between *bcc* and *fcc* phases is also determined by the partial orderliness. As reported, PdCu nanocrystals have evolved from *fcc* phase to monodisperse *bcc* phase by seed-mediated co-reduction.[88] At equal atomic content of Pd and Cu, disordered Pd−Cu nanocrystals favoure an ordered *bcc*-like phase similar to the CsCl-type structure.[89]

Bcc nanocrystals are more commonly observed in transition metals such as Fe and Cr, which are known for their high strength. *Bcc* is not the densest stacking model, but it offers high space utilization and excellent stability. It is theoretically very ductile because it has the same number of slip phases as *fcc* (i.e., 12) and a slip factor of up to 24 in α-Fe. *Bcc* metals have the advantages of high melting point, high strength, creep resistance, and good compatibility with liquid metals. However, they are extremely sensitive to trace amounts of carbon, nitrogen, and oxygen. And the introduction of small amounts of dilute impurities of carbon, nitrogen, and oxygen can cause significant hardening and embrittlement. Han et al. have provided a detailed explanation of the mechanism at the level of screw dislocations.[90]

It has been found that the phase transformation of the *bcc* phase is preferred to the *hcp* and *fcc* phases. It is well known that Bancroft discovered the martensitic phase transformation of iron from α (*bcc*) phase to ε (*hcp)* phase under high pressure in 1956.[91] In recent years, it has been found that *bcc* to *hcp* phase transformation occurred in cold-rolled and 870 °C annealed sub-stable $TiZrHfTa_{0.5}$ specimens, significantly enhancing the wear resistance of the high entropy alloy.[92] As reported, the *bcc* to *fcc* phase transformation occurred at the crack tip in pure Mo at 15.4% tensile strain during *in situ* tensile loading and then transitioned back to the *bcc* phase.[93]

The *bct* lattice is recognized as an intermediate structure bridging the *bcc* and *fcc* lattices. It is characterized by a distortion of the *bcc* lattice, resulting in elongation along one axis and contraction along the other two axes. The *bct* structure can be stabilized by various methods and one approach is the addition of specific elements, such as V and N in the case of FeCoVN films which induces a tetragonal deformation in the lattice.[94] In 2015, *bct* and body-centered orthorhombic (*bco*) were found as stable phases in noble metal Au. These microcrystals were obtained by pyrolysis of ($AuCl_4$)-stabilized with tetraoctylammonium bromide (ToABr) in air at ~220 °C. The appearance of the non-*fcc* phase of Au was attributed to geometrically induced strain in the bipyramid. The samples showed high contents of up to ~55% non-*fcc* phases at ambient pressure. The appearance of *bct* and *bco* phases can be used to suppress the thermal stabilization of noble metals (e.g., Au, Ag, Pd, and Pt) due to broken symmetry.[31]

2.4 Two-dimensional materials

Since the extraordinary electrical properties of graphene were reported in 2004, 2D materials have received numerous attentions. Similarly, 2D materials also possess polymorphic structures with diverse electronic and magnetic properties, thus offering tremendous opportunities for various applications through phase engineering.[40] The most widely studied 2D materials exhibiting structural phase transitions are transition metal dichalcogenide (TMD) monolayers in the formula of MX_2, where M stands for transition metal (Mo or W, etc.) and X stands for chalcogen atom such as S, Se or Te. Monolayer TMDs have three layers of atoms, one layer of metal atoms sandwiched between two layers of chalcogen atoms. By tuning the coordination patterns of the metal atoms, monolayer TMDs have three well known structural polymorphs as 2H, 1T, and 1T'. The X atoms around the metal atoms in the 2H phase have a trigonal prismatic coordination pattern, and the 1T and 1T' phases have octahedral and distorted octahedral coordination patterns, respectively (**Figure 2**).[40, 95] The monolayer MX_2 in the 2H phase is semiconducting with a bandgap in the range of 1.0−2.5 eV, while the 1T and 1T' phases are metallic.[96, 97] The 1T phase is unstable and spontaneously transforms into the lower symmetry 1T' phase by distorting the octahedral coordination. For example, single layer MoS_2 has semiconducting trigonal prismatic (2H) and metallic octahedral (1T) phases depending on the position of the sulfur atoms.

Density functional theory (DFT) calculations have shown that the 2H polymorph is the ground state phase of all monolayer MX_2 except for WTe_2, for which the 1T' phase has the lowest energy.[98] The structural transition between these phases can be observed using *in situ* TEM techniques with various stimuli, including electron beam irradiation, Joule heating, mechanical strain, and electrical bias, etc. Under these stimuli, atomic rearrangement occurs, causing the phase transition. For example, single layer MoS_2 undergoes the phase change between semiconducting (2H) to metallic (1T) using *in situ* STEM technique under electron beam irradiation.[99] Using *in situ* electrochemical TEM technique, lithiated

MoS_2 undergoes a 2H to 1T phase transition with a lithium ion occupying the interlayer S−S tetrahedron site in the 1T $LiMoS_2$.[100]

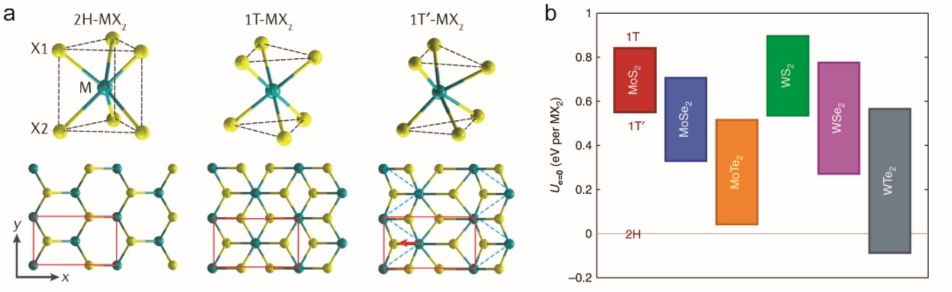

Figure 2. (a) Three polymorph lattice structures (including 2H, 1T, and 1T' phases) of MX_2 monolayers, where M represents transition metal (such as W, Mo) and X represents chalcogen atom (such as S, Se, Te). The unit cell is outlined by red rectangles. Reprinted with permission from ref. [40]. Copyright 2021 Springer Nature Limited. (b) Calculated equilibrium (stress-free) relative energies of the three polymorphs of MoS_2, $MoSe_2$, $MoTe_2$, WS_2, WSe_2, and WTe_2 monolayer. Reprinted with permission from ref. [41]. Copyright 2014 Springer Nature Limited.

In summary, it is essential to recognize that each structure has unique features. A substance may exist in several structures and some may have metastable phases. These variations in structure can lead to significant differences in material properties, which in turn affect its suitability for different applications. Moreover, different phases can coexist or transform into each other under certain conditions, such as pressure or temperature, introducing a new league of complexity and possibilities for manipulating the properties of the material. The exploration of these structural phases and the phase transitions between them is therefore an important area of research.

3. Phase stability theory and phase transformation models

3.1 Electronic structure theories

It is well known that the packing modes of the transition metals can be explained by the "one-electron theory" or the *d*-band filling argument.[101-103] The nonmagnetic transition metals follow the sequence of *hcp* → *bcc* → *hcp* → *fcc* from left to right across the periodic table, as shown in **Figure 3**. While the exception of 3*d* magnetic metals can be explained by the spin-decomposed *d*-band occupations, which are derived from the differences between spin orderings, including ferromagnetic, antiferromagnetic, paramagnetic, and diamagnetic.[101-104] Magnetic Fe is an excellent example of the spin ordering effect. Based on the *d*-band theory, it would be in *hcp* structure as the ground state geometry at low temperatures. However, the large ferromagnetic spin ordering of the *bcc* Fe α-phase lowers the enthalpy and free energy of the system, making the *bcc* structure the energetically lowest geometry. With increasing temperature, the entropic contribution of the spin ordering becomes more prominent, leading to the formation of the paramagnetic *fcc* Fe γ-phase.[105]

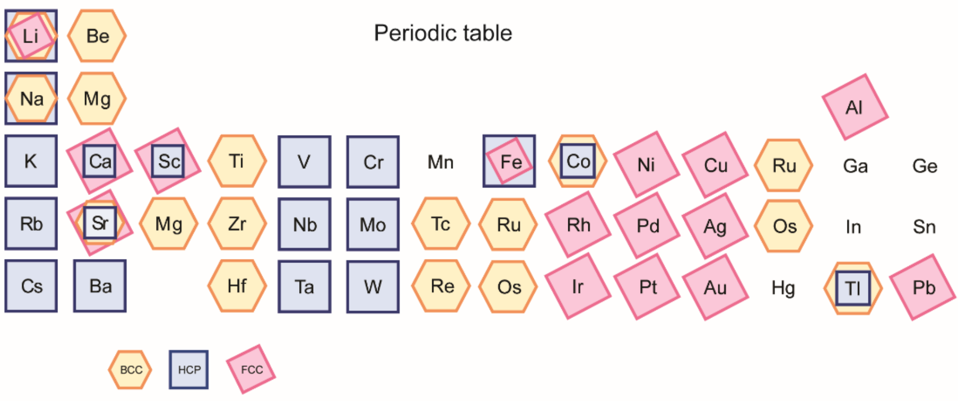

Figure. 3 Periodic table with the marks of possible crystalline structrues.

With the advancement of computational approaches, several theoretical models have been proposed to predict the structures and properties of materials, such as force-field calculations and first-principles calculations.[106-110] Force-field calculations are empirical or semi-empirical methods involving mathematical models or potential energy functions to describe bonded and non-bonded interactions such as covalent bonds, van der Waals forces, and electrostatic interactions. However, these models often simplify the system by approximating complex quantum mechanical effects and treating atoms as point charges with predefined parameters. This simplification also allows force-field calculations to be used for larger systems compared to first-principles calculations. In contrast, first-principles calculations offer a more accurate assessment of the electronic structure and total energy of most materials based on solving the fundamental equations of quantum mechanics. These calculations allow precise control of atomic level structures and provide reliable predictions of phase modulations with consideration of intricate bonding and electronic structures.

3.2 Thermodynamic aspects

3.2.1 Thermodynamic theory

From the thermodynamic point of view, for a given temperature and pressure, the minimization of the Gibbs free energy ($G(p, T)$ for bulk materials) is required for phase stability. Phase transitions occur when the thermodynamic free energy of a system is non-analytic for some choice of thermodynamic variables. The common driving force for phase transformation usually involves any factor that can affect temperature and pressure.

The increased pressure can significantly change the interatomic distances within the material, leading to atomic displacement,[111, 112] or it can enhance the *s*-*p* mixing states and *s* to *d* electron transfer,[101, 113] leading to atomic rearrangements and resulting in a new crystal structure.[67, 114, 115] At high temperatures, non-negligible lattice vibrations increase the entropic contribution of phonons, which can play another important role in stabilizing the dense packing modes, especially those with anharmonic effects. Taking Co as an example, the transformation from *hcp* to *fcc* is mainly driven by the entropic contribution of phonons due to the increased temperatures.[116] In addition, many unusual packing modes of transition metals at low temperatures characterized by the appearance of imaginary frequencies at special *k*-points in the phonon spectra, can also be effectively stabilized at increasing temperatures, again due to anharmonic effects. For instance, Ti with *bcc* structure cannot be stabilized at low temperature due to the presence of imaginary frequencies in the phonon spectra. But it can be stabilized due to the anharmonic effects at elevated temperatures.[117] The coupling between temperature and pressure has been introduced in previous research.[118, 119] But when it comes to the nanoscale, the surface contribution to the free energy cannot be ignored. So the expression can be rewritten as $G(p, T, \gamma)$, where γ is an interfacial free energy.[120] Then the equation $G(p, T)$ can be rewritten as,

$$G(p, T, \gamma) = E - TS + (p + p')V + \gamma A + \text{other terms},$$

where T, p, A are temperature, pressure, and surface area, respectively, p' is an excess internal pressure associated with surface strain. The other terms include additional contributions at the surface, such as edge or defect free energies. If the materials have different stacking orders, there will be different local minimum value of the free energy corresponding to multi-metastable phases, which has been verified in metal phosphate.[121] By surface energy modification, the surface energy can be tailored and used to activate the phase transformation. This is because the surface atoms undergo multilayer relaxation to restore their local optimum electron density, which can go into several layers into the bulk region. This volume atom relaxation is large enough for nanomaterials but can be ignored in bulk samples. To maintain the overall atomic density of the surface layer, the displacive reconstructions may also occur,[122] for example, the reversal of phase stability at small particle size in some systems;[123-125] the lower melting temperatures in nanoparticles;[126] the lower transition temperatures to high temperature phases,[127] while the higher or lower transition pressures to high pressure phases.[128, 129] Thus, the phase diagrams for materials are size dependent.[130]

3.2.2 Size-dependent phase transformation

With decreasing size, the size effect becomes more pronounced and it is widely accepted that the size of crystalline materials is one of the most important parameters in determining their physicochemical properties.[131] The structural stability of nanomaterials is mainly controlled by surface energy and surface stress.[123] In the context of thermodynamics, the reversible work needed to create a new surface per unit area includes surface energy and the reversible work per unit area needed to elastically stretch a pre-existing surface.[132] Assuming a homogenous strain $\varepsilon_{\alpha\beta}$ ($\alpha,\beta \in (x, y)$) is applied to the surface plane, the stress tensor can be expressed as,

$$\tau_{\alpha\beta} = \frac{A_{\mathrm{surf}}^{-1}\partial\left(\gamma_{\mathrm{surf}} A_{\mathrm{surf}}\right)}{\partial\varepsilon_{\alpha\beta}} = \frac{\partial\gamma_{\mathrm{surf}}}{\partial\varepsilon_{\alpha\beta}} + A_{\mathrm{surf}}^{-1}\frac{\gamma_{\mathrm{surf}}\partial A_{\mathrm{surf}}}{\partial\varepsilon_{\alpha\beta}}$$

where A_{surf} is the surface area of the system and γ_{surf} is the surface energy per unit area. The two terms in the equation represent the change in surface energy with respect to strain due to the change in surface atom density and the change in surface area upon mechanical loading, respectively. The first term is always positive for a clean surface, while the second term can be positive or negative, indicative of tensile or compressive interaction, respectively.

The surface energy and surface stress are usually orientation dependent and anisotropic, leading to a preferred surface or faceting in as-grown materials, e.g., the <110>/{111} plane of *fcc* structures with the lowest energy due to the closely packed atom configuration compared to the <100> orientation. Tensile surface stress is usually observed in the order of GPa or even tens of GPa when the size is on the nanometer scale, which is balanced by internal compressive stress. Thus, the structural stability of nanomaterials can be significantly altered by surface conditions and even lead to structural transformations, including surface reconstruction, martensitic phase transformation, pseudo-elastic behavior, and shape memory effect in *fcc*,[133-142] *bcc*,[143-146] and *hcp*[67, 112, 139, 147, 148] of single element, layered composite,[148, 149] intermetallic alloy,[34, 150-153] and even metal oxide[154-156] or nitride[157] compound nanowires.

By reducing the size of nanomaterials, the surface energy can be modulated and the surface reconstruction (reorientation and phase transformation) may occur.[120, 130] The reorientation of Au nanostructures occurs when their size reaches several atomic layers,[158] such as Au (011) to (111) due to surface energy minimization (**Figure 4a**),[159] and the *hcp* surface of Au nanowires but *fcc* in the core region (**Figure 4b,c**).[160] The surface stress induced phase transformation is controlled by wire size, initial orientation, boundary conditions, temperature, and initial cross-sectional shape. It occurs when the compressive stress caused by the tensile surface stress components in the longitudinal direction exceeds the compressive stress required to transform bulk gold into its higher energy metastable crystal structure with initial <100> orientation and square cross-section.[138] Based on the molecular dynamics (MD) simulation, Au nanowires can spontaneously transform from *fcc* to *bct* crystal structure when the cross-sectional area of the nanowires is below 1.83 nm × 1.83 nm **(Figure 4a)**.[138] The critical cross-sectional area size (A) is calculated based on the equation of

$$\sigma = 4fl/A$$

where f is the surface stress component, l is the width of the nanowire (i.e., the length over which the surface stress component acts), σ is the magnitude of the induced compressive stress. When the compressive stress in the nanowires reaches the critical compressive stress from the compression loading of bulk gold, the phase transformation occurs. If the tensile surface stress component in the transverse directions, which hinders the phase transformation, is considered, the critical wire size required for the phase transformation would be reduced. The corresponding experimental verification has also been achieved with *in situ* video recording by TEM, as shown in **Figure 4d**.[161] According to the work, there are two critical sizes for surface-induced structural transformation, l_c and d_c. If l_c < cross section < d_c, the system is metastable and structural reorientation occurs. But if cross section < l_c, the system is unstable and phase transformation occurs.[162] The critical size depends on two important parameters, temperature and pressure of the nanowires. As the temperature increases, the critical size increases due to the contribution of the thermal effect. However, a small increase in size leads to a significant change in the required temperature, which may exceed the melting temperature. Taking Cu as an example, the critical size increases significantly from 1.45 nm × 1.45 nm (4 × 4 lattice constants) at 100 K to 2.9 nm × 2.9 nm (8 × 8 lattice constants) at 900 K, indicating the importance of the size effect in nanomaterials. When the size of the nanostructures is larger than the aforementioned critical size (i.e., spontaneous transformation), the external field stimuli are required to overcome the energy barrier and reach the local metastable phase of the nanostructures.

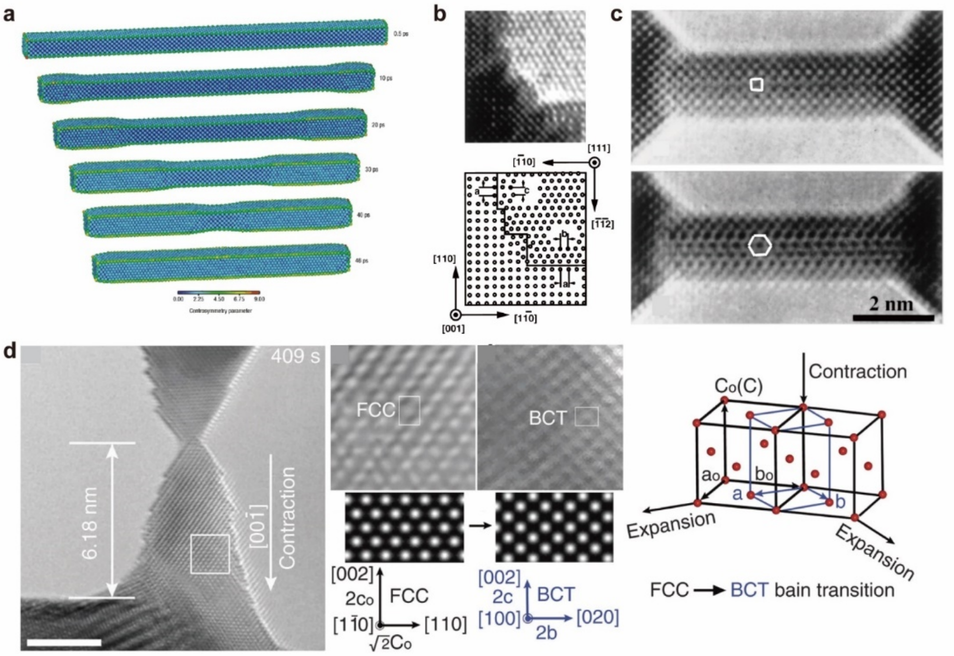

Figure 4. Size effect on phase modulation of nanomaterials. (a) Au nanowire with decreasing diameter. Reprinted with permission from ref. [138]. Copyright 2003 Springer Nature Limited. (b) Au (111) nanofilm transfers to (001) film due to the thickness change. Upper figure is the TEM image and lower figure is trace of the bright dots in upper figure. Reprinted with permission from ref. [159]. Copyright 1999 American Physical Society. (c) One 2 nm thick Au nanobridge with focuses of 65 nm (upper) and 55 nm (lower), showing the square lattice in the upper figure and the hexagonal lattice in the lower figure. Reprinted with permission from ref. [160]. Copyright 1997 American Physical Society. (d) The phase transformation occurs just before the nanocrystal fractures due to the size effect and the illustration of the martensitic transition (*fcc* to *bct*) by the Bain path. The unit cells of *fcc* and *bct* are outlined by black and blue lines, respectively. Reprinted with permission from ref. [161] under a Creative Commons Attribution 4.0 International License. Copyright 2020 The Authors.

In addition, due to the size of the nanomaterials, ligand exchange and metal coating can also be used to modify the surface energy and activate the phase transformation, which have been experimentally verified. Both mechanisms are affected by many factors, including ligand type, lattice mismatch, and phase stability. For example, Au square sheets with 2H phase can be completely transformed into *fcc* phases by exchanging oleylamine with thiols on the surface, driven by the strong interaction between Au atom and −SH group.[81] Ag, Pd, and Pt coating on Au square sheets also induces a phase transformation from 2H to *fcc*.[81] Surface energy minimization is also a key point regarding the epitaxial growth of nanostructures with the same lattice structure to basement, and the surface modification also induces phase transformation. For example, the 4H Ag, Pt, Pd, and their heterostructures[10, 13, 18, 163] have been successfully synthesized.

3.3 Phase transformation models

The mechanistic study of crystal phase transformations attracts numerous researchers. It can be described by electronic structure theories, Gibbs energy as aforementioned to cater the minimization of system energy, and it can also be described quantitatively by the micromechanics constitutive model.[164] The phase transformation mechanisms can also be described by crystallography, which focuses on nucleation and growth with different orientation relationships (ORs) and habit planes, including displacive transformations, diffusional transformations, and displacive-diffusional transformations (**Figure 5**).[165] The displacive transformation occurs at high speed and shape change but no diffusion of atoms within the materials. In contrast, the diffusional transformation takes considerable time at a specific temperature to reconstruct, with changes in composition but no associated shape change. Also, there are some materials show the characteristics of both types of transformation, i.e., the long-range diffusion of the reconstructive diffusional transformation and the shape change of the displacive transformation.

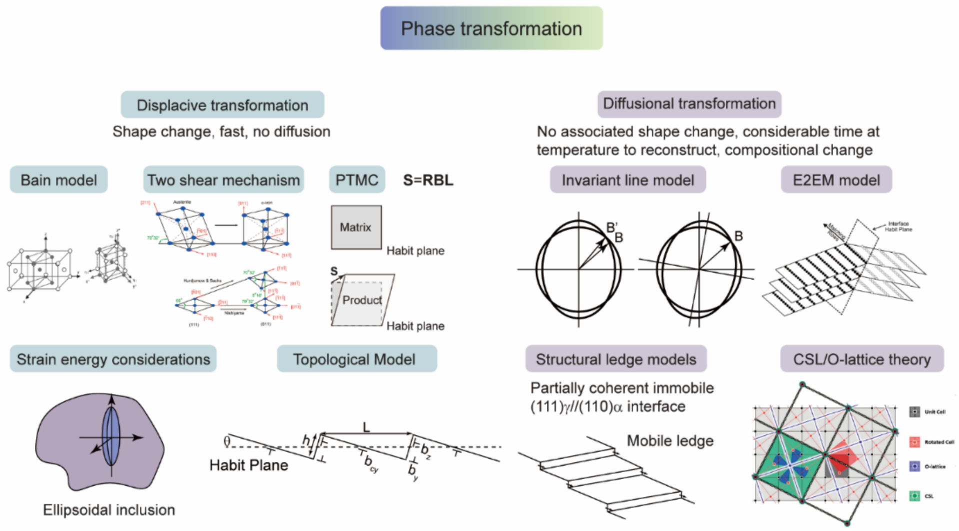

Figure 5. Phase transformation models for displacive and diffusional transformation. Displacive transformation models include the Bain model (Reprinted with permission from ref. [166]. Copyright 2004 Acta Materialia Inc), the two shear mechanism (Reprinted with permission from ref. [167]. Copyright 2013 IOP Publishing, Ltd), the phenomenological theory of martensite crystallography (PTMC), the strain energy model, and the topological model (Reprinted with permission from ref. [165]. Copyright 2009 Elsevier Ltd.). Diffusional models include the invariant line model, the edge to edge model (E2EM) model (Reprinted with permission from ref. [165]. Copyright 2009 Elsevier Ltd.), the structural ledge models, and the coincident site lattice (CSL)/O-lattice theory (Reprinted with permission from ref. [168]. Copyright 2022 the Authors).

3.3.1 Displacive transformation models

The displacive transformation models were developed in the past 150 years and aim to illustrate the internal mechanism based on atomic displacement. These models include the Bain model, the classical

Kurdjumov−Sachs−Nishiyama (KSN) model,[169, 170] and the phenomenological theory of martensite crystallography (PTMC). From a strain energy point of view, the martensite transformation can also be well described by the Eshelby equations due to the similar lenticular plate product (**Figure 5**).[171, 172] Based on the surface dislocation, the topological model makes it possible to describe the actual atomic mechanism of martensitic transformation rather than the phenomenological one.[173]

Initially, the proposed theoretical models are phenomenological. The simplest one is the Bain model with a 20% contraction along the [001] direction and a 12% expansion along the [100] and [010] directions (**Figure 5**), leading to the *fcc* phase transforming into *bct* or *bcc* phase.[174] *in situ* HRTEM confirms the Bain path in Au nanocrystals, which undergo the direct tension and phase transformation from *fcc* to *bct*.[161]

The classical KSN model[169, 170] also proposes two shear mechanisms for the transfer of the *fcc* austenite (γ) to the *bcc* martensite (α) structure, where the first shear is assumed on the $\{111\}_\gamma$ plane in the $<112>_\gamma$ direction to form stacking of an *hcp* structure (ABABAB…) and the second shear is the transfer to the *hcp* structure from a plane normal to the $\{111\}_\gamma$ to $\{110\}_\alpha$ plane of the *bcc* martensite product. HRTEM has revealed the KSN ORs.[175]

Then two groups published the first general version of the theory of martensite phase transformation, called PTMC theory. Compared to the complex matrix algebra used to calculate the lattice transformation, PTMC is used to predict the crystallographic features based on the correspondence between the parent and product phases and the invariant plane strain as given by the matrix algebra,

$$\mathbf{S} = \mathbf{RBL}$$

where **S** is an invariant plane strain, Bain strain (**B**) and rotation (**R**) represent the orientation relationship, **L** is a simple shear leading to a total strain **BL** based on an undistorted line in the same plane as the lattice invariant strain **L**. The **L** ensure that the strain **BL** is an invariant line strain as shown in **Figure 5**.

Based on the surface dislocations, the description of the boundary between two crystal lattices can be used to predict the crystallography of martensite. At first, it is still a phenomenological theory that does not represent the actual phase transformation at the atomic scale. Then the dislocation theory of martensitic transformation is extended to include nucleation, thermoelastic behavior, transformation plasticity, etc., which leads to the atomistic mechanism for the martensitic transformation possible attributed to the topological characteristics of interfacial dislocations. In 2007, Pond and co-workers developed an interface dislocation theory named “Topological Model” based on a habit plane consisting of terraces and step-type defects or disconnections,[176] as shown in **Figure 5**. They clarified that “the condition that must be satisfied for a habit plane in crystals free of long-range coherency stresses", which can be present in,

$$\boldsymbol{b}_z \tan^2 \theta + \boldsymbol{b}_y \tan \theta = \langle h \rangle \varepsilon_{yy},$$

where $\boldsymbol{b}_z$, $\boldsymbol{b}_y$, ε_{yy} and θ are all defined in **Figure 5**, $\langle h \rangle = (h_\beta + h_\alpha)/2$. This equation can be used to calculate the value of the inclination of the habit plane to the terrace plane, which is in complete agreement with that of the PTMC.

3.3.2 Diffusional transformation models

For diffusional transformations, unlike displacive transformations, the morphology of the product phase can have different shapes, including spheres, cubes, rods, plates, and laths, to minimize the interfacial energy between the matrix and the product. In most general cases, the product will be spherical in shape to reduce the ratio of surface area to volume. Therefore, a reproducible OR with matrix is not preferred. The parameter that controls the morphology and interfacial plane is the degree of atomic matching between matrix and product, and the higher degree of matching, the lower the interfacial energy. Various models have been developed to describe the crystallographic features of diffusional transformations based on the criterion of maximizing the degree of matching between matrix and product, including the invariant line models,[177-182] structural ledge models,[183-186] coincident site lattice (CSL)/O-lattice theory[187-189] and edge-to-edge matching (E2EM) models[190-192] (**Figure 5**). These models have been extensively reviewed in the previous literature.[165, 187, 193]

The invariant line model is based on minimizing the interfacial energy by minimizing the atomic misfit across the interface to reduce the elastic strain energy.[177, 178, 194] This minimum atomic misfit can be realized by the invariant line in the interface, which is similar to PTMC. To generate an invariant line, the invariant line model introduces two types of rotation. First, a small rotation of angle θ is applied around a shared normal to a pair of parallel close-packed planes. If this rotation alone is not sufficient to achieve the desired transformation, an additional rotation angle φ is introduced about a common close-packed direction within the close-packed plane. For example, the simple *bcc* to *hcp* structure transformation have different ORs via different rotations, including the Burgers OR and the Pitsch-Schrader OR via θ rotation, and also the Potter OR via φ rotation.[179]

The structure ledge models[183-186] are also based on maximizing the atomic matching across the matrix/product interface. However, it is assumed that the maximization of atomic matching is more easily achieved between the closely packed or nearly closely packed parallel planes. To improve the degree of matching, instead of a planar interface, a stepped version was used to achieve a good fit (**Figure 5**).

The CSL or O-lattice theory is based on the same or very similar atomic sites being occupied by both matrix and product phases (**Figure 5**).[187-189] These atomic sites are termed (near) coincident sites. Thus, the matrix phase and the product phase can be expressed as,

$$\mathbf{x}_2=\mathbf{A}\mathbf{x}_1=\mathbf{R}\mathbf{S}_2\mathbf{S}_1^{-1}\mathbf{x}_1,$$

where $\mathbf{x}_2$ and $\mathbf{x}_1$ are the coordinates of the parent and product phases, $\mathbf{A}$ is the transformation matrix with three components, one is the rotation $\mathbf{R}$, and the others are $\mathbf{S}_1$ and $\mathbf{S}_2$, which possess columns that are the base vectors of the parent and product lattice. The criterion is to find the optimal interface with a high density of (near) coincident sites.

The E2EM model (**Figure 5**)[190-192] proposes to match the atomic rows (closely packed or almost closely packed) in the interface of matrix and product to achieve the high degree of atomic matching and then reduce the interfacial energy. The models can be used to predict the ORs between the matrix and product phases.

3.3.3 Diffusional−displacive transformation models

The features of diffusional-displacive transformation include not only the shape change (feature of displacive transformation), but also long-range diffusion (feature of diffusional transformation). The models are similar to those above, except for the surface relief generated during the phase transformations. Several types of surface relief have been observed for diffusional−displacive transformations, such as single tilt, tent-like, and inverse-tent, as shown in **Figure 6**. The possible mechanisms for the formation of these surface reliefs are illustrated in **Figure 7**, including single tilt representing invariant plane strain (IPS) surface relief in martensitic transformation (a), tent-like resulting from single crystal structure (b), tent-like or inverse tent-like resulting from shearing in opposite directions (c), tent-like resulting from accommodation by slip in matrix (d) or product (e) which makes a small angel to the overall habit plane, and also the zero surface relief resulting from distributed slip in the product (f). The slip-based structural change mechanisms can be applied to all the different systems in diffusional−displacive transformations (including *fcc*−*hcp*, *fcc*−*bcc* and *bcc*−*hcp*).

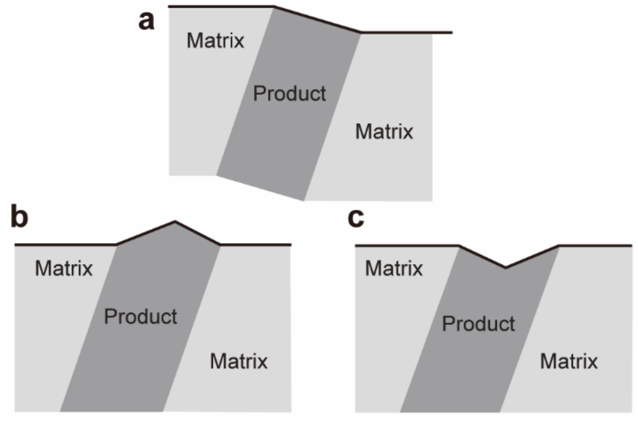

Figure 6. Three types of surface relief in the “diffusional-displacive” transformation. (a) Single-tilt surface relief. (b) “Tent-like” surface relief. (c) “Inverse-tent” surface relief. Reprinted with permission from ref. [165]. Copyright 2009 Elsevier Ltd.

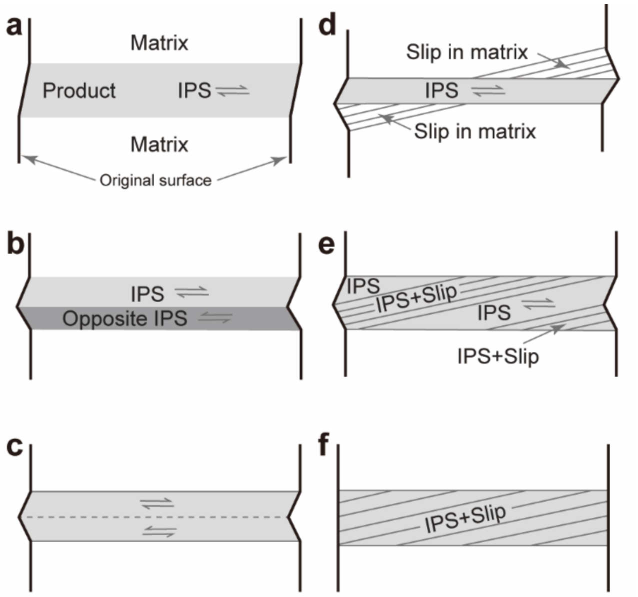

Figure 7. Illustrations for surface relief during the “diffusional-displacive” transformation. The product phase is shaded and the surface relief is indicated by the bold vertical lines. The double arrows indicate shear induced structural changes. (a) Standard single tilt invariant plane strain (IPS). (b) Back-to-back variants with opposing IPS shears. (c) “Tent-like” surface relief in a single crystal caused by opposite shears. Accommodation by slip in the matrix (d) and the product (e) on a slip plane with a small angle (5° to 25° to the habit plane) (f) Distributed slip in the product without surface relief. Reprinted with permission from ref. [165]. Copyright 2009 Elsevier Ltd.

3.4 Section summary

Phase transformations can be separated by different features. The displacive transformations, diffusional transformations, and displacive-diffusional transformations are based on the mechanism of formation of the product phases, including nucleation and growth. Among these categories, displacive transformations stand out due to their rapid structural changes, setting them apart from diffusional transformations, which do not involve atom diffusion over time. In contrast, diffusional transformations require a significant amount of time at a given temperature to undergo both reconstruction and compositional change. Unlike displacive transformations, diffusional transformations occur without accompanying shape alterations. However, some phase transformations exhibit features of both displacive and diffusional transformations, involving both long-range diffusion and structural shape changes. The models used to comprehend and describe these phase transformations have evolved over extended periods and continue to progress. A deeper understanding of these models, in combination with in situ TEM characterization, contributes to the advancement of phase transformation theories.

4. *in situ* Characterization and modulation of phase transformation

To modulate the phase in crystal materials, the driving force can be any external fields that can change the *d*-band occupancy state,[112, 113, 195] temperature, and pressure.[105, 116, 128] The commonly used external fields include mechanical strain,[112, 196, 197] thermal hearing, electrical bias, optical, gas, liquid, and magnetic field, which cooperatively contribute to the overall stability of the densely packed transition metals.[83, 118] These effects mainly influence the dynamic stability, spin state, and strain of crystal materials, leading to the phase transformations.[83] Based on the Nanolab in TEM, the phase modulation can be achieved, the transformation process can be recorded *in situ* to uncover the actual atomic mechanisms for the phase transformation, and guide the phase modulation strategies to achieve property control in crystalline materials (**Figure 8**). The selected examples are given in this section to illustrate the *in situ* characterization and modulation of phase transformations.

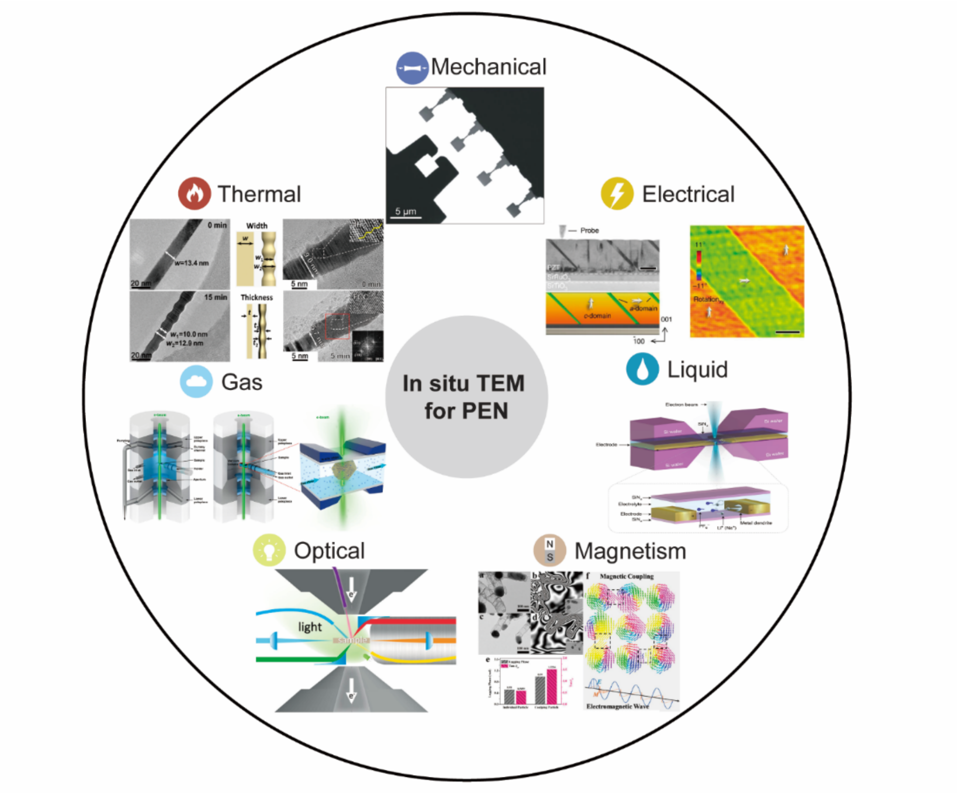

Figure 8. *in situ* TEM for PEN including mechanical (Reprinted with permission from ref. [198]. Copyright 2021 American Association for the Advancement of Science), thermal (Reprinted with permission from ref. [75]. Copyright 2019 Elsevier Inc), electrical (Reprinted with permission from ref. [199]. Copyright 2013, Springer Nature Limited), gas (Reprinted with permission from ref. [200]. Copyright 2023 Accounts of Materials Research), liquid (Reprinted with permission from ref. [201]. Copyright 2022 Springer Nature Limited), optical (Reprinted with permission from ref. [202]. Copyright 2022 The Author. Published by American Chemical Society.) and magnetic (Reprinted with permission from ref. [203]. Copyright 2019 WILEY-VCH) stimuli.

4.1 Irradiation effect for phase engineering of nanomaterials

To obtain the images by TEM, the interaction between the incident electrons and the samples, including atomic nuclei or electrons, is required. At high accelerating voltages (generally 60−300 kV), the irradiation damage is inevitable, especially for *in situ* experiments with long electron beam exposure time.[204, 205] The general irradiation effects include two types. One is electron-nucleus scattering, which generally causes atom displacement (knock-on effect)[206] and sputtering. The other one is electron-electron scattering, which usually induces electrostatic charging, radiolysis, or electron beam heating. Since the 1940s, the damage of electron beam irradiation has been reported,[205, 207] following a series of works reporting unique phenomena under electron beam irradiation,[208-210] including phase transformation.[211]

For example, at 200 kV accelerating voltage, the electron beam heating effect dominates over knock-on damage or radiolysis damage.[212, 213] The maximum temperature change under electron irradiation can be estimated by Fisher's model,

$$\Delta T = \frac{I}{4\pi\kappa}\frac{\Delta E}{d}\left(\gamma + 2\ln\frac{R}{r_0}\right)$$

where I is the total beam current, κ is the thermal conductivity, R is the sample radius, r_0 is the effective beam radius, γ is the Euler's constant, and ΔE is the total energy loss of each electron in the sample of thickness d. The total beam current $I = J\pi r_0^2$, where J is the current intensity. Since the energy loss in the sample is small compared to the initial energy (200 kV), the term $\Delta E/d$ is equal to the stopping power of the electrons. The term $\mathrm{d}E/\mathrm{d}x$ is calculated from the Bethe-Bloch equation,

$$-\frac{\mathrm{d}E}{\mathrm{d}x} = \frac{2\pi e^4 NZ}{mv^2}\left\{\ln\left[\frac{E_0\left(E_0 + m_\mathrm{e}c^2\right)^2\beta^2}{2E_\mathrm{ex}^2 m_\mathrm{e}c^2}\right] + \left(1-\beta^2\right) - \left(1-\sqrt{1-\beta^2}+\beta^2\right)\ln 2 + \frac{1}{8}\left(1-\sqrt{1-\beta^2}\right)^2\right\}$$

where N is the Loschmidt's number and E_ex is the excitation energy, which is approximately proportional to the atomic number Z. From the above equations, we know that the temperature rise is proportional to the beam current I, but inversely proportional to the thermal conductivity.

It has been experimentally demonstrated that the electron beam induced heat can even be used to melt the submicron Al−Si alloy particles if the conductivity of the substrate is poor.[214] Therefore, if the dose rate of the electron beam can be precisely controlled, the electron beam irradiation can be used to activate the phase transformation of nanomaterials, coupled with the knock-on effect[206] and the size effect.[215-217]

4.1.1 Nanoparticles

Phase transformation can occur in larger nanostructures (more than several atomic layers) with the assistance of interface (**Figure 9**), which is related to the surface modification mechanism. Saleem et al. reported the size-dependent phase transformation of noble metal nanomaterials, including the phase transformation between 4H and *fcc* in Au, Pd, Ag, and PtPdAg.[218] With the assistance of 4H/*fcc* interface and electron beam irradiation, the 4H and *fcc* phases can be converted into each other depending on the ratio of the size of the 4H monocrystalline nanoparticles to the diameter of the 4H Au nanodomains. Combined with the MD simulation and DFT calculations, the total energy of the *fcc*-4H sphere can be expressed as,

$$E = E_B + E_S + E_I,$$

where $E_B = \varepsilon_{fcc}V_{fcc} + \varepsilon_{4H}V_{4H}$, $E_S = \gamma_{fcc}A_{fcc} + \gamma_{4H}A_{4H}$ and $E_I = \gamma_I A_I$ are the bulk, surface, and interfacial energies of the *fcc*-4H sphere, respectively. Depending on the ratio of *fcc* to 4H and the diameter of the *fcc*-4H nanostructure, the nanostructure must be transformed into either 4H or *fcc* phase eventually by electron beam irradiation based on the energy minimization among these three energy forms. The critical ratio of the volume and size of the *fcc*-4H nanostructure is also demonstrated in their work.[218]

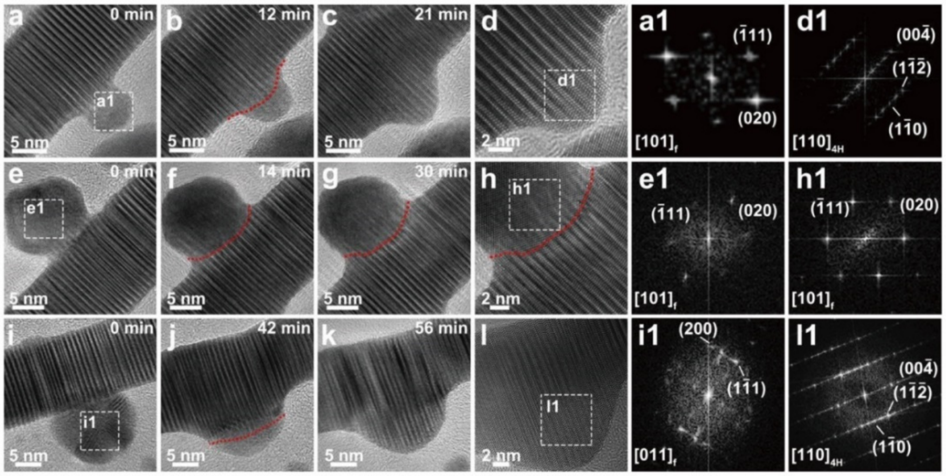

Figure 9. Phase modulation by electron beam irradiation for *fcc*-Au nanoparticles on the surface of 4H-Au nanorods. (a-c) TEM images revealing the phase transformation of single crystalline *fcc*-Au nanoparticles to 4H phase. (d) HRTEM of (c). (a1, d1) Fast Fourier transformation (FFT) patterns of the dashed squares in (a) and (d), respectively. (e-g) TEM images showing partial 4H-Au nanorods converted to *fcc* phase. (h) HRTEM of (g). (e1, h1) FFT patterns of the dashed squares in (e) and (h), respectively. (i-k) TEM images revealing the phase transformation of polycrystalline Au nanoparticles from *fcc* to 4H phase. (l) HRTEM of (k). (i1, k1) FFT patterns of the dashed squares in (i) and (l), respectively. The red dotted curves indicate the *fcc*-4H interfaces during phase transformation. Reprinted with permission from ref. [218]. Copyright 2019 WILEY-VCH.

4.1.2 Nanowires

The phase transformations of noble metal crystals are also demonstrated by *in situ* TEM, which clearly reveals the size effects[219] and the beam irradiation effect on the transition mechanism with real-time process. The gold nanobridge fabricated by electron beam irradiation also contains *hcp* surface but *fcc* in the core region (**Figure 4c**).[160] Ag nanowires with metastable 4H phase transfer to *fcc* phase,[220-222] which have different physicochemical properties.[223]

4.1.3 Two-dimensional materials

2D materials have also been observed to undergo the phase transformation under electron beam irradiation. For example, the (001) Au thin film can transfer to the (111) film under electron beam irradiation when the thickness of the thin film is less than 2 nm, with the hexagonal lattice planes filling in the central area.[11, 159] The phase transition between the carbon polymorphs (including diamond, graphite, fullerene, and even amorphous carbon) can be triggered by electron beam irradiation with/without additional heating and has already been experimentally demonstrated (**Figure 10**). For example, electron beam irradiation below 300 kV induces the transition of graphene to quasi-amorphous 2D membrane, with *in situ* TEM observation showing the stepwise nucleation and growth of low-energy multivacancy structures (**Figure 10a**).[224] While, below 80 kV, the graphene flakes are observed to transfer into fullerenes following the four critical steps, including the loss of carbon atoms at the edge, the formation of pentagons, the curving of the graphene into a bowl-shaped structure, and finally the zipping up to form a fullerene structure (**Figure 10b**).[225] Conversely, amorphous carbon deposited on the graphene or h-BN can be transferred into graphene under 80 kV electron beam irradiation due to van der Waals interactions (**Figure 10c**).[226] Interestingly, the graphitic carbon onions can even be transformed into diamond under electron beam irradiation and high temperature due to the high pressure inside the onion particles caused by the loss of C atoms (**Figure 10d**).[227, 228]. Similarly, under electron beam irradiation, the diamond can also be inversely transferred to the graphitic onions when the size effect is below 5 nm, but to the graphite layer with the size of about 20 nm (**Figure 10e**).[229]

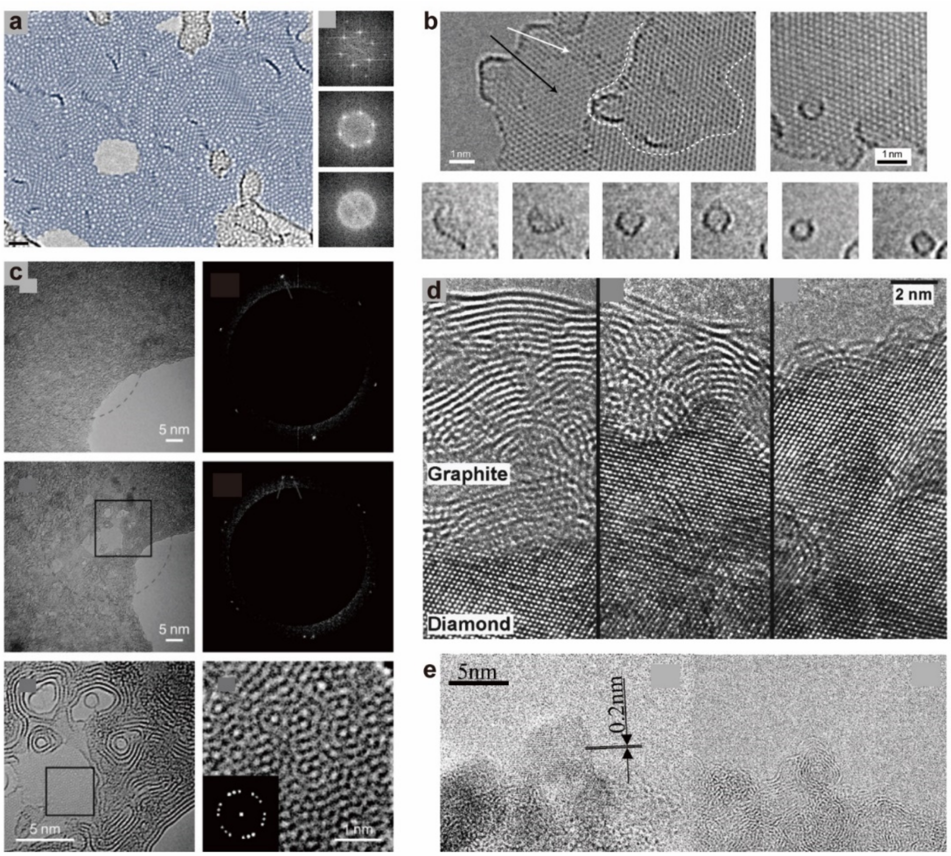

Figure 10. Phase modulation of carbon polymorphism. (a) By 100 kV electron beam irradiation, graphene transfers to amorphous 2D sp^2-bonded carbon membrane. Reprinted with permission from ref. [224]. Copyright 2011 American Physical Society. (b) Graphene transfer to fullerene under the exposure to 80 kV electron beam irradiation. Reprinted with permission from ref. [225]. Copyright 2010 Springer Nature Limited. (c) Fabrication of graphene from amorphous carbon supported on graphene using 80 kV electron beam irradiation. Reprinted with permission from ref. [226]. Copyright 2012 WILEY-VCH Verlag GmbH & Co. KGaA, Weinheim. (d) Transformation of graphite to diamond by electron beam irradiation. Reprinted with permission from ref. [228]. Copyright 1999 American Institute of Physics. (e) Electron irradiation induced transformation of diamond to onion-like carbon. Reprinted with permission from ref. [229]. Copyright 2005 American Institute of Physics.

Single layer MoS_2 has been transformed from semiconducting (2H) to metallic (1T) using the *in situ* STEM technique.[230] The single layer MoS_2 has an initial 2H hexagonal lattice structure (**Figure 11a,b**). Band structures are formed along two zigzag directions and finally a triangular 1T phase is formed under electron beam irradiation. Phase changes in 2D materials alter the physical properties such as electrical conductivity. Zheng et al. used focused electron beam irradiation to achieve phase patterning in 2D ReS_2 and $ReSe_2$.[231] T'' to T' or T phase transition was observed during the electron beam irradiation. The electron beams can collapse the Re−Re bonds in the di- or tetramerized Re clusters along the beam exposure direction and reshape the diamond-shaped Re_4 clusters (T'') into zigzag Re_2 chains (T') (**Figure 11c**). With the phase changes induced by electron beam irradiation, the conductivity measured by *in situ* TEM electrical study gradually increased up to tenfold (**Figure 11d**), providing a method for electrical contact engineering using electron beam irradiation.

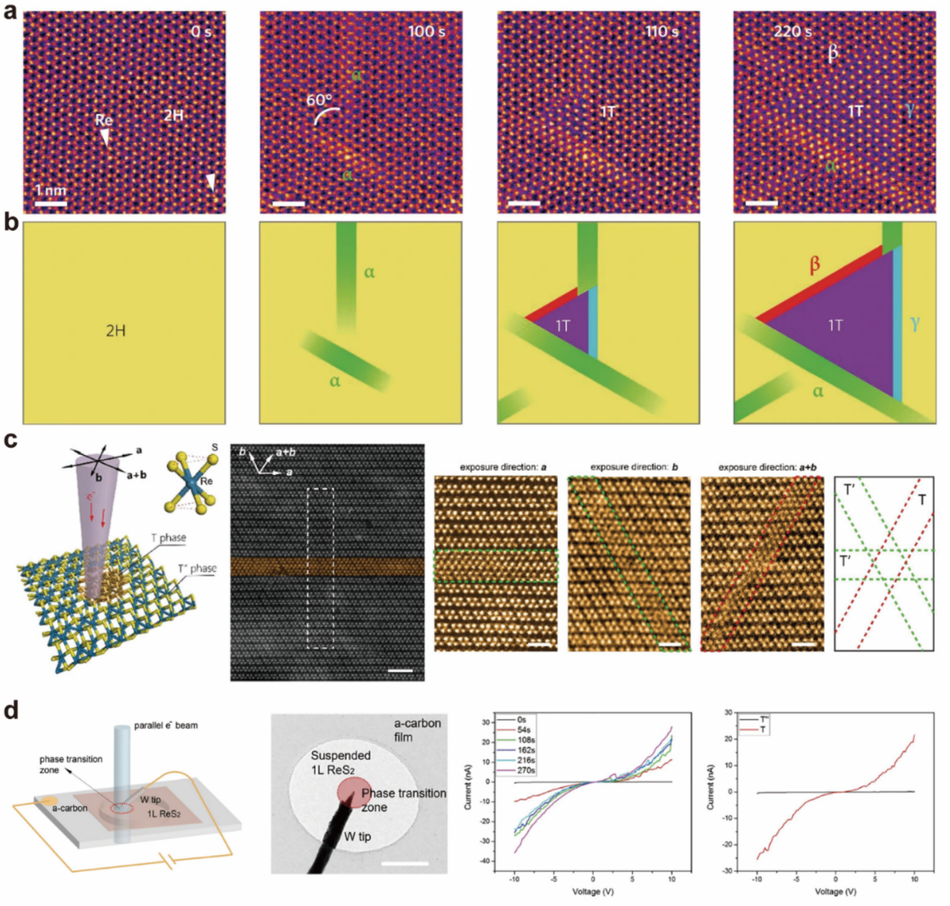

Figure 11. *in situ* TEM study of 2D material phase changes under electron beam irradiation. (a) Sequential annular dark-field (ADF) images of 2H to 1T phase change in single layer MoS_2. (b) Schematic illustrations of the 2H to 1T phase transition corresponding to the ADF images in (a). (a,b) Reprinted with permission from ref. [230]. Copyright 2014 Springer Nature Limited. (c) STEM images of the 2D ReS_2 phase transition from T'' to T' or T under electron beam exposure direction along ***a***, ***b*** and ***a+b*** crystal directions, scale bars, from left to right, 2 nm, 1 nm, 1 nm, 1 nm, respectively. (d) Electron beam patterning and electrical contact engineering on of 2D ReS_2, scale bar, 0.5 μm. (c,d) Reprinted with permission from ref. [231]. Copyright 2022 The Authors. Advanced Science published by Wiley-VCH GmbH.

4.1.4 Section summary

Since the invention of TEM, the interaction between the sample and the electron beam has been considered as a fundamental difficulty and limitation due to the mechanism of image formation in the TEM. The elastic interaction of the samples not only forms the images, but also creates the temporary or permanent changes in the samples. Apart from damage, it can also be considered as a stimulus for phase transformation, especially for nanomaterials. The current and electron dose in TEM can be well controlled to modulate the phase of nanomaterials, providing an important platform to investigate materials under extreme conditions for nuclear engineering and semiconductor technology. The transformation process of nanomaterials acquired by TEM will facilitate the applications of PEN under irradiation conditions.

4.2 *in situ* TEM mechanics for PEN

Stress can be an important stimulus to modulate the phase transformations that are ubiquitous in crystalline materials. These phase transformations can even be used to enhance the mechanical properties of steel, e.g., transformation induced plasticity (TRIP) steel,[232] and also the main feature of shape memory alloys. As early as 1955, the stretching mechanical tests of nylon and rubber ribbons were conducted in the electron microscope by Weichan.[233] Then, Wilsdorf designed the TEM holder for thin film samples, with the capability of tension, compression, and torsion in TEM.[234] These apparatuses enable the thin films to climb on the two substrates and the actuation by an electric motor to achieve the straining of the specimen,[235, 236] However, the stability and resolution of these apparatuses are not sufficient for atomic observation in TEM. Nowadays, piezo-driven probes can be used to apply quantitative mechanical stress to the specimen with *in situ* high resolution observation in TEM. For example, scanning tunnelling microscopy (STM)-TEM holders have been used to introduce controllable stress to study the unique mechanical behaviours of micro/nanomaterials at atomic resolution.[161, 237, 238] To obtain the quantitative description of micro/nanoscale materials, the nanoindentation and atomic force microscopy (AFM) tips have been integrated into TEM[56, 239-241] Especially, with the development of focused ion beam (FIB) and micro-electromechanical system (MEMS) technique, the variety of punch tips, sample stages, and *in situ* MEMS have been integrated into *in situ* nanomechanics platforms, achieving the variety of mechanical tests in *in situ* TEM nanolab.[56, 61, 242-247] The integration of TEM and these stages enables to acquire the quantitative strain−stress data, the real-time TEM images, and even the chemistry/bonding information. By providing precise local stress and strain information, these *in situ* observations enhance our understanding of how crystalline materials respond to external mechanical fields and aid in the design and engineering of materials with desired properties. In this section, we introduce several representative nanomechanics platforms integrated in TEM, including STM, nanoindentation, MEMS, and thermal bimetallic ring, and also use selected examples to demonstrate the great power of *in situ* TEM for PEN.

4.2.1 TEM-STM holder-based nanomechanics platform

Globally recognized as a pioneering endeavor, the first nanoscale manipulation experiment was conducted by Eigler and Schweizer to obtain the IBM logo by moving the xenon atoms on a nickel substrate using the STM technology.[248] Afterward, the integration of STM technology into the TEM chamber provides a new pathway to achieve the *in situ* observation of nanomaterials. Generally, the STM-TEM holder, equipped with a static sample stage and a precisely controlled probe, has been developed for atomic nanomechanics characterizations, as shown in **Figure 12a**.[161] One end is a piezo-operated STM probe where the sample is glued by silver paint, and the other end is a gold wafer which is used to weld the sample into the STM probe using cold welding phenomenon.[249] Compression or tensile tests can be carried out when the STM probe approaches or pulls away from the gold wafer with the real-time TEM observation. The STM probe scanner can cover a very wide range of displacements from the picometers to millimeters, which can be employed to achieve the coarse sample orientation adjustment (millimeters) or accurate probe movement (picometers). The electrical contacts between the probe and the nanoscale interface can reach ultrahigh precise positioning. Besides, this STM probe can be coupled with other stimuli (including electrical bias or pulse)[250] and MEMS under multi-field conditions (including thermal and electrical fields). Based on this multifunctional platform, a variety of *in situ* nanomechanic works has been performed (commercial holders such as Nanofactory and PicoFemto TEM-STM platform), as shown in **Figure 12b**.[251-254]

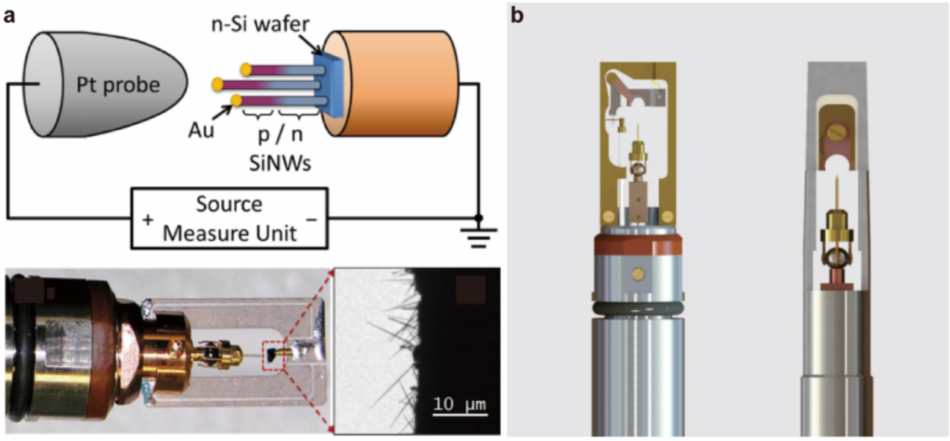

Figure 12. (a) Schematics and photograph of the actual NanoFactory TEM holder with a movable probe to approach the loaded sample, and the TEM image of the SiNWs cantilevered on the substrate. Reprinted with permission from ref.[255]. Copyright 2013 IOP Publishing Ltd. (b) Double-tilt JEOL holder and single-tilt ThermoFisher holder. Reprinted with permission from ref.[256]. Copyright 2016-2019 ZEPTools Technology.

Tensile tests are among the most frequently conducted mechanical tests. To achieve the tensile deformation, in a typical experiment, the bulk sample is first sectioned to produce a clean fracture surface with numerous nanosized tips. Meanwhile, another fractured tip is loaded onto the probe side of the TEM holder. Then, the two nanoscale tips are welded together inside the TEM chamber by applying a voltage potential. At the moment of contact, the pre-applied potential can melt the tips to form a nanowire.

Subsequently, *in situ* tensile experiments are carried out by driving the active end of the nanomanipulation.[257] Based on these platforms, sub-10 nm Au nanocrystals have been successfully modulated from *fcc* to *bct* phase by tensile strain (**Figure 4d**).[161] Combined with MD simulations, the Bain transition mechanism was first verified by *in situ* experiments. Similarly, the *bcc* to *fcc* phase transformation via the Bain model in Nb nanowires was also recorded *in situ* (**Figure 13**),[258] serving as one of three different mechanisms for the superplastic deformation in Nb nanowires. This indicates that PEN engineering can be used as an effective tool to modify the plasticity properties, even in materials traditionally considered to be relatively poorly deformable.

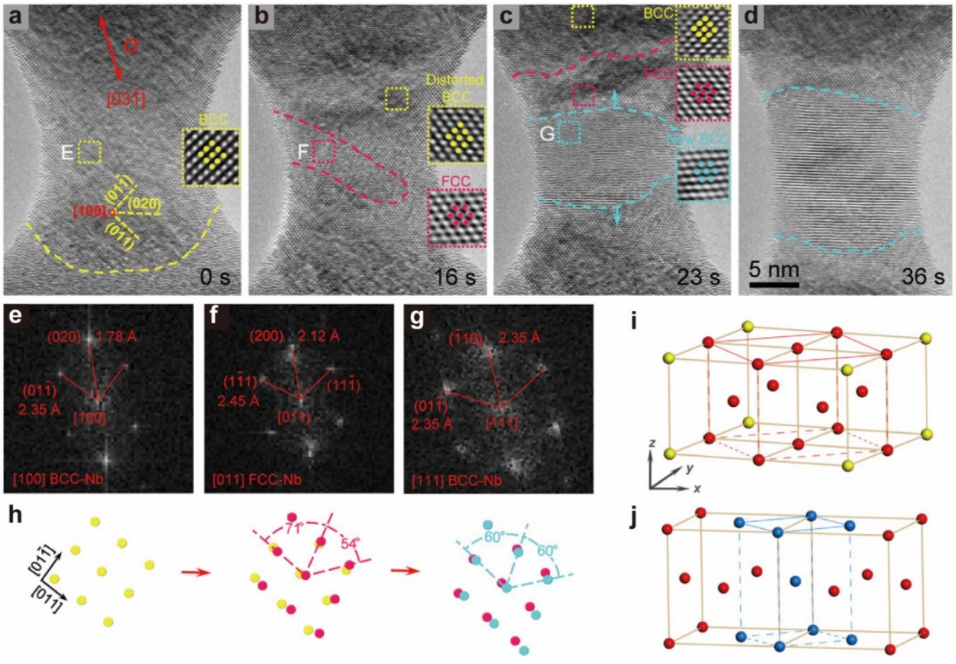

Figure 13. *in situ* Tensile tests for Nb nanowires with phase transformation. (a) Pristine nanowire with a diameter of ~15 nm. (b) Accumulation of elastic strain in the nanowire caused the formation of the *fcc* domain, as marked by the pink dashed line. (c,d) Reorientation from the [100] zone axis to the [111] zone axis finally occurred following a *bcc*-*fcc*-*bcc* pathway, and the reoriented region increased with the migration of phase boundaries. The pink and cyan dashed lines represent the $[100]_{bcc}/[011]_{fcc}$ interface and the $[011]_{fcc}/[111]_{bcc}$ interface, respectively. (e-g) Corresponding FFT patterns showing the structural evolutions during the *bcc*-*fcc*-*bcc* phase transformation. (h) Schematic showing the change of atomic configurations during the phase transformation. (i,j) Phase transformation pathway of Nb nanowire can be described by Bain's model. marked with the matrix (yellow), the *fcc* domain (pink), and new *bcc* (blue). Reprinted with permission from ref. [258] under a Creative Commons Attribution 4.0 International License. Copyright 2021 The Authors.

Bending can also be easily performed with the TEM-STM platform. During the bending process, the ultrahigh stress and large surface image force in nanostructured materials can cause unexpected deformation phenomena, while the high surface energy of nanomaterials facilitates atom diffusion and structural reconstruction. For example, under high bending strains, the core-shell GeSi structure can be modulated to the polycrystalline/amorphous phase in the Si shell region, but the Ge cores retain their single crystal status with the local lattice strains on the compressed side (**Figure 14**).[259]

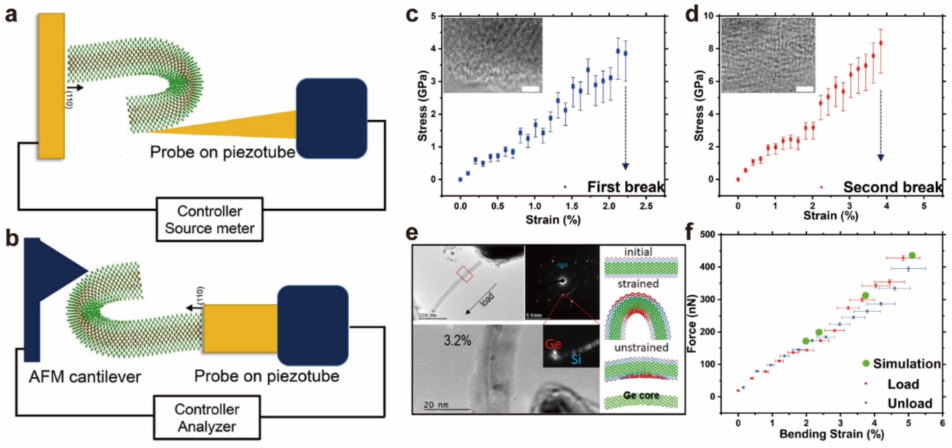

Figure 14. *in situ* Bending tests for Ge/Si core-shell nanowires with phase transformation. (a,b). Designed setups for *in situ* TEM bending of core-shell Ge-Si nanowires during (a) electrical or (b) mechanical measurements. (c,d) Tensile stress-strain curves recorded on an individual Ge/Si core-shell nanowire before (c) and after its first breakage (d), scale bars, 10 nm. (e) TEM images of a strained nanowire, showing local contrast under a 3.2% strain with MD simulation of the Ge/Si core-shell hybrid nanowire. (f) Force values recorded under bending to a 5% strain followed by nanowire reloading. Reprinted with permission from ref. [259]. Copyright 2018 American Chemical Society.

TEM-STM techniques with three-dimensional piezoelectric actuator have also been widely used to simulate the shear deformation process in the TEM holder. One approach is to mimic the sliding against the surface of specimen through the nanoprobe. Another approach is to achieve *in situ* nanoscale "cold welding" in the TEM holder and then move the probe sideways to induce pure shear deformation.[242] Using TEM-STM technology, Zhu et al. observed extreme shear plasticity of coherent twin boundaries in gold nanocrystals dominated by sliding up to 364% strain.[260] Chen et al. systematically investigated the atomistic annihilation mechanism of nanograins embedded in a gold nanocrystal during shear loading via *in situ* TEM-STM technology. They found that the grain annihilation process mainly proceeds by the dislocation annihilation process, which induces grain rotation and the occurrence of the opposite grain boundaries.[261]

4.2.2 Nanoindentation-based technology for *in situ* nanomechanics

Nanoindentation[262] based *in situ* TEM technology is derived from the instrumented indentation technique where a tip is forced into a flat surface to measure the force and displacement. The traditional indentation technique can provide the quantitative value of hardness, elastic modulus, and even yield stress. Although it cannot directly observe the plastic deformation process, the step-like and discontinuous curve obtained during the loading tests also represents the intrinsic plastic deformation.[263] However, integrated into TEM, technological advances give us the opportunity to achieve direct observation during the deformation process. And with the high resolution of TEM, it is possible to access the atomic resolution to image crystalline phase transformation and defect evolution during the deformation process. At the end of the last century, researchers developed several holders to study the plasticity mechanism of metallic materials using the precise positioning capabilities of the piezoelectric stacks and tubes.[264-266] **Figure 15a** shows the typical nanomechanical sample holder from Bruker Hysitron. Different from the TEM-STM system, the PI 95 holder is equipped with a load sensor to obtain load−displacement curves in real time. The noise floor for such device has been declaimed to be less than 0.5 N, and the maximum accessible loads are basically less than 10 mN. The sample holders mainly include two types, sample and tip moving part. According to the specific samples being examined, various tip geometries can be employed, such as Berkovichm, Vickers tip, truncated cone, or wedge. For example, the wedge type tip is usually used for thin section to avoid sample sliding during compression deformation.[262] The sample geometry for nanoindentation based *in situ* TEM experiments mainly includes nanowire,[267] nanoparticle,[161] nanopillar,[268, 269] and nano-sized thin film materials.[270] In addition, customized punch tips[198] (e.g., tensile gripper as shown in **Figure 15b**) and sample geometries[271, 272] (push-to-pull geometry as shown in **Figure 15c**) can be prepared by FIB fabrication and integrated with the nanoindentation platform to perform tensile tests. Different types of MEMS chips actuated by nanoindentation tips also provide many more possibilities for the *in situ* nanomechanics TEM lab, such as push-to-pull (PTP) devices[245, 247] and electrical PTP as shown in **Figure 15d-f**.[273, 274] The PTP device contains a fixed part and a movable part. The sample can be clamped in the region labelled by the red rectangle in **Figure 15d**. Tensile tests can be performed by pushing the indenter tip against the semicircular part of the PTP device indicated by the yellow arrow in **Figure 15d** and the load−displacement curve is recorded by the sensors integrated in the TEM holder.[56] In addition to tensile test,[275] *in situ* friction tests are also available with the integrated lateral sensor.[276, 277] The tip can also be gold-coated for electrical tests coupled with mechanical tests.

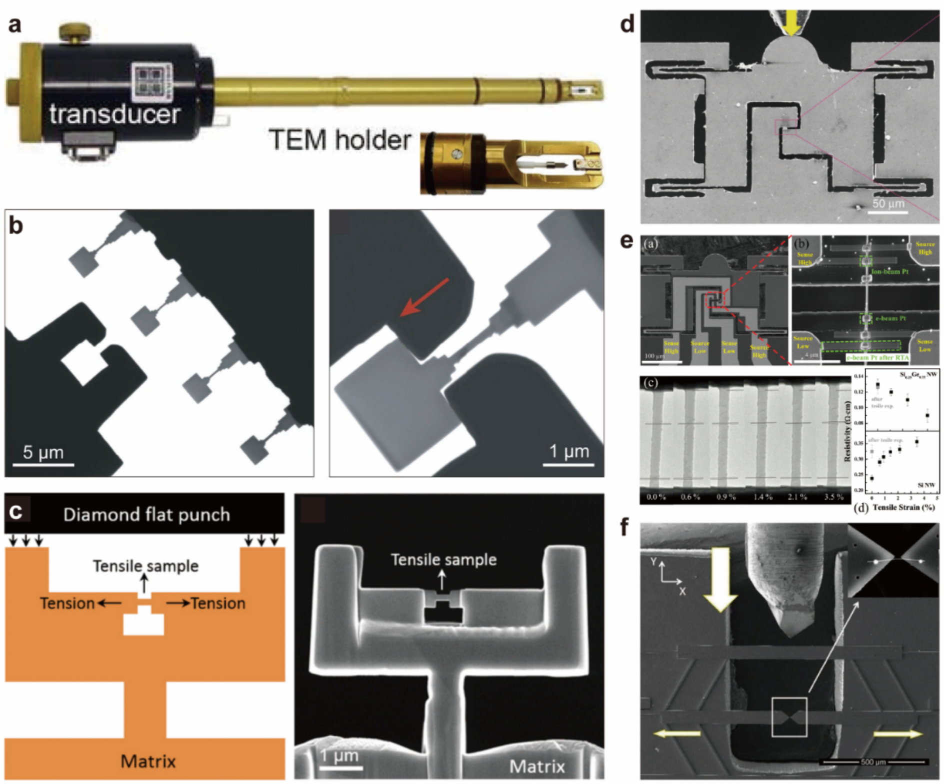

Figure 15. Nanoindentation-based technique for *in situ* nanomechanics. (a) TEM holder from Bruker Hysitron with zoomed in head part. Reprinted with permission from ref. [278]. Copyright 2018 Springer Nature Singapore Pte Ltd. (b) FIB-prepared tensile gripper. Reprinted with permission from ref. [198]. Copyright 2021 American Association for the Advancement of Science. (c) FIB-prepared push-to-pull geometry sample. Reprinted with permission from ref. [271]. Copyright 2016 American Physical Society. (d) Push-to-pull (PTP) device. Reprinted with permission from ref. [245] under a Creative Commons Attribution 4.0 International License. Copyright 2020 The Authors. (e) PTP device integrated with four points electrode. Reprinted with permission from ref. [279]. Copyright 2015 American Chemical Society. (f) PTP device with different geometry designs. Reprinted with permission from ref. [274]. Copyright 2009 Society for Experimental Mechanics.

A well-known experiment for examining the mechanical characteristics of materials at micro- and nanoscale length scales is the micropillar compression test. The *in situ* compression test conducted in the TEM chamber enables real-time visualization of various deformation-induced phase transformation phenomena. By fabricating a core/shell crystalline Si/amorphous Si sample to avoid early cracking during *in situ* TEM uniaxial compression, the deformation-induced crystalline-to-amorphous transition (CAT) by slip-mediated generation and storage of stacking faults (SFs) in silicon is clearly recorded, as shown in **Figure 16a.**[280] The mechanical loading also triggered the phase transformation from 4H to 3C in SiC.[269] The shape memory effect of NiTi alloy is known to occur as a result of reversible martensitic phase transformation. To explore the stress-induced martensitic phase transformation mechanism at the nanometer scale, a nanopillar compression test inside TEM is used to study the deformation behaviour of NiTi. The results reveals that the stress-induced B2 to B19’ transformation persists even when the critical sample size is reduced to below 200 nm (**Figure 16b**), thereby expanding the potential applications of shape memory alloys in micro/nanodevices.[281]

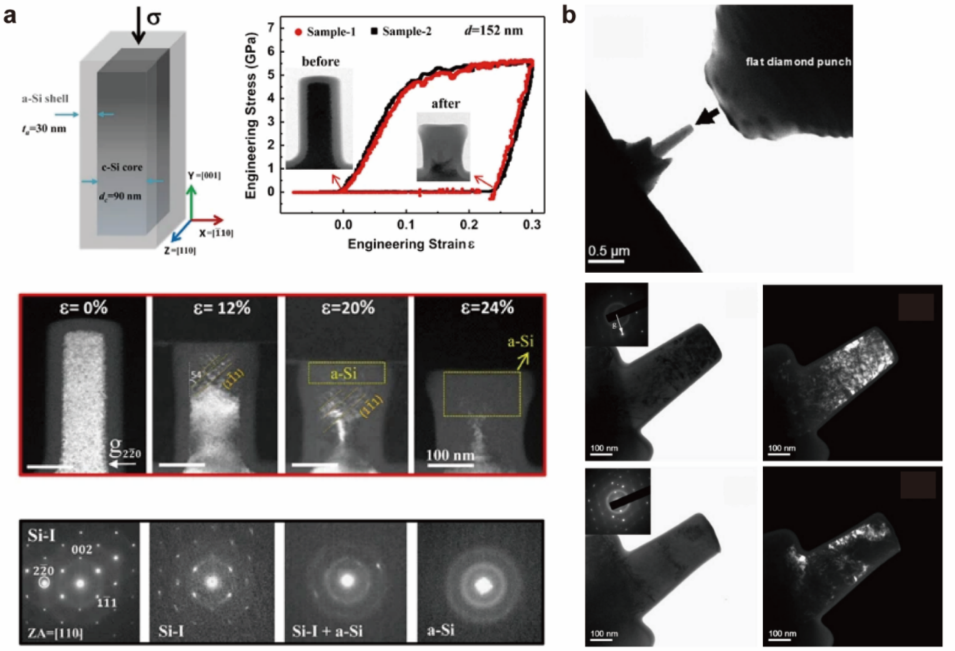

Figure 16. The *in situ* observation of (a) the compression-induced crystalline-to-amorphous transition. and (b) the martensitic phase. (a) Reprinted with permission from ref. [280] under a Creative Commons Attribution 4.0 International License. Copyright 2016 The Authors. (b) Reprinted with permission from ref. [281]. Copyright 2009 Elsevier Ltd.

in situ TEM uniaxial compression on nanopillars is a typical method to induce a shear strain component. Since the shear stress can be calculated with the specimen orientation and slip plane orientation, this type of method provides an effective quantitative way to study the deformation process associated with shear stress. Traditionally, solid amorphization usually happens under special conditions such as melt quenching, irradiation, impact loading, and severe plastic deformation. An *in situ* TEM uniaxial compression experiment for silicon crystals was reported to induce shear-driven solid amorphization.[282] With the increase of applied compressive stress, the nanopillar displayed localized deformation instead of uniform deformation. Shear-driven amorphization of single Si nanocrystals was further achieved within a dominant shear band. Different from the traditional direct transformation from the parent crystalline phase to amorphous by defect accumulation, they found that the intermediate crystalline phase formed in the strip is diamond-hexagonal with a 2H polytype of diamond-cubic with the stacking sequence …AaBbAaBb… along the <111> direction before amorphization (**Figure 17a-**

d).[282] This kind of atomic phase transformation mechanism facilitates the development and application of PEN.

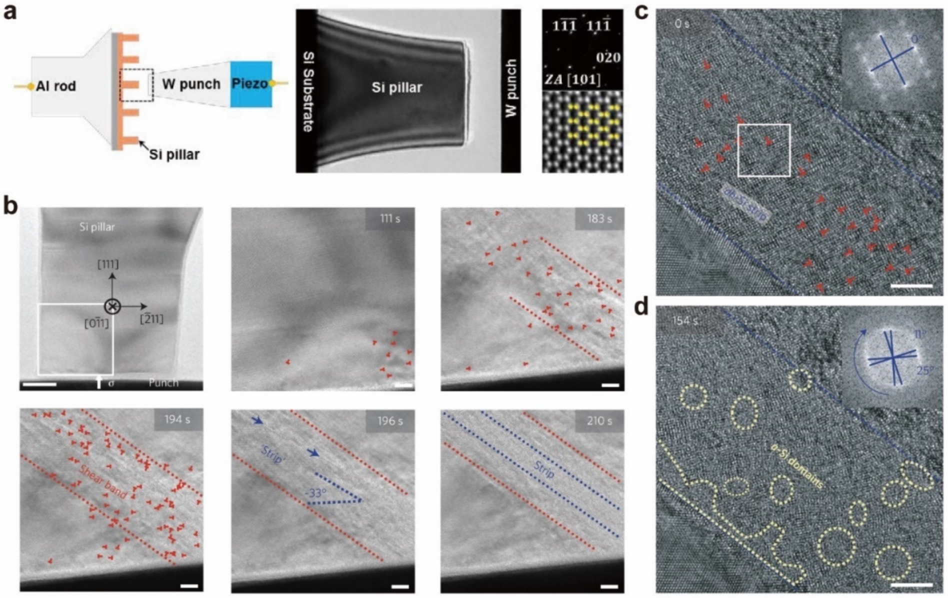

Figure 17. The *in situ* observation of the shear-induced phase transformation in silicon crystals via nanoindentation-based technology. Reprinted with permission from ref.[282]. Copyright 2016 Springer Nature Limited.

4.2.3 MEMS-based technology for *in situ* nanomechanics

MEMS actuated by thermal or electrical stimuli represent another important approach to conducting *in situ* nanomechanics tests in the TEM chamber. Using MEMS, tensile, shear, bending, and compression tests can be easily performed in TEM along with quantitative mechanical properties of the specimen.[283] During mechanical tests, MEMS setups are ideal experimental platforms to observe the microstructure evolution at the nanometer and even atomic scale during the deformation process, facilitating a thorough understanding of the defect mechanism. Moreover, MEMS can be further developed as a multifunctional platform after integration with thermal, gas, and electrical stimuli, displaying the broad application potential of *in situ* TEM technology.[284]

Tensile test is the most straightforward experiment for characterizing mechanical properties. The typical normal macroscale testing machine consists mainly of an actuator, sensor, and specimen grips. However, performing such tests in the TEM chamber is quite challenging due to the limited space and nanoscale sample size. To successfully integrate MEMS chips into TEM, MEMS-based actuation and loading sensors have emerged as excellent candidates. MEMS devices can be classified into three different types, external actuation and loading sensing, external actuation and on-chip load sensing, and on-chip actuation and load sensing.[285] For the first type of MEMS, it is generally combined with nanoindentation as mentioned above (**Figure 15c-f)**. The force and displacement of the sample must be calculated from the nanoindenter signals, and the elastic response of the push-to-pull structure must be carefully considered. In the second type, the MEMS platform is stretched by an external piezoelectric actuator that is either hooked[286] or glued[287] to the gripping pad. The force is obtained by calculating the deflection of the sensor beam, as shown in **Figure 18a**.[288] In the third type (i.e., MEMS based on on-chip actuation), the most widely employed mechanism is electrostatic and thermal actuation, as shown in **Figure 18b,c**, respectively.[283] The comb-drive actuator is popular for electrostatic actuation due to its constant force generation over a wide displacement range.[289] Thermal actuation mainly includes the V-shaped and Z-shaped types.[290, 291] These MEMS-based approaches for *in situ* tensile testing can provide accurate force−displacement data and mechanical properties at the nanoscale. For instance, a study by Sheng et al. used a Hysitron PTP device to convert the compressive motion of the indenter into tensile loading in the TEM. They studied the transformation dynamics from β/ω phase to α' phase in a TiZrCuBe metallic glass composite. The phase transformation produces preferential sites for shear banding nucleation during deformation.[292] Similarly, in another experiment, the superelasticity of VO_2 nanowires induced by phase transformation was studied using the PI 95 PicoIndenter coupled with a Hysitron PTP device (**Figure 18d**). The *in situ* TEM observations demonstrate that the pre-existing M2 phase can act as an initiation site during the M2 phase motion and promote the M1−M2 phase transition. The transformation process between M1 and M2 phases was found to be uniaxial and reversible (**Figure 18e**).[293] These studies provide insights into the mechanisms underlying phase transformations and the effects of PEN on the mechanical properties of nanomaterials.

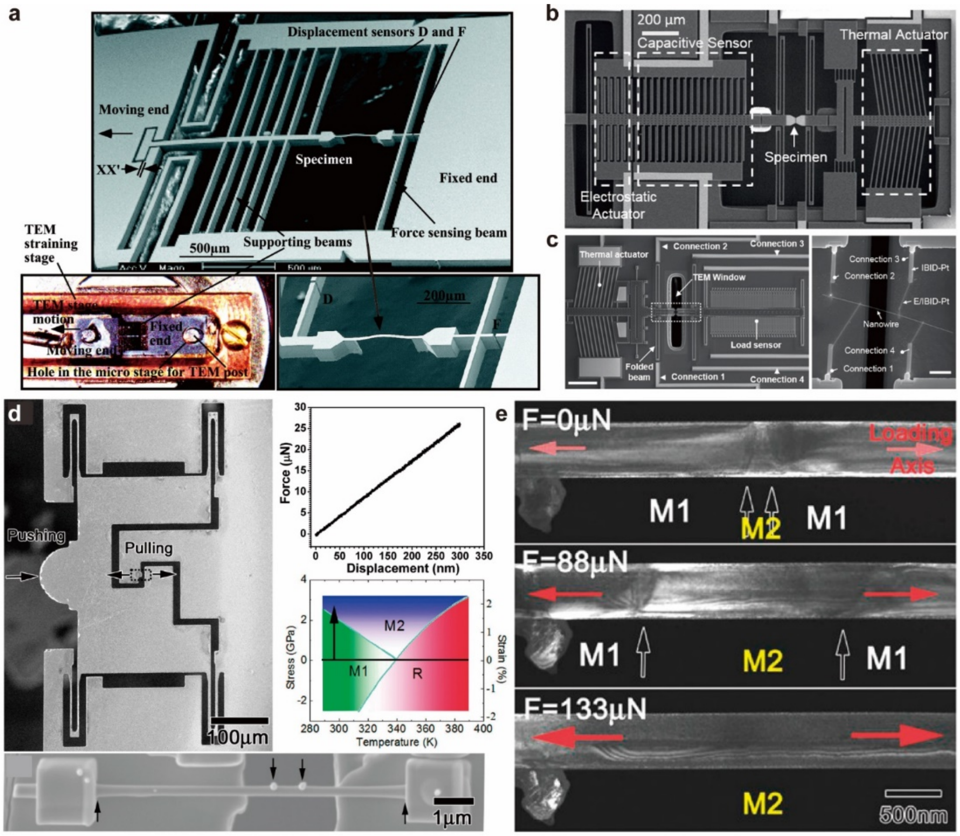

Figure 18. The typical MEMS devices for *in situ* TEM mechanics. (a) External actuation-based MEMS. Reprinted with permission from ref.[288]. Copyright 2004 The National Academy of Sciences. (b,c) On-chip actuation-based MEMS. Reprinted with permission from ref.[283]. Copyright 2020 The Materials Research Society. (d,e) *in situ* Observation of the phase transformation-induced superelasticity via the PTP device and the reversible phase transformation process. Reprinted with permission from ref.[293]. Copyright 2011 American Chemical Society.

Shear deformation behavior at the material surface is of great interest to scientists for a deeper understanding of tribological properties. During tribological deformation, the surface experiences significant plastic strain and *in situ* TEM technology provides a unique opportunity to directly observe the internal structure evolution and phase transition during shear deformation. However, compared to tensile and compression studies, *in situ* shear investigations are relatively limited. In fact, shear deformation can also occur during plastic deformation processes caused by tension, compression, or bending. In 2012, Sato et al.[294] developed an electrostatically driven MEMS specimen holder for TEM that allows precise control of atomic displacement. By employing electrostatic actuators in MEMS devices, the charging drift and thermal drift issues associated with previous piezoelectric actuators can be avoided or significantly suppressed. The proposed MEMS device (**Figure 19a**) brings two opposing tips into contact to form a nanojunction where a shear force can be applied. The shear force is calculated by the product of the stiffness and the displacement difference before and after the junction is formed.

The decreased displacement was considered as the stiffness of the nanojunction. Based on this technique, atomic-scale stick-slip phenomena were successfully visualized during the deformation process of the Ag asperity in **Figure 19b**. In 2021, Lu et al. utilized Lorentz force induced by electric current to achieve the quantitative friction test in TEM.[295] Taking advantage of the strong magnetic field in the TEM chamber, when an electric current flows through the punch of the commercial electromechanical holder, it experiences a Lorentz force. This force causes the punch to deflect vertically in the loading direction of the specimen holder, enabling *in situ* TEM Ag-W friction experiments as shown in **Figure 19c-d**. The Lorentz force based actuator can effectively improve the mechanical stability as it is linearly proportional to the input current.

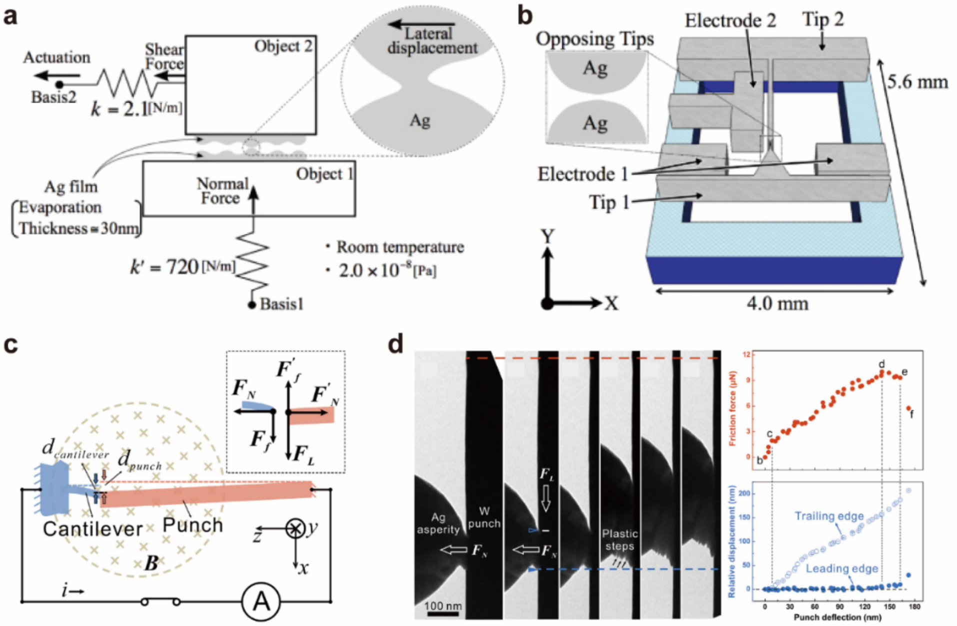

Figure 19. *in situ* MEMS-based shear deformation technique. (a-b) Electrostatically driven MEMS method for Ag−Ag asperity study. Reprinted with permission from ref.[294]. Copyright 2012 IOP Publishing Ltd. (c-d) Lorentz force driven MEMS method for Ag-W asperity study. Reprinted with permission from ref.[295]. Copyright 2021 Elsevier.

In addition to the loading method, another challenge is to achieve double-tilt MEMS holders in the TEM chamber due to space limitations and operational difficulties. To address this issue, researchers have made considerable efforts to develop double-tilt holders using thermal-based actuation methods and electrostatic comb-based actuation mechanisms. Rodrigo designed a double-tilt *in situ* TEM holder with 9 electrical connections, enabling tilting of up to ±15°.[296] The main components of the holder tip are a frame and a tilting table supported by the frame, which rotates around the eucentric axis. As the bar moves back and forth against the incline, the tilt table rotates. A torsion spring maintains contact by pushing the tilt table against the push bar. The relationship between the linear displacement of the bar and the rotation of the table is determined by the geometry of the incline and the radius of the tip of the bar (**Figure 20a**).[296] However, thermal drift remains an unavoidable problem in the tensile test experiments in these works. To address the issue of thermal drift, an electrostatic comb-based actuator has advantages over a thermal-based actuator method. Yang et al. designed and developed an electrostatically actuated double-tilt *in situ* TEM tensile device with an angle tilt within 10° and effective tensile displacement up to 1 μm (**Figure 20b**).[297] However, the electrostatic comb-based actuator faces challenges in achieving large tensile forces and displacements due to the limited space available in standard double-tilt holders.

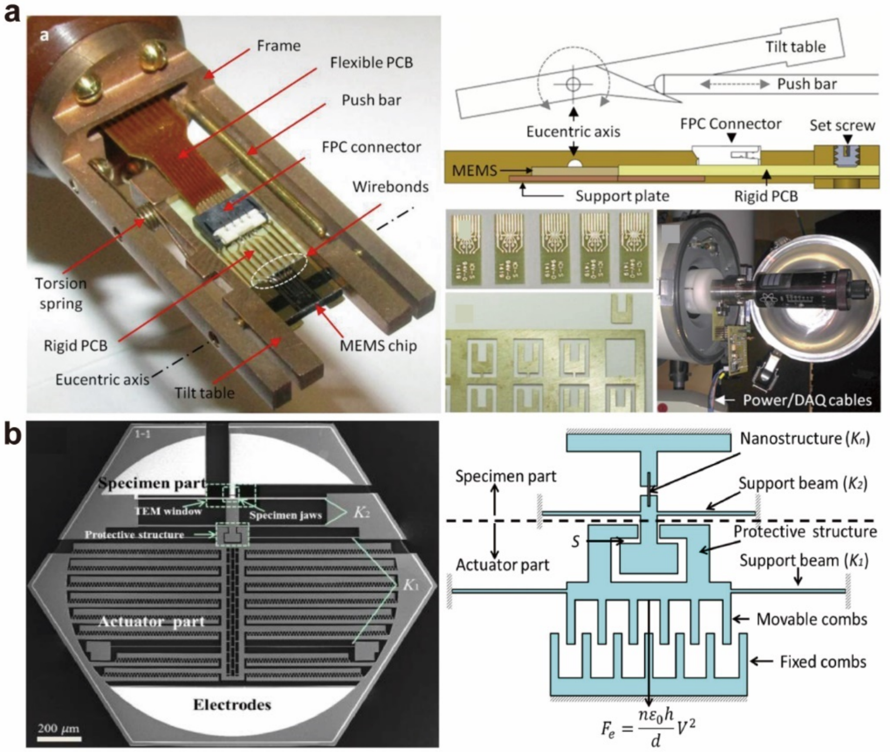

Figure 20. The double-tilt MEMS holders based on (a) thermal actuator method and (b) electrostatic comb actuator. (a) Reprinted with permission from ref [296]. Copyright 2015 Elsevier B.V. (b) Reprinted with permission from ref [297]. Copyright 2018 Elsevier B.V.

4.2.4 *in situ* TEM mechanical technology based on difference in thermal expansion

The utilization of commercial *in situ* TEM loading approach or MEMS allows researchers to obtain quantitative stress and strain results. However, these traditional loading methods also have certain drawbacks. Due to the uncontrollable mechanical vibration, atomic resolution is difficult to access during the *in situ* loading process, which limits the observation of microstructure evolution and phase transformation. In addition, most of the mechanical testing device in TEM can only provide the choice of single-tilt holder, which makes it difficult to observe some planar defects with specific crystallographic orientation. To characterize the atomic scale bending deformation in semiconductor and metallic nanowires, Wang et al. randomly spread the nickel nanowires on a pre-broken colloidal thin film (CTF) on a TEM specimen grid, and then designed a nanowire controllable bending experiment by introducing an expansion of the colloidal thin film under the irradiation of the electron beam, as shown in **Figure 21a**. The introduced mechanical strain drove the reversible continuous phase transformation from *fcc* phase to *bct* phase in Ni nanowires and the atomic scale observation was achieved with this technique, as shown in **Figure 21b**.[298] With the similar approach, a large strain (up to 14%) was achieved during the bending of Si nanowires. The continuous strain on the Lomer dislocations induced a crystalline−amorphous phase transition in the Si nanowires.[299] In another bending experiment conducted on single crystalline Si nanowires, it was observed that the increase in bending strain led to the occurrence of ripple-buckling and the shit of the neutral-strain axis from the compressive zone to the tensile region. The bending is accompanied by frequent and diverse dislocation events such as nucleation, motion, interaction, and annihilation, resulting in inelastic instability and early plasticity in brittle Si nanowires.[300]

Based on the thermal bimetallic technique used in TEM, as shown in **Figure 21c**, Han et al. developed a novel *in situ* controllable tensile testing device for TEM measurements that can slowly and controllably deform the nanowires, nanoparticles, and nanocrystalline thin films.[301-309] Their method allows the measurement of regular TEM samples with the assistance of FIB fabrication. Importantly, this approach retains the double-tilt capability to perform high-resolution TEM observations[310-314] as well as regular “two-beam” dark-field imaging investigations, which is critical for defect analysis. The strain rate is in the range of 10^{-2} to 10^{-5} s^{-1}. The TEM extensor consists of two thermally actuated bimetal strips. With this device, the investigations of PEN can be conducted and observed in real time at the atomic scale.[57, 306] For example, continuous phase modulation of single crystalline Ag nanowires was achieved by compression-induced bending strain in a spherical aberration-corrected TEM. During the *in situ* experiment, the process of transition from *fcc* structure to *bcc* structure, followed by *hcp* structure, and finally to reoriented *fcc* structure under bending was clearly observed, as shown in **Figure 21d**.[243] Using the similar technique, the deformation-induced phase transformation in Au nanoribbons from 4H to *fcc* phase was observed to result from the activated partial dislocations nucleating at the nanoribbon surface and gliding into the nanoribbons. At the last deformation stage, the reverse phase transformation process from *fcc* to 4H is further observed.[196] Besides the noble metal materials, the deformation behavior at the crack tip of nano-sized *bcc* single crystalline Mo were also studied. For the first time, the *bcc* to face-centered orthogonal (*fco*) transformation and the layer-by-layer growth mode in *fco* Mo were recorded.[302]

The atomic level observation of PEN is an essential step to tailor their physicochemical properties with desired phase structure and then broaden their practical applications.

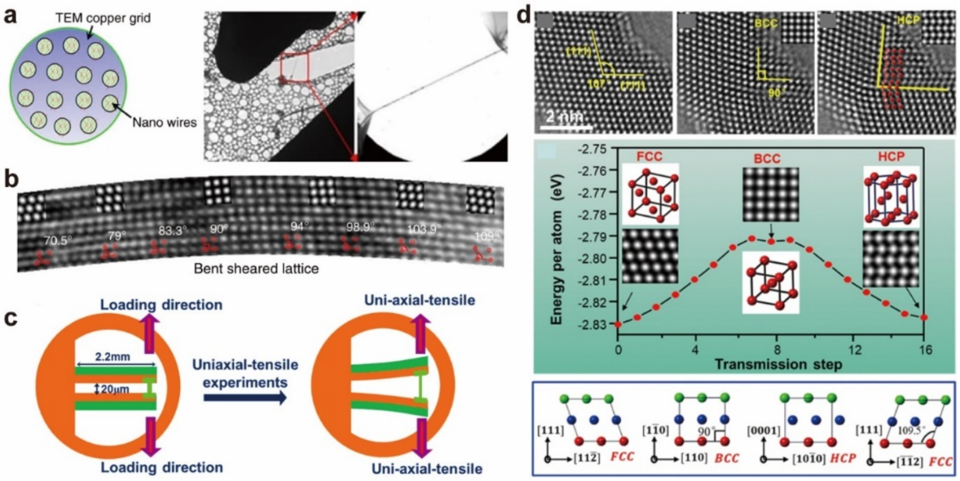

Figure 21. (a) *in situ* Bending deformation via pre-broken colloidal thin film. (b) Observation of the reversible phase transformation in Ni nanowires. Reprinted with permission from ref. [298] under a Creative Commons Attribution-Non-commercial-ShareAlike 3.0 Unported License. Copyright 2013 The Authors. (c) The thermal bimetallic technique. Reprinted with permission from ref. [304]. Copyright 2018 Acta Materialia Inc. (d) Observation of the Ag nanowire phase transformation via the thermal bimetallic technique. Reprinted with permission from ref. [243]. Copyright 2022 American Physical Society.

4.2.5 *in situ* TEM high temperature mechanical test

The MEMS-based heating chip can be easily coupled with other applied physical or chemical factors such as mechanical, electrical, liquid, gas, optical, and magnetic fields to achieve further capabilities and functionalities. For example, the integration of the *in situ* heating platform and the mechanical testing system in the TEM enables to reveal the atomistic mechanisms for the high-temperature mechanical behavior of high-temperature materials. During *in situ* thermomechanical testing, thermal and vibration induced drift is a long-term issue. Although some new drift correction approaches, both hardware and software, have been developed, it is still difficult to acquire the strain−stress results continuously during heating.[315, 316] Temperature measurement under TEM observation has also been a persistent and challenging problem over the years. The accuracy of temperature measurement directly affects the reliability of the thermodynamic and kinetic information obtained. In 2006, Huang et al. achieved high-temperature nanomechanical testing of CNTs through the integration probe-based method and controllable Joule heating in TEM during tensile deformation.[317] A remarkable superplasticity of over 280% was observed in CNTs before fracture, which was attributed to the nucleation and movement of kinks within the nanotube structure. Wang et al. designed and developed a multifunctional microchip incorporating actuators, sensors, micro-heaters, and electrode[318] to achieve both gradient and uniform temperature fields in the sample area. The utilization of MEMS enables precise measurement of elongation and force up to 950 K in the TEM chamber.[318] For example, in 2019, Cheng et al. employed a newly developed MEMS technology to conduct nano-thermomechanical tensile testing in TEM on Si nanowires and found that Si exhibited pronounced dislocation-mediated plastic deformation followed by fracture at elevated temperatures, which is different from the general brittle nature of Si nanowires at ambient temperature.[319] In 2021, Zhang et al. introduced a thermomechanical testing device capable of operating inside the TEM at high temperatures up to 1556 K with atomic resolution imaging capabilities, as shown in **Figure 22a**. The device mainly contains two essential parts, the temperature control part and the deformation application part. To provide a heating source and serve as the temperature monitor, Pt heating circuits were placed at both ends of the sample. The applied force and displacement were driven by a zirconate titanate (PZT) actuator, achieving a resolution of 5 nN and a step size of 0.1 nm, respectively.[320] Using this technology, the nucleation and propagation process of the crack was observed in W at 973 K. Moreover, the deformation-induced *bcc* to *fcc* phase transformation in single crystal W was achieved at the crack tip with atomic resolution (**Figure 22b)**. The phase transformation was considered to enable the elimination of deformation energy and the reductions of local stress concentrations,[320] indicating the potential role of PEN in the design of high-impact resistant materials in the future.

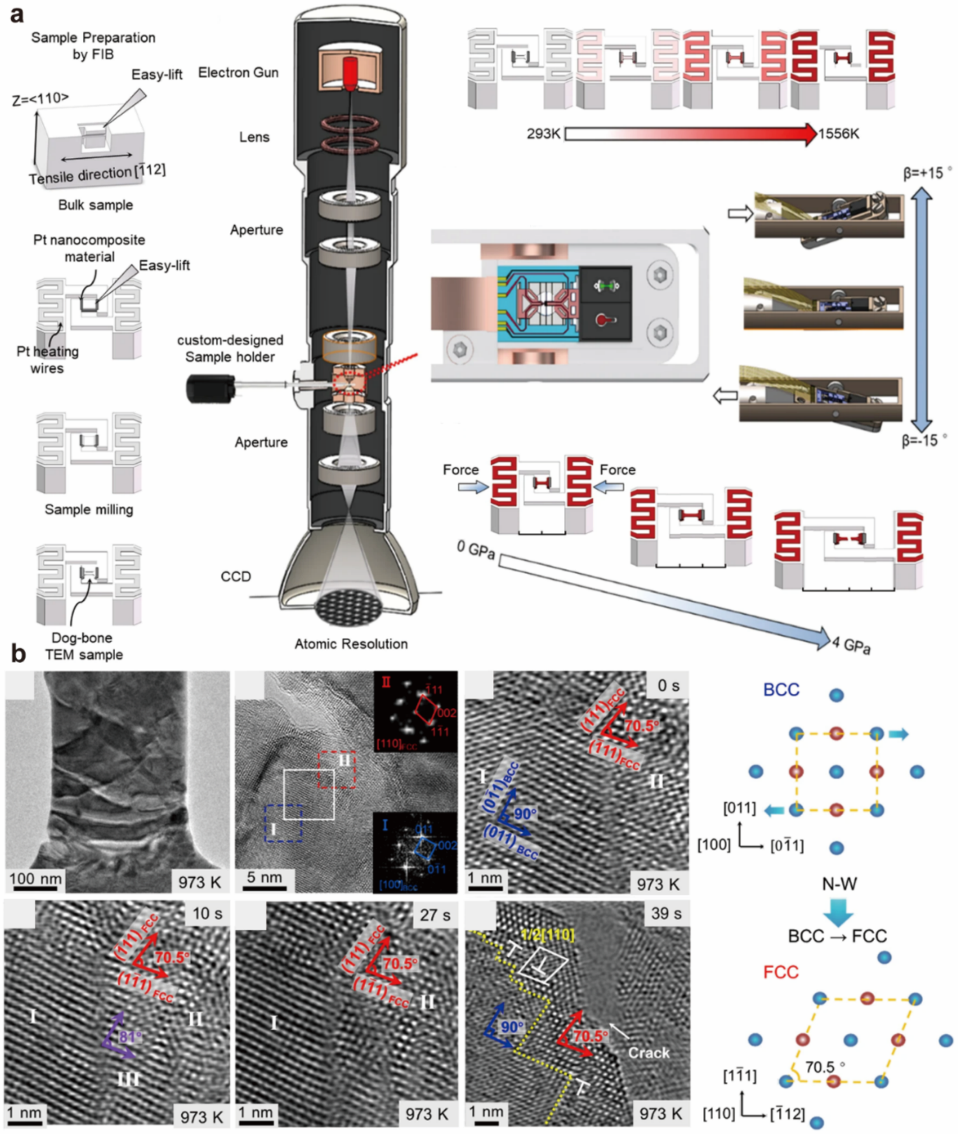

Figure 22. (a) *in situ* TEM high-temperature mechanical testing system.[320] (b) Observation of the stress induced *bcc-fcc* phase transformation in single crystal W during high temperature testing. Reprinted with permission from ref. [320] under a Creative Commons Attribution 4.0 International License. Copyright 2021 The Authors.

4.2.6 Section summary

in situ Nanomechanics in TEM has undergone a long development with more and more stability and variety of loading setups for different mechanical tests, including TEM-STM holder-based nanomechanics platform, nanoindentation-based technology, MEMS-based nanomechanics technology, various home-made setups, and coupled with high-temperature apparatus. The TEM-STM holder provides the stable loading process for high-resolution images, and it can be easily coupled with other fields (e.g., temperature and electrical) by applying electric current through probes. Nanoindentation-based technology equipped with piezo transducers allows quantitative characterization of mechanical tests. MEMS-based nanomecahnics technology utilizes microfabricated devices with integrated mechanical actuators and sensors. These devices enable precise control and measurement of forces and displacements, offering a versatile platform for *in situ* mechanical testing. The *in situ* TEM mechanical tests based on differential thermal expansion can easily achieve double-tilt for characterization of different zone axes. The performance of crystalline materials at elevated temperatures can be easily investigated with high temperature apparatus, providing insight into their thermal stability and diffusion kinetics, as well as their mechanical properties under extreme conditions. These nanomechanics setups also enable the different loading modes for comprehensive characterization of the mechanical properties of nanomaterials, such as direct tensile tests, compression tests, shear tests, et al. In particular for phase modulation by mechanical loading, *in situ* mechanical TEM allows researchers to observe and record the behavior of materials at the atomic level during mechanical loading in real time. This provides valuable insights into the mechanisms of phase modulation caused by mechanical loading. The data obtained from these experiments not only contribute to a better understanding of fundamental aspects of material behaviour, but also serve as a guide for the design of high-performance materials. Furthermore, this knowledge opens up the possibility of tuning physicochemical properties by PEN.

4.3 *in situ* TEM thermal engineering for PEN

Increasing temperature results in significant entropic contributions to the total system energies, which generally lead to phase transformation to lower the system energy. The vibration of phonons is one of the main driving forces related to the thermally induced phase transformation, along with enhanced atomic diffusion to overcome the large energy barrier. Therefore, annealing is widely used to manipulate the packing modes for crystalline materials. The *in situ* heating TEM provides an effective tool with spatial and chemical resolution to achieve the real-time phase modulation process at high temperatures to understand the atomic phase transformation mechanism for PEN. Typically, the heating holder is equipped with an electrical wire or a MEMS chip.[321-323] The typical commercial MEMS-based *in situ* heating TEM holder, e.g., DENS Wildfire holder, is shown in **Figure 23a**.[324] Compared with the traditional hotplates, MEMS technology can minimize the heater and significantly decrease the power consumption, which facilities faster response speed, wider temperature adjustment range, and higher heating uniformity.[325] Generally, the microheater consists of a silicon substrate with a thermally insulating dielectric thin film layer, e.g., amorphous silicon nitride or carbon support films. The electric current passing through the heating area of the MEMS chip produces Joule heating via a voltage or current source and is transferred to the specimens. The overall structural design of the *in situ* heating

MEMS chip can be divided into four types, with the microheater installed on the substrate,[326, 327] on an open or closed membrane,[328-330] or on a cantilever,[331, 332] as shown in **Figure 23b.** Metal materials, e.g., molybdenum (Mo), are widely used in micro-heaters due to the excellent stability, low expansion coefficient, and excellent corrosion resistance at high temperatures. Various metal micro-heater geometries have been developed, such as S-shaped, circular spirals, curved corners, double spirals, and meanders, for better temperature homogeneity in the functional area, as shown in **Figure 23c**.[333, 334]

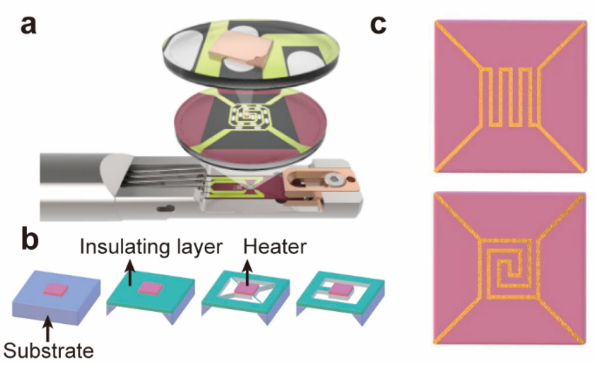

Figure 23. (a) Schematic of the *in situ* heating DENS Wildfire holder. Reprinted with permission from ref [324]. Copyright 2017 Oxford University Press. (b) The overall structure design.[326, 327, 329-332, 335] (c) Microheater geometries for *in situ* TEM heating MEMS.[328, 333, 334]

4.3.1 Nanoparticles and nanowires

Noble metal nanomaterials, e.g., Au, Ag, Pd, Pt, Rh, and Ir, with different shape, composition, and phase structure, show unique properties for surface enhanced Raman scattering (SERS), catalysis, and clean energy applications. Bulk noble metals typically exhibit a highly symmetric *fcc* structure. However, when the feature size is reduced to the nanoscale, the crystal structure can change due to the influence of surface energy, especially under thermal effect. *in situ* TEM heating technology allows atomic observation of the thermally modulated phase transformation process.[336-345] For example, Au nanoparticles exhibit the *fcc* phase at room temperature. Recently, an unusual metastable hexagonal (4H) phase has been synthesized which show promise for plasmonic and catalytic applications. By *in situ* heating, the 4H phase can be modulated back to the *fcc* phase, and the critical transformation point is at 800 K, which is much higher for normal applications. These investigations demonstrated the thermal stability of the 4H phase in Au nanoribbons and guided the applications of 4H Au nanoribbons (**Figure 24a**).[75] Similarly, in 2023, Jiang et al. achieved the phase modulation of PdCu nanoparticles from *fcc* phase to *bcc* phase via *in situ* TEM heating method, as shown in **Figure 24b**.[337] It is revealed that the *bcc* phase always forms a discrete, few-atom-wide coherent *bcc*-*fcc* interface at the edge of the *fcc* nanoparticles and propagates across the nanoparticles from there. The interface always serves as a transitional precursor phase for the formation of *bcc* phase.[337] Because the *fcc*-to-*bcc* phase transition is widely used in the production of durable steels,[165] shape memory alloys,[346] and catalytic materials,[347] the dynamic study of the phase transition enabled by *in situ* TEM technology can effectively guide the material synthesis and modification.

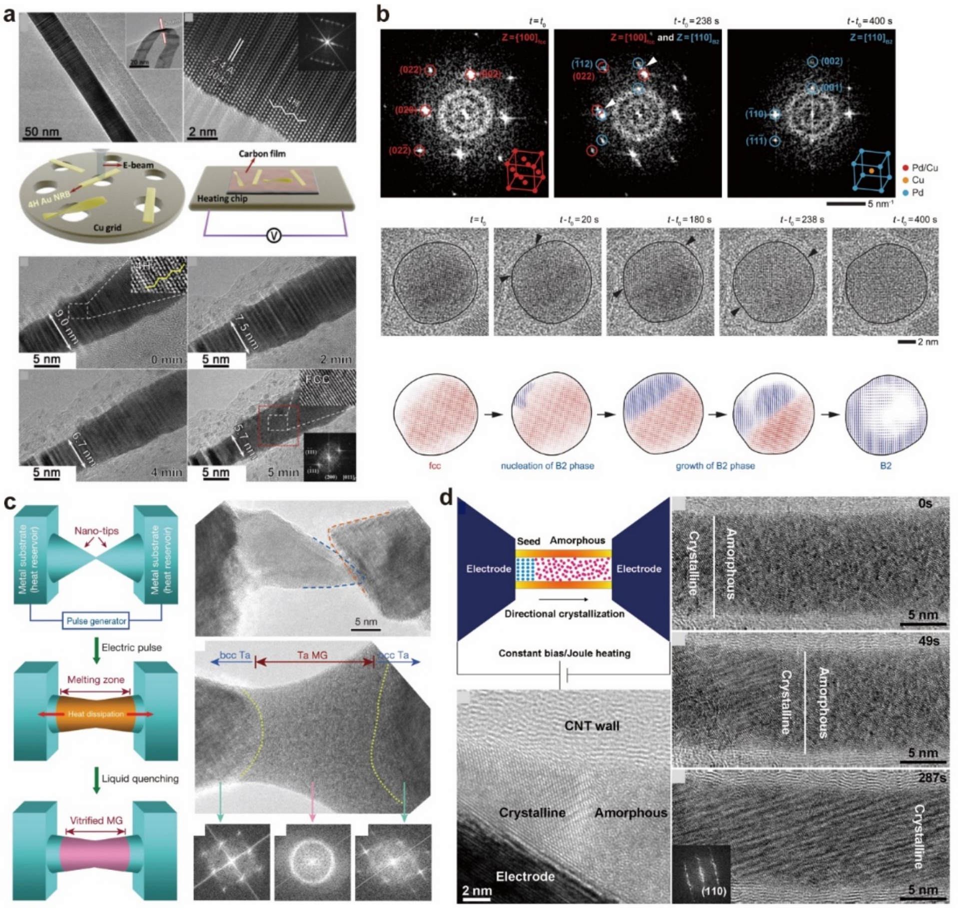

Figure 24. (a) Thermal effect induced 4H to *fcc* transition in Au nanoribbons. Reprinted with permission from ref. [75]. Copyright 2019 Elsevier Inc. (b) The process of the *fcc*-to-*bcc* phase transition in PdCu alloy nanoparticles. Reprinted with permission from ref. [337] under a Creative Commons Attribution 4.0 International License. Copyright 2023 The Authors. (c) The formation of monatomic metallic glasses induces by ultrafast liquid quenching. Reprinted with permission from ref. [348]. Copyright 2014 Springer Nature Limited. (d) Observation of the directional crystallization process of amorphous Fe nanowire in CNT. Reprinted with permission from ref. [349]. Copyright 2015 American Chemical Society.

In combination with the TEM platform, the *in situ* heating technology demonstrates extensive practical applications, including quenching, ultrafast heating, and cyclic heating. Traditionally, monatomic metallic liquids are very difficult to form metallic glass due to their extremely low glass-forming ability resulting from fast nucleation and crystal growth kinetics. In 2014, Zhong et al. reported an ultrafast liquid quenching approach in TEM to observe the formation of monatomic metallic glasses (**Figure 24c**).[348] They fabricated two nano-tips with clean surfaces in contact with each other. Then, a short square electrical pulse was used to produce local Joule heating to melt the extrusion tips. Consequently, the instantaneous stopping of the electrical pulse caused the local heating to dissipate rapidly, achieving the ultrahigh cooling rate of about $\sim 10^{14}$ K/s in the middle area. The ultrahigh cooling rate supported by *in situ* TEM technology can reach the deep quenching and become an effective tool to explore the fast kinetics and formation mechanism of metastable materials under conditions far from the equilibrium.[348] Similar fast heating/cooling was used to observe the amorphization and directional crystallization behavior of Fe in hollow CNTs. The CNT nanocrucibles provide a unique platform to investigate the size related phenomena. Due to the local cooling effect, the Fe nanowire close to the electrode still retains the crystalline structure. The remaining crystalline Fe phase can act as the nucleation seed to achieve directional crystallization under a constant bias, as shown in **Figure 24d**.[349] It indicates that the unique and highly controllable thermal process enabled by the *in situ* TEM heating technology provides wide opportunities to fabricate various novel phase structures for practical applications.

The *in situ* TEM heating techniques also facilitate the study of nanoscale growth and degradation phenomena. The heating rate plays an important role in improving the densification of ceramics, as the coarsening phenomenon is suppressed by using a high heating rate. Therefore, various ceramic sintering techniques, including flash sintering and ultra-fast high-temperature sintering, are applied to achieve high heating rates. However, they cannot provide micro/nanoscale resolution to observe the sintering process and mechanism. Phuah et al. achieved an ultrahigh heating rate of up to 1200 K/s to investigate the sintering process using *in situ* TEM heating technology. It was found that the ultrahigh heating rate significantly benefits the densification of 3 mol.% Yttria (Y)-stabilized zirconia (ZrO_2) nanoparticles.[350] Macroscale $Bi_2Sr_2Ca_{n-1}Cu_nO_{2n+4+x}$ (BSCCO) nanowires were previously reported to be grown using glassy Bi-rich BSCCO precursor seeded with Al_2O_3 powder. In 2014, Boston et al. first observed the growth mechanism of quaternary metal oxide nanowires using a TEM equipped with an *in situ* heating stage.[351] It was found that the sites on the rough surface of the porous matrix can play the role of micro-crucibles, driving the metal oxide nanowire growth at high temperature.[351]

4.3.2 Structural, energy and semiconductor materials

For a wide range of metallic structural materials, heat treatments have a profound effect on the intrinsic microstructure and mechanical behavior as a result of elemental redistribution, phase transition, or precipitation phenomena. However, conventional in-furnace heat treatments for structural evolution studies are fragmented and time-consuming as they need to be conducted on a number of different specimens. The *in situ* heating TEM approach provides the potential to study the microstructure and composition evolution at the atomic level.[352-357] Two-phase Ti-based alloys, consisting of the low-temperature *hcp* *α*-phase and the high-temperature *bcc* *β*-phase, are widely used in aerospace and biomaterials. Through the *in situ* heating TEM technique, the atomic scale observation of nucleation-mediated phase transformation in the Ti-Mo alloy was achieved, as shown in **Figure 25**. The phase transformation experienced a complicated process, starting from a disordered *hcp* to a metastable *hcp* superstructure, followed by a transition to a *bcc* superstructure, and finally resulting in a disordered *bcc* configuration.[352] PEN is widely used in the design and development of advanced metallic alloys. Understanding of the nucleation and transition mechanism through *in situ* technology is critical to developing microstructures with the desired mechanical properties.

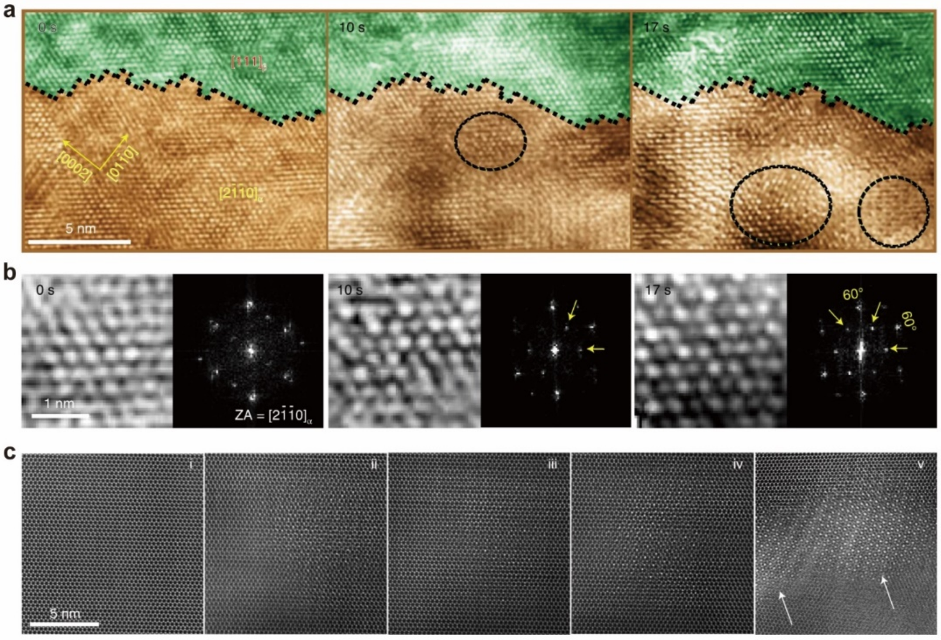

Figure 25. *in situ* Observation of the nucleation process from *hcp* to *bcc* phase transition in Ti−Mo alloy. (a) HRTEM images at 0 s, 10 s, and 17 s, showing the atoms movement and formation of periodic intermediate state, with corresponding zoom in figures and FFT patterns in (b). (c) HAADF images showing atomic structure transformation during *in situ* STEM heating experiments. Reprinted with permission from ref. [352]. Copyright 2016 Springer Nature Limited.

Besides metallic materials, *in situ* TEM can be used to monitor the formation, evolution, and degradation of electrocatalysts. Solar cells based on lead halide perovskite have attracted much attention due to their low fabrication cost and high efficiency. However, the instability of the solar cells has emerged as a major challenge. When exposed to temperatures above ~85 ℃, the devices undergo rapid degradation. In 2016, Divitini et al. first observed the heat-induced degradation process in perovskite solar cells using *in situ* TEM heating technology. The high stability, fast response, and outstanding precise control of novel *in situ* heating holders based on MEMS microheaters are crucial for EDS analysis. They observed the migration path of iodine and lead and identified the relationship between the formation of PbI_2 at the fluorine-doped tin oxide (FTO) interface and the onset of degradation.[358] By integrating nano-beam electron diffraction with *in situ* heating technology in environmental TEM, Meyer et al. studied the phase transition process (orthorhombic to pseudocubic transition) in $Pr_{1-x}Ca_xMnO_3$ thin films epitaxially grown on $SrTiO_3$ in the low-doping regime. Their research showed that oxygen activity, controlled by the oxygen pressure, is crucial to avoid irreversible structural changes.[359] Since the discovery of a significant increase in the thermoelectric figure of merit of stoichiometric Cu_2Se during the phase transition, copper-selenide compounds have attracted much interest. In 2018, Chen et al. observed the coexistence of α and β phases in wedge-shaped nanoscale Cu_2Se single crystals using double-tilt *in situ* TEM heating holder, which was previously thought to be impossible in bulk specimens.[360] Due to its high specific energy, long cycle life, and low cobalt concentration, doped $LiNiO_2$ has recently emerged as one of the most promising cathode materials. In 2021, Wang et al. investigated the atomic scale phase transition and cracking pathways in $LiNiO_2$ and doped $LiNiO_2$ using *in situ* TEM heating technology, as shown in **Figure 26**. Through a two-step process involving cation mixing and shearing along (003) planes, the O1 phase produced at high voltages serves as a preferred site for the transformation of rock-salt (**Figure 26c-e**).[361] The above studies demonstrate the critical role of *in situ* TEM technology in observing the solid phase transformation and degradation process in energy materials, contributing to the development of next-generation batteries with high performance and outstanding stability in vehicles and power grids.

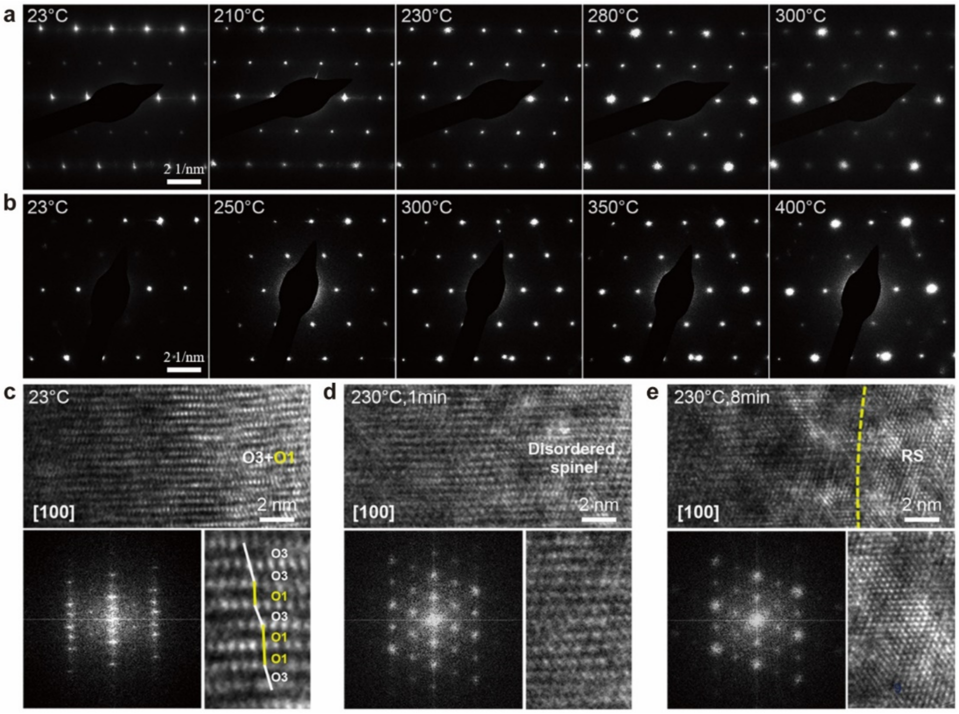

Figure 26. The thermal effect induced phase transition process in ultrahigh-nickel layered cathodes for cobalt-free lithium-ion batteries. (a,b) The diffraction pattern evolution of $LiNiO_2$ and doped $LiNiO_2$ during heating process. (c-e) HRTEM displaying the structural transformation of $LiNiO_2$ from O1 phases (c) to disordered spinel (d) and to rock-salt phase (e). Reprinted with permission from ref. [361] under a Creative Commons Attribution 4.0 International License. Copyright 2021 The Authors.

The field of semiconductors demands a high degree of thermal stability. In this regard, the *in situ* TEM heating technique displays distinct advantages for understanding the peculiarities of the component/interface interaction, microstructure and phase evolution under thermal effect.[342, 362-364] Due to its tunable bandgap and good compatibility with the current Si-based technology, GeSn has been considered as a great potential semiconductor for electronic and photonic applications.[365] Minenkov et al. deposited binary layered Sn/Ge films by physical vapor deposition and observed the interfacial interaction between Ge and Sn using the *in situ* TEM heating approach. They found that upon heating, the layered Sn/amorphous Ge film can form diamond-structured Ge−Sn solid solutions with enhanced Sn content in the range of 20−150 °C.[362] The silicidation or germanidation annealing method, in which the metal enters the semiconductor and generates a low-resistance intermetallic phase, is a promising method for producing high-quality interconnects on semiconductors.[366] In 2019, Hajraoui et al. for the first time observed germanium (Ge) and copper (Cu) diffusion process in opposite directions during the solid state reaction of Cu contacts on Ge nanowires using *in situ* TEM heating technique.[364] According to EDS results, both Ge and Cu were observed to be dispersed on the surface of the newly formed Cu_3Ge segment. Within the temperature range of 360−600 °C, the reaction rate is limited by the surface diffusion of Ge.[364] The use of *in situ* TEM technology provides valuable insights into the reaction kinetics and mechanism involved in the formation of the metal−semiconductor phase, making the Cu−Ge nanowires system highly promising for applications requiring precise size control of the semiconducting region.

4.3.3 Two-dimensional materials

The typical phase modulation for 2D materials is the transformation between 2H and 1T' phase. For example, $MoTe_2$ shows a 2H to 1T' phase transition under local heating by laser irradiation. *in situ* STEM results show the phase change under heating up to 400 °C. The 2H phase is stable without Te vacancy and shows complete overlap of the two Te atoms in the top view STEM images (**Figure 27a**). While the Te atoms start to split with the Te vacancy. This shows that the local phase transition is triggered by the Te vacancy. The DFT calculations also confirm that the 1T' phase is more stable than the 2H phase with Te vacancy concentration higher than 3% (**Figure 27b**). [43] Other 2D materials also exhibit the potential for PEN. When heated from room temperature to 250 °C, the rhombohedral phase $BiFeO_3$ thin film transforms into the tetragonal phase, as shown by the morphological changes and the evolution of electron diffraction pattern (**Figure 27c)**. And only the tetragonal phase remains when heated to 270 °C (i.e., below the Curie and Neel temperatures). This phase transition phenomenon is attributed to the competition between thermodynamic stability and substrate-induced strain.[367] Also using *in situ* TEM heating techniques, Almeida et al. reported that the planar FeRh thin film exhibited thermomagnetic behavior consistent with the transition from an antiferromagnetic to a ferromagnetic phase (**Figure 27d**).[368] Tao et al. observed thermally driven reversible phase changes in 2D In_2Se_3. From the selected area diffraction pattern, the phase changes from β' to β occurred between 173 K and 193 K as the pattern changed from rectangular to hexagonal.[369]

In addition, the loss of atoms during thermal treatments also induces phase transformation. For instance, the CuO nanosheets changed to Cu_2O upon heating at 1120 °C. According to the *in situ* heating video, the CuO nanosheets gradually shrink and form a porous membrane and finally disappear.[370] Gavhane et al. found that cubic $CoSe_2$ transforms to basal plane oriented hexagonal 2D CoSe at elevated temperatures through the removal of chalcogen atoms, as evidenced by the electron diffraction pattern (**Figure 27e**).[371] Ryu et al. revealed the successful phase modulation of 2D layered 1T $PtSe_2$ to PtSe by *in situ* TEM heating over 500 °C.[372]

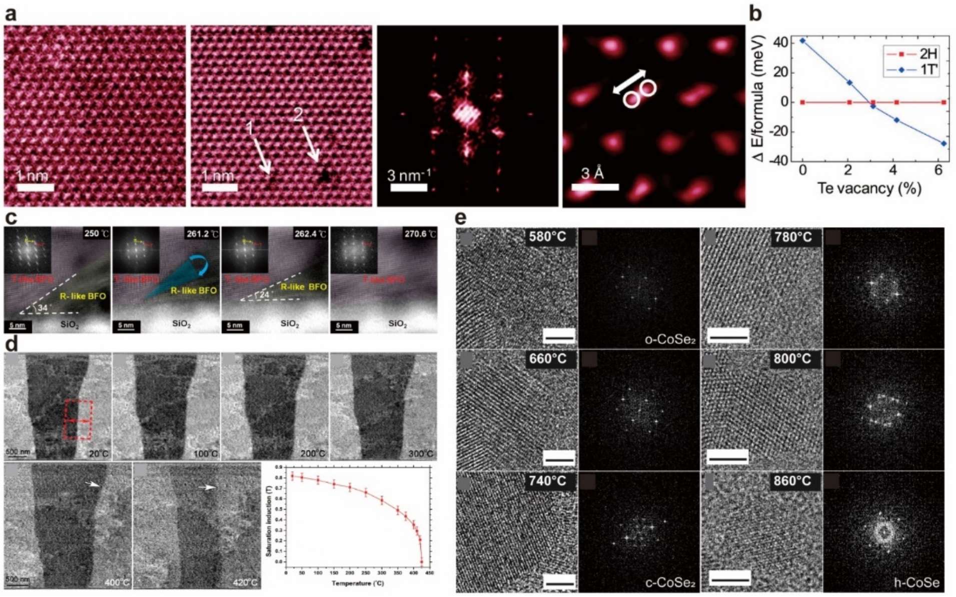

Figure 27. *in situ* TEM study of thermally induced phase changes in 2D materials. (a) Pristine 2H phase monolayer $MoTe_2$ changes to 1T’ phase at 400 °C around Te vacancies. (b) DFT calculated energy differences between the 2H and 1T’ phases as a function of Te vacancy concentration. Reprinted with permission from ref. [43]. Copyright 2015 American Association for the Advancement of Science. (c) Sequential HRTEM images and FFT patterns showing the phase transition of the mixed-phase $BiFeO_3$ thin film. Reprinted with permission from ref. [367]. Copyright 2015 Elsevier Ltd. (d) TEM images of the FeRh thin film upon *in situ* heating to 420 °C, showing the decreasing trend in the contrast between the magnetic domains. The plot denotes the thermomagnetic behavior upon heating. Reprinted with permission from ref. [368] under a Creative Commons Attribution 4.0 International License. Copyright 2017 The Authors. (e) Sequential TEM images and the corresponding FFT images denoting the structural transformations in orthorhombic $CoSe_2$, cubic $CoSe_2$, and hexagonal CoSe upon heating. Reprinted with permission from ref. [371] under a Creative Commons Attribution 4.0 International License. Copyright 2021 The Authors.

4.3.4 Section Summary

MEMS-based *in situ* heating TEM technology has become a breakthrough and multifunctional platform as a micro-scale laboratory, enabling microstructure and phase structure evolution studies, including nanoparticles, nanowires, various structural and functional materials, and two-dimensional materials. For nanoparticles and nanowires, due to the influence of surface energy, their crystal structure displays a distinct change compared to the bulk materials. *in situ* TEM technology can provide the ultrafast heating/cooling speed and cyclic heating function, facilitating the observation of the phase structure transformation process at the atomic scale and promoting the PEN to effectively guide the synthesis and modification of nanomaterials for SERS, catalysis, and energy applications. For energy materials, thermal runaway events triggered by ambient temperature rise have often caused serious injuries to consumers. *in situ* TEM heating technology can assist to study the thermal stability and degradation mechanism of the energy materials, e.g., perovskite, Li-ion battery, and supercapacitor, under thermal effect, contributing to the development of high performance and high stability energy devices. For structural materials, *in situ* TEM is an effective tool to reveal the phase transition process and precipitation formation mechanism, promoting the development of next-generation advanced structural materials with superior mechanical properties via PEN.

4.4 *in situ* TEM electrical probing for PEN

in situ TEM electrical techniques have been developed to study the properties and structures simultaneously. Bias can be introduced into the TEM by developing MEMS devices with electron transparent windows or by using a TEM-scanning probe microscopy (TEM-SPM) platform. A representative electrical holder with a probe is shown in **Figure 28a**.[373] The specimen is mounted on one side of the holder with a W/Au probe. On the other side is the movable counter-electrode driven by the piezoelectric tube, which allows the probe to be moved towards the specimen with high precision in the nanometer scale. Therefore, electrical measurements such as current−voltage (I−V) curves can be acquired through dedicated contacts between the tip and the sample. MEMS chips are also a widely used method for applying bias. The MEMS chips are designed with dedicated electrodes, and the specimen can be accurately transferred and placed at any position of the MEMS electrodes by FIB (**Figure 28b**).[323] To ensure low contact resistance, the two ends of the specimen can be welded together with the electrodes on the MEMS chip by Au/Pt deposition in FIB. The MEMS-based nanochips can also be designed to conduct multi-field experiments, such as *in situ* heating and electrical simultaneously, or *in situ* mechanical and electrical (**Figure 28c,d**), thus allowing multiple structural evolution and properties to be studied simultaneously.[374, 375] The *in situ* electrical TEM techniques with MEMS devices and TEM-SPM enable the physical, electronic, chemical, and mechanical properties to be modulated by *in situ* investigation of structural evolution under electrical bias at the nano- and atomic scale.

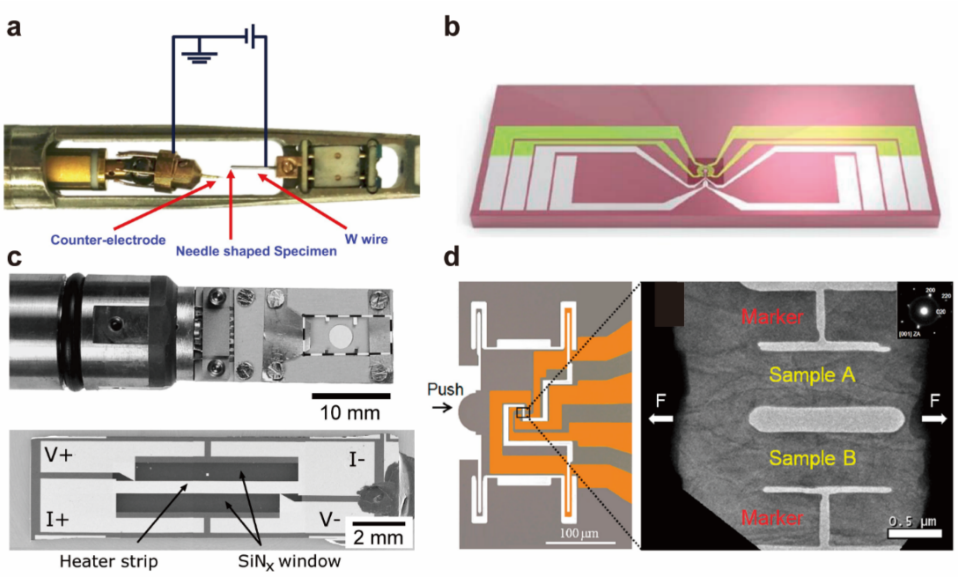

Figure 28. Configuration of the *in situ* electrical TEM holders. (a) A representative TEM-STM holder for applying bias between the specimen and the counter electrode. Reprinted with permission from ref. [373] under a Creative Commons Attribution 4.0 International License. Copyright 2019 The Authors. Published by Elsevier B.V. (b) A MEMS-based nanochip for conducting *in situ* bias TEM experiments. Reprinted with permission from ref. [323]. Copyright 2016 Wiley-VCH. (c) An eight-contact MEMS TEM holder and the MEMS device allow for simultaneous *in situ* heating and bias TEM experiments. Reprinted with permission from ref. [374]. Copyright 2005 Materials Research Society. (d) An EPTP device with gold patterns as conductive electrodes for electric current measurements during the tensile loading of the specimen. Reprinted with permission from ref. [375] under a Creative Commons CC-BY-NC-ND License. Copyright 2021 The Authors. Published by Elsevier Ltd on behalf of Acta Materialia Inc.

4.4.1 Nanoparticles

Different types of nanoparticles have been reported to undergo a phase transition driven by *in situ* electric field in TEM. For example, different types of electrode materials have been investigated. Based on the valuable information obtained from *in situ* electrical TEM, a variety of strategies have been developed to improve their performance. For example, lithiation of crystalline Si is a complex progress that plays a vital role in the performance and lifetime of Li−Si battery systems. By *in situ* electrical TEM, the lithiation of crystalline Si is modulated *in situ* by applied bias and it is demonstrated to be a two-phase reaction in which a reaction front separates the growing Li_xSi amorphous phase from pristine crystalline Si nanoparticles.[376-378] And the crystalline Si is shown to undergo anisotropic lithiation and volume expansion, leading to the fracture of Si particles (**Figure 29a**). This effect is believed to be a major cause of capacity fading in lithium-ion batteries using Si as the anode material. In addition to Si as an anode material, single crystalline Fe_2O_3 nanoparticles, another anode material, have also been investigated under electrical stimuli in TEM and found to transform into multi-crystalline nanoparticles consisting of many Fe nanograins embedded in Li_2O matrix.[379] Through *in situ* electrical TEM, the mechanism of lithiation/delithiation process of lithium-ion batteries can be revealed at nano- and atomic scale, and the electrochemical properties of electrode materials can be tuned by microstructure design or other methods (**Figure 29b**). In addition, Joule heating effects will also be introduced by *in situ* electrical TEM, so that thermally induced phase transformations will occur accordingly. Direct observation of the formation and stabilization of metallic nanoparticles on carbon supports has also been realized using the *in situ* electrically induced Joule heating method.[380] The formation of metallic nanoparticles is associated with the simultaneous phase transition of amorphous carbon to a highly defective turbostratic graphite (T-graphite), as the defective T-graphite provides numerous nucleation sites for the formation of nanoparticles (**Figure 29c**). Therefore, *in situ* electrical TEM provides a platform to elucidate the phase modulation mechanism and facilitates the synthesis of highly stable supported nanoparticles for applications such as energy storage and conversion.

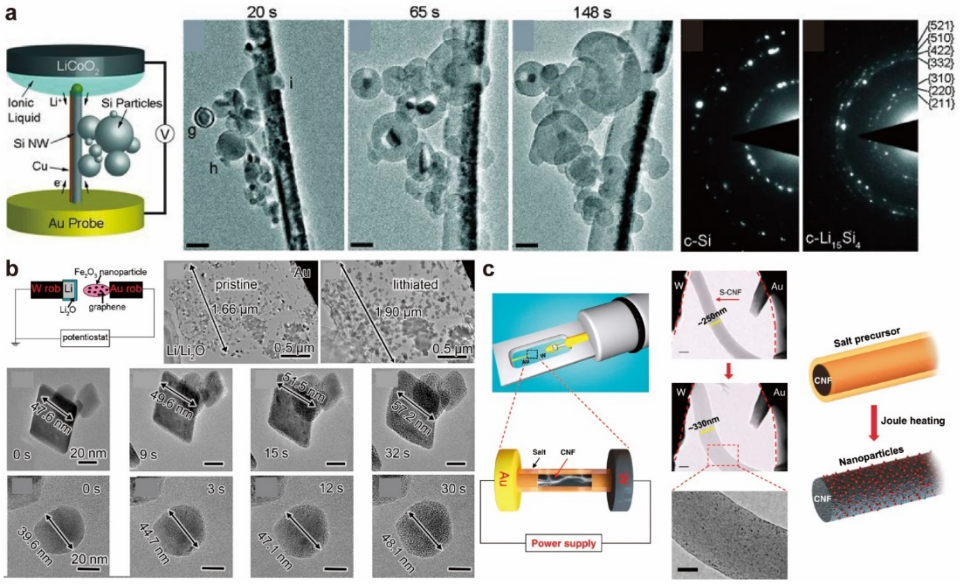

Figure 29. Bias-induced phase transformation of zero-dimensional materials under *in situ* TEM. (a) Phase transformation of crystalline Si nanoparticles to the amorphous Li_xSi phase during the bias-induced lithiation process. Reprinted with permission from ref. [378]. Copyright 2012 WILEY-VCH Verlag GmbH & Co. KGaA, Weinheim. (b) Phase transformation of crystalline Fe_2O_3 nanoparticles into Fe nanograins during bias-induced lithiation process. Reprinted with permission from ref. [379]. Copyright 2013 American Chemical Society. (c) Phase transformation of amorphous carbon to a highly defective turbostratic graphite and the formation of metallic nanoparticles under bias-induced Joule heating. Reprinted with permission from ref. [380] under a Creative Commons Attribution 4.0 International License. Copyright 2020 The Authors. Published by Springer Nature Limited.

4.4.2 Nanowires

Phase modulation of nanowires by *in situ* TEM has been successfully achieved and the whole process has been recorded, unveiling the mechanism behind the phase transformation. For example, the phase of oxide nanowires, including SnO_2 nanowire, MnO_2 nanowire, and VO_2 nanowire, can be modulated by electrical stimuli. The *in situ* TEM clearly revealed that the SnO_2 nanowire would swell, elongate, and spiral upon charging, forming a reaction front with a high density of mobile dislocations, which electrochemically drives the nanowire amorphization. The resulting structural change would influence the electrochemical properties of SnO_2 nanowires as electrodes for lithium-ion batteries (**Figure 30a**).[381] MnO_2 nanowire undergoes the tetragonal−orthorhombic−tetragonal (TOT) symmetric transition upon lithiation (**Figure 30b**).[382] The metal−insulator transition of VO_2 was observed using *in situ* electrical TEM.[383] The applied AC bias triggered a phase transition from a metallic rutile phase to an insulating rutile intermediate phase and finally to a stable insulator monoclinic phase (**Figure 30c**). Besides oxide nanowires, the III−V compound nanowires can also be modulated for PEN to obtain unique electronic and photonic properties.[384] Electrically induced Joule heating has been used to achieve the wurtzite to zinc-blende transition in semiconductor InAs nanowires. And the process was recorded by *in situ* HRTEM to reveal the atomic mechanism, which demonstrated that the wurtzite to zinc-blende transition occurs by gliding of sharp steps with Shockley partial dislocations (**Figure 30e**). In addition to the crystalline structure, the tubule formation process from amorphous carbon nanowires under high bias Joule heating was observed in real time by TEM, which is a process of solid state atom diffusion at high temperatures induced by Joule heating (**Figure 30d**).[385] The graphitization under high input power of the amorphous carbon nanowires leads to increased conductivity.

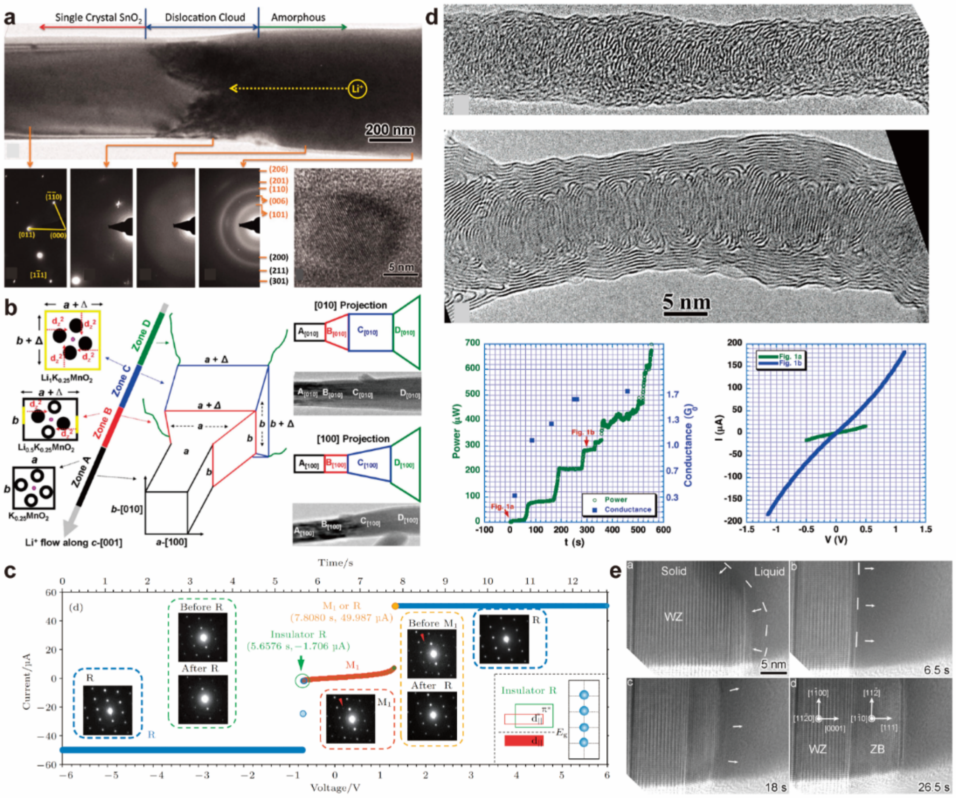

Figure 30. Bias-induced phase transformation of one-dimensional materials under *in situ* TEM. (a) A SnO_2 nanowire undergoes phase transformation from crystalline to amorphous under *in situ* bias study. Reprinted with permission from ref. [381]. Copyright 2010 by the American Association for the Advancement of Science. (b) A MnO_2 nanowire undergoes tetragonal−orthorhombic−tetragonal phase transition upon bias-induced lithiation. Reprinted with permission from ref. [382]. Copyright 2015 American Chemical Society. (c) A VO_2 nanowire shows the phase transformation from a metallic rutile phase to an insulating rutile intermediate phase, and finally to a stable insulator monoclinic phase with *in situ* bias TEM. Reprinted with permission from ref. [383]. Copyright 2018 Chinese Physical Society. (d) A carbon nanowire undergoes phase transformation from amorphous to crystalline under high bias. Reprinted with permission from ref. [385]. Copyright 2006 American Chemical Society. (e) A semiconductor InAs nanowire goes through a phase transformation from wurtzite phase to zinc-blende phase through bias-induced Joule heating. Reprinted with permission from ref. [384]. Copyright 2013 American Chemical Society.

4.4.3 Two-dimensional materials

Phase modulation by electrical stimulus between a trigonal prismatic (2H) and an octahedral (1T) phase has been achieved in various TMDs such as the Ta-based TMDs ($TaSe_2$ and TaS_2), $MoTe_2$, and MoS_2.[100, 386-390] Based on the *in situ* electrical TEM platform mentioned above, a bias can be applied by an STM tip. Under electrical stimuli, the phase of the TMDs can be controlled. It has been reported that the phase transformation of Ta-based TMDs is attributed to the collective motion of many chalcogen atoms at a voltage above the threshold. The electrically induced phase changes of 2D TaS_2 were also thickness dependent. More phase changes can occur in thicker TaS_2 than in thinner samples. Under electrical stimulation, MoS_2 can be tuned from 2H to 1T phase with a lithium ion occupying the interlayer S−S tetrahedral site in 1T $LiMoS_2$ (**Figure 31a**).[100, 388]

In addition to TMDs, other thin films can be modulated by electrical stimuli. For instance, β'-In_2Se_3 and γ-In_2Se_3 can be obtained from α-In_2Se_3 by electrical stimuli at different levels in *in situ* electrical TEM.[391] Specifically, under a low current of 5×10^{-5} A, a phase transition from α phase to β'-In_2Se_3 phase was observed. When a higher current (8×10^{-5} A) was applied to the α phase, it transformed into γ phase. This threshold is crucial for the further application of In_2Se_3. In addition, polarization in lead magnesium niobate-lead titanate (PMN-PT) can be achieved with *in situ* electrical TEM upon bias, showing the reorientation of nanoscale non-180 degree domain walls and movement and/or elimination of microscale domain walls (**Figure 31b**).[392] The $P4mm$-to-$R3c$ ferroelectric to ferroelectric transition of $(Bi_{1/2}Na_{1/2})TiO_3$-$BaTiO_3$ was also achieved with *in situ* electrical TEM, and the real-time evolution of crystal structure and domain morphology during the poling-induced phase transitions was observed with different macroscopic piezoelectric behaviors (**Figure 31c**).[393] Similarly, the electrical stimuli induced the switching of individual ferroelastic domains in thin $Pb(Zr_{0.2}Ti_{0.8})O_3$ films and the dynamic evolution was recorded by *in situ* electrical TEM (**Figure 31d**). The ferroelastic domains were effectively and permanently stabilized by dislocations at the substrate interface, while similar domains at free surfaces without pinning dislocations can be removed by either electric or stress fields, offering crucial ideals for developing non-volatile ferroelectric memory devices.[394]

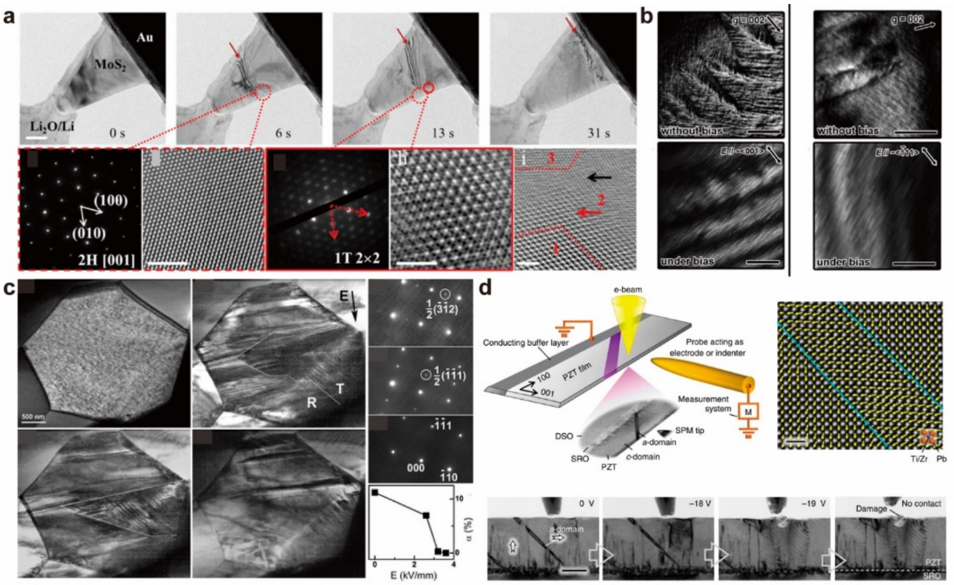

Figure 31. Bias-induced phase transformation of two-dimensional under *in situ* TEM. (a) MoS$_2$ nanosheets undergo a trigonal prismatic (2H)−octahedral (1T) phase transition upon bias-induced lithiation process. Reprinted with permission from ref. [100]. Copyright 2014 American Chemical Society. (b) Piezoelectric PMN-PT shows polarization reversals with the reorientation of nanoscale non-180 degree domain walls and movement and/or elimination of microscale domain walls under *in situ* bias TEM. Reprinted with permission from ref. [392]. Copyright 2011 American Physical Society. (c) Phase-pure *P4bm* (Bi$_{1/2}$Na$_{1/2}$)TiO$_3$-BaTiO$_3$ grain with nanodomains coalesce into lamellar domains and undergoes a *P4bm* to *P4mm* phase transformation under electric field, and to *R3c* upon further increase in electric field. Reprinted with permission from ref. [393]. Copyright 2012 American Physical Society. (d) Observation of the ferroelastic domain switching of thin Pb(Zr$_{0.2}$Ti$_{0.8}$)O$_3$ films, showing that a clamped 90 degree domain is eventually erased at negative bias (−19 V) via *in situ* bias TEM. Reprinted with permission from ref. [394]. Copyright 2014 Springer Nature Limited.

4.4.4 Section summary

As one of the key stimuli for phase transformation, *in situ* electrical TEM provides a platform that combines the high-resolution imaging capabilities of TEM with the ability to apply bias to materials at the nanoscale. It allows researchers to directly visualize and manipulate the phase of nanomaterials by applying an electric field, thereby enabling a deeper understanding of the mechanism for phase transformation of nanomaterials. As mentioned above, numerous nanomaterials have been successfully tuned to different phases, providing the underlying phase transformation mechanism. These valuable data will guide the development of new materials and technologies based on PEN.

4.5 *in situ* TEM gas environment study for PEN

Normally, HRTEM observation requires a high vacuum condition since the gas molecules inside the column severely scatter the accelerated electrons, thus significantly reducing the imaging resolution. However, the behaviour of materials could be rather different under various atmospheres from that of under high vacuum, leading to the imperious demands of introducing designated atmospheres into the TEM specimen chamber during operation. With decades of technological advancement, the so-called controlled atmosphere transmission electron microscopy (CATEM) or environmental transmission electron microscopy (ETEM) has been developed and utilized to investigate the interactions between nanomaterials and various environmental factors including gas type, temperature, and pressure in real time. There are two main types of ETEM methods proposed so far (**Figure 32**), the aperture approach which relies on a specially designed gaseous sample chamber of the TEM (also referred to as the ETEM method) and the window approach which uses a customized TEM holder with a MEMS-based nanoreactor (also referred to as the gas holder method).[200, 395, 396]

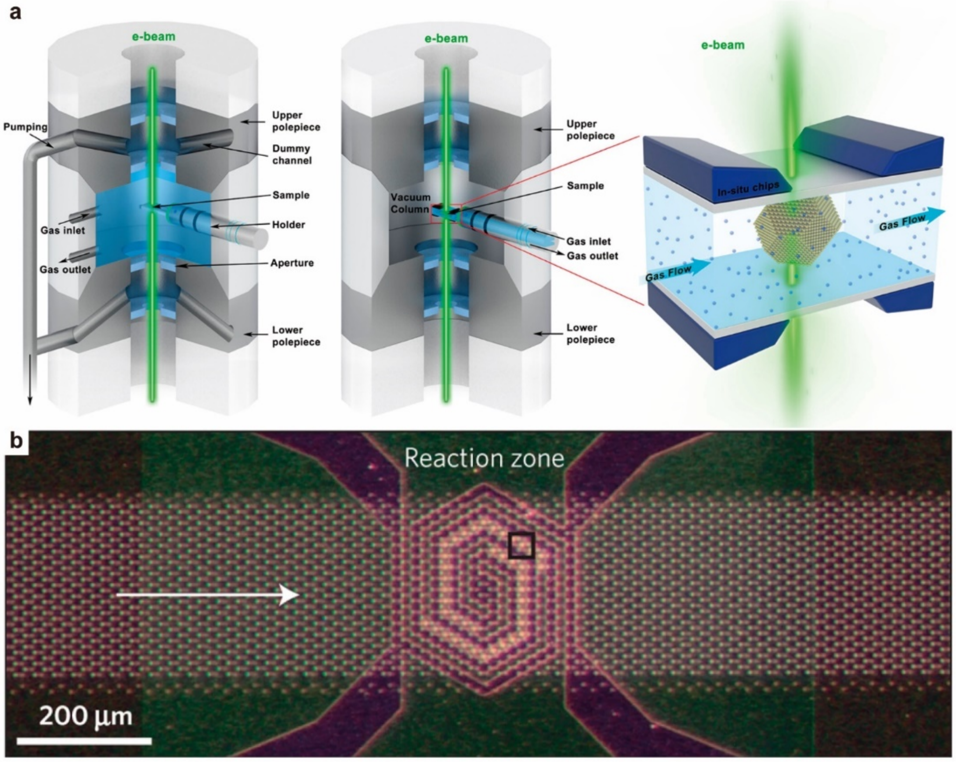

Figure 32. (a) Schematic showing the two approaches of CATEM, aperture approach (left) and window approach (middle and right). Reprinted with permission from ref. [200]. Copyright 2023 American Chemical Society. (b) Optical image of a nanoreactor with the gas channel and the reaction zone including the heater spiral and electron-transparent windows. Reprinted with permission from ref. [397]. Copyright 2014 Springer Nature Limited.

The key feature of the aperture approach is the use of a pair of small pressure limiting apertures located on both sides of the specimen, which restricts the leakage of gas molecules into the high vacuum TEM column (**Figure 32a**, left). The balance of the chamber gas pressure is controlled by the size of the small apertures and the connected differential pumping system. Notably, the aperture size should be carefully determined to maintain the gas chamber atmosphere while allowing a smooth electron beam passage for high-quality imaging.

As for the window approach, the specimen is confined in an airtight cell between two electron-transparent membranes as the windows, with airflow channels and metal resistors as the heater (**Figure 32a**, right). The configuration poses stringent requirements on the electron-transparent material, which needs to be mechanically robust to tolerate the pressure difference (atmospheric pressure) between the two sides and the high temperature heating, while thin enough to reduce the interaction with the penetrating electrons for high-resolution imaging. To avoid interfering with the diffraction information of the characterized materials, amorphous thin films are usually employed, including silicon nitride, amorphous carbon, polyimide, and silicon dioxide with a thickness of less than 50 nm.

The different configuration features bring unique advantages and drawbacks to these two approaches. The primary advantage of the aperture approach is better imaging quality due to the absence of amorphous sealing membranes, which avoids electron scattering. Besides, there are no specific requirements for the TEM sample holder, resulting in good compatibility in combination with other types of *in situ* holders for/using mechanical, electrical, or optical measurements/stimulations. On the other hand, the airtightness of the apertures and the performance of the differential pumps limit the maximum working pressure of the gas chamber (less than 20 mbar), not to mention the adverse effect on the imaging contrast due to the long path of the electrons traveling in the gas layer (5−10 mm). Meanwhile, the membrane-sealed cell in the window approach enables a much higher gas pressure of up to 4.5 bar, and the thin gas layer (generally less than 50 μm) ensures high-resolution imaging. The closed-cell design also allows the characterization of samples in liquids, which will be introduced in the next section. Furthermore, the integrated design with the TEM holder means more economical and simpler applications since it can be directly used on conventional TEM apparatus. Although the interaction between the window membranes and the electron beam could be a problem for high-resolution imaging and spectral characterization, the mechanical failure of the thin membranes may cause more serious issues for contaminating the TEM column or the beam source. Another current technical limitation is the lack of double-tilt capability, which may hindering the availability of multi-orientation observations.

4.5.1 Nanoparticles catalysts

Catalysts are intensively involved in the industrial manufacturing of chemical products, endowing them with incomparable research significance among other nanomaterials. Nevertheless, most catalysts undergo dynamic structural transitions during the catalyzed reactions, which means that pre- or post-mortem characterization methods are inadequate to reveal the catalytic mechanism related with the structural evolutions of catalysts. With the ability to offer dynamic atomic- resolution imaging under a range of gas atmospheres and temperatures, *in situ* ETEM seems to be an inevitable answer to this challenge, as well as to the further goal of engineering and designing the structure of catalysts for optimal activity and selectivity.[398]

The ETEM has been widely used as a powerful tool to capture the structural and compositional evolution of metallic nanoparticle catalysts under redox environments, facilitating the understanding of catalytic mechanisms as well as the engineering of catalytic activity and selectivity, since the first observation of gas-induced geometry evolution of ZnO supported Cu nanoparticles under *in situ* ETEM.[399] The surface reconstruction-induced morphology change of Cu nanoparticles was attributed to the changes in surface energy due to water adsorption, while the introduction of reducing gas such as CO also contributes to the shape change of Cu particles by changing the Cu/ZnO interfacial energy. The long-standing puzzle of the size-dependent catalytic activity of noble metal nanoparticles has been solved by atomic resolution *in situ* ETEM characterization, in which amorphization and reshaping were observed for CeO_2-loaded *fcc*-Au nanoparticles with diameters less than 2 nm in a CO oxidation environment.[400] The structural evolution was attributed to the strong Au−CO bonding, providing insights into the enhanced catalytic performance of ultrasmall Au nanoparticles. Similarly, Nassereddine et al.[74] revealed a dramatic structural change from *fcc* to icosahedral-like non-*fcc* phases in TiO_2-supported Au nanoparticles smaller than 4 nm using an *in situ* HAADF STEM ETEM in a H_2 atmosphere. The phase transition was ascribed to the high mobility of Au atoms due to the strong Au-H interaction as given by AIMD simulations.

The ETEM technology also provides a unique opportunity to the study the phase engineering of single particle nanomaterials by solute intercalation in real time. Pioneering works were presented by Dionne et al.[401, 402], who used an *in situ* ETEM to explore the dynamic process of phase transitions in individual Pd nanoparticles in a hydrogen atmosphere with variable pressure. By increasing the hydrogen pressure, the Pd nanoparticles were able to shift from a dilute α-phase to a hydrogen-concentrated β-phase. The hydrogenation of the Pd nanoparticles and the phase transition were tracked by *in situ* EELS measurements, revealing a transient phase transition manner and a size dependence of the hydrogen absorption induced by the surface effect. Furthermore, the combination of EELS plasmon mapping, selected-area electron diffraction (SAED), and centered dark-field imaging by ETEM, a unique coexistence of hydrogenated α and β phases were found in the twinned icosahedral nanoparticles and the spatial information of the phase distribution was revealed, showing a low-hydrogenated α-phase region near the core of the icosahedral nanoparticle due to the compressive stress from the expanded hydrogen-rich β-phase surface region. It also demonstrated a lower H_2 adsorption threshold pressure as explained by the tensile strain-induced reduction of phase transition chemical potential.[402] The dual-phase coexistence was also found in the penta-twinned Pd nanorods, where the tips with lower coordination number were found to be preferential nucleation sites.[403] The Ag-doped AgPd alloy nanoparticles with enhanced stability and catalytic activity were also studied by *in situ* ETEM to manipulate their hydrogenation process. A similar separation of α and β phases was observed for lightly doped (Ag concentration of ~1%) AgPd nanoparticles at the equilibrium state, which was ascribed to the strain stabilization induced by Ag doping.[404]

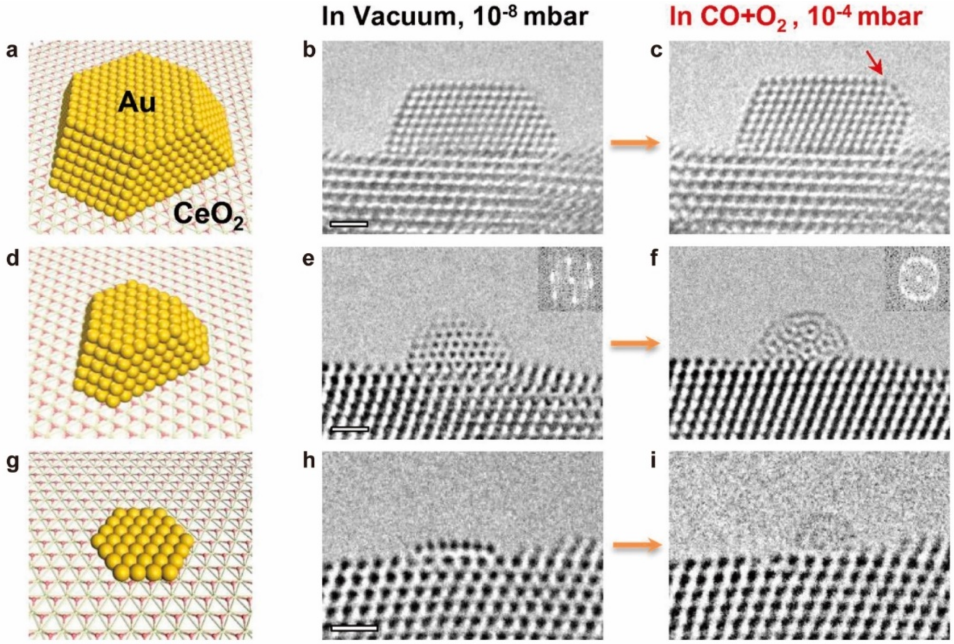

Figure 33. Structural transition of Au nanostructures with different sizes supported on CeO_2 (111) under reactant gases (scale bars, 1 nm). Reprinted with permission from ref. [400]. Copyright 2018 National Academy of Sciences.

The *in situ* ETEM investigation of structural and compositional restructuring in catalytically active bimetallic nanoparticle systems during redox reactions has been presented typified by the redox-driven elemental phase segregation (atom migration between the core and the shell) in Pt-Co bimetallic nanoparticles.[405] It is demonstrated that the different affinities between metal atoms and gas molecules can be exploited to promote the intraparticle atom migration between the surface and the core. In this case, CO was used to draw Pt to the surface, yet a Co-rich shell was obtained in O_2 atmosphere since it tends to bond with Co to form a CoO_x surface layer. However, an adverse phenomenon was observed by Dai et al., who found no Co oxidation in an oxidized environment.[406] They performed an *in situ* O_2 annealing experiment to investigate the core-shell structure in Pt_3Co catalyst nanoparticles using a Protochips gas cell infilled with pure oxygen at one atmospheric pressure and revealed a two-step formation process. In the first step, the original amorphous Pt_3Co transformed into an intermetallic $L1_2$ phase at 720 °C, when a Pt-rich surface layer was formed due to migration and prevented oxidation of Co. The next step was the growth of the Pt surface layer when the temperature was lowered to 300 °C, which was attributed to the lower formation energy of the Pt (100) surface compared to the Pt−Co counterpart in an oxygen environment.

Similar nanostructure engineering has been reported in other bimetallic nanoparticles. Recently, Zhang et al.[407] reported a reversible phase modulation in a Ni−Au bimetallic nanocatalyst system, between a classical core-shell in a relaxed state and a NiAu alloy during CO_2 hydrogenation reaction (9 ± 0.1 mbar, 25% CO_2/75% H_2). As shown in **Figure 34**, the darker Au-rich shell remained visible at 450 °C demonstrating the existence of an Au−Ni core-shell structure. A fully alloyed state was achieved when the temperature reached 600 °C, at which the darker edge disappeared, and separately coordinated Au−Ni columns were observed in HRTEM. The core-shell structure was recovered during cooling at 400 °C with the Au shell reappearing in the TEM image. The reaction-driven phase transition was also confirmed by *in situ* electron diffraction, where the diffraction peak corresponding to the NiAu alloy phase emerges at 400 °C with increasing intensity at elevated temperature. DFT calculations indicate the key role of the reaction-produced CO, which not only lowers the migration energy barrier of the Ni atoms but also contributes to their surface stability. These results demonstrate the strength of *in situ* ETEM characterization in providing insight into catalytic mechanisms and guidance for nanocatalyst design over conventional *ex situ* methods.

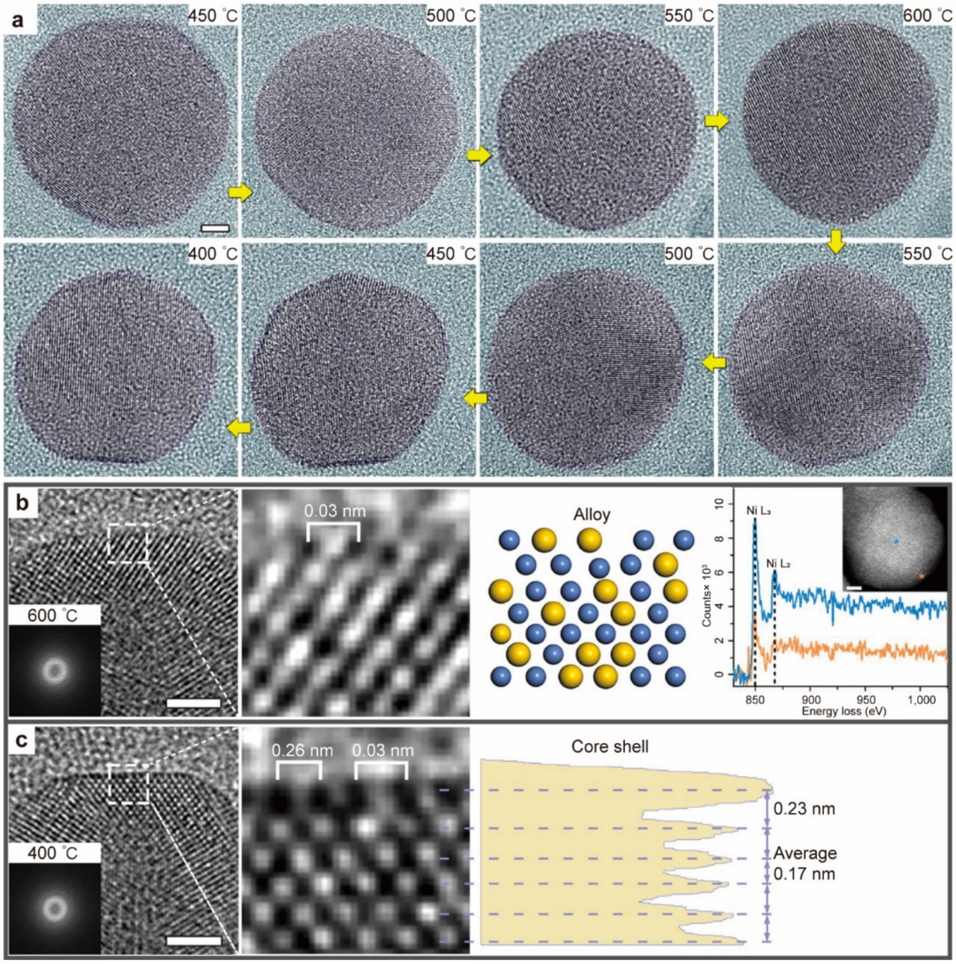

Figure 34. *in situ* observation of the structural change of NiAu nanoparticles during the CO_2 hydrogenation reaction. (a) *in situ* TEM images of the alloying and dealloying evolution of an individual NiAu nanoparticle during the reaction (scale bar, 2 nm). (b,c) Surface atom arrangement of a NiAu nanoparticle reconstructed from (b) the full alloy (600 °C) to (c) the Ni−Au core-shell (400 °C); the right part in (b) shows the schematic of the structure and analysis of the electron energy loss spectra; the right part in (c) show the phase contrast profile of the enlarged surface area (scale bars, 2 nm). Reprinted with permission from ref. [407]. Copyright 2020 Springer Nature Limited.

The *in situ* gas TEM has been widely used to study and modulate the metal nanoparticle-catalyzed growth of nanomaterials. One representative example is the chemical vapor deposition growth of CNTs, of which the Fe_3C nanoparticle-catalyzed nucleation and growth process was firstly observed under ETEM with C_2H_2 by Yoshida et al.[408] A more detailed process was revealed by Sharma et al.[409] using the similar method, including multiple phase transitions of the Fe nanoparticle catalysts with the change of gas atmosphere. The original *fcc* Fe_3O_4 was initially transformed into a *bcc* iron oxide phase due to the reduction of C_2H_2 at 650 °C, and then further reduced to the *α*-Fe with *bcc* structure, which was then carbonized to Fe_3C as indicated by the HRTEM images and diffractograms. A subsequent *in-situ* ETEM study observed structural transitions from Fe_2SiO_4 structure to both Fe_3C and Fe_5C_2 structures under

CNT growth condition (1.7 Pa of C_2H_2, 630 °C) as the highly carburizing atmosphere helps to stabilize the metastable Fe_5C_2 phase. They further concluded that the carbon-rich Fe_5C_2 phase is catalytically inactive for CNT formation in contrast to its less carbonized counterpart, as explained by the higher carbon polymerization energy barrier on its stable surface calculated by DFT.[410] The *in situ* ETEM characterization has been also implemented to study the Co nanoparticle catalyzed growth of CNTs.[411] However, it was later reported that the structures of the catalyst nanoparticles varied between Co and a metastable Co carbide phase under CNT growth condition, instead of just single crystal Co.[412] The puzzle was finally solved by Wang et al., who identified that the real active phase in the Co-catalyzed synthesis of CNTs was the orthorhombic Co_3C through a meticulous statistical analysis of the electron diffractograms from the *in situ* ETEM experiment.[413] These *in situ* ETEM enabled studies not only provide valuable evidence on the growth mechanisms of the nanoparticle-catalyzed synthesis of CNTs, but more importantly, bring insight into the rational selection and design of nanocatalysts for the controlled growth of CNTs with designated chirality and physical properties.

4.5.2 Nanorods

Apart from the application in the study of heterogeneous catalysis processes, *in situ* ETEM has recently been employed to reveal an unusual phase transition in noble metals induced by certain gas atmospheres. Han et al. reported a CO-assisted epitaxial transition of *fcc* Au to a metastable 4H *hcp* phase evidenced by *in situ* ETEM observation.[414] The unusual phenomenon was captured for *fcc* Au nanoparticles attached on the surface of 4H Au nanorod under a 300 kV electron beam and 1 mbar CO atmosphere without additional heating. The detailed phase transition process was studied by HRTEM examination, which showed that the transition occurs gradually from the phase boundary into the *fcc* Au particle after realigning with the lattice orientation of the underlying 4H substrate (**Figure 35a-f**). The phase transition mechanism was elucidated by DFT and AIMD calculations, showing that the CO molecules could bond with Au atoms to reduce their diffusion energy barriers, thus lowering the overall Gibbs free energy for the phase transformation. Interestingly, an inverse phase transformation from the 4H phase to the stable *fcc* phase was also achieved in Au nanorods using the same reaction environment (300 kV electron beam, 1 mbar), and the transition occurs inside the nanorods along the stacking direction of the (111) plane of the *fcc* phase and the (001) plane of the 4H phase (**Figure 35g-j**).[415] DFT calculations manifest that the transition also takes place due to the lowered energy barrier of the CO−Au interaction as well as the electron beam radiation, except that the interfacial energy between the two phases is not large enough to induce the unconventional transition from the stable *fcc* phase to the metastable 4H phase.

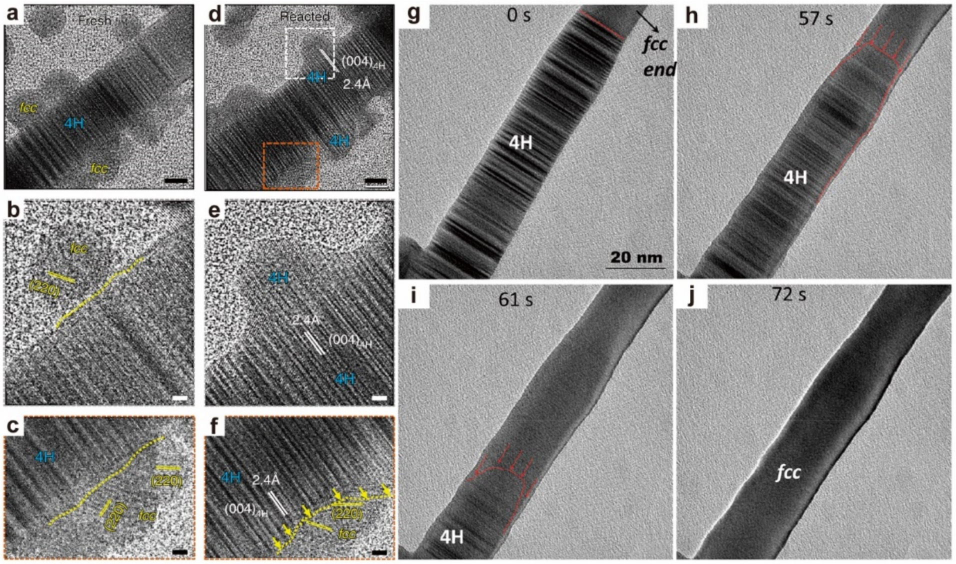

Figure 35. (a-f) HRTEM showing the *fcc* to 4H phase transition in same region of (a-c) original and (d-f) reacted Au nanorod sample. The yellow dotted lines show the boundary between 4H and *fcc* phase, the yellow arrows indicate the phase transition direction (scale bars in (a,d), 5 nm; scale bars in (b,c,e,f), 1 nm). Reprinted with permission from ref. [414]. Copyright 2020 The authors. Published by Springer Nature Limited. (g-j) *in situ* TEM image sequence showing the 4H to *fcc* transformation in 1 mbar of CO. Reprinted with permission from ref. [415]. Copyright 2020 American Chemical Society.

4.5.3 Section summary

Recent advances in *in situ* gas TEM technology, led by the development of nanoreactors, have enabled real-time and atomic resolution imaging of the structural evolution of nanomaterials in the presence of various reactive gases, which is crucial for applications such as the interpretation of the activity and selectivity of nanocatalysts. Compared to traditional post-mortem characterization methods, the dynamic structural and compositional transitions can be captured under fine control of atmospheric and temperature conditions to reveal the structure−property relationship, especially when integrated with other spectral analysis tools such as EDS and EELS. More importantly, the quasi-simultaneous acquisition of structural information of nanomaterials in response to specific gaseous environment makes it a powerful tool to manipulate the atomic arrangement of nanomaterials and provide guidance for the design of highly functional materials. Undoubtedly, there are still many opportunities to exploit the *in situ* ETEM methods. The expansion of information acquisition could be a critical demand. For example, integration with the latest TEM techniques, including 4D STEM, 3D atomic electron tomography, integrated differential phase contrast (iDPC) imaging, and electron holography, to explore the dynamic nanoscale reconstruction in a more elaborate manner. Another promising approach could be the development of *in situ* devices capable of coupling with multiple physical factors such as magnetic, optical, and electric fields, which will significantly broaden the applications.

4.6 *in situ* TEM liquid environment study for PEN

Numerous reactions in nature involve the presence of solutions. A promising technique, liquid-phase TEM (LPTEM), enables direct and real time visualization of dynamic processes within liquid environments. This technique overcomes the limitations of conventional *ex situ* TEM characterization methods in understanding the growth and behavior of nanoparticles in their native solutions.[416] When considering the introduction of solutions into TEM, the primary concern is to prevent liquid leakage and to minimize the electron scattering of liquid molecules that could affect the observation. In light of this, there are three main considerations for LPTEM based on microfabrication techniques. First, LPTEM requires well-encapsulated liquid cells to maintain direct and pure contact between the electron beam and the liquid, avoiding unexpected interactions. Second, the liquid cell needs to accommodate the liquid sample in a confined space while providing a transparent window for the electron beam to achieve high spatial resolution observation. Third, LPTEM requires precise control of chemical reaction conditions such as flow rate and temperature. Advances in microfabrication technology have provided reliable liquid cells that compromise TEM resolution.

The development of LPTEM has undergone several important milestones.[417] In 1935, Marton first proposed the idea of using TEM to observe materials in liquids, but the challenge remained how to confine or control the liquid solution around the specimen in the electron microscope.[418] Subsequently, in 2003, a liquid cell based on amorphous silicon nitride (SiN_x) thin films was successfully developed to study the dynamic growth of Cu nanoclusters. The liquid cell consisted of a lower silicon wafer with an 80-nm-thick SiN_x window and an upper silicon wafer with a matching window, which are separated by a 1-µm-thick silicon dioxide spacer. By transmitting the electron beam through the 160-nm-thick SiN_x window, a resolution of about 5 nm was achieved.[419] In 2008, a similar liquid cell using epoxy resin as the spacer was used to observe biological reactions, but the resolution was not significantly improved.[420] In 2012, researchers encapsulated nanoscale droplets with two suspended graphene sheets and transferred them into TEM, successfully observing the growth of Pt nanocrystals inside the droplets and achieving lattice-level imaging. Due to its single-atomic-layer structure, graphene allowed direct imaging of the lattice structure even at an operating voltage of 80 kV.[421] Subsequently, in 2014, researchers achieved atomic resolution in LPTEM by further reducing the size of the indium (In) spacer and the observation window. They used a 100-nm-thick In spacer and a 10-nm-thick window in a silicon wafer liquid cell, ultimately achieving atomic level resolution. This breakthrough greatly advanced the application of LPTEM.[422] In 2018, researchers demonstrated the stability of amorphous carbon film as an observation window in a liquid environment and successfully observed the growth of gold nanoparticles while maintaining atomic level resolution.[423]

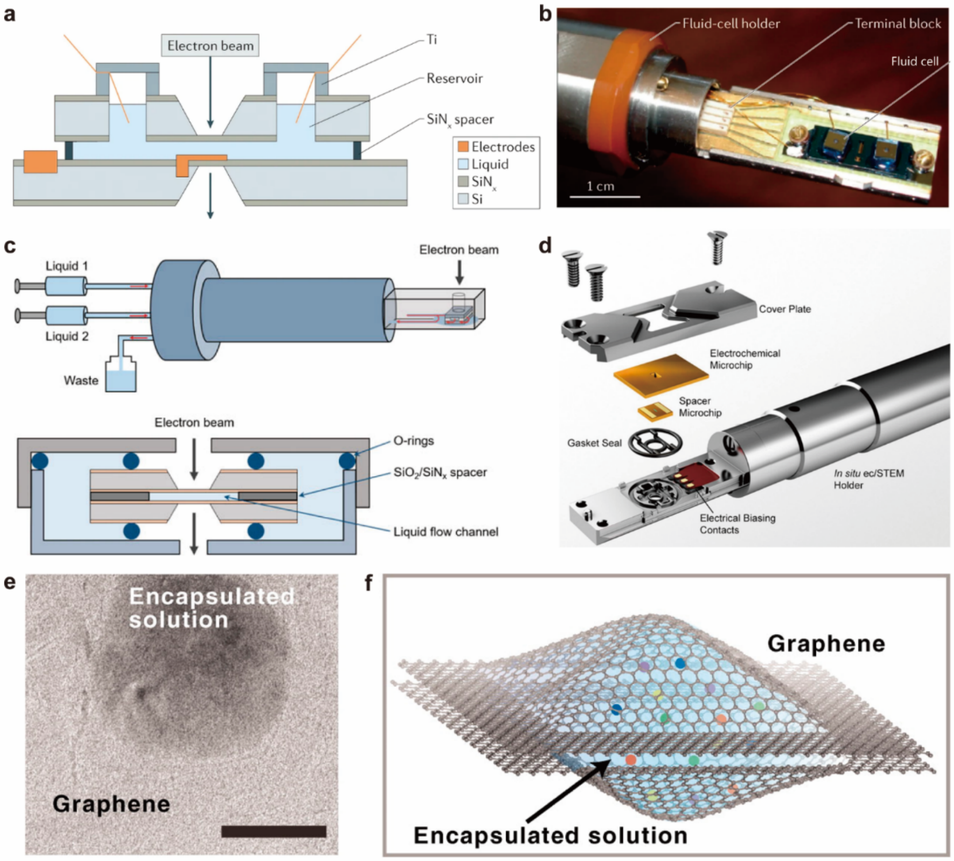

Figure 36. (a-b) Demonstration of a static-type microfabricated silicon liquid cell. Reprinted with permission from ref. [424]. Copyright 2016 Springer Nature Limited. (c-d) Schematic illustrations of flow-type microfabricated silicon cell systems. (c) Reprinted with permission from ref. [417]. Copyright 2023 Elsevier Inc. (d) Reprinted with permission from ref. [425]. Copyrights 2019 The Author(s). (e-f) Schematic illustration shows a graphene liquid cell. Reprinted with permission from ref. [421]. Copyright 2012 AAAS.

Among the proposed liquid cell configurations, microfabricated silicon cells consisting of thin SiN_x membrane windows have been predominately used so far due to their mechanical reliability and applicability in mass production (**Figure 36a-d**). The thickness of the SiN_x membranes can be controlled in the range of several to dozens of nanometers by Si-based semiconductor processing, enabling a balance between high electron transparency and mechanical robustness. There are two main designs for the microfabricated Si liquid cells, static-type and flow-type. The static-type liquid cell utilizes spacers to create a space between the two silicon chips to hold the liquid sample, while O-ring seals provide vacuum isolation. The flow-type liquid cell, which builds on the static-type design, incorporates inlet and outlet ports to allow controlled liquid flow. This design is suitable for studies requiring control of reaction conditions and the introduction of multiple reagents. While static cells offer high resolution imaging with thin liquid layers, flow cells introduce the capability of liquid flow which is closer to the laboratory-scale reaction environment, making them suitable for a wider range of *in situ* experiments. By incorporating an additional liquid flow channel, flow cells allow nanocrystals to be physically moved, enabling the observation of solution changes and the mixing of different reaction solutions. Moreover, flow cells minimize bubble formation which is a common issue in static cells and provide the advantage of controlling the thickness of the fluid layer during experimental. However, a key challenge with flow cells is the variation in fluid layer thickness, which requires careful adjustment.

As a variant of the microfabricated Si cell, graphene liquid cells are fabricated using graphene sheets instead of SiN_x films. Two graphene sheets are bonded together by van der Waals forces to form a liquid enclosure in which the liquid sample is sealed (**Figure 36e-f**). The simple configuration makes it more economically practical without the need for expensive microfabricated chips and a dedicated TEM holder. Due to the single atomic layer structure, graphene liquid cells offer higher electron transparency compared to silicon-based microfabricated liquid cells, allowing for improved spatial resolution and reduced electron scattering. In addition, the graphitic crystal structure ensures robust confinement that is impermeable even to helium or hydrogen molecules. The excellent electrical conductivity of graphene minimizes charge accumulation during observation, thus reducing the corresponding sample movement and charge-induced stress. However, the sensitivity of graphene to radiation damage (with a knock-on voltage of ~82 kV for monolayer graphene) limits the applicable acceleration voltage and electron flux for the observation. And it has been reported that the van der Waals interaction between graphene sheets could create significant pressure onto the confined liquid, leading to unexpected structural changes.[426, 427]

4.6.1 Phase modulation by *in situ* TEM liquid enviroment

Hong et al. performed a pioneering work in the controlled synthesis of metastable phases with the discovery of a metastable *hcp* palladium hydride (PdH_x) in LPTEM.[428]They first synthesized a series of PdH_x nanoparticle samples at different concentrations and suspended them in specific liquid media. The formation and transformation of nanocrystals were observed in real time using LPTEM. Under conditions of high hydrogen and low Pd concentrations, nanocrystals were found to be more prone to adopt *hcp* structure. This can be attributed to the abundance of hydrogen atoms at high hydrogen concentrations which provides sufficient occupancies for the *hcp* structure within the crystal lattice. Additionally, the low Pd concentration favors the formation of the *hcp* structure by reducing the stability of the *fcc* structure due to the lower number of Pd atoms. In contrast, under conditions of low hydrogen and high palladium concentrations, the nanoparticles tend to form the *fcc* structure. The low hydrogen concentration restricts the occupancy of hydrogen atoms in the lattice, making the *fcc* structure more stable (**Figure 37**). The high palladium concentration provides enough palladium atoms for most of the atoms in the nanoparticles to occupy positions within the *fcc* structure. Furthermore, the researchers also observed that the *fcc* structure was more favorable under bubble formation conditions. The formation of bubbles resulted in lattice deformation and distortion, making the *fcc* structure relatively more stable compared to the *hcp* structure. The overall study demonstrates that through the use of LPTEM technology and precise control of the experimental conditions, it is possible to effectively synthesize and control the crystal structure of PdH_x nanoparticles, which is of great importance for the preparation and applications of nanomaterials.

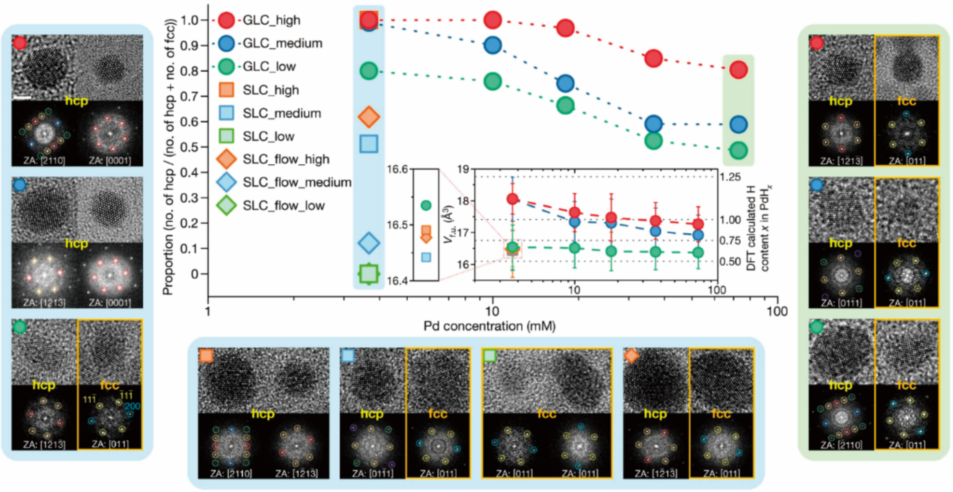

Figure 37. The proportion of *hcp* particles formed under electron beam irradiation was studied under different conditions. Three different conditions, represented by red, blue, and green, corresponded to high, medium, and low electron dose rate (EDR), respectively. Different shapes (circle, square, and diamond) represented different liquid systems (GLC, SLC, and SLC with liquid flow). Reprinted with permission from ref. [428]. Copyright 2022 Springer Nature Limited.

In addition, Wang et al. have revealed an unconventional deformation mechanism of lead selenide (PbSe) semiconductor nanocrystals during superlattice phase transitions in 1,2-ethylenediamine (EDA)/ethylene glycol (EG) solution through *in situ* LPTEM experiments and MD simulations (**Figure 38a**).[429] Experimental observations have shown that when the nanocrystals approach each other at distances of about 2−4 nm, they undergo an elongation, but regain their spherical shape when moving apart. This deformation is reversible, with elongation occurring as they move apart and retaining the deformed state when they come closer (**Figure 38b**). Further HAADF-STEM analysis indicates that the elongation of the nanocrystals is due to the changes in geometry (an increase in the number of atomic planes along the <100> crystal direction) rather than lattice expansion. The researchers proposed that nanocrystals exhibit dipole interactions upon EDA-induced removal of surface ligands, leading to their self-assembly into chain-like structures in solution. EDS results support this hypothesis, showing a change in the Pb and Se atomic ratios of the nanocrystals during the superlattice transition. MD simulations reveal that the nanocrystals with dipole moments undergo shape changes before they encounter each other, and once they fuse to form a superlattice, the deformation remains largely unchanged. These findings elucidate the mechanism of deformation involving dipole-dipole interactions and provide insights into controlling the structural deformation and superlattice formation of semiconducting nanomaterials, which could be essential for the performance of photoelectronic devices.

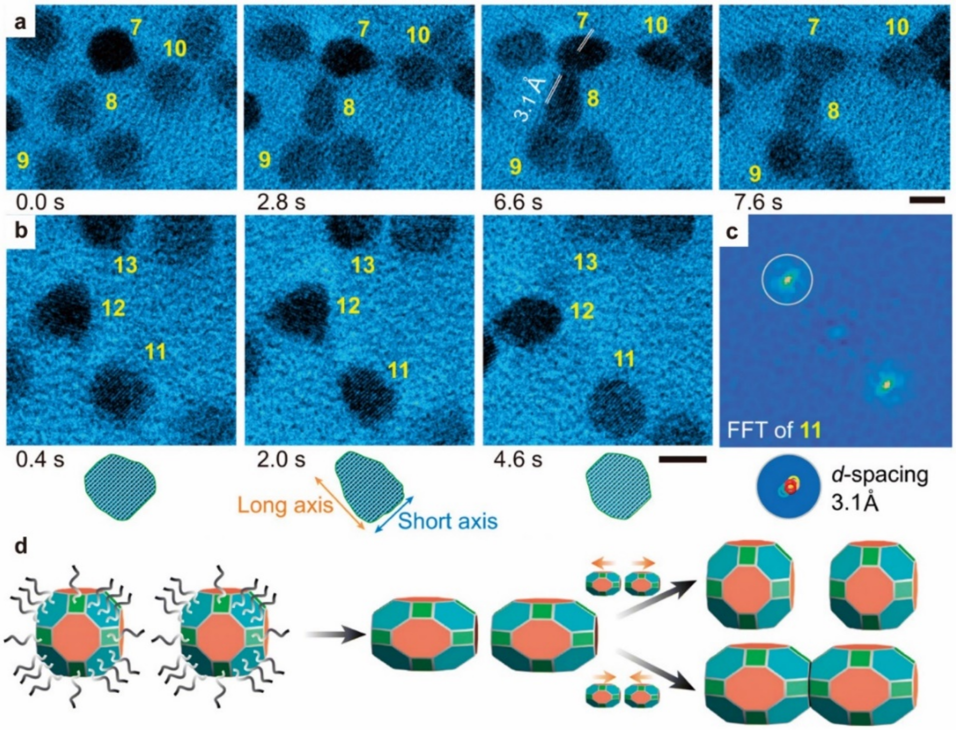

Figure 38. (a) TEM image sequence showing the elongation and following oriented attachment of PbSe nanocrystal 8 with nanocrystals 7 and 9. The oriented {200} planes of attaching nanocrystals are marked by white lines in the third image. (b) TEM image sequence and schematics (below) showing the reversible deformation of PbSe nanocrystal 11 during moving away from the adjacent nanocrystal 12. (c) Superimposed FFT images of nanocrystal 11 during the deformation showing in (b), which shows the overlap of the diffraction spot with a consistent {200} *d*-spacing of 3.1 Å. (d) Schematic showing the proposed reversible deformation mechanism corresponding to the change of the interparticle distance. All scale bars, 5 nm. Reprinted with permission from ref. [429].Copyright 2019 AAAS.

4.6.2 Section summary

The *in situ* LPTEM technique offers unique possibilities for the visualization of nanomaterials in their native liquid environment with exceptional spatial and temporal resolution, enabling direct probe of the kinetic behaviors and structural transition of materials occurring in fluids. The *in situ* LPTEM characterization is promising for a wide range of applications, including the study of nucleation and growth dynamics, the interaction and self-assembly process of nanomaterials, and catalytic reactions in liquid solutions. The technique is particularly useful for studying environmentally sensitive processes, such as those occurring in biological systems or at the interfaces. The application of *in situ* LPTEM will not only promote the understanding of the formation mechanism of materials in real life, but more importantly will provide insights into the controlled synthesis of functional nanomaterials based on the obtained structure−property relationships. However, the *in situ* LPTEM technique is still in its infancy and faces some critical challenges. The radiation damage from high-energy electron beam is inevitable. Long duration of electron beam exposure could induce decomposition of sensitive components or radiolysis of liquid molecules. The sample preparation can be sophisticated and labor-intensive to meet the requirement for fine tuning of liquid volume and composition. Moreover, the introduction of external stimuli such as electric or magnetic fields could be intriguing for a wider range of research interests.

4.7 *in situ* TEM optical stimuli study for PEN

Optical property, the behavior of materials in response to light, is another fundamental physical property of materials for their applications in sensors, biomedical imaging, data storage, display technologies, and solar energy. Especially, nanomaterials and devices with diverse light-responsive mechanisms have gained significant attention in recent years due to their unique properties and potential applications. One of the responses to optical stimuli is phase transformation, which means that phase engineering can also be realized by optical modulation. Several strategies have been proposed and realized to introduced light into TEM,, including the light path setup, TEM-STEM probe holder, and MEMS chips (**Figure 39**).[202]

The light path setup includes mirrors and an optical lens to direct light onto the sample in TEM (**Figure 39a**).[430] The light source is reflected by mirrors and directed into the TEM through an optical window. The light is then focused onto the specimen by the reflection mirror in the TEM column. The reflection mirror is located below the electron source with a small opening for the electron beam. An ellipsoidal mirror is positioned within the gap between the pole pieces of the objective lensto effectively collect and focus the emitted photoluminescence and cathodoluminescence light from the sample. This focused light is then directed into an optical fiber which serves to transmit the collected light into a monochromator for subsequent analysis. However, these setups require a large modification of the TEM.

The second option is to enhance the sample holders by incorporating a built-in light source. This involves integrating a circuit into the holders that allows the light source to be powered by applying a voltage to it. The biggest challenge is to reduce the size of the light source due to the limited space in the TEM column. LEDs are widely used as the light source in optical TEM holders due to their compact structure and wide range of wavelengths (**Figure 39c**)

With the development of MEMS technology, compacted MEMS chips are introduced into *in situ* optical TEM holder. As shown in **Figure 39c**,[431] the light source is fixed in front of the specimen and the circuit is integrated into the chips. Furthermore, the micro- or even nanoscale MEMS chips can be used to introduce localized and various optical stimuli for the specific samples. The MEMS chips provide an efficient, high sample stability, and handy platform for the *in situ* optical TEM platform.

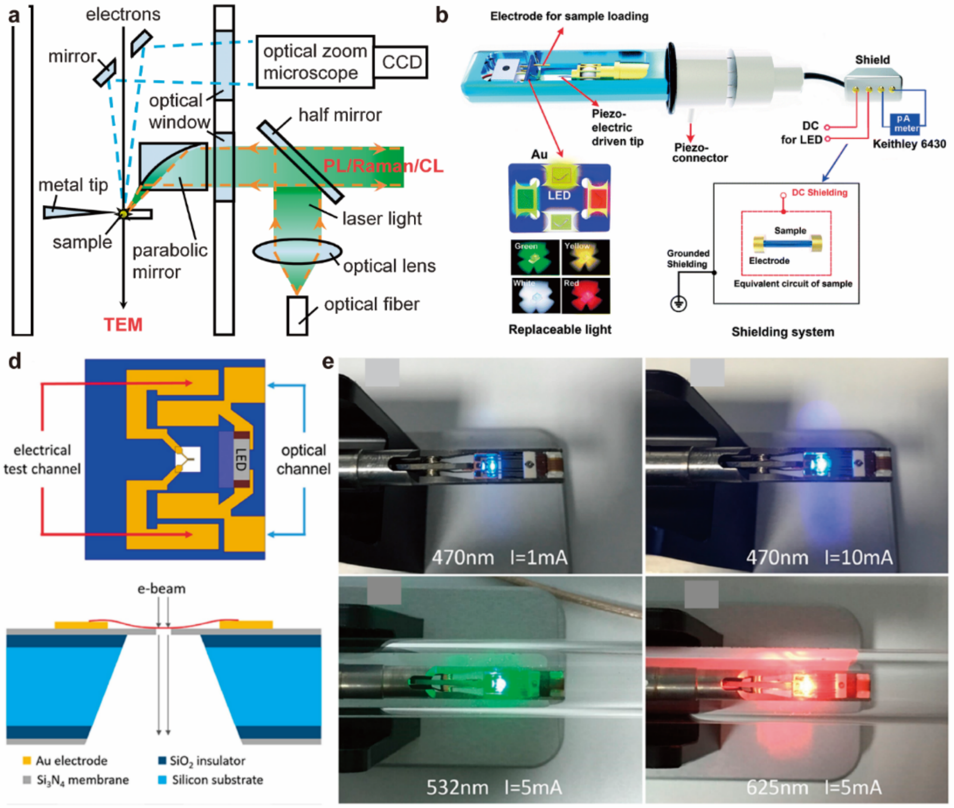

Figure 39. Different configurations for introducing light into TEM via holder modifications. (a) Introducing light by near-field optical probing. Reprinted with permission from ref. [430]. Copyright 2012 The Japan Society of Applied Physics. (b) Schematic of photoelectric TEM holder with replaceable light source. Reprinted with permission from ref.[432] under a Creative Commons Attribution 3.0 Unported Licence. Copyright 2018 The Authors. (d,e) Introducing light by MEMS chip with LEDs. Reprinted with permission from ref. [431]. Copyright 2018 Elsevier B.V.

4.7.1 Nanoparticles

The photo-induced phase transformation is typically triggered by the absorption of photons, which can lead to various effects such as changes in crystal structure, electronic properties, and molecular configurations. In recent years, there has been increasing interest in studying photo-induced phase transitions using *in situ* TEM techniques. These studies aim to understand the mechanisms of the light-induced phase transitions and to explore potential applications in areas such as optoelectronics, phase engineering, and so on. By using *in situ* TEM techniques, the structural changes during photo-induced phase transitions can be directly observed with high spatial and temporal resolution. This allows for a detailed understanding of the underlying processes, such as the nucleation and growth of new phases, structural rearrangements, and the influence of external factors like temperature and light intensity. The light−materials interactions will introduce many effects such as photochemical effect, thermal effect, mechanical effect, and so on. Localized heating caused by absorption of laser energy in the irradiated material is likely to introduce phase changes in materials, usually between ordered and disordered structures caused by laser melting or evaporation.

Upon plasmon stimuli, the Pd nanotube coupled to gold nanoparticles can be modulated from α phase to β phase in environmental TEM. This phase transformation is critical for photocatalytic dehydrogenation. With *in situ* TEM recording, it is shown that the phase transformation starts with the formation of an α phase nucleus at one edge of the particle and propagates across the particle until the β phase is completely pushed out of the particle (**Figure 40a**).[433] Besides the single element nanoparticles, the perovskite, which is sensitive to optical stimuli, was also investigated by *in situ* optical TEM to uncover the degradation mechanism. Coupled with EDS equipped in the TEM, Funk et al. found that a more iodine-rich phase with the approximate composition of $CsPb(Br_{0.6}I_{0.4})_3$ formed at the edges of the particle, while a ternary pure bromide phase of $CsPbBr_3$ remained in the center during irradiation (**Figure 40b**).[434] Another interesting example is the ultrafast switching from an insulating to a metallic state by *in situ* optical TEM. The photo-induced multistage phase transition of Ta_2NiSe_5 was achieved (**Figure 40c**), and the four-order modulation of the resistivity drop was realized. Based on the information obtained by *in situ* TEM, it is revealed that an in-chain Ta atom displacement occurs during the structure transition.[435]

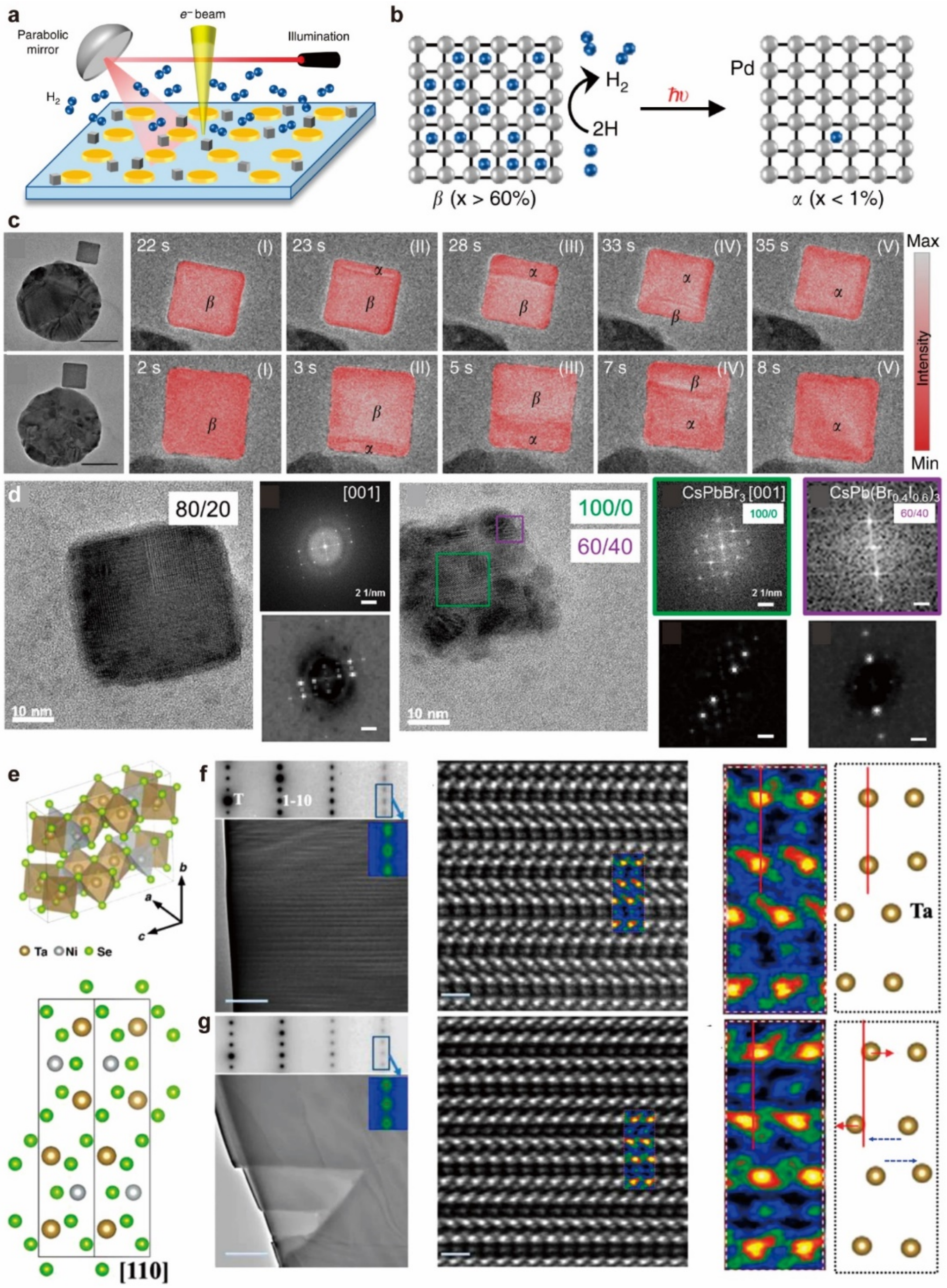

Figure 40. *in situ* TEM study of photoinduced phase transitions of nanoparticles. (a) Schematic of the environmental TEM coupled with *in situ* optical TEM holder. (b) Schematic of α and β phase of Pd nanocubes. (c) Phase transformation of Pd nanocubes from β to α under 690 nm light illumination in H_2 environment. (a-c) Reprinted with permission from ref. [433] under a Creative Commons Attribution 4.0 International License. Copyright 2020 The Authors. (d) Phase separation of $CsPbBr_3$ perovskite. Reprinted with permission from ref. [434]. Copyright 2020 American Chemical Society. (e) Schematic of the structure of Ta_2NiSe_5. (f) Pristine bright field and diffraction pattern of Ta_2NiSe_5 and atomic resolved high-angle annual dark-field image taken in [110] zone axis with schematic of Ta atom columns. (g) Same images for hidden state Ta_2NiSe_5. The red line and arrows in (g) mark the small relative displacement of Ta atoms with respect to the one in (f). (e-g) Reprinted with permission from ref. [435] under a Creative Commons Attribution 4.0 International License. Copyright 2021 The Authors.

4.7.2 Nanorods and two-dimensional materials

Using optical stimuli, the amorphous Si was successfully transferred into crystalline under 532 nm laser irradiation (**Figure 41a**).[436] The amorphous Si/SiO_2/crystalline Si was fabricated by FIB and by precisely positioned illumination by the fiber probe tip, the single crystal seeds are formed for crystallization. This phase modulation provides a pathway for laser processing crystallization for amorphous Si.

For 2D materials, DFT calculations found out a photo-induced phase transition of $MoTe_2$ from 2H to 1T' initiated by a local ordering of Te vacancies,[437] which is also used to tune its electronic structure, verified experimentally but not in TEM.[43] The laser patterning induces the localized phase transformation of $MoTe_2$ from 2H to 1T' with distinct physical and chemical properties.

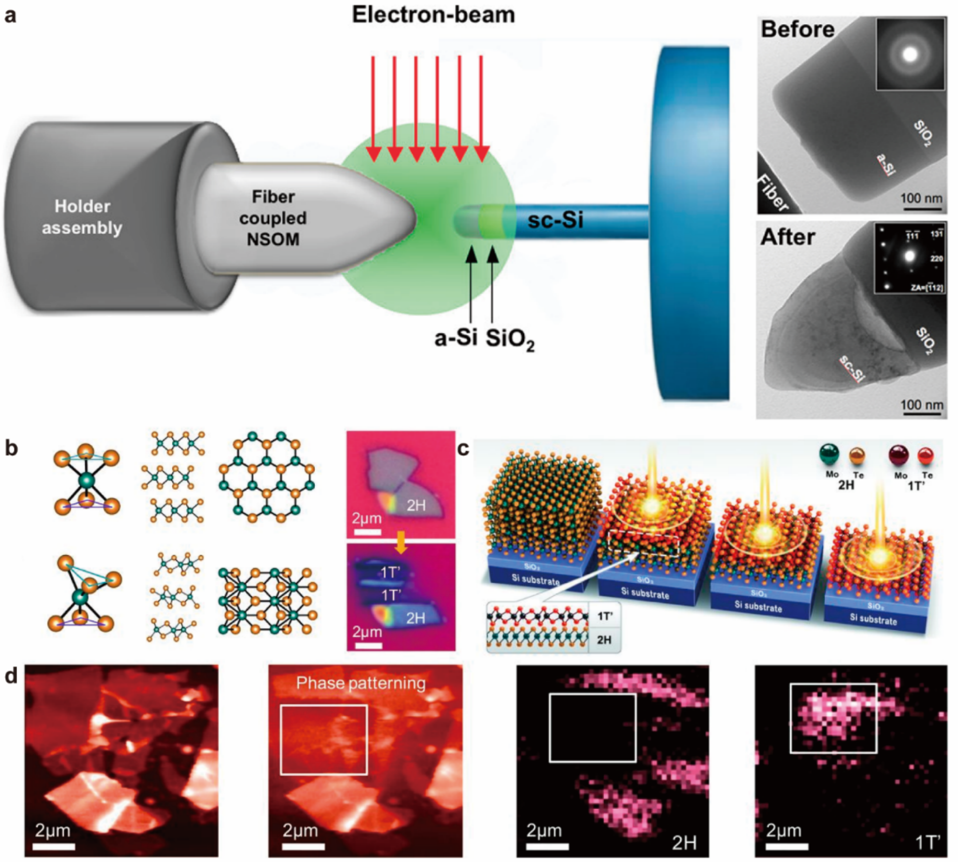

Figure 41. *in situ* TEM study of photoinduced phase transitions for nanorods and 2D materials. (a) Crystallization of Si under laser illumination. Reprinted with permission from ref. [436]. Copyright 2012 American Chemical Society. (b) Schematic and optical microscope images of mechanically exfoliated $MoTe_2$ with 2H and 1T' phase. (c) Schematic of the laser irradiation process. (d) Phase transformation of $MoTe_2$ before and after laser patterning coupled with binding energy map of Mo 3*d* electron for 2H and 1T' phase. Reprinted with permission from ref. [43]. Copyright 2015 AAAS.

4.7.3 Section summary

Various optical setups have been developed in the TEM to introduce optical stimuli into the sample. These setups enable the visualization and study of dynamic processes under optical stimuli, providing valuable insights into phase transitions and modulation mechanisms. The studies we mentioned above offer the important examples of photo-induced phase modulation with the underlying mechanism provided by *in situ* TEM. This knowledge can then be applied to the development of new materials, devices, and PEN applications in areas such as optoelectronics, photonics, and data storage.

4.8 *in situ* TEM magnetic field study for PEN

In addition to the traditional methods of controlling phase transitions, the magnetic field is also an important approach, especially for the phase modulation of ferromagnetic materials. The transition mechanism of the magnetic domain structure under various temperatures, electric fields, and currents is crucial for the development of magnetic materials and other functional materials. However, characterization of the structural phase transition of magnetic materials is quite challenging due to the strong interference of the internal magnetic fields in traditional TEM.[318] Besides, the magnetic material may be absorbed to the poles of the objective lens, which could contaminate the TEM. To address these issues, Lorentz TEM (LTEM) has been developed to characterize magnetic materials by closing the objective lens close to the sample and magnifying the image with different modes such as Fresnel and Foucault modes in **Figure 42**.[438]

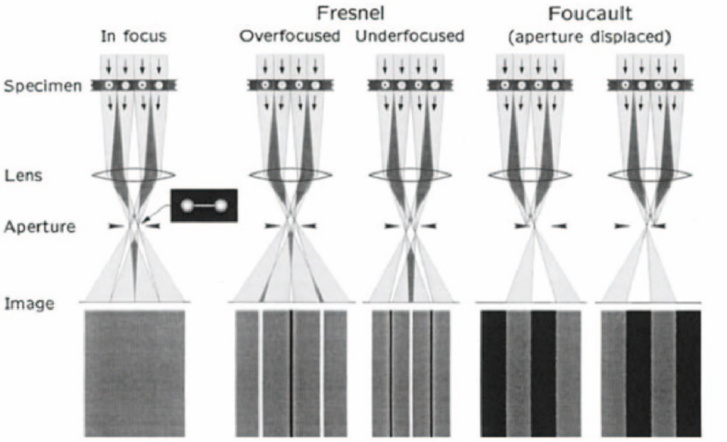

Figure 42 The beam path of different observation methods in the LTEM. Reprinted with permission from ref. [438]. Copyright 1998, Springer Nature Limited.

As a new *in situ* magnetic characterization technique, LTEM plays an important role in the phase engineering of magnetic materials where two strategies have been implemented to apply the magnetic field to the materials. One is to alter the current of the objective lens to apply a gradual magnetization of the sample.[439] The other is to attach an electromagnet to the sample holder.[440] However, it is difficult to obtain a magnetic field parallel to the surface of the material by the first method due to the inherent direction of the magnetic field produced by the objective lens. The second method, however, allows the sample to be exposed to a horizontal magnetic field, making it easier to examine anisotropic samples. To visualize and tune the magnetic domain structures in LTEM, several imaging schemes have been developed, for example, Fresnel mode, which uses defocused imaging to determine the domain wall structure;[441] Foucault mode, which uses dark-field imaging to determine the domain distribution;[442] electron holography method;[443] differential phase contrast (DPC) method;[444] energy-loss magnetic chiral dichroism (EMCD);[445] magnetic circular dichroism of electron waves (MCD);[446] etc.

4.8.1 Phase modulation by magnetic field

LTEM has been used to finely characterize the microstructure of magnetic materials such as traditional magnetic materials, magnetic thin films, magnetic nanowires/particles, and magnetic skyrmions. Besides, more and more studies have employed the *in situ* LTEM setup to achieve magnetic field-controlled structural phase modulations. With the rise of magnetic nanomaterials in the last two decades, phase engineering for different magnetic nanomaterials has also emerged. Here, we summarize some of the research progress on magnetic nanomaterials with different dimensions, as shown in **Figure 43**. For 0D nanomaterials (also termed as nanoparticles), Yamamuro et al. used electron holography and LETM to observe the dipolar ferromagnetic phase transition in Fe_3O_4 nanoparticle arrays.[447] Ghosh et al. observed that magnetic field-driven emission enhancement can be tuned by magnetic nanoparticle size and liquid crystal alignment.[448] For 1D materials (nanowires), Tokura et al. reported the real-space observation of skyrmions and helical magnetic domains in a MnSi nanowire using LTEM.[449] Parkin not only demonstrated the formation of antiskyrmions in $Mn_{1.4}Pt_{0.9}Pd_{0.1}Sn$, but also found evidence for antiskyrmions in $Mn_{1.4}PtSn$.[450] Zhang et al. demonstrated the influence of magnetocrystalline anisotropy on magnetization configurations in uniaxial magnetic nanomaterials, showing a way to tune the magnetization configuration by changing their crystal structures.[451] In addition, nanostrips thinned by microfabrication techniques from bulk to nearly 1D nanostripes also demonstrate interesting magnetic phase changes. For instance, Tian et al. reported direct evidence for the field-dependent character of the interaction between individual magnetic skyrmions and between skyrmions and edges in B20-type FeGe nanostripes observed by high-resolution LTEM.[452] Since the discovery of the first 2D material, graphene, 2D materials with magnetic properties have gradually become a research hotspot.[453] Wang revealed the

Dzyaloshinskii−Moriya interaction and Néel-type skyrmions are induced at the WTe_2/Fe_3GeTe_2 interface, as well as and directly imaged the Néel-type skyrmion lattice and the stripe-like magnetic domain structures.[454] Huang et al. investigated the structural and magnetic properties of the quasi-2D material VBr_3.[455] Tokura reported the real-space observation of the formation of the SkX in a thin film of B20-type $Fe_{0.5}Co_{0.5}Si$, where skyrmions in the form of a hexagonal arrangement of swirling spin textures were directly observed.[456] Furthermore, substantial progress has yet been achieved by layering typical metal materials to generate near-2D materials. Recently, Li et al. demonstrated the formation of metastable Néel-type skyrmion arrays in Pt/Co/Ni/Ir multilayers at zero field following the *ex situ* application of an in-plane magnetic field using LTEM.[457] The resulting skyrmion texture was found to depend on both the strength and misorientation of the applied field as well as the interfacial Dzyaloshinskii−Moriya interaction. Zhang et al. succeeded in generating and tuning the skyrmions by electromagnetic manipulation in Pt/Co(1.85)/Ta perpendicular multilayers.[458] Pollard used LTEM to track the formation of nanoscale Néel skyrmions in Co/Pd multilayers and confirmed the size and spin structure of the Néel skyrmion by phase reconstruction.[459]

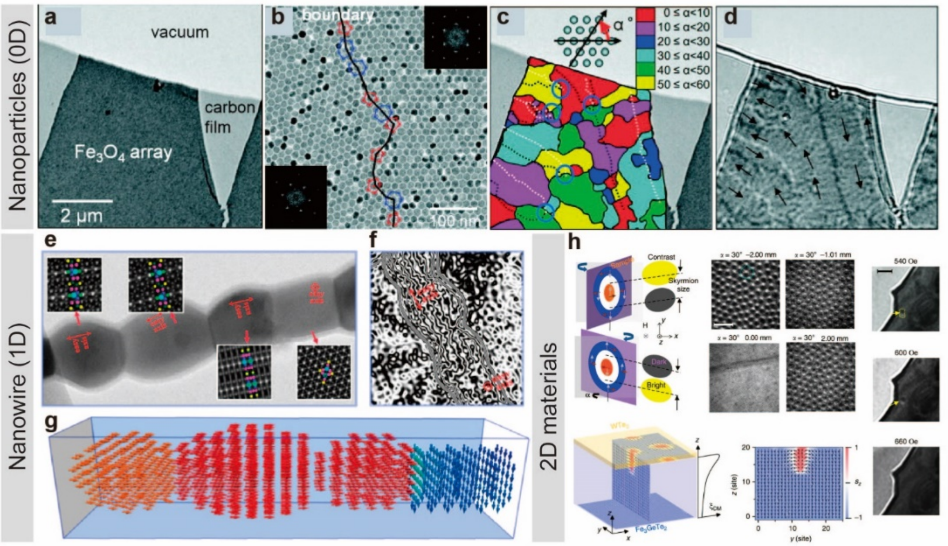

Figure 43. *in situ* phase engineering of typical magnetic nanomaterials (0D, 1D, and 2D). (a) Monolayer array of Fe_3O_4 nanoparticles. (b) Low and high magnification TEM images. (c) Color map of the macro-grain orientations. (d) Lorentz micrograph. (a-d) Reprinted with permission from ref. [447]. Copyright 2011 American Institute of Physics. (e) TEM image of the single-particle-chain BFO nanowires measured by probe-aberration corrected STEM. (f) Magnetic induction maps of the in-plane component of the specimen. (g) Single-particle-chain nanowire. The colors of the arrows represent the orientations of the magnetic moments. (e-g) Reprinted with permission from ref. [451]. Copyright 2018 American Chemical Society. (h) Schematic diagram of a Néel-type skyrmion on a tilt sample for LTEM imaging and LTEM observation of skyrmion lattice from under focus to over focus on WTe_2/40L Fe_3GeTe_2 samples. Reprinted with permission from ref. [454]. Copyright 2020, The author(s). Published by Springer Nature Limited.

4.8.2 Section summary

Overall, *in situ* magnetic TEM is an advanced experimental technique that enables real time observation of the structure and phase transition behavior of materials under an applied magnetic field, facilitating the tuning of the structure and magnetism of magnetic conductors and thin films, thus optimizing their performance. This technique has great potential for controlling the structural phase transitions in nanomaterials, for example, real-time observation of magnetic changes in nanomaterials allows precise tuning of the magnetic properties in nanodevices. Understanding the phase transition behavior of nanomaterials under external magnetic fields is crucial for their properties and applications. This has promising implications for high performance magnetic materials, magnetic electronic devices, and magneto-optical devices. In fact, modulation of the magnetic moment of magnetic materials has been applied to state-of-the-art magnetic storage devices today with *in situ* magnetic phase engineering methods playing an even more prominent role in the development of random-access magnetic memory and trace memory. With the application of spin-transfer torque and spin-orbit torque theories in the design and fabrication of new prototype devices, it is necessary to reveal the underlying mechanism for magnetically induced phase engineering at the micro/nano or even atomic scale, which must incorporate the magnetic field and current control to the magnetic nanomaterial.

By utilizing multi-physical field coupling in magnetic phase engineering, it is confident that more success will be achieved in tuning the magnetic properties of nanomaterials. It should be noted, however, that *in situ* magnetic PEN is a complex experimental technique requiring high-resolution TEM equipment and precise magnetic field control. Additionally, proper sample preparation and nanomaterial handling are crucial. Consequently, research in this field is typically laboratory based and requires interdisciplinary collaboration to fully exploit the potential of *in situ* magnetic TEM in controlling structural phase transitions in nanomaterials.

5. Phase engineering of nanomaterials for distinct properties

Phase transformation materials, including As−Te−I alloys, have been utilized in solid-state memory devices since the 1960s.[460] These materials exhibit threshold switching, enabling a transition between two stable resistive states with distinct resistances for information storage. Additionally, the widely recognized GeSbTe alloy demonstrates laser-induced phase transformation, which serves as the basis for phase-change optical storage by leveraging the optical reflectivity disparity between its crystalline and amorphous phases. The remarkable achievements of phase transformation materials have attracted considerable interest from the research community. As mentioned earlier, the increased capability for phase engineering in nanomaterials has revitalized interest in the field of phase transformation. This is primarily due to the ability to achieve distinct properties through phase engineering, thereby enabling diverse applications. In this section, we present representative examples of phase-engineered distinct properties of nanomaterials, including mechanical, optical, electrical, thermal, and magnetic properties. These examples serve to highlight the immense potential of phase engineering for practical applications.

5.1 Mechanical properties

Mechanical properties are one of the fundamental properties of materials. Phase engineering can be used to tune the mechanical properties. For example, under high pressure, Au nanoparticles have an unexpectedly high stiffness due to crystallinity.[461] The bulk modulus of transferred Au nanoparticles is 290 GPa, showing an increase of 60% and of the order of W or Ir. Similarly, the strength of Ag nanowires is also tied to the structure based on the atomistic simulations[462] and experiments.[463] In contrast, phase engineering can also lead to the ductile mechanical behaviors by modulating the crystalline structure to an amorphous phase, such as deformation-induced *fcc* to amorphous phase transformation in CrMnFeCoNi[236] and amorphous SiC nanowires with maximum strain up to 7.0%, much higher than crystalline SiC.[464]

The well-known transformation induced plasticity (TRIP) effects are also representative examples of phase engineering. The TRIP effect was observed in 1924, involving the martensitic phase transformation. TRIP steels typically consist of a mixture of ferrite, austenite, and other phases. When deformed, the strain or stress induced phase transformation from austenite to martensite occurs, leading to a volume change that redistributes stress within the material. This redistribution delays the onset of localized fracture, resulting in improved ductility and toughness.[465-467] In 2020, using *in situ* TEM technology, Chen et al. observed the fundamental origin and atomic-scale mechanism of TRIP effect induced work hardening in $Cr_{20}Mn_6Fe_{34}Co_{34}Ni_6$ sample (**Figure 44**).[468] From the *in situ* TEM strain test, they found that the phase transformation from *fcc* to phase is mainly based on the 3D SF network defects, in **Figure 44b**. The Lomar−Cottrell locks can produce high density immobile SFs to hinder the movement of dislocations in **Figure 44c**, and can also stabilize the SFs, in turn promoting the nucleation and growth of the *hcp* phase (**Figure 44d,e**).

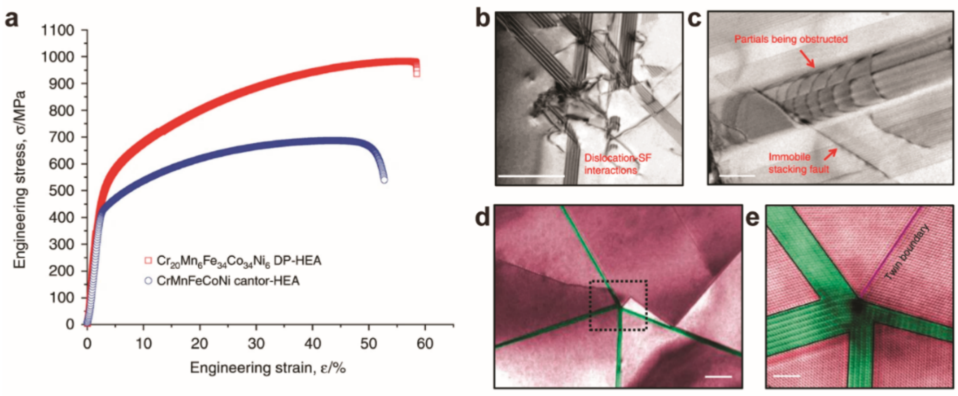

Figure 44. (a) The strain−stress curve of the Cantor alloy and $Cr_{20}Mn_6Fe_{34}Co_{34}Ni_6$. (b-e) The interaction of partial dislocation,s Lomar−Cottrell locks, and *hcp* nanolamellas. Reprinted with permission from ref. [468]. under a Creative Commons Attribution 4.0 International License. Copyright 2020 The Authors.

5.2 Optical properties

Optical properties can also be engineered by phase transformation. By phase engineering, various materials have been reported to obtain the distinct properties.[469-474] For example, the SPR effect in Au and Ag materials can be directly controlled by phase engineering.[10, 14, 475] Compared with *fcc* Au nanowires, the directly synthesized unusual 4H phase of Au nanowire exhibits the distinctive position and magnitude of SPR peaks measured by monochromated EELS in TEM. Combined with theoretical calculations, it is shown that 4H Au exhibits fewer SPR peaks in the 0−2.5 eV energy range and SPR peaks show a red shift compared to *fcc* Au (**Figure 45**).[10] Similarly, 4H Ag thin film exhibits much lower reflectance over the entire visible light range compared to *fcc* Ag thin film, especially at shorter wavelengths. Also, the blue shift is observed in the bulk plasmon frequency of the 4H Ag thin film, in contrast to the *fcc* Ag thin film, providing evidence for the diminished effectiveness of the *d* electrons in the ability of 4H Ag to screen the free *s* electrons.[14]

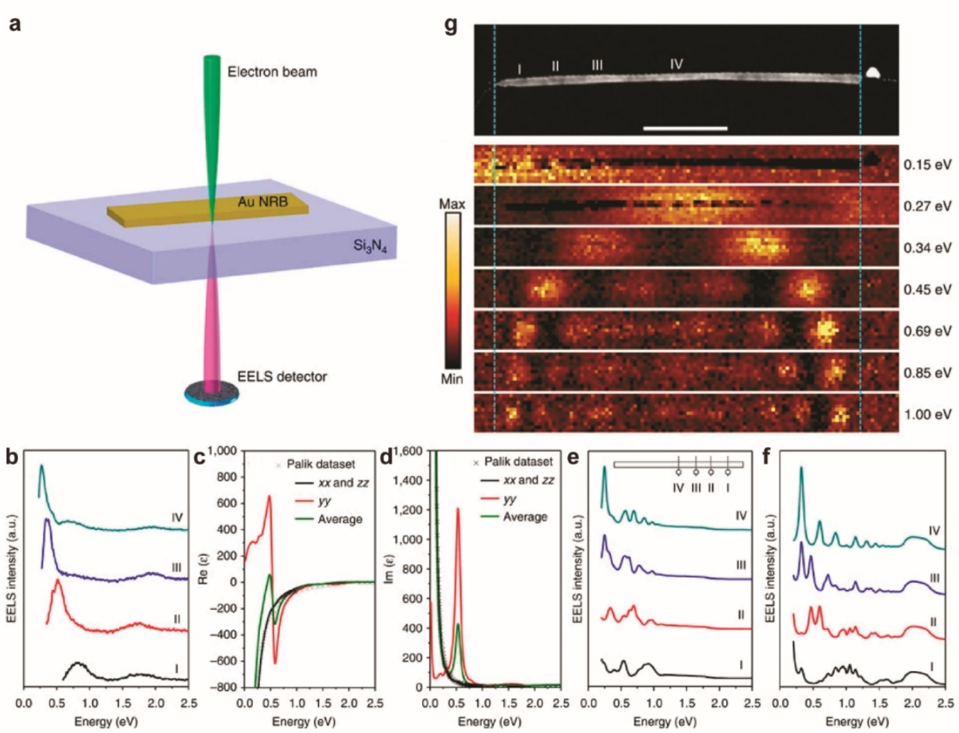

Figure 45. Distinct optical properties of 4H Au nanoribbons (NRBs). (a) Schematic of monochromated EELS measurement on a single 4H Au NRB. (b) EELS spectra acquired from an Au NRB at different positions indicated in (g). (c,d) DFT calculated dielectric function of Au thin film. (e) Calculated EELS spectra of a 4H Au NRB based on the dielectric function in c,d. (f) Calculated EELS spectra of an *fcc* Au NRB with the dielectric function taken from Palik at the same excitation position as (e). (g,h) HAADF-STEM image of single Au NRB (scale bar, 200 nm) and its corresponding EELS maps at different energy loss. Reprinted with permission from ref. [10] under a Creative Commons Attribution 4.0 International License. Copyright 2015 Springer Nature Limited.

In addition, phase engineering of VO_2 has been investigated and proposed for energy efficient smart window applications due to its fully reversible metal−insulator transition triggered by temperature.[476, 477] The tetragonal structure of VO_2 has a higher symmetric lattice, leading to metallic behaviour and infrared light blocking. While M1 phase VO_2 is a semiconductor with infrared light transmission (**Figure 46**).[478] This distinguishing characteristic, particularly in the infrared region, positions VO_2 as a promising material for the development of smart windows for industrial applications (**Figure 46**).[477]

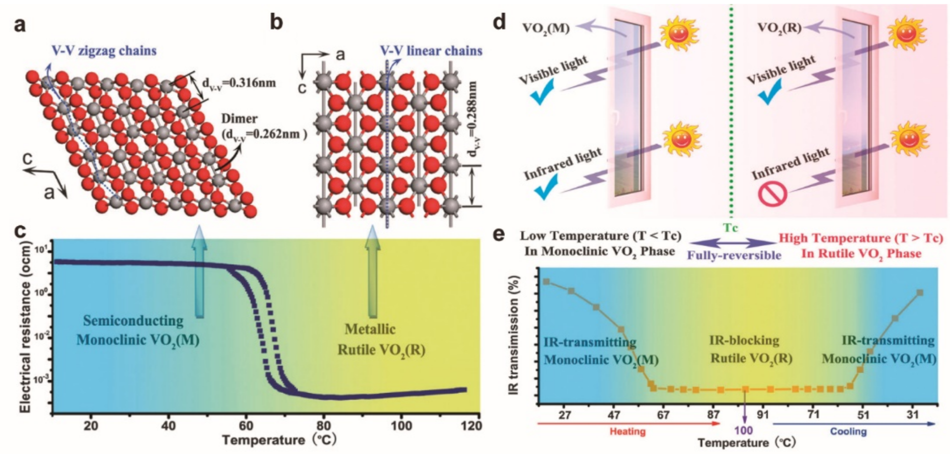

Figure 46. Atomic crystal structure of VO_2. (a) Monoclinic cell. (b) Rutile cell. (c) Temperature dependence of the resistance of the fully reversible phase transition. (d) Schematic of the mechanism of thermochromic smart windows based on VO_2. (b) Temperature dependence of the IR intensity at 2000 cm^{-1} (5000 nm) for a typical phase transition. Reprinted with permission from ref. [477]. Copyright 2013 The Royal Society of Chemistry.

5.3 Electrical properties

The electrical properties can be easily modulated by phase engineering[65], including electrical conductivity, band gap, dielectric constant, piezoelectricity, ferroelectricity and also superconductivity. For example, graphite, graphene, and diamond are carbon polymorphisms with different electrical properties. Graphite and graphene possess layered crystal structure and they are electrical conductors. However, diamond with tetrahedral crystal structure, is an excellent electrical insulator, which is reported recently that the band gap of diamond can be tuned by mechanical strain and drive it to be semiconductors.[198, 479] Transition metal dichalcogenide 2D materials possess different phases (**Figure 47**), such as semiconducting 2H phase, metallic 1T phase, and quasi-metallic 1T' phase.[40] These phases show significantly distinct electrical properties due to the different band structures (**Figure 47**) The semiconducting phase of TMDs make them emerging candidates for the next generation field-effect transistor.[480]

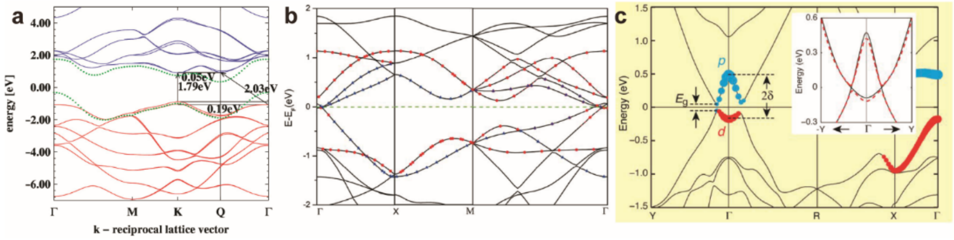

Figure 47. Band structures of different phases of MoS_2 including (a) 2H phase. Reprinted with permission from ref. [481]. Copyright 2012 Elsevier Inc. (b) 1T phase. Reprinted with permission from ref.

[482]. Copyright 2013 AIP Publishing LLC. (c) 1T' phase. Reprinted with permission from ref. [483]. Copyright 2014 American Association for the Advancement of Science.

The GeSbTe alloy, widely used in data storage, is based on the large difference in electrical properties between two phases (i.e., crystalline and amorphous).[484] Similarly, VO_2 also possesses distinct electrical properties between M1 phase and R phase, as shown in **Figure 48**. At temperatures below a critical value, known as the transition temperature (T_c), of around 68 °C, VO_2 behaves as an insulator and exhibits high electrical resistance. However, above T_c, it undergoes a rapid transition to a metallic phase with significantly lower resistance. This transition is due to the changes in its crystal structure and electronic configuration. This property makes VO_2 suitable for various electrical applications, such as switching devices and resistive heating elements.[477]

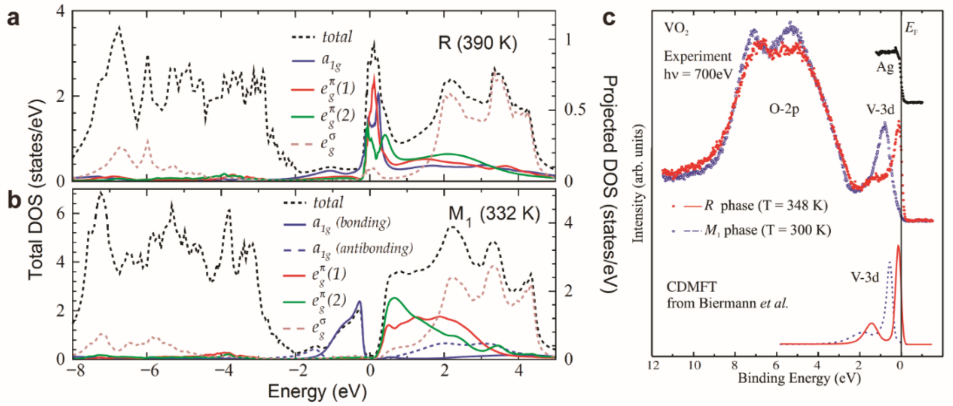

Figure 48. Total and orbital-projected electron density of states (DOS) for (a) R and (b) M1 phases, obtained from DFT + cluster dynamical mean field theory (a) Reprinted with permission from ref. [437]. Copyright 2016 American Physical Society. (c) X-ray photoemission spectra of R (red) and M1 (blue) phases below the Femi level. Reprinted with permission from ref. [485]. Copyright 2006 American Physical Society.

5.4 Thermal properties

The thermal properties of crystalline materials mainly depend on the phonon vibrations and spin of the electrons, which are influenced by the phonon band structure determined by the crystalline phase. The specific phonon frequencies and their dispersion relations play a crucial role in the transport of thermal energy through the material, thus influencing the thermal properties of the material. By modulating the phase of crystalline materials, the thermal properties can be well controlled.

As mentioned above, the polymorphism of carbon, including amorphous carbon, graphene, carbon nanotubes, graphite, and diamond, can be modulated by high pressure or temperature or strain. This phase modulation leads to the wide range of thermal conductivity, which can be up to 5 orders of magnitude, from 0.01 Wm/K for amorphous carbons to 2000 Wm/K for graphene or diamond at room temperature and 10000 Wm/K in type II diamond at 77 K ~~(**Figure 49a**)~~.[486] The large difference in thermal conductivity of these carbon polymorphisms is due to the different lattice structure. For instance, the sp^2 lattice contributes to the high thermal conductivity of carbon nanotubes and graphene. In carbon nanotubes and graphene, carbon atoms are arranged in a hexagonal lattice, forming strong covalent bonds between neighboring atoms. The sp^2 hybridization leads to the formation of a unique phonon band structure with high phonon velocities and long mean free paths. As a result, phonons in carbon nanotubes and graphene can propagate over long distances without significant scattering, resulting in high thermal conductivity. However, amorphous carbon lacks long-range crystalline order and instead has a disordered or random arrangement of atoms. This disorder introduces various types of defects, impurities, and grain boundaries that effectively scatter phonons and hinder their propagation. As a result, amorphous carbon exhibits lower thermal conductivity than its crystalline counterparts, such as carbon nanotubes and graphene.

In metal, the high thermal conductivity is primarily due to the presence of free electrons in metals, which play an important role in heat conduction. The phase modulation to metal can significantly enhance thermal conductivity. For instance, the phase transformation in VO_2 not only alters the lattice structure from metal to insulator, but also influences the electron spin states and carrier concentrations (**Figure 49**).[477, 487] The changes in electron behavior can impact the scattering mechanisms and the transport properties of phonons, which in turn affect the thermal conductivity of the material. By modulating the metal−insulator transition in VO_2, either by temperature or external stimuli such as strain or electric field, it becomes possible to control the thermal conductivity of the material. In the insulating phase, the thermal conductivity is typically lower due to reduced electron and phonon transport. While in the metallic phase, the thermal conductivity increases due to enhanced electron and phonon contributions to heat conduction. Thus, phase engineering can be used to modulate thermal properties over a wide range.

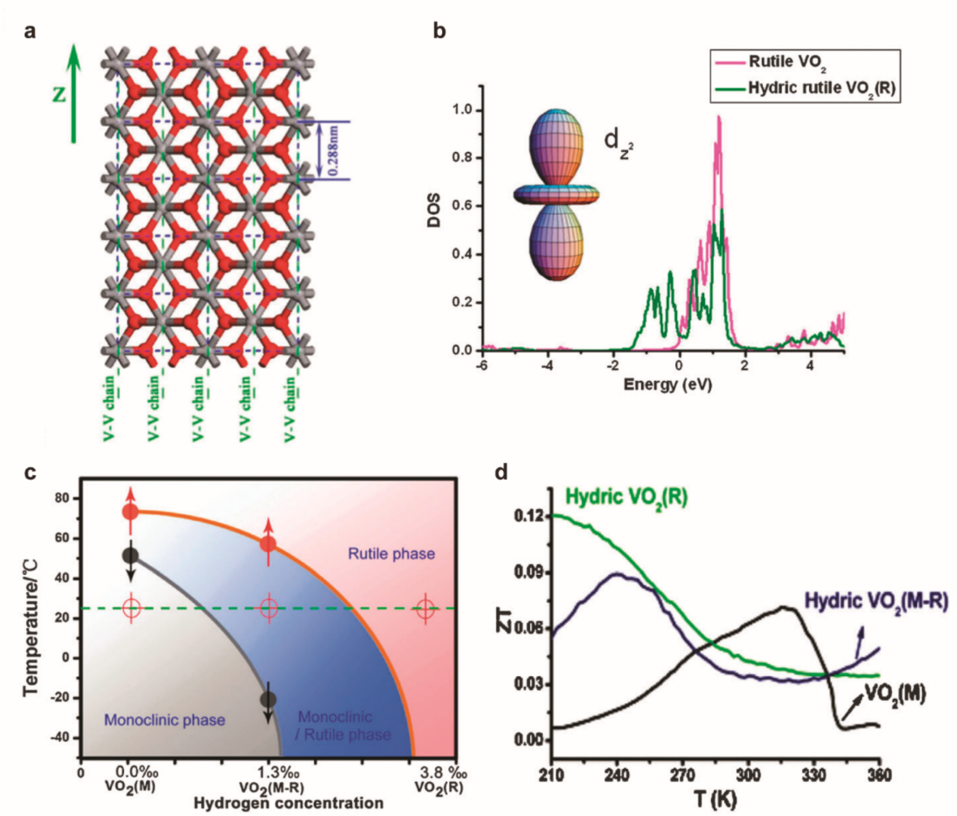

Figure 49. Hydrogen incorporation in VO_2 to achieve enhanced electron-electron correlations, leading to improved thermoelectric performance. (a) Atomic illustration of hydric VO_2 (R). (b) Density of state of the d_{z^2} orbital of vanadium in hydric VO_2 (R), showing the enhanced *e*-*e* correlation by the −2 eV Fermi level. (c) Evolution of the transformation temperature with different hydrogen concentrations. (d) Temperature dependence of the thermoelectric figure of hydric VO_2 (R), hydric (M−R) and VO_2 (M). Reprinted with permission from ref. [487]. Copyright 2011 American Chemical Society.

5.5 Magnetic properties

Phase engineering can also modulate magnetic properties. Among the transition metals, Co, Fe, and Ni are the most important magnetic materials. Co nanoparticles with *fcc*, *hcp*, and *ε* structure have been successfully synthesized with different magnetic properties.[488-490] Different from the *hcp* phase Co nanoparticles, *fcc* and *ε* phase Co nanoparticles are soft magnetic materials. For example, the 9 nm Co with *ε* phase possesses a coercivity (H_c) of 500 Oe at 5 K. However, by annealing at 300 °C in vacuum or Ar/H_2 mixed gas, *ε* phase Co nanoparticles transfer to *hcp* phase with the H_c of 1450 Oe. Further annealing induces the transformation from *hcp* to *fcc* with H_c reduced to 800 Oe at 5 K (**Figure 50**).

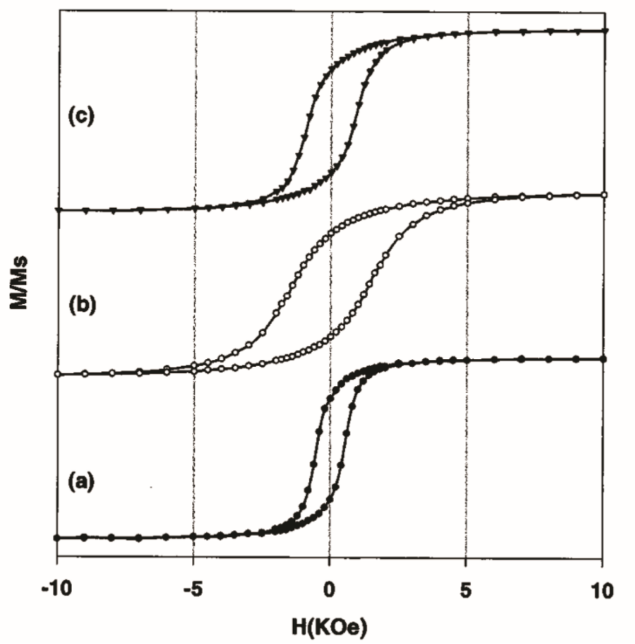

Figure 50. Hysteresis loops of Co particles (a) at 5 K from as-synthesized 9 nm ε phase, (b) *hcp* phase from ε-Co nanocrystals annealed at 300 °C, and (c) *fcc* + *hcp* Co particles from ε-Co nanocrystals annealed at 500 °C. Reprinted with permission from ref. [488]. Copyright 1999 American Institute of Physics.

VO_2 also exhibits a significant change in magnetic susceptibility when it undergoes a transition from the high-temperature rutile (R) phase to the low-temperature monoclinic (M1) phase triggered by temperature. VO_2 in the R phase is paramagnetic, with no permanent magnetic moment and strong magnetic behaviour (**Figure 51**). While, when VO_2 go through cooling, it transfers to the M1 phase with enhanced magnetic susceptibility due to the formation of localized magnetic moments related with V^{3+}.[491] These magnetic properties of VO_2, coupled with its unique metal−insulator transition, have attracted considerable attention for applications in spintronic devices, magneto-optical devices, and sensors.[477]

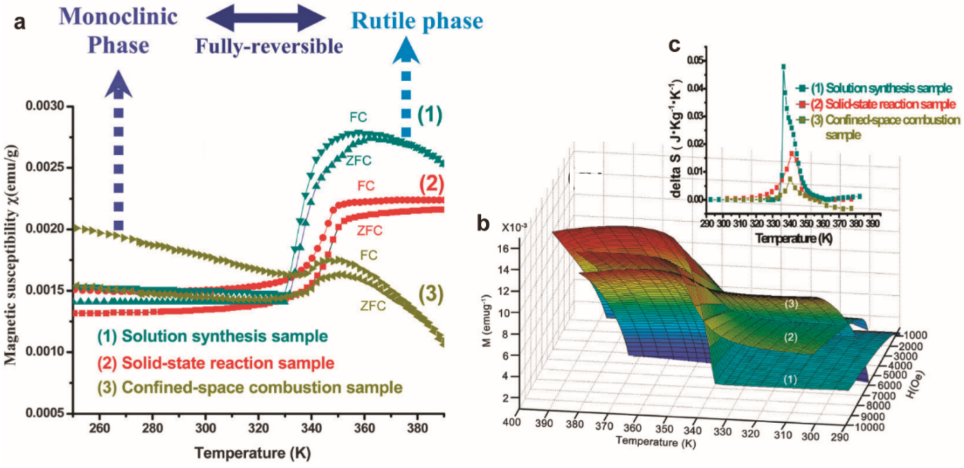

Figure 51. Application of the metal-insulator transitions to the magnetocaloric effect. (a) Temperature dependence of zero field cooled and field cooled magnetization of VO_2 samples in 200 Oe magnetic field. (b) Magnetization isothermals at 290−390 K for VO_2 samples. (c) Magnetic entropy change ΔS of VO_2 sample. (1), (2), and (3) refer to the VO_2 samples obtained from solution synthesis, solid-state reaction, and confined space combustion methods, respectively. Reprinted with permission from ref. [492]. Copyright 2011 The Royal Society of Chemistry.

5.6 Catalytic properties

The catalytic performance of nanomaterials has been found to be closely related to their atomic arrangement in terms of lattice structure and chemical composition (i.e., crystal phase), which fundamentally determines the electronic structure of a material and further defines the catalytic activity related properties such as chemisorption and electrical conductivity.[493] Therefore, controlled engineering of the phase is gaining attention as a method to regulate the physical and chemical properties of nanomaterials with the aim of optimizing their catalytic performance.

It has been widely reported that certain unconventional phases possess superior catalytic activities compared to their counterparts. Geng et al. reported the preparation of metastable 1T phase MoS_2 nanosheets by a hydrothermal method. Compared with the conventional stable 2H phase MoS_2 which shows semiconducting feature, the metallic 1T phase demonstrates excellent catalytic activity in hydrogen evolution reaction (HER) measurements with a reduction in Tafel slope from 135 mV/dec to 41 mV/dec (**Figure 52a,b**). The optimal HER activity is attributed to the five orders of magnitude increase in electrical conductivity as well as the increase in active sites and hydrophilicity.[494] Feng et al. synthesized the 3R phase TaS_2 nanosheets using a unique calcination method and characterized their catalytic performance for HER. The two-dimensional 3R TaS_2 demonstrates remarkable HER activity, which suppresses its 1T and 2H phase counterparts, due to the rich active sites provided by the broken inversion asymmetry and abundant edge exposure.[495] Wang et al. investigated the performance of 4H Au nanoribbons as a catalyst for CO_2 electroreduction reaction with hybrid 4H/*fcc* phase and pure *fcc* phase Au nanoribbons as a comparison. The results indicate the superiority of pure 4H Au nanomaterial in terms of both activity and selectivity for CO production with a Faradaic efficiency of more than 90%. The mechanism was revealed by combined surface structure probe and DFT calculations, suggesting the existence of distinctive and rich uncoordinated sites on the 4H Au nanocrystals instead of its *fcc* counterpart.[496] Qiu et al. proposed a wet-chemical synthesis of PdCu nanoparticles, of which the crystal phase was found to be determined by the following thermal annealing temperature. A *bcc* phase is obtained at elevated temperature of 300−500 °C, while the *fcc* counterpart is obtained at a lower temperature. The as-prepared nanoparticles are then applied as catalysts in hydrogen oxidation reaction

(HOR), where the *bcc* PdCu exhibits a significant advantage of 20-fold in specific activities compared to the *fcc* phase. The dominance in HOR activity is unraveled by DFT calculations, showing that the *bcc* surface has a much stronger adsorption to OH and similar binding to H compared to the *fcc* phase, which resembles the Pt model surface (**Figure 52c,d**).[497] However, it is worth noting that the supremacy in catalytic performance between different phases could vary upon different catalytic process. Yao et al. synthesized a rare *fcc* phase ruthenium (Ru) through epitaxial growth using an *fcc* Pd-Cu alloy seed with matched lattice constant. They find that compared with the conventional *hcp*-based Ru nanocatalyst, the unusual *fcc* phase Ru nanoparticles show enhanced activity in the hydrogenation reaction of 4-nitrochlorobenzene with the conversion rate increasing from 61% to 99%. However, an inversed result was obtained when comparing their activity in the styrene hydrogenation reaction, showing a much higher conversion rate for the *hcp* phase Ru.[498]

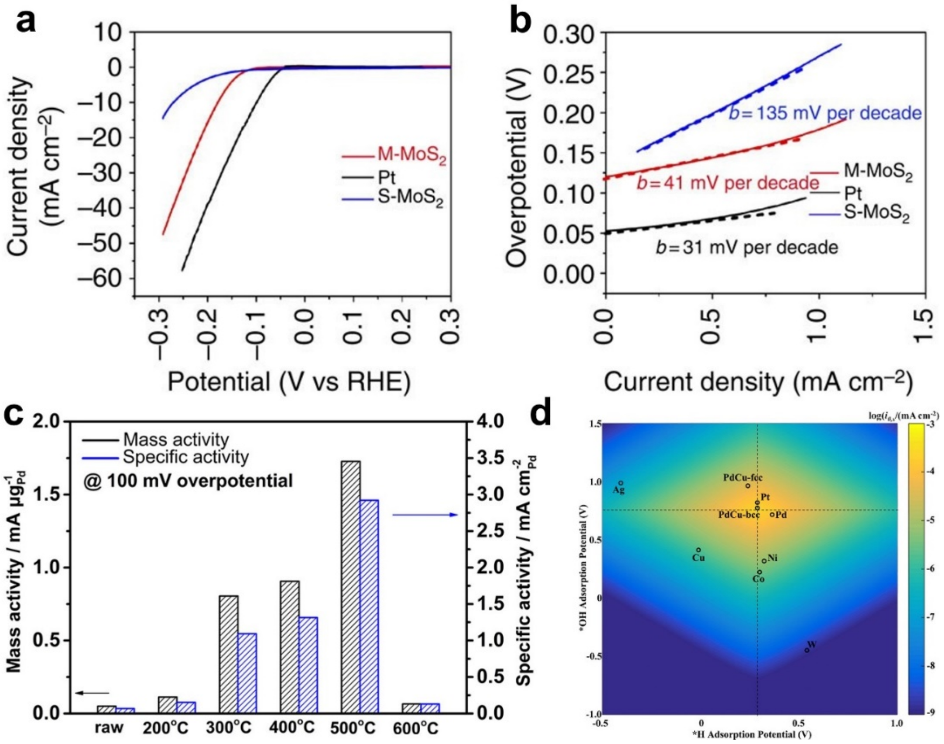

Figure 52. (a-b) HER activity of the 1T (M-MoS$_2$) and 2H (S-MoS$_2$) phase MoS$_2$ nanosheets. (a) Polarization curves of the MoS$_2$ nanosheets. (b) Corresponding Tafel plots obtained from the polarization curves. (a,b) Reprinted with permission from ref. [494]. Copyright 2016 The Author(s). Published by Springer Nature Limited. (c) Comparison of HOR mass and specific activity of PdCu with different phases at 100 mV overpotential in H$_2$-saturated 0.1 M KOH electrolyte. (d) Plot showing the relationship between the experimentally measured exchange current density for hydrogen oxidation in base and the calculated H/OH adsorption strengths, with two dashed lines representing the optimal H and OH adsorption potential, respectively. (c,d) Reprinted with permission from ref. [497]. Copyright 2018 American Chemical Society.

6. Summary and outlook

The powerful TEM makes it possible to obtain information about the crystalline materials at the atomic scale. Recent advances in *in situ* TEM technology have enabled various *in situ* experiments in TEM, including mechanical, thermal, electrical, gas, liquid, optical, and magnetic experiments. A variety of nanomaterials have been investigated by *in situ* TEM for their phase transformation under external stimuli, providing actual phase transformation mechanisms even at the atomic scale, which are systematically reviewed here. The modulation of different phases for nanomaterials demonstrates the great potential for tuning the properties of these nanomaterials. The actual phase transformation mechanism illustrated by *in situ* TEM will pave the way to efficiently modulate the phase and then the desired properties of nanomaterials for their widespread applications. Despite the great progress that has been made in *in situ* TEM for PEN over the past decades, there are still challenges to be overcome before the modulation is widely practiced.

1) *in situ* Mechanical technology for PEN

   First, even though the nanomechanical tests can be performed in TEM with real time recording, the load applied to the nanomaterials is still not stable considering the drift issue, especially for quantitative nanomechanical tests equipped with piezo-actuator and sensor. Second, it is still not real working space conditions, most of the phase transformations are driven by complicated external factors, such as oxidation effect by wet air, complicated loading rather than uniaxial or simple loading in *in situ* TEM. Third, some phase transformations occur at high speed, such as the displacive phase transformations. Therefore, the ultrafast TEM will be useful to clearly reveal the whole process.

2) *in situ* Heating technology for PEN

   First, accurate temperature measurement at the nanoscale is still challenging, making the actual phase transformation temperature inaccurate, especially when the effect of electron beam irradiation is taken into account. Second, heating alone is not sufficient for the real phase transformation. Coupling with other stimuli is still required.

3) *in situ* Electrical technology for PEN

   First, quantitative bias experiments play a vital role in uncovering the mechanism of phase transformation of nanomaterials. However, it is still challenging due to the small reaction volume. Considering the noise induced by the experimental environment, high performance equipment and shielding setups are desired. Second, high spatial resolution, localized measurements, and detailed information on electrical kinetics enable researchers to gain a deeper understanding of electrochemical processes. While these parameters are still difficult to be obtained in *in situ* TEM experiments.

4) *in situ* Gas technology for PEN

   First, the spatial resolution decreases significantly due to the scattering of gas molecules even at low gas pressure. Second, the maximum gas pressure for window type gas holder is 5 bar, which is still much lower compared with realistic conditions. Therefore, the balance between gas pressure and spatial resolution should be optimized by advanced MEMS or aperture design. Third, the temporal resolution needs to be improved for some fast reactions during several milliseconds or even nanoseconds.

5) *in situ* Liquid technology for PEN

   First, the balance between membrane thickness, flatness, and robustness of the view window should be optimized perhaps by a better choice of membrane materials. Second, the liquid volume loading of the liquid cell should be more precisely controlled to ensure the same liquid thickness, which will improve the repeatability of the *in situ* liquid experiments. Third, the conditions of *in situ* liquid experiments are still simple (multiple external fields need to be integrated) and moderate (electron beam or moderate heating initiated), which are far from laboratory conditions. Fourth, the side effects of the electron beam are more severe in *in situ* liquid experiments due to the interaction between the electron beam and the liquid molecules.

6) *in situ* Optical technology for PEN

   First, the *in situ* photoluminescence and cathodoluminescence are still desired for high quality data for *in situ* optical experiments. Second, high efficiency detection is very important for *in situ* optical experiments to reduce radiation damage from the electron beam. Third, combined with computational reconstruction techniques, 3D structural characterization can be realized and electron ptychography can achieve better contrast on light atoms.

7) *in situ* Magnetism technology for PEN

   First, higher spatial resolution is still desired to analyze the magnetic moment distribution among the sample, even at the atomic scale, which will facilitate the study of antiferromagnetic spintronics. Second, multifield *in situ* magnetism experiments are needed to study the transition mechanism of the magnetic domain under different external field stimuli.

As mentioned above, the most common challenges, include higher spatial and temporal resolution under different external fields, low frequency of the image acquisition system based on conventional charge-coupled device (20 frames/s), multi-field coupling in TEM, large differences between *in situ* TEM experiments compared to laboratory conditions, and electron beam irradiation effects. In fact, several advanced technologies have been proposed and realized to solve some of these problems. 4D ultrafast electron microscopy increases the temporal dimension based on the pump-probe scheme and can realize femtosecond/nanosecond temporal resolution, which can be used to visualize the temporal evolution of the changes in the specimen. Different from charge-coupled device, direct electron camera based on complementary metal-oxide semiconductor technology can significantly improve the collection efficiency (10^3 readout rates). Based on the direct electron camera technology, 4D STEM can obtain 2D real space and 2D reciprocal space data for each pixel with high spatial resolution and comparable temporal resolution to traditional STEM. We strongly believe that *in situ* TEM opens up broad prospects for investigating the actual atomic mechanisms underlying phase transformations. It also facilitates the development of strategies to modulate phase transformations in nanomaterials, aiming to achieve precise control over the desired property-oriented phase modulation. These advances hold great potential for a wide range of applications in nanomaterials.

Author information

Corresponding author

Yang Lu - Department of Mechanical Engineering, The University of Hong Kong, Pokfulam 999077, Hong Kong SAR, China. Email: ylu1@hku.hk

Authors

Ying Han - Department of Mechanical Engineering, City University of Hong Kong, Kowloon 999077, Hong Kong SAR, China

Liqiang Wang - Department of Mechanical Engineering, City University of Hong Kong, Kowloon 999077, Hong Kong SAR, China

Ke Cao - School of Advanced Materials and Nanotechnology, Xidian University, Xi’an 710071, China

Jingzhuo Zhou - Department of Mechanical Engineering, City University of Hong Kong, Kowloon 999077, Hong Kong SAR, China

Yingxin Zhu - Department of Mechanical Engineering, City University of Hong Kong, Kowloon 999077, Hong Kong SAR, China

Yuan Hou - Department of Mechanical Engineering, City University of Hong Kong, Kowloon 999077, Hong Kong SAR, China

Notes

The authors declare no competing financial interest.

Biographies

Ying Han is a postdoctoral scholar in the Department of Engineering Science and Mechanics at The Pennsylvania State University now. She received her B.S. degree from Tianjin University in 2017 and her Ph.D. degree under the supervision of Prof. Yang Lu from City University of Hong Kong in 2021. She focuses on *in situ* electron microscopy to provide revealing mechanistic insights into extreme materials.

Liqiang Wang is currently pursuing his Ph.D. degree under the supervision of Prof. Yang Lu at City University of Hong Kong. He received his B.S. degree from Hefei University of Technology in 2015 and his M.S. degree from Beihang University in 2018. His research interests are fabricating and understanding the extreme deformation behavior and their functional application of micro-/nanoscale high-entropy alloy mechanical metamaterials, as well as revealing their plastic deformation mechanism via *in situ* TEM techniques.

Ke Cao is an Associate Professor in School of Advanced Materials and Nanotechnology at Xidian University. He received his Ph.D. degree under the supervision of Prof. Yang Lu from City University of Hong Kong in 2019. He focuses on *in situ* electron microscopy study of the mechanical behavior of thin films and coatings.

Jingzhuo Zhou is currently pursuing his Ph.D. degree under the supervision of Prof. Yang Lu at City University of Hong Kong. He received his B.Eng. degree from Xi'an Jiaotong University in 2017 and his M.S. degree from Tsinghua University in 2020. His research focuses on the *in situ* nanomechanics of 2D materials and their elastic strain engineering.

Yingxin Zhu received his B.S. degree in Department of Mechanical Engineering from City University of Hong Kong. He is pursuing his Ph.D. degree in the Department of Engineering Science and Mechanics at The Pennsylvania State University now. His research involves elastic strain engineering.

Yuan Hou received his Ph.D. degree from the University of Science and Technology of China in 2021. He then worked as postdoc at the City University of Hong Kong during 2021−2023. Since May 2023, he has been working in the Max Planck Institute for Solid State Research as a postdoc researcher. His research interests focus on micro/nanomechanics, twisted 2D materials, ion intercalation, and *in situ* experiment.

Yang Lu is “HKU-100 Scholar” Professor in Mechanical Engineering at the University of Hong Kong. He received his B.S. degree in Physics from Nanjing University, Ph.D. degree in Mechanical Engineering from Rice University, and did his postdoctoral research in the Nanomechanics Lab at MIT. Previously he worked at City University of Hong Kong. Prof. Lu’s research focuses on experimental nanomechanics and nanomanufacturing, with recent focus in “deep elastic strain engineering” of low-dimensional (1D/2D) materials and mechanical metamaterials.

Acknowledgements

This work was supported by NSFC/RGC Joint Research Scheme (N_HKU159/22, Y.L.), Research Grants Council of the Hong Kong Special Administrative Region, China (grant RFS2021-1S05, Y.L.) and National Natural Science Foundation of China (grant No. 12202330, K.C.)

References

[1] Rao, C. N. R.; Cheetham, A. K. Science and Technology of Nanomaterials: Current Status and Future Prospects. *J. Mater. Chem* **2001,** *11*, 2887-2894.

[2] Liu, B.; Zhou, K. Recent Progress on Graphene-Analogous 2d Nanomaterials: Properties, Modeling and Applications. *Prog. Mater. Sci.* **2019,** *100*, 99-169.

[3] Roduner, E. Size Matters: Why Nanomaterials Are Different. *Chem. Soc. Rev.* **2006,** *35*, 583-592.

[4] Gleiter, H. Nanostructured Materials: Basic Concepts and Microstructure. *Acta Mater.* **2000,** *48*, 1-29.

[5] Li, J.; Shan, Z.; Ma, E. Elastic Strain Engineering for Unprecedented Materials Properties. *MRS Bull.* **2014,** *39*, 108-114.

[6] Han, Y.; Gao, L.; Zhou, J.; Hou, Y.; Jia, Y.; Cao, K.; Duan, K.; Lu, Y. Deep Elastic Strain Engineering of 2d Materials and Their Twisted Bilayers. *ACS Appl. Mater. Interfaces* **2022,** *14*, 8655-8663.

[7] Chen, Y.; Lai, Z.; Zhang, X.; Fan, Z.; He, Q.; Tan, C.; Zhang, H. Phase Engineering of Nanomaterials. *Nat. Rev. Chem.* **2020,** *4*, 243-256.

[8] Li, H.; Zhou, X.; Zhai, W.; Lu, S.; Liang, J.; He, Z.; Long, H.; Xiong, T.; Sun, H.; He, Q.; et al. Phase Engineering of Nanomaterials for Clean Energy and Catalytic Applications. *Adv. Energy Mater.* **2020,** *10*, 2002019.

[9] Huang, H.; Fan, X.; Singh, D. J.; Zheng, W. Recent Progress of Tmd Nanomaterials: Phase Transitions and Applications. *Nanoscale* **2020,** *12*, 1247-1268.

[10] Fan, Z.; Bosman, M.; Huang, X.; Huang, D.; Yu, Y.; Ong, K. P.; Akimov, Y. A.; Wu, L.; Li, B.; Wu, J. Stabilization of 4h Hexagonal Phase in Gold Nanoribbons. *Nat. Commun.* **2015,** *6*, 7684.

[11] Huang, X.; Li, S.; Huang, Y.; Wu, S.; Zhou, X.; Li, S.; Gan, C. L.; Boey, F.; Mirkin, C. A.; Zhang, H. Synthesis of Hexagonal Close-Packed Gold Nanostructures. *Nat. Commun.* **2011,** *2*, 292.

[12] He, Y.; He, Q.; Wang, L.; Zhu, C.; Golani, P.; Handoko, A. D.; Yu, X.; Gao, C.; Ding, M.; Wang, X.; et al. Self-Gating in Semiconductor Electrocatalysis. *Nat. Mater.* **2019,** *18*, 1098-1104.

[13] Fan, Z.; Bosman, M.; Huang, Z.; Chen, Y.; Ling, C.; Wu, L.; Akimov, Y. A.; Laskowski, R.; Chen, B.; Ercius, P. Heterophase Fcc-2h-Fcc Gold Nanorods. *Nat. Commun.* **2020,** *11*, 3293.

[14] Chakraborty, I.; Shirodkar, S. N.; Gohil, S.; Waghmare, U. V.; Ayyub, P. A Stable, Quasi-2d Modification of Silver: Optical, Electronic, Vibrational and Mechanical Properties, and First Principles Calculations. *J. Phys. Condens. Matter* **2013,** *26*, 025402.

[15] Mettela, G.; Boya, R.; Singh, D.; Pavan Kumar, G. V.; Kulkarni, G. U. Highly Tapered Pentagonal Bipyramidal Au Microcrystals with High Index Faceted Corrugation: Synthesis and Optical Properties. *Sci. Rep.* **2013,** *3*, 1793.

[16] Peng, S.; Meng, A. C.; Braun, M. R.; Marshall, A. F.; McIntyre, P. C. Plasmons and Inter-Band Transitions of Hexagonal Close Packed Gold Nanoparticles. *Appl. Phys. Lett.* **2019,** *115*, 051107.

[17] Zhou, M.; Higaki, T.; Hu, G.; Sfeir, M. Y.; Chen, Y.; Jiang, D.; Jin, R. Three-Orders-of-Magnitude Variation of Carrier Lifetimes with Crystal Phase of Gold Nanoclusters. *Science* **2019,** *364*, 279-282.

[18] Chen, Y.; Fan, Z.; Luo, Z.; Liu, X.; Lai, Z.; Li, B.; Zong, Y.; Gu, L.; Zhang, H. High-Yield Synthesis of Crystal-Phase-Heterostructured 4h/Fcc Au@ Pd Core-Shell Nanorods for Electrocatalytic Ethanol Oxidation. *Adv. Mater.* **2017,** *29*, 1701331.

[19] Moraes, D. A.; Junior, J. B. S.; Ferreira, F. F.; Mogili, N. V. V.; Varanda, L. C. Gold Nanowire Growth through Stacking Fault Mechanism by Oleylamine-Mediated Synthesis. *Nanoscale* **2020,** *12*, 13316-13329.

[20] Zhang, S.; Zhang, X.; Jiang, G.; Zhu, H.; Guo, S.; Su, D.; Lu, G.; Sun, S. Tuning Nanoparticle Structure and Surface Strain for Catalysis Optimization. *J. Am. Chem. Soc.* **2014,** *136*, 7734-7739.

[21] Li, Q.; Wu, L.; Wu, G.; Su, D.; Lv, H.; Zhang, S.; Zhu, W.; Casimir, A.; Zhu, H.; Mendoza-Garcia, A. New Approach to Fully Ordered Fct-Fept Nanoparticles for Much Enhanced Electrocatalysis in Acid. *Nano Lett.* **2015,** *15*, 2468-2473.

[22] Jani, J. M.; Leary, M.; Subic, A.; Gibson, M. A. A Review of Shape Memory Alloy Research, Applications and Opportunities. *Mater. & Des.* **2014,** *56*, 1078-1113.

[23] Kusada, K.; Kobayashi, H.; Yamamoto, T.; Matsumura, S.; Sumi, N.; Sato, K.; Nagaoka, K.; Kubota, Y.; Kitagawa, H. Discovery of Face-Centered-Cubic Ruthenium Nanoparticles: Facile Size-Controlled Synthesis Using the Chemical Reduction Method. *J. Am. Chem. Soc.* **2013,** *135*, 5493-5496.

[24] Zhao, M.; Xia, Y. Crystal-Phase and Surface-Structure Engineering of Ruthenium Nanocrystals. *Nat. Rev. Mater.* **2020,** *5*, 440-459.

[25] Lu, S.; Liang, J.; Long, H.; Li, H.; Zhou, X.; He, Z.; Chen, Y.; Sun, H.; Fan, Z.; Zhang, H. Crystal Phase Control of Gold Nanomaterials by Wet-Chemical Synthesis. *Accounts Chem. Res.* **2020,** *53*, 2106-2118.

[26] Cheng, H.; Yang, N.; Lu, Q.; Zhang, Z.; Zhang, H. Syntheses and Properties of Metal Nanomaterials with Novel Crystal Phases. *Adv. Mater.* **2018,** *30*, 1707189.

[27] Janssen, A.; Pawlik, V.; von Rueden, A. D.; Xu, L.; Wang, C.; Mavrikakis, M.; Xia, Y. Facile Synthesis of Palladium‐Based Nanocrystals with Different Crystal Phases and a Comparison of Their Catalytic Properties. *Adv. Mater.* **2021,** *33*, 2103801.

[28] Sow, C.; Suchithra, P.; Mettela, G.; Kulkarni, G. U. Noble Metal Nanomaterials with Nontraditional Crystal Structures. *Annu. Rev. Mater. Res.* **2020,** *50*, 345-370.

[29] Fan, Z.; Zhang, H. Crystal Phase-Controlled Synthesis, Properties and Applications of Noble Metal Nanomaterials. *Chem. Soc. Rev.* **2016,** *45*, 63-82.

[30] Liu, C.; Li, T.; Li, G.; Nobusada, K.; Zeng, C.; Pang, G.; Rosi, N. L.; Jin, R. Observation of Body‐Centered Cubic Gold Nanocluster. *Angew. Chem., Int. Ed.* **2015,** *127*, 9964-9967.

[31] Mettela, G.; Bhogra, M.; Waghmare, U. V.; Kulkarni, G. U. Ambient Stable Tetragonal and Orthorhombic Phases in Penta-Twinned Bipyramidal Au Microcrystals. *J. Am. Chem. Soc.* **2015,** *137*, 3024-3030.

[32] You, R.; Wu, Z.; Yu, J.; Wang, F.; Chen, S.; Han, Z.; Yuan, W.; Yang, H.; Wang, Y. Revealing Surface Restraint-Induced Hexagonal Pd Nanocrystals Via *in Situ* Transmission Electron Microscopy. *Nano Lett.* **2022,** *22*, 4333-4339.

[33] Li, S.; Olszta, M.; Li, L.; Gwalani, B.; Soulami, A.; Powell, C. A.; Mathaudhu, S.; Devaraj, A.; Wang, C. *In-Situ* Tem Observation of Shear Induced Microstructure Evolution in Cu-Nb Alloy. *Scr. Mater.* **2021,** *205*, 114214.

[34] Cheng, Q.; Wu, H.; Wang, Y.; Wang, X. Pseudoelasticity of Cu-Zr Nanowires Via Stress-Induced Martensitic Phase Transformations. *Appl. Phys. Lett.* **2009,** *95*, 021911.

[35] Tracy, C. L.; Park, S.; Rittman, D. R.; Zinkle, S. J.; Bei, H.; Lang, M.; Ewing, R. C.; Mao, W. L. High Pressure Synthesis of a Hexagonal Close-Packed Phase of the High-Entropy Alloy Crmnfeconi. *Nat. Commun.* **2017,** *8*, 15634.

[36] Youssef, K. M.; Zaddach, A. J.; Niu, C.; Irving, D. L.; Koch, C. C. A Novel Low-Density, High-Hardness, High-Entropy Alloy with Close-Packed Single-Phase Nanocrystalline Structures. *Mater. Res. Lett.* **2015,** *3*, 95-99.

[37] Takeuchi, A.; Amiya, K.; Wada, T.; Yubuta, K.; Zhang, W. High-Entropy Alloys with a Hexagonal Close-Packed Structure Designed by Equi-Atomic Alloy Strategy and Binary Phase Diagrams. *JOM* **2014,** *66*, 1984-1992.

[38] Feuerbacher, M.; Heidelmann, M.; Thomas, C. Hexagonal High-Entropy Alloys. *Mater. Res. Lett.* **2015,** *3*, 1-6.

[39] Ge, Y.; Shi, Z.; Tan, C.; Chen, Y.; Cheng, H.; He, Q.; Zhang, H. Two-Dimensional Nanomaterials with Unconventional Phases. *Chem* **2020,** *6*, 1237-1253.

[40] Li, W.; Qian, X.; Li, J. Phase Transitions in 2d Materials. *Nat. Rev. Mater.* **2021,** *6*, 829-846.

[41] Duerloo, K. A. N.; Li, Y.; Reed, E. J. Structural Phase Transitions in Two-Dimensional Mo- and W-Dichalcogenide Monolayers. *Nat. Commun.* **2014,** *5*, 4214.

[42] Yu, Y.; Nam, G.; He, Q.; Wu, X.; Zhang, K.; Yang, Z.; Chen, J.; Ma, Q.; Zhao, M.; Liu, Z.; et al. High Phase-Purity 1t′-Mos$_2$-and 1t′-Mose$_2$-Layered Crystals. *Nat. Chem.* **2018,** *10*, 638-643.

[43] Cho, S.; Kim, S.; Kim, J. H.; Zhao, J.; Seok, J.; Keum, D. H.; Baik, J.; Choe, D.-H.; Chang, K. J.; Suenaga, K.; et al. Phase Patterning for Ohmic Homojunction Contact in Mote$_2$. *Science* **2015,** *349*, 625-628.

[44] Wang, Y.; Xiao, J.; Zhu, H.; Li, Y.; Alsaid, Y.; Fong, K. Y.; Zhou, Y.; Wang, S.; Shi, W.; Wang, Y.; et al. Structural Phase Transition in Monolayer Mote$_2$ Driven by Electrostatic Doping. *Nature* **2017,** *550*, 487-491.

[45] Hou, W.; Azizimanesh, A.; Sewaket, A.; Peña, T.; Watson, C.; Liu, M.; Askari, H.; Wu, S. M. Strain-Based Room-Temperature Non-Volatile Mote$_2$ Ferroelectric Phase Change Transistor. *Nat. Nanotechnol.* **2019,** *14*, 668-673.

[46] Zhu, W.; Mao, S.; Wei, X. Finite Deformation Continuum Model for Mechanically Induced Phase Transition in Transition Metal Dichalcogenide Monolayers. *J. Mech. Phys. Solids* **2022,** *166*, 104955.

[47] Keum, D. H.; Cho, S.; Kim, J. H.; Choe, D.; Sung, H.-J.; Kan, M.; Kang, H.; Hwang, J.; Kim, S. W.; Yang, H.; et al. Bandgap Opening in Few-Layered Monoclinic Mote$_2$. *Nat. Phys.* **2015,** *11*, 482-486.

[48] Kim, C.; Issarapanacheewin, S.; Moon, I.; Lee, K. Y.; Ra, C.; Lee, S.; Yang, Z.; Yoo, W. J. High-Electric-Field-Induced Phase Transition and Electrical Breakdown of Mote$_2$. *Adv. Electron. Mater.* **2020,** *6*, 1900964.

[49] Ma, Y.; Liu, B.; Zhang, A.; Chen, L.; Fathi, M.; Shen, C.; Abbas, A. N.; Ge, M.; Mecklenburg, M.; Zhou, C. Reversible Semiconducting-to-Metallic Phase Transition in Chemical Vapor Deposition Grown Monolayer Wse$_2$ and Applications for Devices. *ACS Nano* **2015,** *9*, 7383-7391.

[50] Scalise, E.; Houssa, M.; Pourtois, G.; Afanas'ev, V.; Stesmans, A. Strain-Induced Semiconductor to Metal Transition in the Two-Dimensional Honeycomb Structure of Mos$_2$. *Nano Res.* **2012,** *5*, 43-48.

[51] Yin, X.; Tang, C. S.; Zheng, Y.; Gao, J.; Wu, J.; Zhang, H.; Chhowalla, M.; Chen, W.; Wee, A. T. S. Recent Developments in 2d Transition Metal Dichalcogenides: Phase Transition and Applications of the (Quasi-)Metallic Phases. *Chem. Soc. Rev.* **2021,** *50*, 10087-10115.

[52] Xu, C.; Zou, R.; Peng, Y.; Liu, Q.; Ruan, S.; Hu, J. *In Situ* Transmission Electron Microscope Studies on One-Dimensional Nanomaterials: Manipulation, Properties and Applications. *Prog. Mater. Sci.* **2020,** *113*, 100674.

[53] Xu, T.; Sun, L. Dynamic *in-Situ* Experimentation on Nanomaterials at the Atomic Scale. *Small* **2015,** *11*, 3247-3262.

[54] McDowell, M. T.; Lu, Z.; Koski, K. J.; Yu, J. H.; Zheng, G.; Cui, Y. *In Situ* Observation of Divergent Phase Transformations in Individual Sulfide Nanocrystals. *Nano Lett.* **2015,** *15*, 1264-1271.

[55] Legros, M.; Gianola, D. S.; Motz, C. Quantitative *in Situ* Mechanical Testing in Electron Microscopes. *MRS Bull.* **2010,** *35*, 354-360.

[56] Yu, Q.; Legros, M.; Minor, A. *In Situ* Tem Nanomechanics. *MRS Bull.* **2015,** *40*, 62-70.

[57] Wang, L.; Zhang, Z.; Han, X. *In Situ* Experimental Mechanics of Nanomaterials at the Atomic Scale. *NPG Asia Mater.* **2013,** *5*, e40.

[58] Lu, Y.; Lou, J. Quantitative *in-Situ* Nanomechanical Characterization of Metallic Nanowires. *JOM* **2011,** *63*, 35-42.

[59] Zhu, Y. *In Situ* Nanomechanical Testing of Crystalline Nanowires in Electron Microscopes. *JOM* **2016,** *68*, 84-93.

[60] Chen, Y.; An, X.; Liao, X. Mechanical Behaviors of Nanowires. *Applied Physics Reviews* **2017,** *4*, 031104.

[61] Wang, S.; Shan, Z.; Huang, H. The Mechanical Properties of Nanowires. *Adv. Sci.* **2017,** *4*, 1600332.

[62] Guinier, A.; Bokij, G. B.; Boll-Dornberger, K.; Cowley, J. M.; urovič, S.; Cox, D. E.; Jagodzinski, H.; Krishna, P.; De Wolff, P. M.; Zvyagin, B. B.; et al. Nomenclature of Polytype Structures. Report of the International Union

of Crystallography Ad Hoc Committee on the Nomenclature of Disordered, Modulated and Polytype Structures. *Acta Crystallogr. A* **1984,** *40*, 399-404.

[63] Yoshida, M.; Onodera, A.; Ueno, M.; Takemura, K.; Shimomura, O. Pressure-Induced Phase Transition in Sic. *Phys. Rev. B* **1993,** *48*, 10587.

[64] Hirsch, A. The Era of Carbon Allotropes. *Nat. Mater.* **2010,** *9*, 868-871.

[65] Park, C. H.; Cheong, B.; Lee, K.; Chang, K. J. Structural and Electronic Properties of Cubic, 2h, 4h, and 6h Sic. *Phys. Rev. B* **1994,** *49*, 4485.

[66] Tan, T.; Zhang, S.; Wang, J.; Zheng, Y.; Lai, H.; Liu, J.; Qin, F.; Wang, C. Resolving the Stacking Fault Structure of Silver Nanoplates. *Nanoscale* **2021,** *13*, 195-205.

[67] Guo, Q.; Zhao, Y.; Mao, W. L.; Wang, Z.; Xiong, Y.; Xia, Y. Cubic to Tetragonal Phase Transformation in Cold-Compressed Pd Nanocubes. *Nano Lett.* **2008,** *8*, 972-975.

[68] Sun, Y.; Ren, Y.; Liu, Y.; Wen, J.; Okasinski, J. S.; Miller, D. J. Ambient-Stable Tetragonal Phase in Silver Nanostructures. *Nat. Commun.* **2012,** *3*, 971.

[69] Gu, L.; Meng, A.; Chen, X.; Zhao, Y. Simultaneously Enhancing Strength and Ductility of Hcp Titanium Via Multi-Modal Grain Induced Extra <C+a> Dislocation Hardening. *Acta Mater.* **2023,** *252*, 118949.

[70] Kowbel, W.; Gao, F.; Withers, J. C. Enhanced Thermal Conductivity of Cvd Sic Via Beryllium and Boron Dopings. *Mater. Res. Soc. Symp. Proc.* **1994,** *337-342*.

[71] Lee, M.; Yang, M.; Song, K. M.; Park, S. Ingan/Gan Blue Light Emitting Diodes Using Freestanding Gan Extracted from a Si Substrate. *ACS Photonics* **2018,** *5*, 1453-1459.

[72] Fan, Z.; Zhang, H. Template Synthesis of Noble Metal Nanocrystals with Unusual Crystal Structures and Their Catalytic Applications. *Accounts Chem. Res.* **2016,** *49*, 2841-2850.

[73] Rao, S.; Mallemace, E. D.; Cocorullo, G.; Faggio, G.; Messina, G.; Della Corte, F. G. Temperature Dependence of the Thermo-Optic Coefficient in 4h-Sic and Gan Slabs at the Wavelength of 1550 Nm. *Sci. Rep.* **2022,** *12*, 4809.

[74] Nassereddine, A.; Wang, Q.; Loffreda, D.; Ricolleau, C.; Alloyeau, D.; Louis, C.; Delannoy, L.; Nelayah, J.; Guesmi, H. Revealing Size Dependent Structural Transitions in Supported Gold Nanoparticles in Hydrogen at Atmospheric Pressure. *Small* **2021,** *17*, 2104571.

[75] Li, P.; Han, Y.; Zhou, X.; Fan, Z.; Xu, S.; Cao, K.; Meng, F.; Gao, L.; Song, J.; Zhang, H.; et al. Thermal Effect and Rayleigh Instability of Ultrathin 4h Hexagonal Gold Nanoribbons. *Matter* **2020,** *2*, 658-665.

[76] Xie, X.; Sun, L.; Chen, X.; Yang, X.; Hu, X.; Xu, X. Sublimation Growth and Property Characterization of P-Type 4h-Sic by Al-B Co-Doping Technique. *Scr. Mater.* **2019,** *167*, 76-80.

[77] He, L.; Polsin, D.; Zhang, S.; Collins, G. W.; Abdolrahim, N. Phase Transformation Path in Aluminum under Ramp Compression; Simulation and Experimental Study. *Sci. Rep.* **2022,** *12*, 18954.

[78] Zhang, H.; Wei, B.; Ou, X.; Ni, S.; Yan, H.; Song, M. Atomic-Scale Understanding of the Reversible Hcp↔Fcc Phase Transition Mechanisms at {101¯1} Twin Tip in Pure Titanium. *Int. J. Plast.* **2022,** *156*, 103357.

[79] Manna, I.; Chattopadhyay, P.; Banhart, F.; Fecht, H. Formation of Face-Centered-Cubic Zirconium by Mechanical Attrition. *Appl. Phys. Lett.* **2002,** *81*, 4136-4138.

[80] Ram, S. Allotropic Phase Transformations in Hcp, Fcc and Bcc Metastable Structures in Co-Nanoparticles. *Mater. Sci. Eng. A* **2001,** *304*, 923-927.

[81] Fan, Z.; Huang, X.; Han, Y.; Bosman, M.; Wang, Q.; Zhu, Y.; Liu, Q.; Li, B.; Zeng, Z.; Wu, J.; et al. Surface Modification-Induced Phase Transformation of Hexagonal Close-Packed Gold Square Sheets. *Nat. Commun.* **2015,** *6*, 6571.

[82] Zhang, H.; Ou, X.; Wei, B.; Ni, S.; Song, M. Strain Direction Dependency of Deformation Mechanisms in an Hcp-Ti Crystalline by Molecular Dynamics Simulations. *Comput. Mater. Sci.* **2020,** *172*, 109328.

[83] Chen, Q.; Cheng, T.; Fu, H.; Zhu, Y. Crystal Phase Regulation in Noble Metal Nanocrystals. *Chinese J. Catal.* **2019,** *40*, 1035-1056.

[84] Lai, W.; Vogel, F.; Zhao, X.; Wang, B.; Yi, Y.; You, D.; Tong, X.; Li, W.; Yu, X.; Wang, X. Design of Bcc Refractory Multi-Principal Element Alloys with Superior Mechanical Properties. *Mater. Res. Lett.* **2022,** *10*, 133-140.

[85] Mak, E.; Yin, B.; Curtin, W. A Ductility Criterion for Bcc High Entropy Alloys. *J. Mech. Phys. Solids* **2021,** *152*, 104389.

[86] Parakh, A.; Vaidya, M.; Kumar, N.; Chetty, R.; Murty, B. S. Effect of Crystal Structure and Grain Size on Corrosion Properties of Alcocrfeni High Entropy Alloy. *J. Alloy. Compd.* **2021,** *863*, 158056.

[87] Zidane, M.; Salmani, E. M.; Majumdar, A.; Syad, B. A.; Ez-Zahraouy, H.; Benyoussef, A.; Ahuja, R. Determination and Comparison of the Electrical and Thermal Transport Properties of Bcc and Fcc Fe-Ni Based Ternary Alloys in the Earth's Inner Core. *J. Earth Syst. Sci.* **2022,** *131*, 221.

[88] Wang, C.; Chen, D. P.; Sang, X.; Unocic, R. R.; Skrabalak, S. E. Size-Dependent Disorder-Order Transformation in the Synthesis of Monodisperse Intermetallic Pdcu Nanocatalysts. *ACS Nano* **2016,** *10*, 6345-6353.

[89] Marakatti, V. S.; Sarma, S. C.; Joseph, B.; Banerjee, D.; Peter, S. C. Synthetically Tuned Atomic Ordering in Pdcu Nanoparticles with Enhanced Catalytic Activity toward Solvent-Free Benzylamine Oxidation. *ACS Appl. Mater. Interfaces* **2017,** *9*, 3602-3615.

[90] Yang, P.; Li, Q.; Tsuru, T.; Ogata, S.; Zhang, J.; Sheng, H.; Shan, Z.; Sha, G.; Han, W.; Li, J. Mechanism of Hardening and Damage Initiation in Oxygen Embrittlement of Body-Centred-Cubic Niobium. *Acta Mater.* **2019,** *168*, 331-342.

[91] Bancroft, D.; Peterson, E. L.; Minshall, S. Polymorphism of Iron at High Pressure. *J. Appl. Phys.* **1956,** *27*, 291-298.

[92] Yang, W.; Luo, J.; Fu, H.; Cheung, C. F.; Ruan, H.; Yang, X.-S. Bcc→Hcp Phase Transition Significantly Enhancing the Wear Resistance of Metastable Refractory High-Entropy Alloy. *Scr. Mater.* **2022,** *221*, 114966.

[93] Wang, S. J.; Wang, H.; Du, K.; Zhang, W.; Sui, M. L.; Mao, S. X. Deformation-Induced Structural Transition in Body-Centred Cubic Molybdenum. *Nat. Commun.* **2014,** *5*, 3433.

[94] Hasegawa, T.; Niibori, T.; Takemasa, Y.; Oikawa, M. Stabilisation of Tetragonal Feco Structure with High Magnetic Anisotropy by the Addition of V and N Elements. *Sci. Rep.* **2019,** *9*, 5248.

[95] Wilson, J. A.; Yoffe, A. The Transition Metal Dichalcogenides Discussion and Interpretation of the Observed Optical, Electrical and Structural Properties. *Adv. Phys.* **1969,** *18*, 193-335.

[96] Xia, F.; Wang, H.; Xiao, D.; Dubey, M.; Ramasubramaniam, A. Two-Dimensional Material Nanophotonics. *Nat. Photonics* **2014,** *8*, 899-907.

[97] Py, M. A.; Haering, R. R. Structural Destabilization Induced by Lithium Intercalation in Mos_2 and Related Compounds. *Can. J. Phys.* **1983,** *61*, 76-84.

[98] Duerloo, K. A. N.; Li, Y.; Reed, E. J. Structural Phase Transitions in Two-Dimensional Mo-and W-Dichalcogenide Monolayers. *Nat. Commun.* **2014,** *5*, 4214.

[99] Lin, Y. C.; Dumcenco, D. O.; Huang, Y. S.; Suenaga, K. Atomic Mechanism of the Semiconducting-to-Metallic Phase Transition in Single-Layered Mos_2. *Nat. Nanotechnol.* **2014,** *9*, 391-396.

[100] Wang, L.; Xu, Z.; Wang, W.; Bai, X. Atomic Mechanism of Dynamic Electrochemical Lithiation Processes of Mos_2 Nanosheets. *J. Am. Chem. Soc.* **2014,** *136*, 6693-6697.

[101] Skriver, H. L. Crystal Structure from One-Electron Theory. *Phys. Rev. B* **1985,** *31*, 1909.

[102] Duthie, J. C.; Pettifor, D. G. Correlation between D-Band Occupancy and Crystal Structure in the Rare Earths. *Phys. Rev. Lett.* **1977,** *38*, 564.

[103] Pettifor, D. G. Theory of the Crystal Structures of Transition Metals. *J. Phys. C: Solid State Phys.* **1970,** *3*, 367.

[104] Söderlind, P.; Ahuja, R.; Eriksson, O.; Wills, J. M.; Johansson, B. Crystal Structure and Elastic-Constant Anomalies in the Magnetic 3d Transition Metals. *Phys. Rev. B* **1994,** *50*, 5918.

[105] Massalski, T. B.; Laughlin, D. E. The Surprising Role of Magnetism on the Phase Stability of Fe (Ferro). *Calphad* **2009,** *33*, 3-7.

[106] Frenkel, D.; Smit, B., *Understanding Molecular Simulation: From Algorithms to Applications*. Elsevier: 2001; Vol. 1.

[107] Plimpton, S. Fast Parallel Algorithms for Short-Range Molecular Dynamics. *J. Comput. Phys.* **1995,** *117*, 1-19.

[108] Becker, C. A.; Tavazza, F.; Trautt, Z. T.; Buarque de Macedo, R. A. Considerations for Choosing and Using Force Fields and Interatomic Potentials in Materials Science and Engineering. *Curr. Opin. Solid State Mater. Sci.* **2013,** *17*, 277-283.

[109] Payne, M. C.; Teter, M. P.; Allan, D. C.; Arias, T. A.; Joannopoulos, J. D. Iterative Minimization Techniques for Ab Initio Total-Energy Calculations: Molecular Dynamics and Conjugate Gradients. *Rev. Mod. Phys.* **1992,** *64*, 1045.

[110] Bockstedte, M.; Kley, A.; Neugebauer, J.; Scheffler, M. Density-Functional Theory Calculations for Poly-Atomic Systems: Electronic Structure, Static and Elastic Properties and Ab Initio Molecular Dynamics. *Comput. Phys. Commun.* **1997,** *107*, 187-222.

[111] Koski, K. J.; Kamp, N. M.; Smith, R. K.; Kunz, M.; Knight, J. K.; Alivisatos, A. P. Structural Distortions in 5-10 Nm Silver Nanoparticles under High Pressure. *Phys. Rev. B* **2008,** *78*, 165410.

[112] Li, Q.; Niu, W.; Liu, X.; Chen, Y.; Wu, X.; Wen, X.; Wang, Z.; Zhang, H.; Quan, Z. Pressure-Induced Phase Engineering of Gold Nanostructures. *J. Am. Chem. Soc.* **2018,** *140*, 15783-15790.

[113] Kotmool, K.; Li, B.; Chakraborty, S.; Bovornratanaraks, T.; Luo, W.; Mao, H.; Ahuja, R. High Pressure-Induced Distortion in Face-Centered Cubic Phase of Thallium. *Proc. Natl. Acad. Sci.* **2016,** *113*, 11143-11147.

[114] Guo, Q.; Zhao, Y.; Wang, Z.; Skrabalak, S. E.; Lin, Z.; Xia, Y. Size Dependence of Cubic to Trigonal Structural Distortion in Silver Micro-and Nanocrystals under High Pressure. *J. Phys. Chem. C* **2008,** *112*, 20135-20137.

[115] Sun, Y.; Yang, W.; Ren, Y.; Wang, L.; Lei, C. Multiple-Step Phase Transformation in Silver Nanoplates under High Pressure. *Small* **2011,** *7*, 606-611.

[116] Lizárraga, R.; Pan, F.; Bergqvist, L.; Holmström, E.; Gercsi, Z.; Vitos, L. First Principles Theory of the *Hcp-Fcc* Phase Transition in Cobalt. *Sci. Rep.* **2017,** *7*, 3778.

[117] Abrikosov, I. A.; Ponomareva, A. V.; Nikonov, A. Y.; Zharmukhambetova, A. M.; Mosyagin, I. Y.; Lugovskoy, A. V.; Hellman, O.; Lind, H.; Dmitriev, A. I.; Barannikova, S. A. Theoretical Description of Pressure-Induced Phase Transitions: A Case Study of Ti-V Alloys. *High Press. Res.* **2015,** *35*, 42-48.

[118] Inoue, T.; Wang, Z. Coupling between Stress, Temperature, and Metallic Structures During Processes Involving Phase Transformations. *Mater. Sci. Technol.* **1985,** *1*, 845-850.

[119] Fernandes, F. M. B.; Denis, S.; Simon, A. Mathematical Model Coupling Phase Transformation and Temperature Evolution During Quenching of Steels. *Mater. Sci. Technol.* **1985,** *1*, 838-844.

[120] Gilbert, B.; Zhang, H.; Huang, F.; Finnegan, M. P.; Waychunas, G. A.; Banfield, J. F. Special Phase Transformation and Crystal Growth Pathways Observed in Nanoparticles. *Geochem. Trans.* **2003,** *4*, 20-27.

[121] Chung, S. Y.; Kim, Y. M.; Kim, J. G.; Kim, Y. J. Multiphase Transformation and Ostwald's Rule of Stages During Crystallization of a Metal Phosphate. *Nat. Phys.* **2009,** *5*, 68-73.

[122] Titmuss, S.; Wander, A.; King, D. A. Reconstruction of Clean and Adsorbate-Covered Metal Surfaces. *Chem. Rev.* **1996,** *96*, 1291-1306.

[123] McHale, J. M.; Auroux, A.; Perrotta, A. J.; Navrotsky, A. Surface Energies and Thermodynamic Phase Stability in Nanocrystalline Aluminas. *Science* **1997,** *277*, 788-791.

[124] Zhang, H.; Banfield, J. Thermodynamic Analysis of Phase Stability of Nanocrystalline Titania. *J. Mater. Chem* **1998,** *8*, 2073-2076.

[125] Djurado, E.; Bouvier, P.; Lucazeau, G. Crystallite Size Effect on the Tetragonal-Monoclinic Transition of Undoped Nanocrystalline Zirconia Studied by Xrd and Raman Spectrometry. *J. Solid State Chem.* **2000,** *149*, 399-407.

[126] Goldstein, A. N.; Echer, C. M.; Alivisatos, A. P. Melting in Semiconductor Nanocrystals. *Science* **1992,** *256*, 1425-1427.

[127] Qadri, S. B.; Skelton, E. F.; Hsu, D.; Dinsmore, A. D.; Yang, J.; Gray, H. F.; Ratna, B. R. Size-Induced Transition-Temperature Reduction in Nanoparticles of Zns. *Phys. Rev. B* **1999,** *60*, 9191.

[128] Jiang, J. Z.; Olsen, J. S.; Gerward, L.; Mørup, S. Enhanced Bulk Modulus and Reduced Transition Pressure in Γ-Fe_2o_3 Nanocrystals. *EPL (Europhysics Letters)* **1998,** *44*, 620.

[129] Qadri, S. B.; Skelton, E. F.; Dinsmore, A. D.; Hu, J. Z.; Kim, W. J.; Nelson, C.; Ratna, B. R. The Effect of Particle Size on the Structural Transitions in Zinc Sulfide. *J. Appl. Phys.* **2001,** *89*, 115-119.

[130] Banfield, J. F.; Zhang, H. Nanoparticles in the Environment. *Rev. Mineral. Geochem.* **2001,** *44*, 1-58.

[131] Uchic, M. D.; Dimiduk, D. M.; Florando, J. N.; Nix, W. D. Sample Dimensions Influence Strength and Crystal Plasticity. *Science* **2004,** *305*, 986-989.

[132] Cammarata, R. C. Surface and Interface Stress Effects in Thin Films. *Prog. Surf. Sci.* **1994,** *46*, 1-38.

[133] Liang, W.; Zhou, M. Pseudoelasticity of Single Crystalline Cu Nanowires through Reversible Lattice Reorientations. *J. Eng. Mater. Technol.* **2005,** *127*, 423-433.

[134] Liang, W.; Zhou, M. Atomistic Simulations Reveal Shape Memory of Fcc Metal Nanowires. *Phys. Rev. B* **2006,** *73*, 115409.

[135] Diao, J.; Gall, K.; Dunn, M. L. Surface Stress Driven Reorientation of Gold Nanowires. *Phys. Rev. B* **2004,** *70*, 075413.

[136] Gall, K.; Diao, J.; Dunn, M. L.; Haftel, M.; Bernstein, N.; Mehl, M. J. Tetragonal Phase Transformation in Gold Nanowires. *J. Eng. Mater. Technol.* **2005,** *127*, 417-422.

[137] Gumbsch, P.; Daw, M. S. Interface Stresses and Their Effects on the Elastic Moduli of Metallic Multilayers. *Phys. Rev. B* **1991,** *44*, 3934.

[138] Diao, J.; Gall, K.; Dunn, M. L. Surface-Stress-Induced Phase Transformation in Metal Nanowires. *Nat. Mater.* **2003,** *2*, 656-660.

[139] Delogu, F. Numerical Investigation of the Cubic-to-Tetragonal Phase Transition in Ag Nanorods. *J. Phys. Chem. C* **2010,** *114*, 3364-3370.

[140] Park, H. S.; Gall, K.; Zimmerman, J. A. Shape Memory and Pseudoelasticity in Metal Nanowires. *Phys. Rev. Lett.* **2005,** *95*, 255504.

[141] Liang, W.; Zhou, M.; Ke, F. Shape Memory Effect in Cu Nanowires. *Nano Lett.* **2005,** *5*, 2039-2043.

[142] Liang, W.; Srolovitz, D. J.; Zhou, M. A Micromechanical Continuum Model for the Tensile Behavior of Shape Memory Metal Nanowires. *J. Mech. Phys. Solids* **2007,** *55*, 1729-1761.

[143] Li, S.; Ding, X.; Li, J.; Ren, X.; Sun, J.; Ma, E. High-Efficiency Mechanical Energy Storage and Retrieval Using Interfaces in Nanowires. *Nano Lett.* **2010,** *10*, 1774-1779.

[144] Sandoval, L.; Urbassek, H. M. Finite-Size Effects in Fe-Nanowire Solid-Solid Phase Transitions: A Molecular Dynamics Approach. *Nano Lett.* **2009,** *9*, 2290-2294.

[145] Cao, A. Shape Memory Effects and Pseudoelasticity in Bcc Metallic Nanowires. *J. Appl. Phys.* **2010,** *108*, 113531.

[146] Li, S.; Ding, X.; Deng, J.; Lookman, T.; Li, J.; Ren, X.; Sun, J.; Saxena, A. Superelasticity in Bcc Nanowires by a Reversible Twinning Mechanism. *Phys. Rev. B* **2010,** *82*, 205435.

[147] Li, S.; Ding, X.; Li, J.; Ren, X.; Sun, J.; Ma, E.; Lookman, T. Inverse Martensitic Transformation in Zr Nanowires. *Phys. Rev. B* **2010,** *81*, 245433.

[148] Sutrakar, V. K.; Mahapatra, D. R. Size and Temperature Dependent Stability and Phase Transformation in Single-Crystal Zirconium Nanowire. *J. Nanopart. Res.* **2011,** *13*, 5335-5346.

[149] Abdolrahim, N.; Mastorakos, I.; Zbib, H. M. Deformation Mechanisms and Pseudoelastic Behaviors in Trilayer Composite Metal Nanowires. *Phys. Rev. B* **2010,** *81*, 054117.

[150] Sutrakar, V. K.; Mahapatra, D. R. Coupled Effect of Size, Strain Rate, and Temperature on the Shape Memory of a Pentagonal Cu Nanowire. *Nanotechnol.* **2008,** *20*, 045701.

[151] Sutrakar, V. K.; Mahapatra, D. R. Single and Multi-Step Phase Transformation in Cuzr Nanowire under Compressive/Tensile Loading. *Intermetallics* **2010,** *18*, 679-687.

[152] Sutrakar, V. K.; Mahapatra, D. R. Asymmetry in Structural and Thermo-Mechanical Behavior of Intermetallic Nial Nanowire under Tensile/Compressive Loading: A Molecular Dynamics Study. *Intermetallics* **2010,** *18*, 1565-1571.

[153] Saitoh, K.-i.; Liu, W. K. Molecular Dynamics Study of Surface Effect on Martensitic Cubic-to-Tetragonal Transformation in Ni-Al Alloy. *Comput. Mater. Sci.* **2009,** *46*, 531-544.

[154] Kulkarni, A. J.; Zhou, M.; Sarasamak, K.; Limpijumnong, S. Novel Phase Transformation in Zno Nanowires under Tensile Loading. *Phys. Rev. Lett.* **2006,** *97*, 105502.

[155] Wang, J.; Kulkarni, A.; Ke, F.; Bai, Y.; Zhou, M. Novel Mechanical Behavior of Zno Nanorods. *Comput. Methods Appl. Mech. Eng.* **2008,** *197*, 3182-3189.

[156] Wang, J.; Kulkarni, A. J.; Sarasamak, K.; Limpijumnong, S.; Ke, F. J.; Zhou, M. Molecular Dynamics and Density Functional Studies of a Body-Centered-Tetragonal Polymorph of Zno. *Phys. Rev. B* **2007,** *76*, 172103.

[157] Jung, K.; Cho, M.; Zhou, M. Thermal and Mechanical Response of [0001]-Oriented Gan Nanowires During Tensile Loading and Unloading. *J. Appl. Phys.* **2012,** *112*, 083522.

[158] Hasmy, A.; Medina, E. Thickness Induced Structural Transition in Suspended Fcc Metal Nanofilms. *Phys. Rev. Lett.* **2002,** *88*, 096103.

[159] Kondo, Y.; Ru, Q.; Takayanagi, K. Thickness Induced Structural Phase Transition of Gold Nanofilm. *Phys. Rev. Lett.* **1999,** *82*, 751.

[160] Kondo, Y.; Takayanagi, K. Gold Nanobridge Stabilized by Surface Structure. *Phys. Rev. Lett.* **1997,** *79*, 3455.

[161] Zheng, H.; Cao, A.; Weinberger, C. R.; Huang, J. Y.; Du, K.; Wang, J.; Ma, Y.; Xia, Y.; Mao, S. X. Discrete Plasticity in Sub-10-Nm-Sized Gold Crystals. *Nat. Commun.* **2010,** *1*, 144.

[162] Sutrakar, V. K.; Roy Mahapatra, D. Universal Stability and Temperature Dependent Phase Transformation in Group Viiib-Ib Transition Metal Fcc Nanowires. *J. Phys. Chem. C* **2011,** *115*, 10394-10398.

[163] Huang, X.; Li, S.; Wu, S.; Huang, Y.; Boey, F.; Gan, C. L.; Zhang, H. Graphene Oxide-Templated Synthesis of Ultrathin or Tadpole-Shaped Au Nanowires with Alternating *Hcp* and *Fcc* Domains. *Adv. Mater.* **2012,** *24*, 979-983.

[164] Sun, Q. P.; Hwang, K. C. Micromechanics Modelling for the Constitutive Behavior of Polycrystalline Shape Memory Alloys—I. Derivation of General Relations. *J. Mech. Phys. Solids* **1993,** *41*, 1-17.

[165] Zhang, M.-X.; Kelly, P. M. Crystallographic Features of Phase Transformations in Solids. *Prog. Mater. Sci.* **2009,** *54*, 1101-1170.

[166] Han, H. N.; Lee, C. G.; Oh, C. S.; Lee, T. H.; Kim, S. J. A Model for Deformation Behavior and Mechanically Induced Martensitic Transformation of Metastable Austenitic Steel. *Acta Mater.* **2004,** *52*, 5203-5214.

[167] Holzweissig, M. J.; Canadinc, D.; Maier, H. J. Computation of Parent Austenite Grain Orientation from Product Grain Orientations Upon Displacive Phase Transformations. *Model. Simul. Mat. Sci. Eng.* **2013,** *21*, 085009.

[168] Liu, H. A Simplified Relationship between the Modified O-Lattice and the Rotation Matrix for Generating the Coincidence Site Lattice of an Arbitrary Bravais Lattice System. *Acta Crystallogr. A* **2022,** *78*, 139-148.

[169] Kurdjumow, G.; Sachs, G. Über Den Mechanismus Der Stahlhärtung. *Zeitschrift für Physik* **1930,** *64*, 325-343.

[170] Nishiyama, Z. X-Ray Investigation of the Mechanism of the Transformation from Face Centered Cubic Lattice to Body Centered Cubic. *Sci. Rep. Tohoku Univ.* **1934,** *23*, 637.

[171] Eshelby, J. D. The Determination of the Elastic Field of an Ellipsoidal Inclusion, and Related Problems. *Proc. R. Soc. A: Math. Phys. Eng. Sci.* **1957,** *241*, 376-396.

[172] Eshelby, J. D. The Elastic Field Outside an Ellipsoidal Inclusion. *Proc. R. Soc. A: Math. Phys. Eng. Sci.* **1959,** *252*, 561-569.

[173] Olson GB, C. M., Dislocation Theory of Martensitic Transformations. In *Dislocations in Solids*, FRN, N., Ed. North-Holland Pub. Co: Amesterdam (NY), 1986; p 295.

[174] Cayron, C. Continuous Atomic Displacements and Lattice Distortion During Fcc–Bcc Martensitic Transformation. *Acta Mater.* **2015,** *96*, 189-202.

[175] Yang, X. S.; Sun, S.; Zhang, T. Y. The Mechanism of *Bcc A′* Nucleation in Single *Hcp E* Laths in the *Fcc Γ*→ *Hcp E*→ *Bcc A′* Martensitic Phase Transformation. *Acta Mater.* **2015,** *95*, 264-273.

[176] Pond, R. e. a., In *Dislocations in Solids*, Nabarro FRN, H. J., Ed. Amsterdam: North-Holland, 2007; p 225.

[177] Dahmen, U. The Role of the Invariant Line in the Search for an Optimum Interphase Boundary by O-Lattice Theory. *Scr. Mater.* **1980,** *15*, 77-81.

[178] Dahmen, U.; Ferguson, P.; Westmacott, K. Invariant Line Strain and Needle-Precipitate Growth Directions in Fe-Cu. *Acta Metall.* **1984,** *32*, 803-810.

[179] Dahmen, U. Orientation Relationships in Precipitation Systems. *Acta Metall.* **1982,** *30*, 63-73.

[180] Luo, C. P.; Weatherly, G. C. The Invariant Line and Precipitation in a Ni-45 Wt% Cr Alloy. *Acta Metall.* **1987,** *35*, 1963-1972.

[181] Luo, C. P.; Dahmen, U.; Westmacott, K. H. Morphology and Crystallography of Cr Precipitates in a Cu-0.33 Wt% Cr Alloy. *Acta Metall. Mater.* **1994,** *42*, 1923-1932.

[182] Luo, C. P.; Dahmen, U. Interface Structure of Faceted Lath-Shaped Cr Precipitates in a Cu-0.33 Wt% Cr Alloy. *Acta Mater.* **1998,** *46*, 2063-2081.

[183] Hall, M.; Aaronson, H. Réunion De La Société Royale De Microscopie Electronique. *Surf Sci* **1972,** *31*, 257.

[184] Rigsbee, J. M.; Aaronson, H. I. A Computer Modeling Study of Partially Coherent Fcc: Bcc Boundaries. *Acta Metall.* **1979,** *27*, 351-363.

[185] Zhou, D. S.; Shiflet, G. J. Interfacial Steps and Growth Mechanism in Ferrous Pearlites. *Metall. Mater. Trans. A* **1991,** *22*, 1349-1365.

[186] Howe, J. M.; Smith, D. A. Comparison between the Invariant Line and Structural Ledge Theories for Predicting the Habit Plane, Orientation Relationship and Interphase Boundary Structure of Plate-Shaped Precipitates. *Acta Metall. Mater.* **1992,** *40*, 2343-2350.

[187] Zhang, W. Z.; Weatherly, G. C. On the Crystallography of Precipitation. *Prog. Mater. Sci.* **2005,** *50*, 181-292.

[188] Chen, J. K.; Reynolds Jr, W. T. The Role of Atomic Matching and Lattice Correspondences in the Selection of Habit Planes. *Acta Mater.* **1997,** *45*, 4423-4430.

[189] Liang, Q.; Reynolds, W. T. Determining Interphase Boundary Orientations from near-Coincidence Sites. *Metall. Mater. Trans. A* **1998,** *29*, 2059-2072.

[190] Kelly, P. M.; Zhang, M. X. Edge-to-Edge Matching-a New Approach to the Morphology and Crystallography of Precipitates. *Mater. Forum* **1999,** *23*, 41-62.

[191] Kelly, P. M.; Zhang, M. X. Edge-to-Edge Matching-the Fundamentals. *Metall. Mater. Trans.* **2006,** *37*, 833.

[192] Zhang, M. X.; Kelly, P. M. Crystallography and Morphology of Widmanstätten Cementite in Austenite. *Acta Mater.* **1998,** *46*, 4617-4628.

[193] Howe, J. M.; Pond, R. C.; Hirth, J. P. The Role of Disconnections in Phase Transformations. *Prog. Mater. Sci.* **2009,** *54*, 792-838.

[194] Pond, R. C.; Ma, X.; Hirth, J. P. Kinematic and Topological Models of Martensitic Interfaces. *Mater. Sci. Eng. A* **2006,** *438*, 109-112.

[195] Maeda, T.; Kai, T.; Kikitsu, A.; Nagase, T.; Akiyama, J. Reduction of Ordering Temperature of an Fept-Ordered Alloy by Addition of Cu. *Appl. Phys. Lett.* **2002,** *80*, 2147-2149.

[196] Kismarahardja, A.; Wang, Z.; Li, D.; Wang, L.; Fu, L.; Chen, Y.; Fan, Z.; Chen, Y.; Han, X.; Zhang, H.; et al. Deformation-Induced Phase Transformations in Gold Nanoribbons with the 4h Phase. *ACS Nano* **2022,** *16*, 3272-3279.

[197] Nie, A.; Wang, H. Deformation-Mediated Phase Transformation in Gold Nano-Junction. *Mater. Lett.* **2011,** *65*, 3380-3383.

[198] Dang, C.; Chou, J. P.; Dai, B.; Chou, C. T.; Yang, Y.; Fan, R.; Lin, W.; Meng, F.; Hu, A.; Zhu, J.; et al. Achieving Large Uniform Tensile Elasticity in Microfabricated Diamond. *Science* **2021,** *371*, 76-78.

[199] Gao, P.; Britson, J.; Jokisaari, J. R.; Nelson, C. T.; Baek, S. H.; Wang, Y.; Eom, C. B.; Chen, L. Q.; Pan, X. Atomic-Scale Mechanisms of Ferroelastic Domain-Wall-Mediated Ferroelectric Switching. *Nat. Commun.* **2013,** *4*, 2791.

[200] Yuan, W.; Fang, K.; You, R.; Zhang, Z.; Wang, Y. Toward *in Situ* Atomistic Design of Catalytic Active Sites Via Controlled Atmosphere Transmission Electron Microscopy. *Accounts Mater. Res.* **2023**.

[201] Yang, R.; Mei, L.; Fan, Y.; Zhang, Q.; Liao, H. G.; Yang, J.; Li, J.; Zeng, Z. Fabrication of Liquid Cell for *in Situ* Transmission Electron Microscopy of Electrochemical Processes. *Nat. Protoc.* **2023,** *18*, 555-578.

[202] Żak, A. M. Light-Induced *in Situ* Transmission Electron Microscopy-Development, Challenges, and Perspectives. *Nano Lett.* **2022,** *22*, 9219-9226.

[203] Wu, Z.; Pei, K.; Xing, L.; Yu, X.; You, W.; Che, R. Enhanced Microwave Absorption Performance from Magnetic Coupling of Magnetic Nanoparticles Suspended within Hierarchically Tubular Composite. *Adv. Funct. Mater.* **2019,** *29*, 1901448.

[204] Egerton, R.; Li, P.; Malac, M. Radiation Damage in the Tem and Sem. *Micron* **2004,** *35*, 399-409.

[205] Lembke, A.; Ruska, H. Vergleichende Mikroskopische Und Übermikroskopische Beobachtungen Un Den Erregern Der Tuberkulose. *Klin. Wochenschr.* **1940,** *19*, 217-220.

[206] Makin, M. Electron Displacement Damage in Copper and Aluminium in a High Voltage Electron Microscope. *Philos. Mag.* **1968,** *18*, 637-653.

[207] Burton, E. F.; Sennett, R. S.; Ellis, S. G. Specimen Changes Due to Electron Bombardment in the Electron Microscope. *Nature* **1947,** *160*, 565-567.

[208] Wilkes, P. Phase Stability under Irradiation - a Review of Theory and Experiment. *J. Nucl. Mater.* **1979,** *83*, 166-175.

[209] Krasheninnikov, A. V.; Nordlund, K. Ion and Electron Irradiation-Induced Effects in Nanostructured Materials. *J. Appl. Phys.* **2010,** *107*, 071301.

[210] Fischer, R. B. Decompositions of Inorganic Specimens During Observation in the Electron Microscope. *J. Appl. Phys.* **1954,** *25*, 894-896.

[211] Cherns, D.; Hutchison, J. L.; Jenkins, M. L.; Hirsch, P. B.; White, S. Electron Irradiation Induced Vitrification at Dislocations in Quartz. *Nature* **1980,** *287*, 314-316.

[212] Egerton, R. F. Choice of Operating Voltage for a Transmission Electron Microscope. *Ultramicroscopy* **2014,** *145*, 85-93.

[213] Zheng, K.; Wang, C.; Cheng, Y.; Yue, Y.; Han, X.; Zhang, Z.; Shan, Z.; Mao, S. X.; Ye, M.; Yin, Y.; et al. Electron-Beam-Assisted Superplastic Shaping of Nanoscale Amorphous Silica. *Nat. Commun.* **2010,** *1*, 1-8.

[214] Yokota, T.; Murayama, M.; Howe, J. M. *In Situ* Transmission-Electron-Microscopy Investigation of Melting in Submicron Al-Si Alloy Particles under Electron-Beam Irradiation. *Phys. Rev. Lett.* **2003,** *91*, 265504.

[215] Malm, J. O.; Bovin, J. O.; Petford Long, A.; Smith, D. J.; Schmid, G.; Klein, N. D. C. Real-Time Atomic-Resolution Imaging of Polymorphic Changes in Ruthenium Clusters. *Angew. Chem. Int. Ed.* **1988,** *27*, 555-558.

[216] Wallenberg, L. R.; Bovin, J. O.; Petford-Long, A. K.; Smith, D. J. Atomic-Resolution Study of Structural Rearrangements in Small Platinum Crystals. *Ultramicroscopy* **1986,** *20*, 71-75.

[217] Smith, D. J.; PetfordLong, A. K.; Wallenberg, L.; Bovin, J. O. Dynamic Atomic-Level Rearrangements in Small Gold Particles. *Science* **1986,** *233*, 872-875.

[218] Saleem, F.; Cui, X.; Zhang, Z.; Liu, Z.; Dong, J.; Chen, B.; Chen, Y.; Cheng, H.; Zhang, X.; Ding, F.; et al. Size-Dependent Phase Transformation of Noble Metal Nanomaterials. *Small* **2019,** *15*, 1903253.

[219] Huang, J. L.; Li, Z.; Duan, H. H.; Cheng, Z. Y.; Li, Y. D.; Zhu, J.; Yu, R. Formation of Hexagonal-Close Packed (Hcp) Rhodium as a Size Effect. *J. Am. Chem. Soc.* **2017,** *139*, 575-578.

[220] Liang, C.; Terabe, K.; Hasegawa, T.; Aono, M. Formation of Metastable Silver Nanowires of Hexagonal Structure and Their Structural Transformation under Electron Beam Irradiation. *Jpn. J. Appl. Phys.* **2006,** *45*, 6046.

[221] Wang, B.; Fei, G. T.; Zhou, Y.; Wu, B.; Zhu, X.; Zhang, L. Controlled Growth and Phase Transition of Silver Nanowires with Dense Lengthwise Twins and Stacking Faults. *Cryst. Growth Des.* **2008,** *8*, 3073-3076.

[222] Zhou, Y.; Fei, G. T.; Cui, P.; Wu, B.; Wang, B.; Zhang, L. D. The Fabrication and Thermal Expansion Properties of 4h-Ag Nanowire Arrays in Porous Anodic Alumina Templates. *Nanotechnol.* **2008,** *19*, 285711.

[223] Liu, X.; Zhu, J.; Jin, C.; Peng, L.-M.; Tang, D.; Cheng, H. *In Situ* Electrical Measurements of Polytypic Silver Nanowires. *Nanotechnol.* **2008,** *19*, 085711.

[224] Kotakoski, J.; Krasheninnikov, A. V.; Kaiser, U.; Meyer, J. C. From Point Defects in Graphene to Two-Dimensional Amorphous Carbon. *Phys. Rev. Lett.* **2011,** *106*, 105505.

[225] Chuvilin, A.; Kaiser, U.; Bichoutskaia, E.; Besley, N. A.; Khlobystov, A. N. Direct Transformation of Graphene to Fullerene. *Nat. Chem.* **2010,** *2*, 450-453.

[226] Börrnert, F.; Avdoshenko, S. M.; Bachmatiuk, A.; Ibrahim, I.; Büchner, B.; Cuniberti, G.; Rümmeli, M. H. Amorphous Carbon under 80 Kv Electron Irradiation: A Means to Make or Break Graphene. *Adv. Mater.* **2012,** *24*, 5630-5635.

[227] Banhart, F.; Ajayan, P. M. Carbon Onions as Nanoscopic Pressure Cells for Diamond Formation. *Nature* **1996,** *382*, 433-435.

[228] Lyutovich, Y.; Banhart, F. Low-Pressure Transformation of Graphite to Diamond under Irradiation. *Appl. Phys. Lett.* **1999,** *74*, 659-660.

[229] Hiraki, J.; Mori, H.; Taguchi, E.; Yasuda, H.; Kinoshita, H.; Ohmae, N. Transformation of Diamond Nanoparticles into Onion-Like Carbon by Electron Irradiation Studied Directly inside an Ultrahigh-Vacuum Transmission Electron Microscope. *Appl. Phys. Lett.* **2005,** *86*, 223101.

[230] Lin, Y.-C.; Dumcenco, D. O.; Huang, Y.-S.; Suenaga, K. Atomic Mechanism of the Semiconducting-to-Metallic Phase Transition in Single-Layered Mos2. *Nature Nanotechnology* **2014,** *9*, 391-396.

[231] Zheng, F.; Guo, D.; Huang, L.; Wong, L. W.; Chen, X.; Wang, C.; Cai, Y.; Wang, N.; Lee, C. S.; Lau, S. P.; et al. Sub‐Nanometer Electron Beam Phase Patterning in 2d Materials. *Advanced Science* **2022,** *9*, 2200702.

[232] Zaefferer, S.; Ohlert, J.; Bleck, W. A Study of Microstructure, Transformation Mechanisms and Correlation between Microstructure and Mechanical Properties of a Low Alloyed Trip Steel. *Acta Mater.* **2004,** *52*, 2765-2778.

[233] WEICHAN, C. Electron Microscopical Study of Extension Processes by Means of a Spreading Cartridge. *Z. Wiss. Mikrosk.* **1955,** *62*, 147-151.

[234] Wilsdorf, H. G. F. Apparatus for the Deformation of Foils in an Electron Microscope. *Rev. Sci. Instrum.* **1958,** *29*, 323-324.

[235] Legros, M. *In Situ* Mechanical Tem: Seeing and Measuring under Stress with Electrons. *C. R. Phys.* **2014,** *15*, 224-240.

[236] Wang, H.; Chen, D.; An, X.; Zhang, Y.; Sun, S.; Tian, Y.; Zhang, Z.; Wang, A.; Liu, J.; Song, M.; et al. Deformation-Induced Crystalline-to-Amorphous Phase Transformation in a Crmnfeconi High-Entropy Alloy. *Sci. Adv.* **2021,** *7*, eabe3105.

[237] Sun, J.; He, L.; Lo, Y. C.; Xu, T.; Bi, H.; Sun, L.; Zhang, Z.; Mao, S. X.; Li, J. Liquid-Like Pseudoelasticity of Sub-10-Nm Crystalline Silver Particles. *Nat. Mater.* **2014,** *13*, 1007-1012.

[238] Zhong, L.; Sansoz, F.; He, Y.; Wang, C.; Zhang, Z.; Mao, S. X. Slip-Activated Surface Creep with Room-Temperature Super-Elongation in Metallic Nanocrystals. *Nat. Mater.* **2017,** *16*, 439-445.

[239] Wang, X.; Zhong, L.; Mao, S. X. Advances in Understanding Atomic-Scale Deformation of Small-Sized Face-Centered Cubic Metals with *in Situ* Transmission Electron Microscopy. *Materials Today Nano* **2018,** *2*, 58-69.

[240] Spiecker, E.; Oh, S. H.; Shan, Z. W.; Ikuhara, Y.; Mao, S. X. Insights into Fundamental Deformation Processes from Advanced *in Situ* Transmission Electron Microscopy. *MRS Bull.* **2019,** *44*, 443-449.

[241] Zhu, Y.; Espinosa, H. D. An Electromechanical Material Testing System for *in Situ* Electron Microscopy and Applications. *Proc. Natl. Acad. Sci.* **2005,** *102*, 14503-14508.

[242] Li, S.; Powell, C. A.; Mathaudhu, S.; Gwalani, B.; Devaraj, A.; Wang, C. Review of Recent Progress on *in Situ* Tem Shear Deformation: A Retrospective and Perspective View. *J. Mater. Sci.* **2022**, 1-25.

[243] Sun, S.; Li, D.; Yang, C.; Fu, L.; Kong, D.; Lu, Y.; Guo, Y.; Liu, D.; Guan, P.; Zhang, Z. Direct Atomic-Scale Observation of Ultrasmall Ag Nanowires That Exhibit *Fcc*, *Bcc*, and *Hcp* Structures under Bending. *Phys. Rev. Lett.* **2022,** *128*, 015701.

[244] Carlton, C. E.; Ferreira, P. J. *In Situ* Tem Nanoindentation of Nanoparticles. *Micron* **2012,** *43*, 1134-1139.

[245] Cao, K.; Feng, S.; Han, Y.; Gao, L.; Hue Ly, T.; Xu, Z.; Lu, Y. Elastic Straining of Free-Standing Monolayer Graphene. *Nat. Commun.* **2020,** *11*, 284.

[246] Han, Y.; Feng, S.; Cao, K.; Wang, Y.; Gao, L.; Xu, Z.; Lu, Y. Large Elastic Deformation and Defect Tolerance of Hexagonal Boron Nitride Monolayers. *Cell Rept. Phys. Sci.* **2020,** *1*, 100172.

[247] Zhang, H.; Tersoff, J.; Xu, S.; Chen, H.; Zhang, Q.; Zhang, K.; Yang, Y.; Lee, C. S.; Tu, K. N.; Li, J.; et al. Approaching the Ideal Elastic Strain Limit in Silicon Nanowires. *Sci. Adv.* **2016,** *2*, e1501382.

[248] Eigler, D. M.; Schweizer, E. K. Positioning Single Atoms with a Scanning Tunnelling Microscope. *Nature* **1990,** *344*, 524-526.

[249] Lu, Y.; Huang, J. Y.; Wang, C.; Sun, S.; Lou, J. Cold Welding of Ultrathin Gold Nanowires. *Nat. Nanotechnol.* **2010,** *5*, 218-224.

[250] Mei, S.; He, L.; Wu, X.; Sun, J.; Wang, B.; Xiong, X.; Sun, L. Dynamic Investigation of Interface Atom Migration During Heterostructure Nanojoining. *Nanoscale* **2014,** *6*, 405-411.

[251] Firestein, K. L.; Kvashnin, D. G.; Fernando, J. F. S.; Zhang, C.; Siriwardena, D. P.; Sorokin, P. B.; Golberg, D. V. Crystallography-Derived Young's Modulus and Tensile Strength of Aln Nanowires as Revealed by *in Situ* Transmission Electron Microscopy. *Nano Lett.* **2019,** *19*, 2084-2091.

[252] Svensson, K.; Jompol, Y.; Olin, H.; Olsson, E. Compact Design of a Transmission Electron Microscope-Scanning Tunneling Microscope Holder with Three-Dimensional Coarse Motion. *Rev. Sci. Instrum.* **2003,** *74*, 4945-4947.

[253] Zhu, C.; Zheng, D.; Wang, H.; Zhang, M.; Li, Z.; Sun, S.; Xu, P.; Tian, H.; Li, Z.; Yang, H. Development of Analytical Ultrafast Transmission Electron Microscopy Based on Laser-Driven Schottky Field Emission. *Ultramicroscopy* **2020,** *209*, 112887.

[254] Zhu, Q.; Zhao, S. C.; Deng, C.; An, X. H.; Song, K. X.; Mao, S. X.; Wang, J. W. *In Situ* Atomistic Observation of Grain Boundary Migration Subjected to Defect Interaction. *Acta Mater.* **2020,** *199*, 42-52.

[255] He, K.; Cho, J.-H.; Jung, Y.; Picraux, S. T.; Cumings, J. Silicon Nanowires: Electron Holography Studies of Doped P-N Junctions and Biased Schottky Barriers. *Nanotechnol.* **2013,** *24*, 115703.

[256] http://www.picofemto.cn/tem-stm.html.

[257] Zhu, Q.; Cao, G.; Wang, J.; Deng, C.; Li, J.; Zhang, Z.; Mao, S. X. *In Situ* Atomistic Observation of Disconnection-Mediated Grain Boundary Migration. *Nat. Commun.* **2019,** *10*, 156.

[258] Wang, Q.; Wang, J.; Li, J.; Zhang, Z.; Mao, S. X. Consecutive Crystallographic Reorientations and Superplasticity in Body-Centered Cubic Niobium Nanowires. *Sci. Adv.* **2018,** *4*, eaas8850.

[259] Zhang, C.; Kvashnin, D. G.; Bourgeois, L.; Fernando, J. F. S.; Firestein, K.; Sorokin, P. B.; Fukata, N.; Golberg, D. Mechanical, Electrical, and Crystallographic Property Dynamics of Bent and Strained Ge/Si Core–Shell Nanowires as Revealed by *in Situ* Transmission Electron Microscopy. *Nano Lett.* **2018,** *18*, 7238-7246.

[260] Zhu, Q.; Kong, L.; Lu, H.; Huang, Q.; Chen, Y.; Liu, Y.; Yang, W.; Zhang, Z.; Sansoz, F.; Zhou, H.; et al. Revealing Extreme Twin-Boundary Shear Deformability in Metallic Nanocrystals. *Sci. Adv.* **2021,** *7*, eabe4758.

[261] Chen, Y.; Huang, Q.; Zhu, Q.; Song, K.; Zhou, Y.; Zhou, H.; Wang, J. Coordinated Grain Boundary Deformation Governed Nanograin Annihilation in Shear Cycling. *J. Mater. Sci. Technol.* **2021,** *86*, 180-191.

[262] Joly Pottuz, L.; Calvié, E.; Réthoré, J.; Meille, S.; Esnouf, C.; Chevalier, J.; Masenelli Varlot, K. Mechanical Properties of Nanoparticles: Characterization by *in Situ* Nanoindentation inside a Transmission Electron Microscope. *Handb. Mech. Nanostructuring* **2015**, 163-180.

[263] Schweizer, P.; Dolle, C.; Dasler, D.; Abellán, G.; Hauke, F.; Hirsch, A.; Spiecker, E. Mechanical Cleaning of Graphene Using *in Situ* Electron Microscopy. *Nat. Commun.* **2020,** *11*, 1743.

[264] Ohnishi, H.; Kondo, Y.; Takayanagi, K. Quantized Conductance through Individual Rows of Suspended Gold Atoms. *Nature* **1998,** *395*, 780-783.

[265] Kizuka, T. Atomistic Visualization of Deformation in Gold. *Phys. Rev. B* **1998,** *57*, 11158.

[266] Poncharal, P.; Wang, Z. L.; Ugarte, D.; de Heer, W. A. Electrostatic Deflections and Electromechanical Resonances of Carbon Nanotubes. *Science* **1999,** *283*, 1513-1516.

[267] Wang, J.; Sansoz, F.; Huang, J.; Liu, Y.; Sun, S.; Zhang, Z.; Mao, S. X. Near-Ideal Theoretical Strength in Gold Nanowires Containing Angstrom Scale Twins. *Nat. Commun.* **2013,** *4*, 1472.

[268] Li, N.; Mara, N. A.; Wang, J.; Dickerson, P.; Huang, J. Y.; Misra, A. *Ex Situ* and *in Situ* Measurements of the Shear Strength of Interfaces in Metallic Multilayers. *Scr. Mater.* **2012,** *67*, 479-482.

[269] Chen, B.; Wang, J.; Zhu, Y.; Liao, X.; Lu, C.; Mai, Y.-W.; Ringer, S. P.; Ke, F.; Shen, Y. Deformation-Induced Phase Transformation in 4h–Sic Nanopillars. *Acta Mater.* **2014,** *80*, 392-399.

[270] Li, N.; Wang, J.; Misra, A.; Zhang, X.; Huang, J. Y.; Hirth, J. P. Twinning Dislocation Multiplication at a Coherent Twin Boundary. *Acta Mater.* **2011,** *59*, 5989-5996.

[271] Ding, M.; Tian, L.; Han, W.; Li, J.; Ma, E.; Shan, Z. Nanobubble Fragmentation and Bubble-Free-Channel Shear Localization in Helium-Irradiated Submicron-Sized Copper. *Phys. Rev. Lett.* **2016,** *117*, 215501.

[272] Lin, W. T.; Chen, D.; Dang, C. Q.; Yu, P. J.; Wang, G.; Lin, J. H.; Meng, F. L.; Yang, T.; Zhao, Y. L.; Liu, S. F.; et al. Highly Pressurized Helium Nanobubbles Promote Stacking-Fault-Mediated Deformation in Fenicocr High-Entropy Alloy. *Acta Mater.* **2021,** *210*, 116843.

[273] Bhowmick, S.; Stauffer, D.; Guo, H.; Kaps, S.; Mishra, Y. K.; Hrkac, V.; Warren, O.; Adelung, R.; Minor, A.; Kienle, L. *In Situ* Electromechanical Study of Zno Nanowires. *Microsc. Microanal.* **2013,** *19*, 434-435.

[274] Lu, Y.; Ganesan, Y.; Lou, J. A Multi-Step Method for *in Situ* Mechanical Characterization of 1-D Nanostructures Using a Novel Micromechanical Device. *Expe. Mech.* **2010,** *50*, 47-54.

[275] Shan, Z.; Mishra, R. K.; Syed Asif, S. A.; Warren, O. L.; Minor, A. M. Mechanical Annealing and Source-Limited Deformation in Submicrometre-Diameter Ni Crystals. *Nat. Mater.* **2008,** *7*, 115-119.

[276] Merkle, A.; Marks, L. Friction in Full View. *Appl. Phys. Lett.* **2007,** *90*, 064101.

[277] Merkle, A. P.; Marks, L. D. Liquid-Like Tribology of Gold Studied by *in Situ* Tem. *Wear* **2008,** *265*, 1864-1869.

[278] Chang, S. *In-Situ* Nanomechanical Testing in Electron Microscopes. *Handb. Mech. Mater.* **2018**, 1-47.

[279] Ma, J. W.; Lee, W. J.; Bae, J. M.; Jeong, K. S.; Oh, S. H.; Kim, J. H.; Kim, S. H.; Seo, J. H.; Ahn, J. P.; Kim, H.; et al. Carrier Mobility Enhancement of Tensile Strained Si and Sige Nanowires Via Surface Defect Engineering. *Nano Lett.* **2015,** *15*, 7204-7210.

[280] Wang, Y.; Zhang, W.; Wang, L.; Zhuang, Z.; Ma, E.; Li, J.; Shan, Z. *In Situ* Tem Study of Deformation-Induced Crystalline-to-Amorphous Transition in Silicon. *NPG Asia Mater.* **2016,** *8*, e291-e291.

[281] Ye, J.; Mishra, R. K.; Pelton, A. R.; Minor, A. M. Direct Observation of the Niti Martensitic Phase Transformation in Nanoscale Volumes. *Acta Mater.* **2010,** *58*, 490-498.

[282] He, Y.; Zhong, L.; Fan, F.; Wang, C.; Zhu, T.; Mao, S. X. *In Situ* Observation of Shear-Driven Amorphization in Silicon Crystals. *Nat. Nanotechnol.* **2016,** *11*, 866-871.

[283] Bhowmick, S.; Espinosa, H.; Jungjohann, K.; Pardoen, T.; Pierron, O. Advanced Microelectromechanical Systems-Based Nanomechanical Testing: Beyond Stress and Strain Measurements. *MRS Bull.* **2019,** *44*, 487-493.

[284] Kacher, J.; Zhu, T.; Pierron, O.; Spearot, D. E. Integrating *in Situ* Tem Experiments and Atomistic Simulations for Defect Mechanics. *Curr. Opin. Solid State Mater. Sci.* **2019,** *23*, 117-128.

[285] Zhu, Y. Mems Platforms for *in-Situ* Testing of Mechanical Properties of Nanostructures. **2023**.

[286] Samuel, B. A.; Haque, M. A.; Yi, B.; Rajagopalan, R.; Foley, H. C. Mechanical Testing of Pyrolysed Poly-Furfuryl Alcohol Nanofibres. *Nanotechnol.* **2007,** *18*, 115704.

[287] Naraghi, M.; Chasiotis, I.; Kahn, H.; Wen, Y.; Dzenis, Y. Novel Method for Mechanical Characterization of Polymeric Nanofibers. *Rev. Sci. Instrum.* **2007,** *78*, 085108.

[288] Haque, M. A.; Saif, M. T. A. Deformation Mechanisms in Free-Standing Nanoscale Thin Films: A Quantitative *in Situ* Transmission Electron Microscope Study. *Proc. Natl. Acad. Sci.* **2004,** *101*, 6335-6340.

[289] Saif, M. T. A.; MacDonald, N. C. A Millinewton Microloading Device. *Sens. Actuat. A* **1996,** *52*, 65-75.

[290] Que, L.; Park, J. S.; Gianchandani, Y. B. Bent-Beam Electrothermal Actuators-Part I: Single Beam and Cascaded Devices. *J. Micromech. Syst.* **2001,** *10*, 247-254.

[291] Ouyang, J.; Zhu, Y. Z-Shaped Mems Thermal Actuators: Piezoresistive Self-Sensing and Preliminary Results for Feedback Control. *J. Micromech. Syst.* **2012,** *21*, 596-604.

[292] Sheng, H.; Zhang, L.; Zhang, H.; Wang, J.; Eckert, J.; Gammer, C. *In Situ* Tem Observation of Phase Transformation in Bulk Metallic Glass Composites. *Mater. Res. Lett.* **2021,** *9*, 189-194.

[293] Guo, H.; Chen, K.; Oh, Y.; Wang, K.; Dejoie, C.; Asif, S. A. S.; Warren, O. L.; Shan, Z. W.; Wu, J.; Minor, A. M. Mechanics and Dynamics of the Strain-Induced M1-M2 Structural Phase Transition in Individual Vo_2 Nanowires. *Nano Lett.* **2011,** *11*, 3207-3213.

[294] Sato, T.; Ishida, T.; Jalabert, L.; Fujita, H. Real-Time Transmission Electron Microscope Observation of Nanofriction at a Single Ag Asperity. *Nanotechnol.* **2012,** *23*, 505701.

[295] Lu, H.; Wang, Z.; Yun, D.; Li, J.; Shan, Z. A New Approach of Using Lorentz Force to Study Single-Asperity Friction inside Tem. *J. Mater. Sci. Technol.* **2021,** *84*, 43-48.

[296] Bernal, R. A.; Ramachandramoorthy, R.; Espinosa, H. D. Double-Tilt *in Situ* Tem Holder with Multiple Electrical Contacts and Its Application in Mems-Based Mechanical Testing of Nanomaterials. *Ultramicroscopy* **2015,** *156*, 23-28.

[297] Yang, Y.; Fu, Z.; Zhang, X.; Cui, Y.; Xu, F.; Li, T.; Wang, Y. *In Situ* Tem Mechanical Characterization of One-Dimensional Nanostructures Via a Standard Double-Tilt Holder Compatible Mems Device. *Ultramicroscopy* **2019,** *198*, 43-48.

[298] Wang, L.; Liu, P.; Guan, P.; Yang, M.; Sun, J.; Cheng, Y.; Hirata, A.; Zhang, Z.; Ma, E.; Chen, M.; et al. *In Situ* Atomic-Scale Observation of Continuous and Reversible Lattice Deformation Beyond the Elastic Limit. *Nat. Commun.* **2013,** *4*, 2413.

[299] Wang, L.; Zheng, K.; Zhang, Z.; Han, X. Direct Atomic-Scale Imaging About the Mechanisms of Ultralarge Bent Straining in Si Nanowires. *Nano Lett.* **2011,** *11*, 2382-2385.

[300] Zheng, K.; Han, X.; Wang, L.; Zhang, Y.; Yue, Y.; Qin, Y.; Zhang, X.; Zhang, Z. Atomic Mechanisms Governing the Elastic Limit and the Incipient Plasticity of Bending Si Nanowires. *Nano Lett.* **2009,** *9*, 2471-2476.

[301] Wang, L.; Du, K.; Yang, C.; Teng, J.; Fu, L.; Guo, Y.; Zhang, Z.; Han, X. *In Situ* Atomic-Scale Observation of Grain Size and Twin Thickness Effect Limit in Twin-Structural Nanocrystalline Platinum. *Nat. Commun.* **2020,** *11*, 1167.

[302] Lu, Y.; Sun, S.; Zeng, Y.; Deng, Q.; Chen, Y.; Li, Y.; Li, X.; Wang, L.; Han, X. Atomistic Mechanism of Nucleation and Growth of a Face-Centered Orthogonal Phase in Small-Sized Single-Crystalline Mo. *Mater. Res. Lett.* **2020,** *8*, 348-355.

[303] Fu, L.; Kong, D.; Yang, C.; Teng, J.; Lu, Y.; Guo, Y.; Yang, G.; Yan, X.; Liu, P.; Chen, M. Ultra-High Strength yet Superplasticity in a Hetero-Grain-Sized Nanocrystalline Au Nanowire. *J. Mater. Sci. Technol.* **2022,** *101*, 95-106.

[304] Liu, P.; Wei, X.; Song, S.; Wang, L.; Hirata, A.; Fujita, T.; Han, X.; Zhang, Z.; Chen, M. Time-Resolved Atomic-Scale Observations of Deformation and Fracture of Nanoporous Gold under Tension. *Acta Mater.* **2019,** *165*, 99-108.

[305] Han, X.; Yue, Y.; Zhang, Y.; Liu, P.; Zheng, K.; Wang, X.; Zhang, Z., Double Tilt Transmission Electron Microscope Sample Holder for in-Situ Measurement of Microstructures. Google Patents: 2013.

[306] Wang, L.; Zhang, Y.; Zeng, Z.; Zhou, H.; He, J.; Liu, P.; Chen, M.; Han, J.; Srolovitz, D. J.; Teng, J.; et al. Tracking the Sliding of Grain Boundaries at the Atomic Scale. *Science* **2022,** *375*, 1261-1265.

[307] Wang, L.; Guan, P.; Teng, J.; Liu, P.; Chen, D.; Xie, W.; Kong, D.; Zhang, S.; Zhu, T.; Zhang, Z.; et al. New Twinning Route in Face-Centered Cubic Nanocrystalline Metals. *Nat. Commun.* **2017,** *8*, 2142.

[308] Zhang, Y.; Han, X.; Zheng, K.; Zhang, Z.; Zhang, X.; Fu, J.; Ji, Y.; Hao, Y.; Guo, X.; Wang, Z. L. Direct Observation of Super-Plasticity of Beta-Sic Nanowires at Low Temperature. *Adv. Funct. Mater.* **2007,** *17*, 3435-3440.

[309] Wang, L.; Teng, J.; Kong, D.; Yu, G.; Zou, J.; Zhang, Z.; Han, X. In Situ Atomistic Deformation Mechanisms of Twin-Structured Nanocrystal Pt. *Scr. Mater.* **2018,** *147*, 103-107.

[310] Jin, H.; Zhang, J.; Li, P.; Zhang, Y.; Zhang, W.; Qin, J.; Wang, L.; Long, H.; Li, W.; Shao, R.; et al. Atomistic Mechanism of Phase Transformation between Topologically Close-Packed Complex Intermetallics. *Nat. Commun.* **2022,** *13*, 2487.

[311] Chu, S.; Liu, P.; Zhang, Y.; Wang, X.; Song, S.; Zhu, T.; Zhang, Z.; Han, X.; Sun, B.; Chen, M. In Situ Atomic-Scale Observation of Dislocation Climb and Grain Boundary Evolution in Nanostructured Metal. *Nat. Commun.* **2022,** *13*, 4151.

[312] Kong, D.; Kovács, A.; Charilaou, M.; Zheng, F.; Wang, L.; Han, X.; Dunin-Borkowski, R. E. Direct Observation of Tensile-Strain-Induced Nanoscale Magnetic Hardening. *Nat. Commun.* **2023,** *14*, 3963.

[313] Lu, Y.; Chen, Y.; Zeng, Y.; Zhang, Y.; Kong, D.; Li, X.; Zhu, T.; Li, X.; Mao, S.; Zhang, Z.; et al. Nanoscale Ductile Fracture and Associated Atomistic Mechanisms in a Body-Centered Cubic Refractory Metal. *Nat. Commun.* **2023,** *14*, 5540.

[314] Yang, C.; Zhang, B.; Fu, L.; Wang, Z.; Teng, J.; Shao, R.; Wu, Z.; Chang, X.; Ding, J.; Wang, L.; et al. Chemical Inhomogeneity–Induced Profuse Nanotwinning and Phase Transformation in Aucu Nanowires. *Nat. Commun.* **2023,** *14*, 5705.

[315] Taheri, M. L.; Stach, E. A.; Arslan, I.; Crozier, P. A.; Kabius, B. C.; LaGrange, T.; Minor, A. M.; Takeda, S.; Tanase, M.; Wagner, J. B.; et al. Current Status and Future Directions for *in Situ* Transmission Electron Microscopy. *Ultramicroscopy* **2016,** *170*, 86-95.

[316] Zhang, F.; Zhang, X.; Jia, Z.; Liu, W. Precise Drift Tracking for *in Situ* Transmission Electron Microscopy Via a Thon-Ring Based Sample Position Measurement. *Microsc. Microanal.* **2022,** *28*, 1945-1951.

[317] Huang, J. Y.; Chen, S.; Wang, Z. Q.; Kempa, K.; Wang, Y. M.; Jo, S. H.; Chen, G.; Dresselhaus, M. S.; Ren, Z. F. Superplastic Carbon Nanotubes. *Nature* **2006,** *439*, 281-281.

[318] Wang, B.; Haque, M. *In Situ* Microstructural Control and Mechanical Testing inside the Transmission Electron Microscope at Elevated Temperatures. *JOM* **2015,** *67*, 1713-1720.

[319] Cheng, G.; Zhang, Y.; Chang, T.; Liu, Q.; Chen, L.; Lu, W. D.; Zhu, T.; Zhu, Y. *In Situ* Nano-Thermomechanical Experiment Reveals Brittle to Ductile Transition in Silicon Nanowires. *Nano Lett.* **2019,** *19*, 5327-5334.

[320] Zhang, J.; Li, Y.; Li, X.; Zhai, Y.; Zhang, Q.; Ma, D.; Mao, S.; Deng, Q.; Li, Z.; Li, X. Timely and Atomic-Resolved High-Temperature Mechanical Investigation of Ductile Fracture and Atomistic Mechanisms of Tungsten. *Nat. Commun.* **2021,** *12*, 2218.

[321] Qi, Y.; Chen, Z.; Wang, L.; Han, X.; Wang, J.; Sritharan, T.; Chen, L. Temperature-Driven Evolution of Hierarchical Nanodomain Structure in Tetragonal-Like Bifeo3 Films. *Appl. Phys. Lett.* **2012,** *100*, 002908.

[322] Liu, C.; Wu, S.; Zheng, H.; Cao, F.; Sheng, H.; Zhao, D.; Wang, J. Size-Controllable Fabrication of Cu Nanoparticles on Carbon Nanotubes by Simple Heating. *Mater. Res. Bull.* **2015,** *61*, 270-274.

[323] Pérez Garza, H. H.; Zuo, K.; Pivak, Y.; Morsink, D.; Zakhozheva, M.; Pen, M.; van Weperen, S.; Xu, Q. In *Mems-Based System for in-Situ Biasing and Heating Solutions inside the Tem*, European Microscopy Congress 2016: Proceedings, Wiley Online Library: 2016; pp 237-238.

[324] Pokle, A.; Canavan, M.; Daly, D.; Gomes, F. O. V.; Marinkovic, M.; Wagner, V.; Nicolosi, V. *In-Situ* Tem Analyses over Fib Lamellae-Investigating High Temperature Conversion of Solution Processed Mo-Precursor to Mos_2 Semiconductor Films. *Microsc. Microanal.* **2017,** *23*, 258-259.

[325] Saka, H.; Kamino, T.; Ara, S.; Sasaki, K. *In Situ* Heating Transmission Electron Microscopy. *MRS Bull.* **2008,** *33*, 93-100.

[326] Tiggelaar, R. M.; Berenschot, J. W.; De Boer, J.; Sanders, R. G. P.; Gardeniers, J. G. E.; Oosterbroek, R. E.; van den Berg, A.; Elwenspoek, M. C. Fabrication and Characterization of High-Temperature Microreactors with Thin Film Heater and Sensor Patterns in Silicon Nitride Tubes. *Lab on a Chip* **2005,** *5*, 326-336.

[327] Song, N. K.; Yun, J. I.; Joo, S. K. A Study on the Electrical Properties of Pb(Zr, Ti)O_3 Thin Films Crystallized by the Electrical Resistive Heating of Pt Thin Film. *Mater. Res. Bull.* **2008,** *43*, 292-296.

[328] Beckel, D.; Briand, D.; Bieberle-Hütter, A.; Courbat, J.; de Rooij, N. F.; Gauckler, L. J. Micro-Hotplates-a Platform for Micro-Solid Oxide Fuel Cells. *J. Power Sources* **2007,** *166*, 143-148.

[329] Allard, L. F.; Bigelow, W. C.; Jose-Yacaman, M.; Nackashi, D. P.; Damiano, J.; Mick, S. E. A New Mems-Based System for Ultra-High-Resolution Imaging at Elevated Temperatures. *Microsc. Res. Technique* **2009,** *72*, 208-215.

[330] Savage, N. O.; Roberson, S.; Gillen, G.; Tarlov, M. J.; Semancik, S. Thermolithographic Patterning of Sol-Gel Metal Oxides on Micro Hot Plate Sensing Arrays Using Organosilanes. *Anal. Chem.* **2003,** *75*, 4360-4367.

[331] Duvigneau, J.; Schonherr, H.; Vancso, G. J. Nanoscale Thermal Afm of Polymers: Transient Heat Flow Effects. *ACS Nano* **2010,** *4*, 6932-6940.

[332] Gargate, R. V.; Banerjee, D. *In Situ* Synthesis of Carbon Nanotubes on Heated Scanning Probes Using Dip Pen Techniques. *Scanning: J. Scanning Microsc.* **2008,** *30*, 151-158.

[333] Spruit, R. G.; Van Omme, J. T.; Ghatkesar, M. K.; Garza, H. H. P. A Review on Development and Optimization of Microheaters for High-Temperature *in Situ* Studies. *J. Micromech. Syst.* **2017,** *26*, 1165-1182.

[334] Lee, K. N.; Lee, D. S.; Jung, S. W.; Jang, Y. H.; Kim, Y. K.; Seong, W. K. A High-Temperature Mems Heater Using Suspended Silicon Structures. *J. Micromech. Microengr.* **2009,** *19*, 115011.

[335] Beckel, D.; Briand, D.; Bieberle-Hütter, A.; Courbat, J.; De Rooij, N. F.; Gauckler, L. J. Micro-Hotplates—a Platform for Micro-Solid Oxide Fuel Cells. *Journal of Power Sources* **2007,** *166*, 143-148.

[336] Wei, S.; Li, A.; Liu, J. C.; Li, Z.; Chen, W.; Gong, Y.; Zhang, Q.; Cheong, W. C.; Wang, Y.; Zheng, L.; et al. Direct Observation of Noble Metal Nanoparticles Transforming to Thermally Stable Single Atoms. *Nat. Nanotechnol.* **2018,** *13*, 856-861.

[337] Jiang, Y.; Duchamp, M.; Ang, S. J.; Yan, H.; Tan, T. L.; Mirsaidov, U. Dynamics of the *Fcc*-to-*Bcc* Phase Transition in Single-Crystalline Pdcu Alloy Nanoparticles. *Nat. Commun.* **2023,** *14*, 104.

[338] Zhang, X.; Meng, J.; Zhu, B.; Yu, J.; Zou, S.; Zhang, Z.; Gao, Y.; Wang, Y. *In Situ* Tem Studies of the Shape Evolution of Pd Nanocrystals under Oxygen and Hydrogen Environments at Atmospheric Pressure. *Chem. Commun.* **2017,** *53*, 13213-13216.

[339] Kotula, P. G.; Prasad, S. V. Visualization of Kirkendall Voids at Cu-Au Interfaces by *in Situ* Tem Heating Studies. *JOM* **2019,** *71*, 3521-3530.

[340] Tan, S. F.; Bisht, G.; Anand, U.; Bosman, M.; Yong, X. E.; Mirsaidov, U. In Situ Kinetic and Thermodynamic Growth Control of Au-Pd Core-Shell Nanoparticles. *J. Am. Chem. Soc.* **2018,** *140*, 11680-11685.

[341] Hui, F.; Li, C.; Chen, Y.; Wang, C.; Huang, J.; Li, A.; Li, W.; Zou, J.; Han, X. Understanding the Structural Evolution of Au/$Wo_{2.7}$ Compounds in Hydrogen Atmosphere by Atomic Scale *in Situ* Environmental Tem. *Nano Res.* **2020,** *13*, 3019-3024.

[342] Kryshtal, A. P.; Minenkov, A. A.; Ferreira, P. J. Interfacial Kinetics in Nanosized Au/Ge Films: An *in Situ* Tem Study. *Appl. Surf. Sci.* **2017,** *409*, 343-349.

[343] Lu, N.; Wang, J.; Xie, S.; Xia, Y.; Kim, M. J. Enhanced Shape Stability of Pd-Rh Core-Frame Nanocubes at Elevated Temperature: *In Situ* Heating Transmission Electron Microscopy. *Chem. Commun.* **2013,** *49*, 11806-11808.

[344] Sato, K.; Kovács, A.; Hirotsu, Y. Order-Disorder Transformation in Fe-Pd Alloy Nanoparticles Studied by *in Situ* Transmission Electron Microscopy. *Thin Solid Films* **2011,** *519*, 3305-3311.

[345] Mayoral, A.; Allard, L. F.; Ferrer, D.; Esparza, R.; Jose-Yacaman, M. On the Behavior of Ag Nanowires under High Temperature: *In Situ* Characterization by Aberration-Corrected Stem. *J. Mater. Chem* **2011,** *21*, 893-898.

[346] Otsuka, K.; Kakeshita, T. Science and Technology of Shape-Memory Alloys: New Developments. *MRS Bull.* **2002,** *27*, 91-100.

[347] Tong, W.; Huang, B.; Wang, P.; Li, L.; Shao, Q.; Huang, X. Crystal-Phase-Engineered Pdcu Electrocatalyst for Enhanced Ammonia Synthesis. *Angew. Chem. Int. Ed.* **2020,** *59*, 2649-2653.

[348] Zhong, L.; Wang, J.; Sheng, H.; Zhang, Z.; Mao, S. X. Formation of Monatomic Metallic Glasses through Ultrafast Liquid Quenching. *Nature* **2014,** *512*, 177-180.

[349] Tang, D. M.; Ren, C. L.; Lv, R.; Yu, W. J.; Hou, P. X.; Wang, M. S.; Wei, X.; Xu, Z.; Kawamoto, N.; Bando, Y.; et al. Amorphization and Directional Crystallization of Metals Confined in Carbon Nanotubes Investigated by *in Situ* Transmission Electron Microscopy. *Nano Lett.* **2015,** *15*, 4922-4927.

[350] Phuah, X. L.; Jian, J.; Wang, H.; Wang, X.; Zhang, X.; Wang, H. Ultra-High Heating Rate Effects on the Sintering of Ceramic Nanoparticles: An *in Situ* Tem Study. *Mater. Res. Lett.* **2021,** *9*, 373-381.

[351] Boston, R.; Schnepp, Z.; Nemoto, Y.; Sakka, Y.; Hall, S. R. *In Situ* Tem Observation of a Microcrucible Mechanism of Nanowire Growth. *Science* **2014,** *344*, 623-626.

[352] Fu, X.; Wang, X.; Zhao, B.; Zhang, Q.; Sun, S.; Wang, J.; Zhang, W.; Gu, L.; Zhang, Y.; Zhang, W.; et al. Atomic-Scale Observation of Non-Classical Nucleation-Mediated Phase Transformation in a Titanium Alloy. *Nat. Mater.* **2022,** *21*, 290-296.

[353] Malladi, S. K.; Xu, Q.; van Huis, M. A.; Tichelaar, F. D.; Batenburg, K. J.; Yücelen, E.; Dubiel, B.; Czyrska-Filemonowicz, A.; Zandbergen, H. W. Real-Time Atomic Scale Imaging of Nanostructural Evolution in Aluminum Alloys. *Nano Lett.* **2014,** *14*, 384-389.

[354] Yao, T.; Sen, A.; Wagner, A.; Teng, F.; Bachhav, M.; El-Azab, A.; Murray, D.; Gan, J.; Hurley, D. H.; Wharry, J. P. Understanding Spinodal and Binodal Phase Transformations in U-50zr. *Mater.* **2021,** *16*, 101092.

[355] Orava, J.; Balachandran, S.; Han, X.; Shuleshova, O.; Nurouzi, E.; Soldatov, I.; Oswald, S.; Gutowski, O.; Ivashko, O.; Dippel, A. C.; et al. *In Situ* Correlation between Metastable Phase-Transformation Mechanism and Kinetics in a Metallic Glass. *Nat. Commun.* **2021,** *12*, 2839.

[356] Sunde, J. K.; Wenner, S.; Holmestad, R. *In Situ* Heating Tem Observations of Evolving Nanoscale Al-Mg-Si-Cu Precipitates. *J. Microsc.* **2020,** *279*, 143-147.

[357] Li, T.; Lai, M.; Kostka, A.; Salomon, S.; Zhang, S.; Somsen, C.; Dargusch, M. S.; Kent, D. Composition of the Nanosized Orthorhombic O′ Phase and Its Direct Transformation to Fine A During Ageing in Metastable B-Ti Alloys. *Scr. Mater.* **2019,** *170*, 183-188.

[358] Divitini, G.; Cacovich, S.; Matteocci, F.; Cinà, L.; Di Carlo, A.; Ducati, C. *In Situ* Observation of Heat-Induced Degradation of Perovskite Solar Cells. *Nat. Energy* **2016,** *1*, 15012.

[359] Meyer, T.; Kressdorf, B.; Roddatis, V.; Hoffmann, J.; Jooss, C.; Seibt, M. Phase Transitions in a Perovskite Thin Film Studied by Environmental *in Situ* Heating Nano-Beam Electron Diffraction. *Small Methods* **2021,** *5*, 2100464.

[360] Chen, L.; Liu, J.; Jiang, C.; Zhao, K.; Chen, H.; Shi, X.; Chen, L.; Sun, C.; Zhang, S.; Wang, Y.; et al. Nanoscale Behavior and Manipulation of the Phase Transition in Single-Crystal Cu_2se. *Adv. Mater.* **2019,** *31*, 1804919.

[361] Wang, C.; Han, L.; Zhang, R.; Cheng, H.; Mu, L.; Kisslinger, K.; Zou, P.; Ren, Y.; Cao, P.; Lin, F.; et al. Resolving Atomic-Scale Phase Transformation and Oxygen Loss Mechanism in Ultrahigh-Nickel Layered Cathodes for Cobalt-Free Lithium-Ion Batteries. *Matter* **2021,** *4*, 2013-2026.

[362] Minenkov, A.; Groiss, H. Evolution of Phases and Their Thermal Stability in Ge-Sn Nanofilms: A Comprehensive *in Situ* Tem Investigation. *J. Alloy. Compd.* **2021,** *859*, 157763.

[363] Luong, M. A.; Robin, E.; Pauc, N.; Gentile, P.; Sistani, M.; Lugstein, A.; Spies, M.; Fernandez, B.; Den Hertog, M. I. *In-Situ* Transmission Electron Microscopy Imaging of Aluminum Diffusion in Germanium Nanowires for the Fabrication of Sub-10 Nm Ge Quantum Disks. *ACS Appl. Nano Mater.* **2020,** *3*, 1891-1899.

[364] El Hajraoui, K.; Robin, E.; Zeiner, C.; Lugstein, A.; Kodjikian, S.; Rouviere, J.; Den Hertog, M. *In Situ* Transmission Electron Microscopy Analysis of Copper–Germanium Nanowire Solid-State Reaction. *Nano Lett.* **2019,** *19*, 8365-8371.

[365] Seifner, M. S.; Dijkstra, A.; Bernardi, J.; Steiger-Thirsfeld, A.; Sistani, M.; Lugstein, A.; Haverkort, J. E.; Barth, S. Epitaxial $Ge_{0.81}sn_{0.19}$ Nanowires for Nanoscale Mid-Infrared Emitters. *ACS Nano* **2019,** *13*, 8047-8054.

[366] Hsu, S.; Hsin, C.; Huang, C.; Yu, S.; Wang, C.; Lu, C.; Lu, K.; Wu, W. Single-Crystalline Ge Nanowires and Cu_3ge/Ge Nano-Heterostructures. *Cryst. Eng. Comm.* **2012,** *14*, 4570-4574.

[367] Chiu, C. H.; Liang, W. I.; Huang, C. W.; Chen, J. Y.; Liu, Y. Y.; Li, J. Y.; Hsin, C. L.; Chu, Y. H.; Wu, W. W. Atomic Visualization of the Phase Transition in Highly Strained $Bifeo_3$ Thin Films with Excellent Pyroelectric Response. *Nano Energy* **2015,** *17*, 72-81.

[368] Almeida, T. P.; Temple, R.; Massey, J.; Fallon, K.; McGrouther, D.; Moore, T.; Marrows, C. H.; McVitie, S. Quantitative Tem Imaging of the Magnetostructural and Phase Transitions in Ferh Thin Film Systems. *Sci. Rep.* **2017,** *7*, 17835.

[369] Zhang, F.; Wang, Z.; Dong, J.; Nie, A.; Xiang, J.; Zhu, W.; Liu, Z.; Tao, C. Atomic-Scale Observation of Reversible Thermally Driven Phase Transformation in 2d In_2se_3. *ACS Nano* **2019,** *13*, 8004-8011.

[370] Yang, B.; Ai, Y. Facile Fabrication of Cuo Nanosheets and *in Situ* Transmission Electron Microscopy/X-Ray Diffraction Heating Characterization of Microstructure Evolution. *Phys. Status Solidi (A)* **2022,** *219*, 2100617.

[371] Gavhane, D. S.; van Gog, H.; Thombare, B.; Lole, G.; Christiaan Post, L.; More, M. A.; van Huis, M. A. *In Situ* Electron Microscopy Study of Structural Transformations in 2d $Cose_2$. *NPJ 2D Mater. Appl.* **2021,** *5*, 24.

[372] Ryu, G. H.; Chen, J.; Wen, Y.; Warner, J. H. *In-Situ* Atomic-Scale Dynamics of Thermally Driven Phase Transition of 2d Few-Layered 1t $Ptse_2$ into Ultrathin 2d Nonlayered Ptse Crystals. *Chem. Mater.* **2019,** *31*, 9895-9903.

[373] Zheng, F.; Caron, J.; Migunov, V.; Beleggia, M.; Pozzi, G.; Dunin-Borkowski, R. E. Measurement of Charge Density in Nanoscale Materials Using Off-Axis Electron Holography. *J. Electron Spectrosc. Relat. Phenom.* **2020,** *241*, 146881.

[374] Zhang, M.; Olson, E. A.; Twesten, R. D.; Wen, J. G.; Allen, L. H.; Robertson, I. M.; Petrov, I. *In Situ* Transmission Electron Microscopy Studies Enabled by Microelectromechanical System Technology. *J. Mater. Res.* **2005,** *20*, 1802-1807.

[375] Li, X.; Turner, J.; Bustillo, K.; Minor, A. M. *In Situ* Transmission Electron Microscopy Investigation of Electroplasticity in Single Crystal Nickel. *Acta Mater.* **2022,** *223*, 117461.

[376] Li, W.; Wang, Q.; Cao, K.; Tang, J.; Wang, H.; Zhou, L.; Yao, H. Mechanics-Based Optimization of Yolk-Shell Carbon-Coated Silicon Nanoparticle as Electrode Materials for High-Capacity Lithium Ion Battery. *Compos. Commun.* **2016,** *1*, 1-5.

[377] Xu, Z. L.; Cao, K.; Abouali, S.; Garakani, M. A.; Huang, J.; Huang, J.; Heidari, E. K.; Wang, H.; Kim, J. K. Study of Lithiation Mechanisms of High Performance Carbon-Coated Si Anodes by *in-Situ* Microscopy. *Energy Storage Mater.* **2016,** *3*, 45-54.

[378] McDowell, M. T.; Ryu, I.; Lee, S. W.; Wang, C.; Nix, W. D.; Cui, Y. Studying the Kinetics of Crystalline Silicon Nanoparticle Lithiation with *in Situ* Transmission Electron Microscopy. *Adv. Mater.* **2012,** *24*, 6034-6041.

[379] Su, Q.; Xie, D.; Zhang, J.; Du, G.; Xu, B. *In Situ* Transmission Electron Microscopy Observation of the Conversion Mechanism of Fe_2o_3/Graphene Anode During Lithiation-Delithiation Processes. *ACS Nano* **2013,** *7*, 9115-9121.

[380] Huang, Z.; Yao, Y.; Pang, Z.; Yuan, Y.; Li, T.; He, K.; Hu, X.; Cheng, J.; Yao, W.; Liu, Y.; et al. Direct Observation of the Formation and Stabilization of Metallic Nanoparticles on Carbon Supports. *Nat. Commun.* **2020,** *11*, 6373.

[381] Huang, J. Y.; Zhong, L.; Wang, C. M.; Sullivan, J. P.; Xu, W.; Zhang, L. Q.; Mao, S. X.; Hudak, N. S.; Liu, X. H.; Subramanian, A.; et al. *In Situ* Observation of the Electrochemical Lithiation of a Single Sno_2 Nanowire Electrode. *Science* **2010,** *330*, 1515-1520.

[382] Yuan, Y.; Nie, A.; Odegard, G. M.; Xu, R.; Zhou, D.; Santhanagopalan, S.; He, K.; Asayesh-Ardakani, H.; Meng, D. D.; Klie, R. F. Asynchronous Crystal Cell Expansion During Lithiation of K^+-Stabilized *A*-Mno_2. *Nano Lett.* **2015,** *15*, 2998-3007.

[383] Wang, Z. L.; Zhang, Z.; Zhao, Z.; Shao, R.; Sui, M. Mechanism of Electrically Driven Metal-Insulator Phase Transition in Vanadium Dioxide Nanowires. *Acta. Phys. Sin.* **2018,** *67*, 177201.

[384] Zheng, H.; Wang, J.; Huang, J. Y.; Wang, J.; Zhang, Z.; Mao, S. X. Dynamic Process of Phase Transition from Wurtzite to Zinc Blende Structure in Inas Nanowires. *Nano Lett.* **2013,** *13*, 6023-6027.

[385] Huang, J. Y.; Chen, S.; Ren, Z. F.; Chen, G.; Dresselhaus, M. S. Real-Time Observation of Tubule Formation from Amorphous Carbon Nanowires under High-Bias Joule Heating. *Nano Lett.* **2006,** *6*, 1699-1705.

[386] Zhang, J.; Liu, J.; Huang, J. L.; Kim, P.; Lieber, C. M. Creation of Nanocrystals through a Solid-Solid Phase Transition Induced by an Stm Tip. *Science* **1996,** *274*, 757-760.

[387] Kim, J. J.; Park, C.; Yamaguchi, W.; Shiino, O.; Kitazawa, K.; Hasegawa, T. Observation of a Phase Transition from the *T* Phase to the *H* Phase Induced by a Stm Tip in 1*t* Tas_2. *Phys. Rev. B* **1997,** *56*, R15573-R15576.

[388] Cui, J.; Zheng, H.; He, K. *In Situ* Tem Study on Conversion‐Type Electrodes for Rechargeable Ion Batteries. *Adv. Mater.* **2021,** *33*, 2000699.

[389] Li, Y.; Duerloo, K.-A. N.; Wauson, K.; Reed, E. J. Structural Semiconductor-to-Semimetal Phase Transition in Two-Dimensional Materials Induced by Electrostatic Gating. *Nat. Commun.* **2016,** *7*, 10671.

[390] Zheng, S.; Liu, F.; Zhu, C.; Liu, Z.; Fan, H. J. Room-Temperature Electrically Driven Phase Transition of Two-Dimensional 1t-Tas_2 Layers. *Nanoscale* **2017,** *9*, 2436-2441.

[391] Zheng, X.; Han, W.; Yang, K.; Wong, L. W.; Tsang, C. S.; Lai, K. H.; Zheng, F.; Yang, T.; Lau, S. P.; Ly, T. H.; et al. Phase and Polarization Modulation in Two-Dimensional In_2se_3 Via *in Situ* Transmission Electron Microscopy. *Sci. Adv.* **2022,** *8*, eabo0773.

[392] Sato, Y.; Hirayama, T.; Ikuhara, Y. Real-Time Direct Observations of Polarization Reversal in a Piezoelectric Crystal: $Pb(Mg_{1/3}nb_{2/3})O_3$−$Pbtio_3$ Studied Via *in Situ* Electrical Biasing Transmission Electron Microscopy. *Phys. Rev. Lett.* **2011,** *107*, 187601.

[393] Ma, C.; Guo, H.; Beckman, S. P.; Tan, X. Creation and Destruction of Morphotropic Phase Boundaries through Electrical Poling: A Case Study of Lead-Free $(Bi_{1/2}\ Na_{1/2})Tio_3$−$Batio_3$ Piezoelectrics. *Phys. Rev. Lett.* **2012,** *109*, 107602.

[394] Gao, P.; Britson, J.; Nelson, C. T.; Jokisaari, J. R.; Duan, C.; Trassin, M.; Baek, S.-H.; Guo, H.; Li, L.; Wang, Y.; et al. Ferroelastic Domain Switching Dynamics under Electrical and Mechanical Excitations. *Nat. Commun.* **2014,** *5*, 3801.

[395] Tang, M.; Yuan, W.; Ou, Y.; Li, G.; You, R.; Li, S.; Yang, H.; Zhang, Z.; Wang, Y. Recent Progresses on Structural Reconstruction of Nanosized Metal Catalysts Via Controlled-Atmosphere Transmission Electron Microscopy: A Review. *ACS Catal.* **2020,** *10*, 14419-14450.

[396] Fang, K.; Yuan, W.; Wagner, J. B.; Zhang, Z.; Wang, Y., *In-Situ* Gas Transmission Electron Microscopy. In *In-Situ Transmission Electron Microscopy*, Sun, L.; Xu, T.; Zhang, Z., Eds. Springer Nature Singapore: Singapore, 2023; pp 251-325.

[397] Vendelbo, S. B.; Elkjær, C. F.; Falsig, H.; Puspitasari, I.; Dona, P.; Mele, L.; Morana, B.; Nelissen, B. J.; van Rijn, R.; Creemer, J. F.; et al. Visualization of Oscillatory Behaviour of Pt Nanoparticles Catalysing Co Oxidation. *Nat. Mater.* **2014,** *13*, 884-890.

[398] Pu, Y.; He, B.; Niu, Y.; Liu, X.; Zhang, B. Chemical Electron Microscopy (Cem) for Heterogeneous Catalysis at Nano: Recent Progress and Challenges. *Res.* **2023,** *6*, 0043.

[399] Hansen, P. L.; Wagner, J. B.; Helveg, S.; Rostrup-Nielsen, J. R.; Clausen, B. S.; Topsøe, H. Atom-Resolved Imaging of Dynamic Shape Changes in Supported Copper Nanocrystals. *Science* **2002,** *295*, 2053-2055.

[400] He, Y.; Liu, J. C.; Luo, L.; Wang, Y. G.; Zhu, J.; Du, Y.; Li, J.; Mao, S. X.; Wang, C. Size-Dependent Dynamic Structures of Supported Gold Nanoparticles in Co Oxidation Reaction Condition. *Proc. Natl. Acad. Sci.* **2018,** *115*, 7700-7705.

[401] Baldi, A.; Narayan, T. C.; Koh, A. L.; Dionne, J. A. *In Situ* Detection of Hydrogen-Induced Phase Transitions in Individual Palladium Nanocrystals. *Nat. Mater.* **2014,** *13*, 1143-1148.

[402] Narayan, T. C.; Baldi, A.; Koh, A. L.; Sinclair, R.; Dionne, J. A. Reconstructing Solute-Induced Phase Transformations within Individual Nanocrystals. *Nat. Mater.* **2016,** *15*, 768-774.

[403] Hayee, F.; Narayan, T. C.; Nadkarni, N.; Baldi, A.; Koh, A. L.; Bazant, M. Z.; Sinclair, R.; Dionne, J. A. *In-Situ* Visualization of Solute-Driven Phase Coexistence within Individual Nanorods. *Nat. Commun.* **2018,** *9*, 1775.

[404] Angell, D. K.; Bourgeois, B.; Vadai, M.; Dionne, J. A. Lattice-Resolution, Dynamic Imaging of Hydrogen Absorption into Bimetallic Agpd Nanoparticles. *ACS Nano* **2022,** *16*, 1781-1790.

[405] Tao, F.; Grass, M. E.; Zhang, Y.; Butcher, D. R.; Renzas, J. R.; Liu, Z.; Chung, J. Y.; Mun, B. S.; Salmeron, M.; Somorjai, G. A. Reaction-Driven Restructuring of Rh-Pd and Pt-Pd Core-Shell Nanoparticles. *Science* **2008,** *322*, 932-934.

[406] Dai, S.; You, Y.; Zhang, S.; Cai, W.; Xu, M.; Xie, L.; Wu, R.; Graham, G. W.; Pan, X. *In Situ* Atomic-Scale Observation of Oxygen-Driven Core-Shell Formation in Pt_3co Nanoparticles. *Nat. Commun.* **2017,** *8*, 204.

[407] Zhang, X.; Han, S.; Zhu, B.; Zhang, G.; Li, X.; Gao, Y.; Wu, Z.; Yang, B.; Liu, Y.; Baaziz, W. Reversible Loss of Core–Shell Structure for Ni–Au Bimetallic Nanoparticles During Co_2 Hydrogenation. *Nat. Catal.* **2020,** *3*, 411-417.

[408] Yoshida, H.; Takeda, S.; Uchiyama, T.; Kohno, H.; Homma, Y. Atomic-Scale *in-Situ* Observation of Carbon Nanotube Growth from Solid State Iron Carbide Nanoparticles. *Nano Lett.* **2008,** *8*, 2082-2086.

[409] Sharma, R.; Moore, E.; Rez, P.; Treacy, M. M. Site-Specific Fabrication of Fe Particles for Carbon Nanotube Growth. *Nano Lett.* **2009,** *9*, 689-694.

[410] Mazzucco, S.; Wang, Y.; Tanase, M.; Picher, M.; Li, K.; Wu, Z.; Irle, S.; Sharma, R. Direct Evidence of Active and Inactive Phases of Fe Catalyst Nanoparticles for Carbon Nanotube Formation. *J. Catal.* **2014,** *319*, 54-60.

[411] He, M.; Jiang, H.; Liu, B.; Fedotov, P. V.; Chernov, A. I.; Obraztsova, E. D.; Cavalca, F.; Wagner, J. B.; Hansen, T. W.; Anoshkin, I. V.; et al. Chiral-Selective Growth of Single-Walled Carbon Nanotubes on Lattice-Mismatched Epitaxial Cobalt Nanoparticles. *Sci. Rep.* **2013,** *3*, 1460.

[412] Lin, P. A.; Gomez-Ballesteros, J. L.; Burgos, J. C.; Balbuena, P. B.; Natarajan, B.; Sharma, R. Direct Evidence of Atomic-Scale Structural Fluctuations in Catalyst Nanoparticles. *J. Catal.* **2017,** *349*, 149-155.

[413] Wang, Y.; Qiu, L.; Zhang, L.; Tang, D.; Ma, R.; Wang, Y.; Zhang, B.; Ding, F.; Liu, C.; Cheng, H. Precise Identification of the Active Phase of Cobalt Catalyst for Carbon Nanotube Growth by *in Situ* Transmission Electron Microscopy. *ACS Nano* **2020,** *14*, 16823-16831.

[414] Han, S.; Xia, G. J.; Cai, C.; Wang, Q.; Wang, Y. G.; Gu, M.; Li, J. Gas-Assisted Transformation of Gold from *Fcc* to the Metastable 4h Phase. *Nat. Commun.* **2020,** *11*, 552.

[415] Han, S.; Cai, C.; Xia, G. j.; Sun, C.; Shi, X.; Zhou, W.; Li, J.; Wang, Y. G.; Gu, M. Carbon Monoxide Gas Induced 4h-to-*Fcc* Phase Transformation of Gold as Revealed by *in-Situ* Transmission Electron Microscopy. *Inorg. Chem.* **2020,** *59*, 14415-14423.

[416] Kim, B. H.; Yang, J.; Lee, D.; Choi, B. K.; Hyeon, T.; Park, J. Liquid‐Phase Transmission Electron Microscopy for Studying Colloidal Inorganic Nanoparticles. *Adv. Mater.* **2018,** *30*, 1703316.

[417] Zhu, C.; Wang, W.; Liao, H.; Sun, L., *In-Situ* Liquid Cell Tem. In *In-Situ Transmission Electron Microscopy*, Springer: 2023; pp 221-250.

[418] Marton, L. La Microscopie Electronique Des Objets Biologiques. *Bull. Acad. Roy. Med. Belg* **1935,** *21*, 600-617.

[419] Williamson, M. J.; Tromp, R. M.; Vereecken, P. M.; Hull, R.; Ross, F. M. Dynamic Microscopy of Nanoscale Cluster Growth at the Solid–Liquid Interface. *Nat. Mater.* **2003,** *2*, 532-536.

[420] Liu, K. L.; Wu, C. C.; Huang, Y. J.; Peng, H. L.; Chang, H. Y.; Chang, P.; Hsu, L.; Yew, T. R. Novel Microchip for *in Situ* Tem Imaging of Living Organisms and Bio-Reactions in Aqueous Conditions. *Lab on a Chip* **2008,** *8*, 1915-1921.

[421] Yuk, J. M.; Park, J.; Ercius, P.; Kim, K.; Hellebusch, D. J.; Crommie, M. F.; Lee, J. Y.; Zettl, A.; Alivisatos, A. P. High-Resolution Em of Colloidal Nanocrystal Growth Using Graphene Liquid Cells. *Science* **2012,** *336*, 61-64.

[422] Liao, H. G.; Zherebetskyy, D.; Xin, H.; Czarnik, C.; Ercius, P.; Elmlund, H.; Pan, M.; Wang, L. W.; Zheng, H. Facet Development During Platinum Nanocube Growth. *Science* **2014,** *345*, 916-919.

[423] Zhu, C.; Liang, S.; Song, E.; Zhou, Y.; Wang, W.; Shan, F.; Shi, Y.; Hao, C.; Yin, K.; Zhang, T.; et al. *In-Situ* Liquid Cell Transmission Electron Microscopy Investigation on Oriented Attachment of Gold Nanoparticles. *Nat. Commun.* **2018,** *9*, 421.

[424] de Yoreo, J. J.; Sommerdijk, N. A. J. M. Investigating Materials Formation with Liquid-Phase and Cryogenic Tem. *Nat. Rev. Mater.* **2016,** *1*, 16035.

[425] Stricker, E. A.; Ke, X.; Wainright, J. S.; Unocic, R. R.; Savinell, R. F. Current Density Distribution in Electrochemical Cells with Small Cell Heights and Coplanar Thin Electrodes as Used in Ec-S/Tem Cell Geometries. *J. Electrochem. Soc.* **2019,** *166*, H126.

[426] Algara-Siller, G.; Lehtinen, O.; Wang, F. C.; Nair, R. R.; Kaiser, U.; Wu, H. A.; Geim, A. K.; Grigorieva, I. V. Square Ice in Graphene Nanocapillaries. *Nature* **2015,** *519*, 443-445.

[427] Hou, Y.; Dai, Z.; Zhang, S.; Feng, S.; Wang, G.; Liu, L.; Xu, Z.; Li, Q.; Zhang, Z. Elastocapillary Cleaning of Twisted Bilayer Graphene Interfaces. *Nat. Commun.* **2021,** *12*, 5069.

[428] Hong, J.; Bae, J. H.; Jo, H.; Park, H. Y.; Lee, S.; Hong, S. J.; Chun, H.; Cho, M. K.; Kim, J.; Kim, J.; et al. Metastable Hexagonal Close-Packed Palladium Hydride in Liquid Cell Tem. *Nature* **2022,** *603*, 631-636.

[429] Wang, Y.; Peng, X.; Abelson, A.; Xiao, P.; Qian, C.; Yu, L.; Ophus, C.; Ercius, P.; Wang, L. W.; Law, M.; et al. Dynamic Deformability of Individual Pbse Nanocrystals During Superlattice Phase Transitions. *Sci. Adv.* **2019,** *5*, eaaw5623.

[430] Ohno, Y. Development of an Apparatus for *in-Situ* near-Field Photoexcitation in a Transmission Electron Microscope. *Appl. Phys. Express* **2012,** *5*, 125204.

[431] Cai, S.; Gu, C.; Wei, Y.; Gu, M.; Pan, X.; Wang, P. Development of *in Situ* Optical-Electrical Mems Platform for Semiconductor Characterization. *Ultramicroscopy* **2018,** *194*, 57-63.

[432] Dong, H.; Xu, T.; Sun, Z.; Zhang, Q.; Wu, X.; He, L.; Xu, F.; Sun, L. Simultaneous Atomic-Level Visualization and High Precision Photocurrent Measurements on Photoelectric Devices by *in Situ* Tem. *RSC Adv.* **2018,** *8*, 948-953.

[433] Vadai, M.; Angell, D. K.; Hayee, F.; Sytwu, K.; Dionne, J. A. *In-Situ* Observation of Plasmon-Controlled Photocatalytic Dehydrogenation of Individual Palladium Nanoparticles. *Nat. Commun.* **2018,** *9*, 4658.

[434] Funk, H.; Shargaieva, O.; Eljarrat, A.; Unger, E. L.; Koch, C. T.; Abou-Ras, D. In Situ Tem Monitoring of Phase-Segregation in Inorganic Mixed Halide Perovskite. *J. Phys. Chem. Lett.* **2020,** *11*, 4945-4950.

[435] Liu, Q. M.; Wu, D. d.; Li, Z. A.; Shi, L. Y.; Wang, Z. X.; Zhang, S. J.; Lin, T.; Hu, T. C.; Tian, H. F.; Li, J. Q. Photoinduced Multistage Phase Transitions in Ta_2nise_5. *Nat. Commun.* **2021,** *12*, 2050.

[436] Xiang, B.; Hwang, D. J.; In, J. B.; Ryu, S. G.; Yoo, J. H.; Dubon, O.; Minor, A. M.; Grigoropoulos, C. P. *In Situ* Tem near-Field Optical Probing of Nanoscale Silicon Crystallization. *Nano Lett.* **2012,** *12*, 2524-2529.

[437] Si, C.; Choe, D.; Xie, W.; Wang, H.; Sun, Z.; Bang, J.; Zhang, S. Photoinduced Vacancy Ordering and Phase Transition in $Mote_2$. *Nano Lett.* **2019,** *19*, 3612-3617.

[438] Hubert, A.; Schäfer, R., *Magnetic Domains: The Analysis of Magnetic Microstructures*. Springer Science & Business Media: 2008.

[439] Zhang, S.; Zhang, J.; Wen, Y.; Chudnovsky, E. M.; Zhang, X. X. Creation of a Thermally Assisted Skyrmion Lattice in Pt/Co/Ta Multilayer Films. *Appl. Phys. Lett.* **2018,** *113*, 192403.

[440] Zhang, J.; Zhu, S.; Li, H.; Zhu, L.; Hu, Y.; Xia, W.; Zhang, X.; Peng, Y.; Fu, J. Direct Observation of Dynamical Magnetization Reversal Process Governed by Shape Anisotropy in Single $Nife_2o_4$ Nanowire. *Nanoscale* **2018,** *10*, 10123-10129.

[441] Chapman, J. The Investigation of Magnetic Domain Structures in Thin Foils by Electron Microscopy. *J. Phys. D: Appl. Phys.* **1984,** *17*, 623.

[442] Daykin, A.; Petford-Long, A. K. Quantitative Mapping of the Magnetic Induction Distribution Using Foucault Images Formed in a Transmission Electron Microscope. *Ultramicroscopy* **1995,** *58*, 365-380.

[443] Shindo, D.; Murakami, Y. Electron Holography of Magnetic Materials. *J. Phys. D: Appl. Phys.* **2008,** *41*, 183002.

[444] Chapman, J. N.; Ploessl, R.; Donnet, D. M. Differential Phase Contrast Microscopy of Magnetic Materials. *Ultramicroscopy* **1992,** *47*, 331-338.

[445] Masseboeuf, A.; Gatel, C.; Bayle-Guillemaud, P.; Lamy, Y.; Viala, B. The Use of Lorentz Microscopy for the Determination of Magnetic Reversal Mechanism of Exchange-Biased $Co_{30}fe_{70}$/Nimn Bilayer. *J. Magn. Magn. Mater.* **2009,** *321*, 3080-3083.

[446] Chen, C.; Idzerda, Y.; Lin, H.; Smith, N.; Meigs, G.; Chaban, E.; Ho, G.; Pellegrin, E.; Sette, F. Experimental Confirmation of the X-Ray Magnetic Circular Dichroism Sum Rules for Iron and Cobalt. *Phys. Rev. Lett.* **1995,** *75*, 152.

[447] Yamamoto, K.; Hogg, C. R.; Yamamuro, S.; Hirayama, T.; Majetich, S. A. Dipolar Ferromagnetic Phase Transition in Fe_3o_4 Nanoparticle Arrays Observed by Lorentz Microscopy and Electron Holography. *Appl. Phys. Lett.* **2011,** *98*, 072509.

[448] Bartolo, M.; Amaral, J. J.; Hirst, L. S.; Ghosh, S. Directed Assembly of Magnetic and Semiconducting Nanoparticles with Tunable and Synergistic Functionality. *Sci. Rep.* **2019,** *9*, 15784.

[449] Yu, X.; DeGrave, J. P.; Hara, Y.; Hara, T.; Jin, S.; Tokura, Y. Observation of the Magnetic Skyrmion Lattice in a Mnsi Nanowire by Lorentz Tem. *Nano Lett.* **2013,** *13*, 3755-3759.

[450] Nayak, A. K.; Kumar, V.; Ma, T.; Werner, P.; Pippel, E.; Sahoo, R.; Damay, F.; Rößler, U. K.; Felser, C.; Parkin, S. S. P. Magnetic Antiskyrmions above Room Temperature in Tetragonal Heusler Materials. *Nature* **2017,** *548*, 561-566.

[451] Zhu, S.; Fu, J.; Li, H.; Zhu, L.; Hu, Y.; Xia, W.; Zhang, X.; Peng, Y.; Zhang, J. Direct Observation of Magnetocrystalline Anisotropy Tuning Magnetization Configurations in Uniaxial Magnetic Nanomaterials. *ACS Nano* **2018,** *12*, 3442-3448.

[452] Du, H.; Zhao, X.; Rybakov, F. N.; Borisov, A. B.; Wang, S.; Tang, J.; Jin, C.; Wang, C.; Wei, W.; Kiselev, N. S.; et al. Interaction of Individual Skyrmions in a Nanostructured Cubic Chiral Magnet. *Phys. Rev. Lett.* **2018,** *120*, 197203.

[453] Hossain, M.; Qin, B.; Li, B.; Duan, X. Synthesis, Characterization, Properties and Applications of Two-Dimensional Magnetic Materials. *Nano Today* **2022,** *42*, 101338.

[454] Wu, Y.; Zhang, S.; Zhang, J.; Wang, W.; Zhu, Y. L.; Hu, J.; Yin, G.; Wong, K.; Fang, C.; Wan, C.; et al. Néel-Type Skyrmion in Wte_2/Fe_3gete_2 Van Der Waals Heterostructure. *Nat. Commun.* **2020,** *11*, 3860.

[455] Lyu, B.; Wang, L.; Gao, Y.; Guo, S.; Zhou, X.; Hao, Z.; Wang, S.; Zhao, Y.; Huang, L.; Shao, J.; et al. Structural and Magnetic Phase Transitions in Quasi-Two-Dimensional Vbr_3. *Phys. Rev. B* **2022,** *106*, 085430.

[456] Yu, X. Z.; Onose, Y.; Kanazawa, N.; Park, J. H.; Han, J. H.; Matsui, Y.; Nagaosa, N.; Tokura, Y. Real-Space Observation of a Two-Dimensional Skyrmion Crystal. *Nature* **2010,** *465*, 901-904.

[457] Li, M.; Rai, A.; Pokhrel, A.; Sapkota, A.; Mewes, C.; Mewes, T.; Graef, M. D.; Sokalski, V. Formation of Zero-Field Skyrmion Arrays in Asymmetric Superlattices. *Appl. Phys. Lett.* **2020,** *117*, 112403.

[458] He, M.; Peng, L.; Zhu, Z.; Li, G.; Cai, J.; Li, J.; Wei, H.; Gu, L.; Wang, S.; Zhao, T.; et al. Realization of Zero-Field Skyrmions with High-Density Via Electromagnetic Manipulation in Pt/Co/Ta Multilayers. *Appl. Phys. Lett.* **2017,** *111*, 202403.

[459] Pollard, S. D.; Garlow, J. A.; Yu, J.; Wang, Z.; Zhu, Y.; Yang, H. Observation of Stable Néel Skyrmions in Cobalt/Palladium Multilayers with Lorentz Transmission Electron Microscopy. *Nat. Commun.* **2017,** *8*, 14761.

[460] Ovshinsky, S. R. Reversible Electrical Switching Phenomena in Disordered Structures. *Phys. Rev. Lett.* **1968,** *21*, 1450.

[461] Gu, Q. F.; Krauss, G.; Steurer, W.; Gramm, F.; Cervellino, A. Unexpected High Stiffness of Ag and Au Nanoparticles. *Phys. Rev. Lett.* **2008,** *100*, 045502.

[462] Leach, A. M.; McDowell, M.; Gall, K. Deformation of Top-Down and Bottom-up Silver Nanowires. *Adv. Funct. Mater.* **2007,** *17*, 43-53.

[463] Wu, B.; Heidelberg, A.; Boland, J. J.; Sader, J. E.; Sun; Li, Y. Microstructure-Hardened Silver Nanowires. *Nano Lett.* **2006,** *6*, 468-472.

[464] Wang, S.; Wu, Y.; Lin, L.; He, Y.; Huang, H. Fracture Strain of Sic Nanowires and Direct Evidence of Electron‐Beam Induced Amorphisation in the Strained Nanowires. *Small* **2015,** *11*, 1672-1676.

[465] Liu, L.; He, B.; Huang, M. The Role of Transformation‐Induced Plasticity in the Development of Advanced High Strength Steels. *Adv. Eng. Mater.* **2018,** *20*, 1701083.

[466] Olson, G.; Cohen, M. A Mechanism for the Strain-Induced Nucleation of Martensitic Transformations. *J. Less-Common Met.* **1972,** *28*, 107-118.

[467] Yang, X.-S.; Sun, S.; Ruan, H.-H.; Shi, S.-Q.; Zhang, T.-Y. Shear and Shuffling Accomplishing Polymorphic *Fcc Γ→Hcp Ε→Bct Α* Martensitic Phase Transformation. *Acta Mater.* **2017,** *136*, 347-354.

[468] Chen, S.; Oh, H. S.; Gludovatz, B.; Kim, S. J.; Park, E. S.; Zhang, Z.; Ritchie, R. O.; Yu, Q. Real-Time Observations of Trip-Induced Ultrahigh Strain Hardening in a Dual-Phase Crmnfeconi High-Entropy Alloy. *Nat. Commun.* **2020,** *11*, 826.

[469] Cheng, X.; Li, Y.; Shang, J.; Hu, C.; Ren, Y.; Liu, M.; Qi, Z. Thickness-Dependent Phase Transition and Optical Behavior of Mos$_2$ Films under High Pressure. *Nano Res.* **2018,** *11*, 855-863.

[470] Liu, W.-T.; Cao, J.; Fan, W.; Hao, Z.; Martin, M. C.; Shen, Y.; Wu, J.; Wang, F. Intrinsic Optical Properties of Vanadium Dioxide near the Insulator-Metal Transition. *Nano Lett.* **2011,** *11*, 466-470.

[471] Tripathi, A. K.; Singh, M. K.; Mathpal, M. C.; Mishra, S. K.; Agarwal, A. Study of Structural Transformation in Tio$_2$ Nanoparticles and Its Optical Properties. *J. Alloy. Compd.* **2013,** *549*, 114-120.

[472] Kole, A. K.; Kumbhakar, P. Cubic-to-Hexagonal Phase Transition and Optical Properties of Chemically Synthesized Zns Nanocrystals. *Results in Physics* **2012,** *2*, 150-155.

[473] Tan, S. J.; Abdelwahab, I.; Ding, Z.; Zhao, X.; Yang, T.; Loke, G. Z. J.; Lin, H.; Verzhbitskiy, I.; Poh, S. M.; Xu, H.; et al. Chemical Stabilization of 1t′ Phase Transition Metal Dichalcogenides with Giant Optical Kerr Nonlinearity. *J. Am. Chem. Soc.* **2017,** *139*, 2504-2511.

[474] Zardo, I.; Yazji, S.; Marini, C.; Uccelli, E.; Fontcuberta i Morral, A.; Abstreiter, G.; Postorino, P. Pressure Tuning of the Optical Properties of Gaas Nanowires. *ACS Nano* **2012,** *6*, 3284-3291.

[475] Li, B.; Wen, X.; Li, R.; Wang, Z.; Clem, P. G.; Fan, H. Stress-Induced Phase Transformation and Optical Coupling of Silver Nanoparticle Superlattices into Mechanically Stable Nanowires. *Nat. Commun.* **2014,** *5*, 4179.

[476] Ke, Y.; Zhou, C.; Zhou, Y.; Wang, S.; Chan, S. H.; Long, Y. Emerging Thermal‐Responsive Materials and Integrated Techniques Targeting the Energy‐Efficient Smart Window Application. *Adv. Funct. Mater.* **2018,** *28*, 1800113.

[477] Wu, C.; Feng, F.; Xie, Y. Design of Vanadium Oxide Structures with Controllable Electrical Properties for Energy Applications. *Chem. Soc. Rev.* **2013,** *42*, 5157-5183.

[478] Barker Jr, A. S.; Verleur, H. W.; Guggenheim, H. J. Infrared Optical Properties of Vanadium Dioxide above and Below the Transition Temperature. *Phys. Rev. Lett.* **1966,** *17*, 1286.

[479] Banerjee, A.; Bernoulli, D.; Zhang, H.; Yuen, M.-F.; Liu, J.; Dong, J.; Ding, F.; Lu, J.; Dao, M.; Zhang, W.; et al. Ultralarge Elastic Deformation of Nanoscale Diamond. *Science* **2018,** *360*, 300-302.

[480] Radisavljevic, B.; Radenovic, A.; Brivio, J.; Giacometti, V.; Kis, A. Single-Layer Mos$_2$ Transistors. *Nat. Nanotechnol.* **2011,** *6*, 147-150.

[481] Kadantsev, E. S.; Hawrylak, P. Electronic Structure of a Single Mos$_2$ Monolayer. *Solid State Commun.* **2012,** *152*, 909-913.

[482] Hu, T.; Li, R.; Dong, J. A New (2×1) Dimerized Structure of Monolayer 1t-Molybdenum Disulfide, Studied from First Principles Calculations. *J. Chem. Phys.* **2013,** *139*, 174702.

[483] Qian, X.; Liu, J.; Fu, L.; Li, J. Quantum Spin Hall Effect in Two-Dimensional Transition Metal Dichalcogenides. *Science* **2014,** *346*, 1344-1347.

[484] Zheng, Q.; Wang, Y.; Zhu, J. Nanoscale Phase-Change Materials and Devices. *J. Phys. D: Appl. Phys.* **2017,** *50*, 243002.

[485] Koethe, T. C.; Hu, Z.; Haverkort, M. W.; Schüßler-Langeheine, C.; Venturini, F.; Brookes, N. B.; Tjernberg, O.; Reichelt, W.; Hsieh, H. H.; Lin, H. J. Transfer of Spectral Weight and Symmetry across the Metal-Insulator Transition in Vo$_2$. *Phys. Rev. Lett.* **2006,** *97*, 116402.

[486] Balandin, A. A. Thermal Properties of Graphene and Nanostructured Carbon Materials. *Nat. Mater.* **2011,** *10*, 569-581.

[487] Wu, C.; Feng, F.; Feng, J.; Dai, J.; Peng, L.; Zhao, J.; Yang, J.; Si, C.; Wu, Z.; Xie, Y. Hydrogen-Incorporation Stabilization of Metallic Vo_2(R) Phase to Room Temperature, Displaying Promising Low-Temperature Thermoelectric Effect. *J. Am. Chem. Soc.* **2011,** *133*, 13798-13801.

[488] Sun, S.; Murray, C. B. Synthesis of Monodisperse Cobalt Nanocrystals and Their Assembly into Magnetic Superlattices. *J. Appl. Phys.* **1999,** *85*, 4325-4330.

[489] Petit, C.; Taleb, A.; Pileni, M. Cobalt Nanosized Particles Organized in a 2d Superlattice: Synthesis, Characterization, and Magnetic Properties. *J. Phys. Chem. B* **1999,** *103*, 1805-1810.

[490] Yang, H. T.; Shen, C. M.; Su, Y. K.; Yang, T. Z.; Gao, H. J.; Wang, Y. G. Self-Assembly and Magnetic Properties of Cobalt Nanoparticles. *Appl. Phys. Lett.* **2003,** *82*, 4729-4731.

[491] Liu, K.; Lee, S.; Yang, S.; Delaire, O.; Wu, J. Recent Progresses on Physics and Applications of Vanadium Dioxide. *Mater. Today* **2018,** *21*, 875-896.

[492] Wu, C.; Zhang, X.; Dai, J.; Yang, J.; Wu, Z.; Wei, S.; Xie, Y. Direct Hydrothermal Synthesis of Monoclinic Vo_2(M) Single-Domain Nanorods on Large Scale Displaying Magnetocaloric Effect. *J. Mater. Chem* **2011,** *21*, 4509-4517.

[493] Zhou, X.; Zhang, A.; Chen, B.; Zhu, S.; Cui, Y.; Bai, L.; Yu, J.; Ge, Y.; Yun, Q.; Li, L.; et al. Synthesis of 2h/Fcc-Heterophase Aucu Nanostructures for Highly Efficient Electrochemical Co_2 Reduction at Industrial Current Densities. *Adv. Mater.* **2023,** *n/a*, 2304414.

[494] Geng, X.; Sun, W.; Wu, W.; Chen, B.; Al Hilo, A.; Benamara, M.; Zhu, H.; Watanabe, F.; Cui, J.; Chen, T. Pure and Stable Metallic Phase Molybdenum Disulfide Nanosheets for Hydrogen Evolution Reaction. *Nat. Commun.* **2016,** *7*, 10672.

[495] Feng, Y.; Gong, S.; Du, E.; Chen, X.; Qi, R.; Yu, K.; Zhu, Z. 3r Tas_2 Surpasses the Corresponding 1t and 2h Phases for the Hydrogen Evolution Reaction. *J. Phys. Chem. C* **2018,** *122*, 2382-2390.

[496] Wang, Y.; Li, C.; Fan, Z.; Chen, Y.; Li, X.; Cao, L.; Wang, C.; Wang, L.; Su, D.; Zhang, H.; et al. Undercoordinated Active Sites on 4h Gold Nanostructures for Co_2 Reduction. *Nano Lett.* **2020,** *20*, 8074-8080.

[497] Qiu, Y.; Xin, L.; Li, Y.; McCrum, I. T.; Guo, F.; Ma, T.; Ren, Y.; Liu, Q.; Zhou, L.; Gu, S.; et al. Bcc-Phased Pdcu Alloy as a Highly Active Electrocatalyst for Hydrogen Oxidation in Alkaline Electrolytes. *J. Am. Chem. Soc.* **2018,** *140*, 16580-16588.

[498] Yao, Y., Modulating *Fcc* and *Hcp* Ruthenium on the Surface of Palladium-Copper Alloy through Tunable Lattice Mismatch. In *Controllable Synthesis and Atomic Scale Regulation of Noble Metal Catalysts*, Springer: 2022; pp 33-53.